Nuclear Analyses for Shielding Design of the Divertor Tokamak Test (DTT) Facility

Ph.D. candidate

Andrea Colangeli

Internal Supervisor

Prof. Romolo Remetti

External Supervisor

Dr. Rosaria Villari

SAPIENZA
UNIVERSITÀ DI ROMA

Nuclear Analyses for Shielding Design of the Divertor Tokamak Test (DTT) Facility

PhD Energy and Environment – XXXIII cycle

Coordinator
Prof. Massimo Corcione

Ph.D. candidate
Andrea Colangeli

Internal Supervisor
Prof. Romolo Remetti

External Supervisor
Dr. Rosaria Villari

SAPIENZA
UNIVERSITÀ DI ROMA

ENEA
Agenzia nazionale per le nuove tecnologie, l'energia e lo sviluppo economico sostenibile

© Tutti i diritti riservati - All rights reserved

Ad Alessandro, Flavio, Filippo e Leonardo.

Perché ogni giorno mi ricordate cos'è la curiosità.

A voi l'augurio di non dimenticarlo mai.

"Guardate l'idrogeno tacere nel mare, guardate l'ossigeno al suo fianco dormire.
Soltanto la legge che io riesco a capire ha potuto sposarli senza farli scoppiare, soltanto la legge che io riesco a capire"

Fabrizio de André

Summary

List of Figures

List of Tables

Introduction

The main goal for nuclear fusion research is to make a new energy source available which is clean, inexhaustible, safety and economically competitive. Fusion energy will substantially contribute to reduce the use of fossil resources with great benefit for the environment and for the energy supply. Two different method, since the start of fusion research, have been used to try to gain energy from fusion processes: magnetic and inertial confinement. In our understanding, the first one is the most promising method of achieving a fusion power plant, providing an important contribution to sustain energy supply.

Fusion energy enumerates several advantages with respect to the other energy types. It is clean because there are no greenhouse gas emissions; it is powerful since a single fusion event release about 17 MeV while combustion reaction generates at most few eV per event. Comparted with nuclear fission, fusion is intrinsically safe since only a very small amount of fuels are present in the reactor chamber at any time and any failure results in a rapid shutdown and, in a fusion machine, chain reactions cannot occur so that meltdown accidents are not possible.

Furthermore, the hazards of a fusion device related with the radioactive waste are very low for some simple reason:

- The reactor components that are activated (the structures close to the plasma fuel) will decay over several decades allowing possible reuse in about 100 year or less: this is a very short time with respect to the fission radioactive waste which can decade even after thousands of years.
- The only radioactive fuel burned in a D-T fusion reactor is Tritium, a radioactive isotope of hydrogen with a half-life of 12.3 years. It is a

low energy beta emitter so not dangerous externally (beta particles don't overcome the skin thickness), but it is a radiation hazard when inhaled, ingested via food or water.

Another advantage of fusion energy is that the basic fuel for the easiest fusion reaction to accomplish on Earth, which is the following:

$$D+T \rightarrow {}^{4}He + n + 17.586\ MeV$$

are abundant and widely distributed around the world. In fact, Deuterium can be extracted from seawater and Tritium can be produced in the so-called breather blanket (a Li-based structures around the reactor chamber) from the reaction between Li and the neutron formed by the D+T reaction, according to:

$$^{7}Li + n \rightarrow {}^{4}He + T + n - 2.47\ MeV$$

$$^{6}Li + n \rightarrow {}^{4}He + T + 4.8\ MeV$$

Lithium, from which Tritium can be produced within the reactor, is a readily available metal in the Earth crust. Then in the future fusion plants such as ITER[1] (International Thermonuclear Experimental Reactor) and DEMO[2] (Demonstration Power Plant) reactor, Tritium will be produced in the Li-based breeding blanket surrounding the fusion chamber.

Several steps must be done before arriving to the realisation of a fusion power plant, suitable to deliver the energy around the World. Many years of research and experiments related to several aspects involved in the thermonuclear fusion field, have taught which are the most critical points for the fusion science.

Among these points, one of the most important, indicated as a possible *showstopper* for the fusion, is the *power exhaust* issue. The great amount of energy released from the nuclear fusion reactions inside the plasma could damage the surrounding

[1] www.iter.org

[2] See Appendix D: "*DEMO Fusion Power Plant: scope and main Parameters"*

structures of the tokamak. In particular, those particles which could escape from the confinement, finish their life in a component called *divertor*. This component is particularly stressed by the heat loads, which could arise to the impressive value of 50 MW/m^2, foreseen in ITER.

Such a big power density can damage every known material in a non-reversible way. Thus, is of primary importance to study every possible plasma configuration and every feasible material and cooling systems which can work under these amount of power heat loads.

For this reason, a facility called Divertor Tokamak Test (DTT)[3], has been planned in the "*roadmap to the fusion energy*"[4] with the aim at studying and testing different divertor concepts in a reactor-scale environment.

The DTT facility will be built in Italy, within the ENEA Frascati research centre[5], in the next decade. In its high-performance phase (H-mode), DTT will produce a great amount of neutrons equal to 1.5x10^{17} n/s from DD reactions:

$$D+D \rightarrow {}^{3}He + n + 3.27\ MeV \quad (50\%)$$

$$D+D \rightarrow {}^{3}H + n + 4.03\ MeV \quad (50\%)$$

Furthermore, a 1% of DT neutron production is also foreseen due to the triton burn-up inside the plasma.

For this reason, the nuclear analyses in support of DTT is of paramount importance since the beginning phase of the project. Neutronics plays a fundamental role in the definition of the shielding needs to respect the design constraints and radiological limits for non-radiation workers and for the public.

[3] https://www.dtt-project.it/#
[4] See Appendix C: "*Roadmap to Fusion Energy*"
[5] https://www.enea.it/

This work of thesis is devoted to the three-dimensional neutronics analyses in support of the DTT development and, to the analyses for the shielding design of machine and buildings.

After an introduction related to the particle interaction and shielding, carried out in the first chapter, a description of the fusion neutronics and the codes used to perform the neutronics calculation for DTT is reported in chapter two.

The description of the engineering design of the machine and the site layout is given in chapter three.

Chapter four gives a description of the strategy used for the DTT neutronics. In particular, two Monte Carlo MCNP[6] model are presented as the reference models used to carry out the analyses.

In chapter five the calculations performed to assess the thickness of the Torus Hall Building (THB) is presented with a sensitivity study of different shielding materials and thicknesses.

Chapter six shows the analyses performed to assess the level of the effective dose due to the Skyshine effects and, thus, the thickness of the THB roof.

Several penetrations in the THB due to the auxiliary system transmission lines (i.e. Heating Systems, cooling systems, diagnostics) is planned. These penetrations can cause a large neutron streaming through the holes and have a big impact on the level of doses outside the building. In the chapter seven, the study of neutron streaming through penetrations in the south and east area of the DTT THB is presented with some solutions to mitigate their impact.

Chapter eight shows the integration of an auxiliary component inside the machine. The Nuclear loads on the Electron Cyclotron Resonance Heating (ECRH) equatorial

[6] https://mcnp.lanl.gov/

launcher have been assessed as well as the evaluation of the contact dose rate and the Shut Down Dose Rate (SDDR).

In the last part, conclusions of the work will be presented as well as the future development of the work for DTT neutronics.

1 Principle of radiation shielding

"Stands at the sea, wonders at wondering:
I a universe of atoms in an atom in the Universe"
R. P. Feynman

The fuel used in a Tokamak Device is a fully ionized gas at temperature around 100 million °C. It is the results of the fusion nuclear reactions[7] listed below:

D+T → 4He + n + 17.586 MeV

D+D → ^{3}He + n + 3.27 MeV (50%)

D+D → ^{3}H + n + 4.03 MeV (50%)

Neutrons represents one of the reaction products and, depending on the operating conditions of the machine (DD or DT reactions), they have high energy, typically 2.45 or 14.1 MeV energy peak. Neutrons interact with surrounding structures of the devices and, by escaping from them, with the buildings and people causing multiple effects. For these reasons, is of fundamental importance to know the basis of their interaction with matter in order to prevent damages on materials and protect people and workers. In this chapter a general overview of these interactions will be given.

1.1 Neutron Reaction Cross-Section

Neutrons are uncharged particles and so, their interactions rely on collisions with nuclei where they can be scattered, elastically or with energy loss or absorbed, with subsequent emission of secondary particles. The most important parameter that

[7] See Appendix A: "*Nuclear Reactions*" and Appendix B: "*Thermonuclear Fusion*"

determines how often a neutron interacts with matter is the cross section. The cross section is defined as the "effective size of the nucleus". It is an area, and its unit of measurement is the Barn[8]. It represents, in a broad sense, the likelihood of a neutron undergoing a specific reaction as a function of energy and/or angle. In fig. 1.1 the energy dependent cross section for a number of reactions.

In the region of energy below 1 keV the cross sections show the typical 1/v behaviour. At later energy there is the resonance region and the fast region. In the fast region, typically greater than 1 MeV, the neutron cross section can sometimes increase with the increase of the energy due to the increasing probability of reaction, this is where reaction channel widths are increasing, and threshold reactions can take place.

The resonance region of the cross section is due to the nuclear resonances, which are the discrete levels in the compound nucleus. These levels have a high probability of formation and very small widths, hence if there are a large number of these energy levels, it can be very hard to distinguish between the adjacent values resonances.

The so-called "$1/v$" region of the cross – section is due to the thermal wavelength that become the dominant factor at those energies.

[8] 1 barn = 10^{-24} cm^2

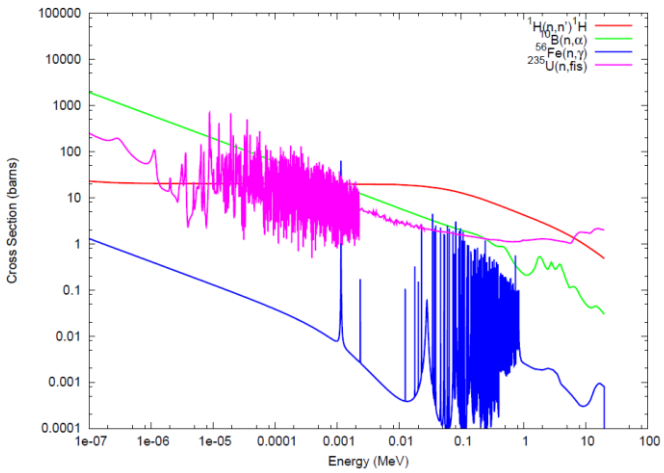

Figure 1-1 Energy dependent cross-section for some interesting reactions

Very far from a resonance, when the exit channel is independent of the neutron energies [1] the behaviour of the cross section is described by the Bright and Wigner formula, showed below:

$$\sigma \approx \frac{\pi}{k^2} \frac{\Gamma_a \Gamma_b}{(E - E_r)^2 + \frac{\Gamma^2}{4}} \propto \frac{1}{v} \qquad (1.1)$$

Where σ is the total cross section of the reaction in cm^2, k is the neutron wave length in cm^{-1}, Γa and Γb are the width of the incoming and outgoing reaction channels respectively in eV, Γ is the total width of the channels in eV, E_r is the energy of the resonance in eV and v is the neutron velocity in cm s^{-1}. The thermal region of the cross section is where the capture is more probable.

It's worth noting that, for fast neutrons, the total cross section follows the scaling law [2]:

$$\sigma_T = 2\pi(1.4A^{\frac{1}{3}} + 1.2)^2 fm^2 \propto 2\pi r^2 \qquad (1.2)$$

Where σ_T is the total cross section in cm^2, A is the number of nucleons and r is the nuclear radius in cm.

1.2 Neutron interaction with matter

Neutrons interact with matter in several ways, but they can be summarized in two groups:

- Scattering: elastic scattering and inelastic scattering
- Absorption: fission, radiative capture, multiplication and charged particle emission

Every interaction has its own cross section that gives the probability that a reaction can occur.

1.2.1 Elastic Scattering

In the process called elastic scattering, the neutron interacts with a nucleus and the total kinetic energy of the system (nucleus + incident neutron) is conserved. Thus, a fraction of the kinetic energy of the incident neutron is transferred to the nucleus during the interaction.

The average energy loss from neutron due to the interaction is:

$$\frac{dE}{E} = \frac{2EA}{(A+1)^2} \qquad (1.3)$$

Where E is the energy of the incoming neutron and A is the mass number of the nucleus. From the equation is clear that to moderate a neutron with as low interaction as possible, an element with small mass number is necessary. If we use Hydrogen (A=1) the energy loss during an interaction is E/2. A neutron with incoming energy E=2 MeV needs 27 interactions before reaching the thermal energy of 0.025 eV.

1.2.2 Inelastic Scattering

In an inelastic interaction the target nucleus undergoes an excited state. The process is very similar to the elastic scattering. From the decay of the formed compound nucleus a gamma radiation is released. The total kinetic energy of the system (incident neutron + target nucleus) after the reaction is less than that before the interaction. The energy difference is necessary to excite the target nucleus. As for the elastic scattering, the final effect is to slow down the incident neutron and change its direction. This process can only occur once the neutron has enough energy (0.1-10 MeV) to raise the target nucleus to its first excited state.

The inelastic scattering is possible only if the target nucleus has excited states and it is the most effective process to slow down high energy neutrons in heavy metal media like iron.

1.2.3 Radiative capture

The radiative capture is also called the *(n, γ) reaction*. During this process the neutron can be absorbed by the atomic nucleous inside the shield. The result of the interaction is a compound nucleus in a highly excited state. This compound nucleus decay after the interaction and emits a gamma ray which could be energetic and deeply penetrating.

1.2.4 Charged particle emission

The compound nucleus resulting by the interaction between the neutron and the target nucleus, rearrange its internal structures and can emits charged particles: typically, deuterons, protons and alpha particles. Commonly we speak about (n,p), (n,d) and (n,α) reactions.

1.2.5 Neutronic multiplications

This type of interaction can occur when a neutron interacts with heavier nucleus. The resultant reaction can result in the emission on two or more neutrons (n, xn) emitted by the compound nucleus. If the outgoing neutrons have higher energy than the inbound neutron, the material is probably not suitable for a shielding problem. On the contrary, when the sum of the outgoing neutrons energy is less than the incoming neutron the material could be suitable for the situation.

1.3 Photon interaction with matter

Photons are quantum of electromagnetic radiation, regarded as discrete elementary particles having zero rest mass and zero charge. They are electrically neutral so,

they don't steadily lose energy via coulombic interactions with atomic electrons, making them far more penetrating than charged particles of similar energy.

The penetration of this type of particle depending on the incident gamma ray energy and material characteristic. The energy of gamma radiation ranging between 10 keV and 10 MeV. In this range three different interaction are possible:

- Photoelectric effect;
- Compton effect;
- Pair production

These interactions of the photons with matter depend upon the linear attenuation coefficient, μ, which has the dimension of the inverse length (cm^{-1}). The attenuation coefficient depends on the photon energy and on the material begin traversed.

Fig. 1.2 shows the mass attenuation coefficient depend on the energy

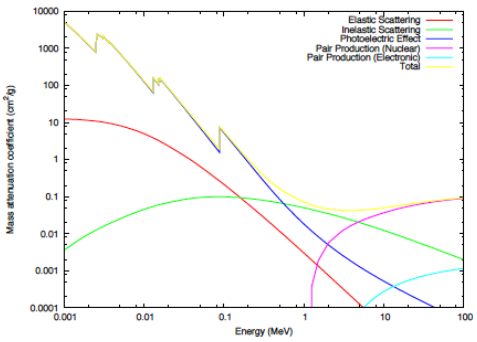

Figure 1-2 attenuation coefficient as a function of the energy

The mass attenuation coefficient is obtained by dividing the attenuation coefficient by the density ρ of the material. It is expressed in $cm^2\ g^{-1}$ and represents the probability of an interaction per g cm^2 of material traversed [3].

1.3.1 Photoelectric effect

During the photoelectric effect the incident photon may be absorbed by the target material with the consequent emission of a bounding electron. (fig. 1.3)

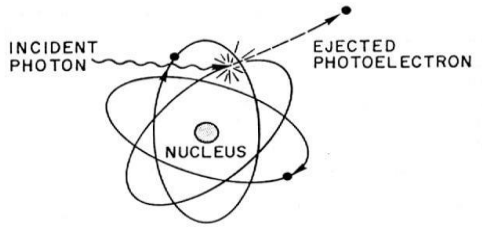

Figure 1-3 Photoelectric effect

Some of the incident photon energy is used to overcome the electron binding energy and most of the reminder is transferred to the freed electron as kinetic energy. The small amount of remaining energy is necessary for the atom to conserve the momentum.

The probability of the photoelectric effect can occur depending upon the incident photon energy, the electron binding energy and the atomic number of the target material. The cross section is:

$$\sigma_{PE} \propto \frac{Z^4}{E^3} \qquad (1.4)$$

The vacancy left by the electron is occupied by another electron of a superior state. The process ends with an emission of:

- X Fluorescence radiation with the energy given by the difference of the two orbital involved (typically K and L);
- Auger electron.

1.3.2 Compton effect

The Compton scattering can occur when a photon collides with a free or weakly bound electron. If the photon energy $E_0=h\nu_0$ is big enough, the target electron will receive sufficient kinetic energy and it will diffuse with energy $E=h\nu$.

The resulting electron becomes free with a kinetic energy equal to the difference between the energy lost by the gamma ray and the electron's binding energy. The gamma ray, after the Compton interaction, is deflected through an angle θ with respect to its original direction. Since all the angle is theoretically possible, the

energy transferred to the electron can vary from zero to a large value of the initial energy of the incident gamma ray. For the energy of the gamma ray after the deflection results:

$$E = \frac{E_0}{1 + \frac{E_0}{m_0 c^2}(1 - cos\theta)} \qquad (1.5)$$

While for the electron results:

$$T = E_0 - E = m_0 c^2 \frac{2\left(\frac{E_0}{m_0 c^2}\right)^2 \cos^2 \varphi}{\left(1 + \frac{E_0}{m_0 c^2}\right)^2 - \left(\frac{E_0}{m_0 c^2}\right)^2 \cos^2 \varphi} \qquad (1.6)$$

$$\tan^{-1} \varphi = \frac{\cot\left(\frac{\theta}{2}\right)}{1 + \frac{E_0}{m_0 c^2}} \qquad 0 \leq \varphi \leq \frac{\pi}{2} \qquad (1.7)$$

Because the Compton scattering only involved the photon – electron interaction, the cross section for the electron is valid for all the materials $\sigma^e{}_C(E)$. Thus, the atom cross section is:

$$\sigma_C(Z, E) = Z\, \sigma_C^e(E) \qquad (1.8)$$

1.3.3 Pair production

In the Coulombic field of a nucleus (or electrons), a photon with sufficient energy may create a couple of particles and antiparticles. (fig. 1.4)

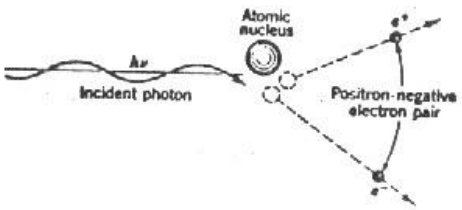

Figure 1-4 Pair production

For the gamma radiation with energy < 10 MeV the creation of an electron – positron couple is possible in the coulombic field of the nucleus. When the energy of the

incident gamma is greater than the energy necessary to create the two electron masses ($E_\gamma > 2m_0c^2$) the reaction can occur with the following energetic balance:

$$E_\gamma = 2m_0c^2 + T_{e^-} + T_{e^+} \qquad (1.9)$$

where T_{e^-} and T_{e^+} are the kinetic energies of the electron and positron respectively.

The threshold energy for the reaction is:

$$E_\gamma^s = 2m_0c^2\left(1 + \frac{m_0}{M}\right) \cong 2m_0c^2 = 1.02\ MeV \qquad (1.10)$$

Then, in the coulombic field the pair production reaction can occur only if

$$E_\gamma \geq 2m_0c^2\left(1 + \frac{m_0}{m_0}\right) = 4m_0c^2 = 2.04\ MeV \qquad (1.11)$$

Indeed, it is a very rare process. The electron and the positron are created with the same kinetic energy and different momenta: the electron loses its energy with ionization processes while the positron will annihilate with an orbital electron in atom producing two 511 keV gammas which will travel almost in opposite directions. The pair production is dominant when the energy of the particles is greater than 6 MeV and the cross section is given by:

$$\sigma \propto Z^2 \qquad (1.12)$$

1.4 Effects of radiation on Materials

The particle interaction with matter is the basis of the radiation shielding. The particle interaction causes damages on materials and humans and they must be shielded in order to prevent those damages.

Basically, these effects, can be divided in the following groups:

- Effects on materials;
- Biological effects on humans.

All these effects can cause a detrimental to materials following the interaction with the nucleus, such effects are termed radiation damage.

1.4.1 Atomic Displacement

When neutrons interact with atoms in a material, the neutron can impart some of its kinetic energy to an atom via elastic or inelastic collisions [4]. If more energy than the displacement energy is supplied, then the atom will leave its equilibrium position leaving behind a vacancy. The displaced atom is known as the primary knock on atom (PKA). If the atom has enough kinetic energy it can cause further displacements along its flight path, known as secondary displacements, and in turn these secondary displacements can cause tertiary displacements. The creation of the PKA, secondaries and tertiaries is known as a damage cascade. When the PKA has a kinetic energy less than the displacement energy, then the PKA has insufficient energy to create further displacements, it will then quickly loose the remainder of its kinetic energy via Coulombic repulsion and be absorbed into an existing atomic vacancy or could lie outside a vacancy and hence create an interstitial atom. The damage cascade is responsible for the majority of damage during irradiation by heavy particles (fast neutrons or heavy atoms) [5].

1.4.2 Dissociation Effect

A side effect of atomic displacements is a build-up of internal energy in the atomic lattice [6], this is known as the dissociation effect or Wigner energy. The internal energy increases because atoms that have been displaced may end up lying between two crystal planes, the potential at this location is higher than in an equilibrium position. When the material is heated, the atoms that have been displaced to non-equilibrium positions will gain more kinetic energy and are likely to find a vacancy.

The atom then has to de-excite as there is a difference in energy between the vacancy and the inter-planar position. This energy excess will be deposited into the atomic lattice and will increase the temperature of the material. The amount of energy deposited from de-excitation can become excessive if the applied dose is large.

1.4.3 Transmutation

When neutrons are absorbed in capture reactions such as $^{59}Co(n,\gamma)^{60}Co$, the nuclide after absorption is different to that before the reaction due to the absorption of a neutron. This new nuclide may be stable or radioactive, in which case it can decay via a number of different decay schemes such as α, β, γ, Internal Transition (IT) or positron decay. When a nuclide undergoes decays via any decay but γ -decay or IT then the atomic number of the nuclide is changed. This new atom will affect the bonding structure of the crystal planes around the atom. If the neutron irradiation continues for a long period or is very intense, then a large number of material nuclides will transmute to other nuclides. If this occurs, then the material which was first put into the device will be different.

The rate of decay of a given nuclide is described by the Batemann equation, which describes the production and destruction of a given isotope

$$\frac{dN_i}{dt} = -N_i(\lambda_i + \sigma_i\phi) + \sum_{j\neq i} N_j\left(\lambda_{ij} + \sigma_{ij}\phi\right) + S_i \qquad (2.13)$$

$$S_i = \sum_k N_k \sigma_f^k \phi\, Y_{ik} \qquad (2.14)$$

where Ni is the amount of nuclide i at time t, N_j is the amount of nuclide j at time t, N_k is the amount of nuclide k at time t, ¸i is the decay constant of nuclide i (s^{-1}), ¸ij is the decay constant of nuclide j producing i (s^{-1}), σ_i is the total cross section for reactions on i (cm^2), σ_{ij} is the reaction cross section for reactions on j producing i (cm^2), σ_k^f is the fission cross section for reactions on actinide k (cm^2), ϕ is the neutron flux (n cm^{-2} s^{-1}), S_i is the source of nuclide i from fission and Y_{ik} is the yield of nuclide i from the fission of nuclide k.

If we consider a simple system in a neutron capture reaction A(n,γ)B, then B is described by Equation 2.15 [7];

$$A_B(t) = \phi \sum_{act} V(1 - e^{-\lambda t}) \qquad (2.15)$$

where $A_B(T)$ is the activity induced in nuclide B at a time t in Bq, ϕ is the neutron flux in $cm^{-2}\,s^{-1}$, Σ_{act} is the activation cross section, e.g. that of the (n, γ) reaction in cm^{-1}, V is the volume of the sample in cm^3, λ is the decay constant of the excited state of the nuclide B in s^{-1} and t is the irradiation time in s.

It can be seen from Equation 2.15 that when the exponential term is small, the activity of B is at its maximum, this is known as secular equilibrium. Thus when materials are irradiated activity builds up due to the activation of various nuclides, when the irradiation ends however, the activity will decay away, the timescale of which is determined by the half-lives of the created nuclides. When materials are irradiated, the number of possible reactions, decays and half lives are huge. To compute this manually is possible but is very labour intensive and prone to mistakes.

There are some activation-decay schemes that are impossible to solve analytically such $^{59}Co(n, \gamma)^{60m}Co(IT)^{60}Co(\beta-)^{60}Ni(n,2n)^{59}Ni$.

The reason that this reaction is analytically unsolvable is the backward step possible due to the decay of ^{59}Ni. The combination of analytically unsolvable reactions and the number of possible reactions means that a reliable computational technique must be found. Fortunately, these problems have been examined previously and there are a large number of nuclear inventory codes already existing.

1.4.4 Gas Production

If the capture reaction was a (n,p),(n,d),(n,t) or (n,α) then either a hydrogen or helium nucleus is emitted. At some point the nucleus will absorb some electrons from the crystal lattice. These gas atoms tend to accrue along crystal grain boundaries or at voids in the crystal structure, which exert a pressure from the inside of the material. The production of gas, in particular production of helium,

can affect the reweldability of steels if the helium concentration is above 1 appm then it is not possible to make the welds stick. Helium is typically produced in (n,α) capture reactions such as that of $^{10}B(n, \alpha)^{7}Li$, although it can be produced via α decays.

1.4.5 Radiation Heating

When radiation interacts in matter some energy is transferred to the atom. The amount of energy transferred depends on the radiation type, the material and interaction type. This is known as radiation or nuclear heating. In the case of energetic photons, the amount of energy deposited is proportional to the energy transfer coefficient, μ_{en}. Neutrons can heat material through the production of gamma rays from inelastic scattering and from elastic scattering events which knock on nuclei, and also via nuclear reactions which produce charged particles. The amount of heating is strongly dependant on the material in which the energy is deposited, the energy distribution and type of radiation impinging on the material. Nuclear heating is related to KERMA (kinetic Energy Released per unit Matter). Nuclear heating is the sum of all processes which lead to the deposition of energy in a material.

1.5 Biological Effects of Ionising Radiation

The effects of ionising radiation upon humans can be broken into two discrete effects, namely deterministic and stochastic effects.

Deterministic Effects of Ionising Radiation

Deterministic effects of ionising radiation generally arise shortly after exposure to a radiation dose, only if this dose is greater than some threshold value. The severity of these effects, but not the probability of occurrence, depends on the total dose absorbed. An example of a deterministic effect is damage to body tissues such as the red bone marrow.

Stochastic Effects of Ionising Radiation

Opposing deterministic effects are stochastic effects, the dose influences the probability of occurrence, but not the severity. There appears to be no dose threshold with regards to stochastic effects. Most stochastic effects lay dormant after irradiation, such as the induction of cancer, or the damaged DNA inheritance to later generations.

1.5.1 Absorbed Dose

Absorbed dose, D, is defined by the relationship [8];

$$D = \frac{d\epsilon}{dm} \qquad (1.16)$$

where $d\epsilon$ is the mean energy imparted by ionising radiation to the matter in a volume element and dm is the mass of the matter in this volume element.

1.5.2 Effective Dose Equivalent

The International Commission on Radiation Protection introduced the concept of equivalent dose in ICRP Publication 60 [8]. Equivalent dose is defined as

$$H_{T,R} = w_r \cdot D_{T,R} \qquad (1.17)$$

where $H_{T,R}$ is the equivalent dose over a particular mass of tissue T, due to radiation R, w_r is the radiation weighting factor the value of which depends on the type of radiation R and $D_{T,R}$ is the absorbed dose in a particular mass of tissue T, due to radiation R.

To account for differing amounts of organ and tissue radio sensitivity there are also tissue weighting factors, w_T, the product of the equivalent dose with the tissue weighting factor results in the effective dose, E [7];

$$E = \sum_T w_T \cdot H_T \qquad (1.18)$$

The factors are normalised such that the sum over all tissues is equal to unity. The implication of this is that a uniform equivalent dose, H of 1 Sv to the whole body will result in an effective dose, E of 1 Sv. Computer human models and neutron/photon transport codes have been applied to calculate energy deposition and dose for various tissues and organ systems. These calculations are sensitive to the direction of incidence of the radiation because of self-shielding and attenuation effects in the body through the tissue weighting factors recommended by the ICRP, the individual components can be then combined into an effective dose equivalent, H_E [9]. The effective dose equivalent represents an estimate of the overall biological effect of a uniform whole body exposure to the assumed fluence. The effective dose equivalent is then written as

$$H_E = h_E \cdot \phi \qquad (2.19)$$

where H_E is the effective dose equivalent in Sv, h_E is the fluence-to-dose conversion factor in Sv cm^2 and ϕ is the radiation fluence in cm^{-2}. There are several sets of fluence-to-dose conversion factors, for example ANSI-ANS-6.1.1-1977 [9] and ANSI-ANS-6.1.1-1991 [10]. The ANSIANS- 1991 standard chooses to represent an analytic fit to the derived dose data at a fourth order polynomial

$$h_e(E) = 10^{-12} \cdot e^{(C_0+C_1X+C_2X^2+C_3X^3+C_4X^4)} \qquad (2.20)$$

$$X = \ln E \qquad (2.21)$$

where $h_E(E)$ is the fluence-to-dose conversion factor in Sv cm^2 and E is the particle energy in MeV.

1.6 Radiation Shielding

In order to mitigate the potentially harmful effects of radiation in materials and humans, and achieve the limits imposed by the regulations or by the radiation protection expert, we must shield radiosensitive (biological or inanimate) objects from the radiation field. Before the design of any radiation shielding can take place,

the radiation shielding designer must be aware of any consequences to their actions. Some general principles of shielding design are as follows [11].

A radiation shield must balance the following aspects while ensuring that the attenuation of the radiation field is sufficient:

- Activation
- Dose
- Heating/Cooling
- Handling Weight
- Radiation damage.

The radiation shielding of a system must attenuate the primary radiation incident upon it and it must not become prohibitively activated. Ideally a shield would be made of a substance that cannot be activated, however in practice making a shield of such materials, for example a "low" activation material such as vanadium, would be rather expensive. Through careful shield design activation can be minimised or the effects of the decay radiation attenuated to a large degree.

Typically, the purpose of a radiation shield is to reduce radiation dose to levels considered acceptable. Although, there are a number of cases where thermal shields have been included in systems like the thermal shielding placed in front of the DTT TF coils, where its primary purpose is to reduce the nuclear heating of the coils. The nuclear heating of the shield should not be so large as to cause excessive amounts of energy to be deposited in the shield, where this cannot be avoided as is the case when shielding intense charged particle sources, cooling methods must be introduced to the shield. Fluid coolants require some form of penetration through the shielding, these penetrations should not align with the major regions of the radiation source emission. Electrical cooling is a method of cooling that requires no penetrations, the heat generated inside the shield is conducted to the outside world via thermal conduits or cooling veins. The issue with electrical cooling in a radiation

environment is the loss of conductivity experienced by metals when damaged by ionising radiation. The radiation shielding must not imbalance the system, where overhead crane handling is required the shield should sit balanced in the handling sling [12].

Shield weight is not typically a concern in stationary reactor applications, such as the reactor bioshield, where it can made as thick as is required, however certain parts of reactors may have strict weight limits if moving or maintenance is required.

In the case of these movable shields it is important that shield weight is not excessive and that the equipment designed to move the shield around will not become damaged.

This is the case of the movable shielding presented in chapter 7 for the ECRH DTT corridor for EC transmission lines.

One concern of radiation shielding is that of the time evolution of the shield, where radiation damage can cause many microscopic defects, which can lead to Macroscopic effects such as embrittlement and voiding. It is important to consider the level to which a shield will become damaged in the reactor application, and if this damage cannot be avoided then shield replacement lifetimes should be recommended.

Indeed, in severe circumstances the virgin shield will be more attenuating than the shield at its end of life.

1.6.1 Stages in Radiation Shielding Design

There are a number of stages when designing a radiation shield, the procedures used when moving from concept to final design can be broken down into a number of steps. Previously, radiation shielding calculations were challenging and error prone. With the advent of high power computing, these calculations have become less challenging. However, with increased computing power comes the desire for

more accurate answers and inclusion of effects that otherwise would have been neglected.

The following stages are based on those of Price [11], however they have been modified to take into account the changes in radiation shielding design procedure in the 50 years, such as digital computing.

1.6.1.1 Study of the Primary Radiation Source

It is the primary radiation source that determines the materials and geometry that the resulting shield is required to be constructed from. Knowledge of the spatial, angular and energetic distribution of the source is essential for any future calculations.

Without an accurate source definition, it is impossible to accurately estimate not only the uncertainty in the answer with respect to the source definition but also important transport effects such as streaming.

1.6.1.2 Formulation of the Basic Shield

Once the radiation type and energy distribution of the source particles is known, the primary shielding materials can be selected depending upon how much attenuation is required. For example, when considering an energetic neutron source, a shield with a high density and with two component materials would be considered, one component for slowing down the neutron and another component for absorption. Often, for DTT, shields made of Stainless Steel and Polyethylene have been choose.

The principal shield materials available to the designer can be divided into 2 categories according to their function: (1) materials that are used primarily to attenuate one kind of radiation, either neutrons or gamma rays, and (2) materials that serve a dual purpose and are used as the main attenuator of both types of radiation. Characteristic of the first category are hydrogenous materials, typically

water, to attenuate fast neutrons by moderation down to energies where they can be captured, and dense materials of high atomic weight, typically lead, to attenuate gamma rays.

Although each of these materials are chosen for their properties with regard to a particular type of radiation, each, of course actually attenuates both types. In the second category are materials such as concrete which is effective at attenuating many different types of radiation.

The shield design at this point is subject to revision, as are the materials of which the shield is made. Revisions are made on the basis of calculated radiation levels, excessive heating, secondary radiation production, or material damage.

1.6.1.3 Calculation of the Attenuation of Primary Radiations

On the basis of the over-all system evaluation and the choice of material discussed above, approximate calculations can be performed to obtain the thicknesses required to attenuate the primary radiation. Calculation at this stage will be approximate with minimal details considered to give a reliable answer. Shield design is by its nature an iterative process and after each design stage more detail is added to the calculation.

1.6.1.4 Calculation of Production and Attenuation of Secondary Radiations

Once the attenuation of primary radiation has been calculated, the distribution and intensity of secondary radiations produced from interactions of the primary adaption can be determined (if any). In the case of neutrons as primary radiation, an example of secondary radiation would be gamma rays produced via capture, transmutation and inelastic scattering reactions. There are many types of secondary radiations such as gamma rays, protons, alpha particles, bremsstrahlung and a number of the other processes. It is because of these secondary radiations that shield

design can become a complex problem when considering shielding systems composed of many different materials.

1.6.1.5 Optimisation of the Shield

The problem of optimisation is common to most engineering designs, whether the object is to minimise the cost or to reduce the size, weight, or some other parameter of the system. In shielding, the parameter of interest may be the cost, as in the case of a stationary reactor. The optimisation is usually carried out subject to certain constraints, or subsidiary requirements; for example, a limit may be imposed on post shutdown radiation levels at the surface of the reactor shield, or the shield dimensions may be restricted to some maximal value.

1.6.2 Neutron Shielding

There are a number of so called standard neutron shielding materials such as boron carbide, steel-water mixtures or concrete. The choice of material will usually be subject to a number of constraints.

Neutron shielding typically is partly composed of materials that both moderate and absorb, Bethe-Bloch for example boron carbide (B4C) or even simple mixtures such as steel and water. Moderating materials are required to reduce the kinetic energy of the incoming neutron flux, when these neutrons slow down through a number of collisions, its kinetic energy will be low enough to be in the "1/v" part of an absorber's cross section. Moderating materials differ from absorbers in that the absorption cross section in moderators are typically very low, but have large cross sections for scattering, either elastic or inelastic. There is a need to moderate neutrons to lower energies because typical absorption cross sections can be 6 orders of magnitude higher at thermal energies than at fast energies. Neutron shields have a dual purpose one of screening the primary radiation field from persons outside the shielding, and also attenuating any secondary radiation that is produced. A

shield that is composed of only absorbent material will not shield as well as a mixture of moderator and absorber.

Consider a neutron source impinging from one side of a semi-infinite slab of material. It is known that a certain distance into a specific material the neutron spectrum is in equilibrium, this is due to the build-up of neutrons scattered down in energy and the absorption of those neutrons accordingly either in the "1/v" part of the cross section or in the resonance region. This means that at depths greater than this equilibrium distance the neutron spectrum no longer changes in energy, only in intensity.

1.6.3 Photon Shielding

Photon attenuation is determined by 3 microscopic interaction methods; photoelectric effect, Compton scattering, and pair production and as such the macroscopic design of shielding is determined by these interaction coefficients. However, since these cross sections scale with the number of electrons present in the material, the more effective shields tend to be high atomic number and high density materials such as lead and tungsten.

2.7 Conclusion

The Divertor Tokmak Test facility is a nuclear facility with a neutron production, in its high performance phase, greater than $1x10^{17}$ n/s. This means that the study of the neutron and gamma shielding to prevent effects on materials and humans is fundamental for the development of the project. In the next chapters these aspects will be investigate and the theory of particle shielding will be applied to the DTT project development.

2 Fusion Neutronics

"Simulation is better than reality"

Richard W. Hamming

Fusion neutronics plays a fundamental role in the fusion science. Neutrons are one of the reaction products in the most promising nuclear reactions at the basis of the future energy production. Both D-D and D-T reactions produce high energy neutrons (2.45 and 14.1 MeV) which escape from the plasma and interact with the surrounding structures causing multiple effects which must be prevented. These effects are affecting most of the technical and operational scenarios and often dictate the technical solutions to be applied and by consequence impact on the design/cost/operation/maintenance of the plant. Radiation transport calculations for the prediction and confirmation of expected neutronics parameters are an essential part of the design. Accurate 3D-calculations are needed to well characterize the environment and allow to account for the streaming effects on penetrations. Neutron and gamma fluxes detailed assessment in reactor components is a basic requirement for their mechanical design. Furthermore, accurate mapping of the radiation field is required inside and outside the machine for the planning operator's activity and maintenance. All these needs require detailed neutron calculations based upon the state-of-the-art of the calculation tools and nuclear data libraries.

2.1 Radiation Transport Equation

Neutrons interaction with matter previously discussed and explained, modify both the energy and direction of the motion of neutrons. Is important to foresee the

behaviour of the neutron, their spectrum in the different part of the machine (fig. 2.1) and how they lose energy (see chapter 1).

The behaviour of the individual neutrons is too difficult to predict due to the large number of possible reactions which are possible between neutrons and matter. The composition of materials also represents another difficult because of the changes in the composition of matter along the particle path, as it often happened in the complex structures as a magnetic confinement fusion device.

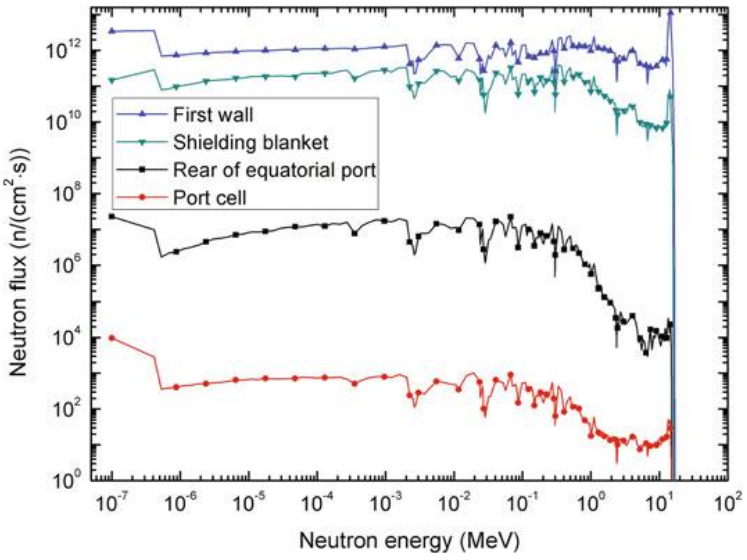

Figure 2-1 Example of neutron spectra in the representative part of the machine

However, the average behaviour of a large population of neutrons can be described quite accurately if we have sufficient knowledge of neutron fluxes, cross-sections and reaction rates.

Transport theory is based on, and is identifiable with, the solution of the Boltzmann transport equation. This equation is relatively easy to derive but is, in general, intractable from the analytic point of view and it is can be only analytical solved if severe restrictions are imposed(energy and spatial dependence of the radiation cross sections of the materials in the region of interest). Anyway, those solutions could be un-useful.

Fusion neutronics aim for the knowledge of neutrons and gammas spatial and energy distribution starting from the nuclear cross section data, describing the interaction processes of particles and atomic nuclei, thus, the mathematical transport problem needs to be solved.

$$\frac{1}{v}\frac{\partial}{\partial t}\phi(\underline{r},E,\underline{\Omega},t) + \underline{\Omega}\cdot\nabla\phi(\underline{r},E,\underline{\Omega},t) + \sum\nolimits_t(\underline{r},E,\underline{\Omega},t)\ \phi(\underline{r},E,\underline{\Omega},t) = \int_{\underline{\Omega}'}\int_{E'}\sum\nolimits_s(\underline{r},E'\to E,\underline{\Omega}'\to\underline{\Omega},t)\ \phi(\underline{r},E',\underline{\Omega}',t)dE'd\Omega + S(\underline{r},E,\underline{\Omega},t) \quad (2.1)$$

The terms of the equation are explained below:

- $\frac{1}{v}\frac{\partial}{\partial t}\phi(\underline{r},E,\underline{\Omega},t)$ is the particle flux variation rate with respect to time due to the phenomena such as isotopes decay or delayed neutrons production,
- $\underline{\Omega}\cdot\nabla\phi(\underline{r},E,\underline{\Omega},t)$ is the so called "*transport*" term and represent the balance of the neutron density in the elementary volume dr;
- $\sum_t(\underline{r},E,\underline{\Omega},t)\ \phi(\underline{r},E,\underline{\Omega},t)$ is the total reaction rate, including the scattering and absorption interactions previously treated;
- $\int_{\underline{\Omega}}\int_{E'}\sum_s(\underline{r},E'\to E,\underline{\Omega}'\to\underline{\Omega},t)\ \phi(\underline{r},E',\underline{\Omega}',t)dE'd\Omega$ is the scattering term that describes the interaction probability of particles from some direction and energy range into our direction and energy range of interest. Σ_s is called the "*transferring scattering macroscopic cross section*" and represent the probability for a neutron to be scattered (elastic or inelastic) and to change both its energy and direction. It is strongly related to the slowing down process;

- $S(\underline{r}, E, \underline{\Omega}, t)$ is the source term

The general form of the equation contains six independent variables (x, y, z, ϕ, ϑ and E). Furthermore, the dependence of the cross-sections on position and energy can be extremely complicated in a real system (i.e. tokamak) so, the analytical solution in not possible. In certain cases, the only way to solve the Boltzmann equation is by numerical methods that can be used to attempt to solve the equation.

Two main methodological approaches that can be used to attempt to numerically solve the Boltzmann equation:

- Macroscopic description (deterministic approach): perform the balance of particles gains and losses, solving the integro-differential Boltzmann equation for flux and density in infinitesimal phase space elements.
- Microscopic description (probabilistic approach): simulation of real physical process on microscopic level, tracking the individual particle histories from its generation, in nuclear reactions, to its disappearance with the interaction probabilities given by nuclear cross section.

2.2 Deterministic and probabilistic approach

The solution of the transport equation allows to know the map of neutron and gamma fluxes in the system. Neutrons and gammas are the basic information needed to calculate all the others nuclear quantities by multiplying n & γ flux spectra by proper coefficients.

Deterministic and probabilistic methods are described below.

2.2.1 Deterministic method

Analytical transport equation that describe the exact behaviour of neutrons in matter are well known. Analytical solutions are instead impossible to derive. So, only approximated numerical solutions can be obtained for complicated systems. Procedures to achieve these numerical solutions are classified as discrete ordinates or deterministic methods. At the basis of the deterministic methods there are one or all the approximation techniques:

- Discretization in energy (multigroup approximation)
- Discretization in angle (Discrete Ordinates)
- Spherical harmonics expansion of the scattering term

The neutron flux is represented in the phase space by six coordinates (three spatial, direction (Angle), Energy and Time) as continuous variables. The discretization procedure is one of the main points of concern for these variables. The multigroup approximation is, indeed, the main method used in the case of deterministic codes [13]. In this approach the main parameters of the problem, such as the energy and cross-section, are divided into a finite number of discrete energy groups (typically 175 for fusion applications), where the energy centroid of the group determines the interaction energy. The most important source of uncertainties in the deterministic method is represented by the resolution in the energy groups in the resonance zone. The risk is that after averaging over the resonances there are insufficient resolution that can lead to wrong results.

Similar to the energy discretization, in the same way deterministic methods applies this approximation to the angular variation of the direction vector ($\underline{\Omega}$) into a number of discrete directions in space with associated solid angle elements [14]. For Each portion of angular distribution, the Transport equation is evaluated. Those number of directions considered must be high enough in order to deal with the possibility

highly anisotropic angular flux. This method of angular splitting into several groups is the so-called S_n approximation.

Cross-sections are expanded in terms of orthogonal Legendre Polynomials. This allows the scattering term to be expanded in terms of spherical harmonics. This representation in the deterministic codes is known as P_n approximation.

Discrete ordinated process, as described hereinabove, is only suitable for one- or two-dimensional geometries. In fact, neutrons and gammas are considered to be in discrete locations instead of moving freely through a three-dimensional geometry. The energy dependence in the transport equation is also simplified by averaging over the energy intervals to be selected from a finite set, in contrast to the continuously varying energy of a particle in a real situation.

Anyway, for those problems that implies a large volumes and amount of materials in a simple geometrical framework the deterministic methods and, thus, the discrete ordinates solution is feasible. They also allow to drastically reduce the computational time needs.

2.2.2 Probabilistic method

In the probabilistic or statistic methods the Boltzmann equation is not solved as it is. The algorithm simulates the story of every particles including all the collisions, energy and direction changes. The individual particle histories were tracked from "*birth*" to "*death*" (absorption or exit from the system) according to a source distribution and interaction coefficients. The probability distribution governing these events is statistically sampled to describe the total phenomenon. When enough of these histories are sampled the results can be considered statistically significant. The average behavior of the particles in the studied system is inferred (through the *Central Limit Theorem*) from the average behavior of the individually simulated particles. This is widely known as the Monte-Carlo method.

The origin of this approach can be found in first decades of '900 centuries by Stanislaw Ulam during the famous *Manhattan Project* at the Los Alamos National Laboratories. Ulam and J. Von Neumann suggested that aspects of research into nuclear fission at Los Alamos could be aided by use of computer experiments based on chance. Since the Manhattan Project was a top-secret work the inventors of the method, Von Neumann in particular, chose the name *Monte Carlo* with the reference to the Casino in Monaco [15]. Fascinated from this method Nick Metropolis built new control computer system in order to handle the calculations needed for the Monte Carlo method [16]. Ulam and Von Neumann, collaborating with the likes of Fermi, published a paper in 1949 [17], in which they gave the basis of the method such as a bootstrap filter [18].

Monte Carlo codes can be used to simulate theoretically a statistical process and is particularly useful for those problems that cannot be modeled using the codes which are based on the deterministic approach. The individual probabilistic events that comprise a process are simulated sequentially. The probability distribution governing these events are statistically sampled to describe the total phenomenon. Since the number of histories needed to achieve a statistically significant results is very high (in the most complicate geometries could be greater than 10^9 source particles), the Monte Carlo simulations are usually performed on a high performance computing resources.

The basis of the statistical sampling process stands in the selection of the so-called *random numbers*, the analog of the dice rolling in the casino. In the transport, the Monte Carlo technique is pre-eminently realistic such as a numerical experiment.

The probability distribution is randomly sampled using transport data to determine the outcome at each step of its life.

In fig. 2.2 the random history of a neutron incident on a slab of material which can undergo to a fission process is shown. Numbers between 0 and 1 are selected

randomly to determine what and where interaction take place, based on the rules (physics) and probabilities (transport data, cross- section) governing the processes and material involved. In this particular and representative example, the occurred (probable) events are:

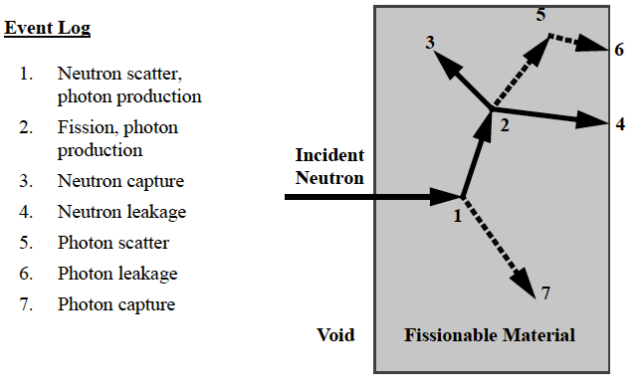

Figure 2-2 History of a neutron transport inside a material slab

1. The neutron undergoes an inelastic scattering reaction and is deflected through some angle, which is determined from the physical scattering distribution stored in the nuclear data. During the inelastic scattering event a photon was created, which is temporarily stored in memory for later analysis.
2. The neutron is captured in some nuclide capable of a (n,2n) fission reaction and then two neutrons and one photon are generated, with energies and directions appropriate to the reaction. One neutron and the photon are banked for later analysis.
3. The first fission neutron from the previous (n,2n) reaction undergoes an absorption reaction and terminated.
4. The banked neutron, retrieved from memory, leaks from the system.
5. The fission-produced photon undergoes a collision.
6. The photon leaks out of the slab.
7. The remaining photon, produced in the event 1, is captured, and the neutron history is now complete.

As more and more such histories are followed, the neutron and photon distributions become better known. The quantities of interest are measured (tallied), along with estimates of the statistical precision (uncertainty) of the results.

2.2.3 Deterministic Vs. Probabilistic method

As explained in the previous chapters, the two methods are fundamentally different but only in the way of applications. Deterministic method, which is mostly based on the discretizing methods, solves the Boltzmann equation for the average particle behaviour. Monte Carlo method obtain answers by simulating individual particles and recording some aspects of their average behaviour. This average behaviours of the particles in the physical system is then inferred from the average behaviour of the simulated particles. From the transport equation point of view, the two methods are not so different. It is in the common sense considering that the Monte Carlo method solves the integral transport equation, as if it weren't the Boltzmann equation, while the deterministic method solves the integro-differential transport equation. This is a misleading about this treatment. The integral and the integro-differential transport equation, in fact, are the same equation written in two different form, thus, solving one means solving the other. The second important remark is that there's no need to write a transport equation to solve a Monte Carlo problem but, theoretically, is possible to write down an equation that describes the probability density of particle in phase space and it will result to be the same to the Boltzmann equation.

The deterministic method visualises the phase space to be divided into many small boxes and the particles move from one box to another. In the limit, as the boxes get progressively smaller, particles moving from box to box take a differential amount of time to move a differential distance in space.

By the contrast, the particle transport in the Monte Carlo method happens between one event (i.e. collision) to another which are separated in space and time. Neither

differential space nor time are inherent parameters of Monte Carlo transport. The integral Boltzmann equation does not have terms involving time or space derivatives.

The most important difference between the two approaches is the geometry field of application. Monte Carlo is particularly suited for those problem with complex three-dimensional, time-dependent problems, allowing detailed representations of all aspects of physical data. Moreover, deterministic methods typically give fairly complete information (for example, flux) throughout the phase space of the problem while Monte Carlo supplies information only about specific locations requested by the user.

All these peculiarities make the Monte Carlo method particularly appropriate for fusion neutronics applications, where particles transport through very complex three-dimensional geometries is needed.

2.3 The MCNP Monte Carlo code

The MCNP (Monte Carlo N-Particle) is a general-purpose code that can be used for neutron, photon, electron or coupled neutron/photon/electron transport. Specific areas of application include, but are not limited to, radiation protection and dosimetry, radiation shielding, radiography, medical physics, nuclear criticality safety, Detector Design and analysis, nuclear oil well logging, Accelerator target design, Fission and fusion reactor design, decontamination and decommissioning. The code trats and arbitrary three dimensional configuration of materials in geometric cells bounded by first- and second-degree surfaces and fourth-degree elliptical tori. [19].

Pointwise cross-section data are typically used, although group-wise data also are available. Concerning neutron transport problems, all reaction given in a particular cross-section evaluation are accounted for. Free gas and S(α,β) are both used for the thermal neutrons treatment.

Regarding the photon transport, the code accounts for incoherent and coherent scattering, the possibility of fluorescent emission after photoelectric absorption, absorption in pair production with local emission of annihilation radiation, and bremsstrahlung. A continuous-slowing-down model is used for electron transport that includes positron, k x-rays, and bremsstrahlung. Photonuclear physics is available for a limited number of isotopes. Energy ranges are from 10-11 keV to 1 GeV for electrons, and from 1 keV to 100 GeV for photons.

Important features that make MCNP very versatile include a powerful general source, criticality source, and surface source; a set of variance reduction techniques; a flexible detector (tally) structure and an extensive collection of cross-section data. Moreover, the code contains numerous flexible tallies: surface current and flux, volume flux (track length), point or ring detectors, particle heating, fission heating, pulse height tally for energy or change deposition, mesh tallies and radiography tallies.

This wide range of possible use makes MCNP the reference code for the neutronics analyses in fusion applications. In the framework of DTT development and, during the Ph.D. course for many other activities such as benchmark experiment, MCNP has been widely used to carry out this work of thesis.

MCNP used to read pointwise cross section formatted data. The use of pointwise data means that no approximation of averaging has been applied and hence a very good representation of transport is maintained.

2.3.1 Geometry description

The geometry description inside the MCNP input covers two of the three sections (the latter is the physical description). The user must define the surfaces that compose the model and then, the cells.

The combination of the surfaces results in a three-dimensional space where the particles transport is simulated. There are several types of surfaces in MCNP and

the Boolean combination between them allows to reproduce most of the real situation and experiment.

Cells are defined by the intersection, unions, and complements of the regions bounded by the surfaces [20]. Building a surface is relatively simple: adding the coefficient to the relative analytical equation is enough to create the wanted surface. Once the surface is written, to create the cell is necessary to specify the "sense" of all its points with respect to the bounding surfaces, which is either positive or negative. Supposing that $S=f(x, y, z)$ is the surface equation. For any set of points S could be 0, < 0 or > 0. If S = 0 then the points is on the surface, otherwise it has a negative or positive sense with respect to the surface.

The cell card section defines the second part of the geometry definition. Each cell is described by means of surface and is flagged by a cell number, a material number with its density. Each cell divides the space in two regions, one with positive sense with respect to the cell and the other with negative sense.

Using the bounding surfaces specified on cell cards, MCNP tracks particles through the geometry, calculates the intersection of a track's trajectory with each bounding surface, and finds the minimum positive distance to an intersection. If the distance to the next collision is greater than this minimum distance the particle leaves the current cell. At the appropriate surface intersection, MCNP finds the correct cell that the particle will enter by checking the sense of the intersection point for each surface listed for the cell. When a complete match is found, MCNP has found the correct cell on the other side and the transport continues.

2.3.2 Source Specifications

MCNP code allows the user to define a wide variety range of possible radiation sources without having a code modification through dedicated input cards (i.e. sdef, kcode, rdum, idum). In addition to the geometry position and shape in the space,

the user can add the probability distribution for the source variables of energy, time, position and direction.

In addition to input probability distributions for source variables, certain built-in functions are available. These include various analytic functions for fission and fusion energy spectra such as Watt, Maxwellian, and Gaussian spectra; Gaussian for time; and isotropic, cosine, and mono-directional for direction. Biasing may also be accomplished by special built–in functions.

2.3.3 Tallies

In the output file created by MCNP there are lots of useful information on the status of the run include a complete accounting of the creation and loss of all tracks and their energy, the number of tracks entering and re-entering a cell plus the track population in the cell, the number of collisions in a cell, the average weight, mean free path, energy of tracks in a cell, the activity of each nuclide in a cell and a complete weight balance for each cell. However, the user can define suitable tallies in particular regions of the model where specific nuclear responses are needed. In the wide range of tallies available in MCNP, the most used in this work are listed below:

$$F2 = \frac{W}{|\mu|A} = \bar{\phi}_S = \frac{1}{A}\int dE \int dt \int dA \int d\Omega\, \Psi(r,\Omega,E,t) \qquad (2.2)$$

$$F4 = \frac{WT_l}{V} = \bar{\phi}_V = \frac{1}{V}\int dE \int dt \int dV \int d\Omega\, \Psi(r,\Omega,E,t) \qquad (2.3)$$

$$F5 = \frac{Wp(\Omega_p)e^{-\lambda}}{R^2} = \phi_P = \int dE \int dt \int d\Omega\, \Psi(r,\Omega,E,t)) \qquad (2.4)$$

$$F6 = \frac{WT_l\sigma_t(E)H(E)\rho_a}{m} \quad H_t = \frac{\rho_a}{m}\int dE \int dt \int dV \int d\Omega\, \sigma_t(E)H(E)\Psi(r,\Omega,E,t) \qquad (2.5)$$

where W is the sum of the statistical weights of all of the particles that have crossed area A, $|\mu|$ is the cosine of the angle between the direction vector Ω and the surface normal, A is the area of the surface (cm), E is the energy of the particle (MeV), t is

the time since the particle was created (time shakes), ϕ is the angular flux of particles (cm^{-2}), ϕS is the surface averaged flux of particles (cm^{-2}), ϕV is the volume averaged flux of particles (cm^{-2}), ϕP is the flux at a point, $p\Omega P$ is probability density function for scattering in the direction ΩP towards the point detector (Azimuthal symmetry), r is particle position vector (cm), Tl is the track length in the cell (cm), V is the volume of the cell (cm3), m is the mass of the cell (g), σt is the microscopic total cross section (barns), ϱa is the atom density in (atoms/barn·cm), H(E) is the heating number (MeV/collision), Ht is the total energy deposition in a cell (MeV/g) and finally Ψ is the angular flux coming from the nuclear reactor theory (particles/cm2/time shakes/MeV/steradian) [21].

In addition to the standard tallies, MCNP allows the user to tally particles on a mesh superimposed to the geometry (FMESH tally). By default, the mesh tally calculates the track length estimate of the particle flux, averaged over a mesh cell (voxel, namely volume element), in units of particles/cm^2: the spatial resolution is much higher as the volume over which the average is performed is much smaller since the recording of weight and track length is performed on a regular basis within each mesh voxel.

2.3.4 Variance reduction techniques

There is a standard method in MCNP to decrease the statistical error of a certain tally to acceptable values: increasing the number of source particles. However, there are some problems in increasing "indefinitely" the number of particles. In 32 bit computers there is a limit in the size of integer stored in the system, which is 2^{32}~4 x 10^9 but the maximum signed integer is a factor two or more less than this (i.e. 2 x 10^9). This problem is partially overcome in the modern 64-bit computers where the maximum number of signed integers are 2^{63}. This number implies however a huge computational effort that is not desirable. For this reason, special techniques, known as *variance reduction techniques* have been implemented in the MCNP code whit the aim at reducing the uncertainties in the tallies calculations with an acceptable

computational effort. The idea at the basis of the method is to reduce the contribution of those particles which are far away from the scoring region of interest by increasing the number of particles that contribute to the tally in an unbiased way. There are three main groups of variance reduction techniques: Truncation Methods, Population Control Methods and Sampling methods. The Truncation Method consists in truncating parts of the phase space that do not contribute significantly to the solution. The simplest example is the geometry cutting in which areas far from the scoring region are simply not modelled. There is also specific truncation model in which the particles that have energy or time below a user defined threshold are killed: the energy and/or time cut-off.

The most interesting for the large use within this dissertation is the Population Control method. This method uses the particle splitting and Russian roulette to control the number of samples taken in various parts of the geometry. In important regions many samples of low weight are tracked while in less important region few samples with high weight are tracked. With the aim at unbiasing the problem, the weights of the samples are rearranged. This method is of particular importance in the fusion neutronics where shielding problems are often faced up. The MCNP manual [19] gives the following definition of cell importance: "*the importance of a cell can be defined as the expected score generated by a unit weight particle after entering the cell*" and gives the following formula:

$$importance\ (expected\ score) = \frac{Total\ score\ because\ of\ particles\ (and\ their\ progeny) entering\ a\ cell}{total\ weight\ entering\ a\ cell}$$

Where the term "cell" means a part of the phase space in the geometric and energy sense. Low importance means that few high weight particles are tracked in those cells, whereas high importance means that many particles with low weight are tracked. This method coupled with the weight windows has been widely used in the simulations showed in next chapters. If a particle of weight w_0, leaves a cell of low importance (I_1) and enters a cell of higher importance (I_2) and is absorbed in the higher importance cell, then a I_2/ I_1 particles are created with a statistical weight w,

of w_0 (I_1/ I_2) each. If a particle of weight w_0 moves from a cell with a higher importance and enters a cell with lower importance it will undergo under the so-called Russian Roulette and killed with a probability (1- I_1 / I_2) and a new particle is created with weight w, w_0 (I_2/ I_1). This means that in a problem with a good importance map the number of particles remains roughly constant during the process, on the contrary in a normal analog calculation, where all cell importance are unity, the number of simulated particles decrease with the attenuation coefficient of the problem.

Modified Sampling Methods alter the statistical sampling of a problem to increase the number of tallies per particle. For any Monte Carlo event it is possible to sample from any arbitrary distribution rather than the physical probability as long as the particle weights are then adjusted to compensate. Thus, with modified sampling methods, sampling is done from distributions that send particles in desired directions or into other desired regions of phase space such as time or energy, or change the location or type of collisions. Modified sampling methods in MCNP include the exponential transform, implicit capture, forced collisions, source biasing, and neutron-induced photon production biasing. [22]

2.4 ADVANTG Hybrid transport code

The implementation of the variance reduction techniques in MCNP requires the mapping of the geometry by means the creation of a 3-D mesh in which voxels became smaller approaching the scoring region. MCNP5 has its own weight windows (ww) generator that allows the generation of the importance map (called *wwinp* file) after a step-by-step procedure in which the tally of interest (usually f4 or f5 tallies) is moved from a region with statistically acceptable values to the region of interest where normally the statistical error is unacceptable. The MCNP ww-generator is often difficult to use and requires a lot of time of implementation and lots of computing resources because, usually, many iterations are needed to

generate a suitable *wwinp* file. In addition, once the wwinp file is created, it could be not properly suitable for the calculation and in some cases, it has to be manipulated in order to became reliable to speed up the calculation in the right manner.

For this reason, in the last decades many tools have been created to shorten this procedure.

The *AutomateD VAriaNce reducTion Generator* (ADVANTG) [22] hybrid transport code has been developed at ORNL laboratories and automates the process of generating variance reduction parameters for fixed-source MCNP5 calculations. It generates space and energy-dependent mesh-based weight windows using 3-D discrete ordinates solutions of the direct and adjoint transport equations for neutrons and gamma rays. Deterministic transport calculations are performed using the Denovo package [23] that can be performed in parallel on multiple processors.

The MCNP model, provided as input, is processed and converted into an equivalent geometry for deterministic calculations by means of a ray-tracing routine.

Successively the generated model is used to perform de Denovo simulations for a given tally or a ww and specific wwp cards to be included in the original MCNP input. As far as the nuclear data concerned, the ANISN format is used in DENOVO particle transport calculations. In particular the 27n19g and 200n47g (27 or 200 energy groups for neutrons and 19 or 47 energy group for photons, respectively) libraries are general-purpose shielding libraries based on ENDF/B-VII.0, that represent the higher number of isotopes and elements with respect to the other available and are particularly suitable for fusion neutronics transport applications.

ADVANTG is a very powerful tool because generates the weight window file in a complete automated way (figure 2.3). The time scale for the generation of the wwinp file is in the order of the few hours. In the calculation phase the CADIS method [24]

is developed for individual tally responses, while FW-CADIS [25] can be used for achieving uniform statistical convergence across multiple individual tallies as well as mesh tallies.

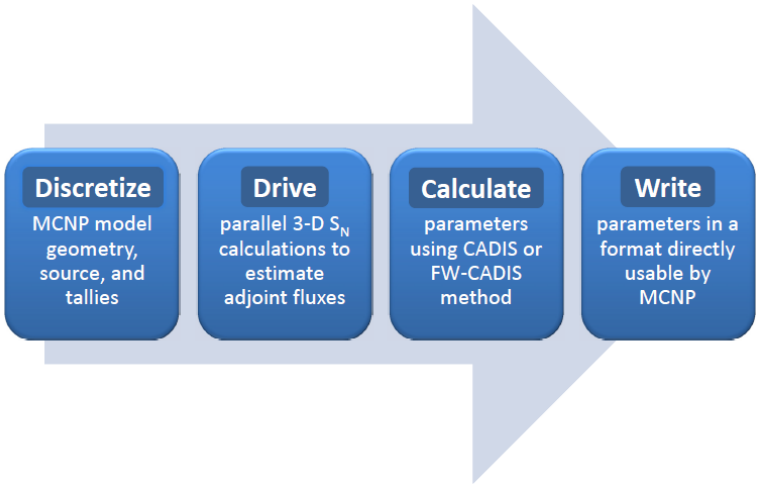

Figure 2-3 diagram of ADVANTG step to write weight windows parameters

Currently is the most widely used tool for the variance reduction in fusion neutronics problems and it is widely used for the analyses in this dissertation. Example of ADVANTG mesh implementation for DTT analyses is shown in fig. 2.4. In this figure the mesh used for ADVANTG input is shown. The scoring point is far from the source and after a concrete slab where the statistic is very poor in a normal calculation with statistical errors greater than 40%. The use of ADVANTG reduce the statistical error at levels below 5%.

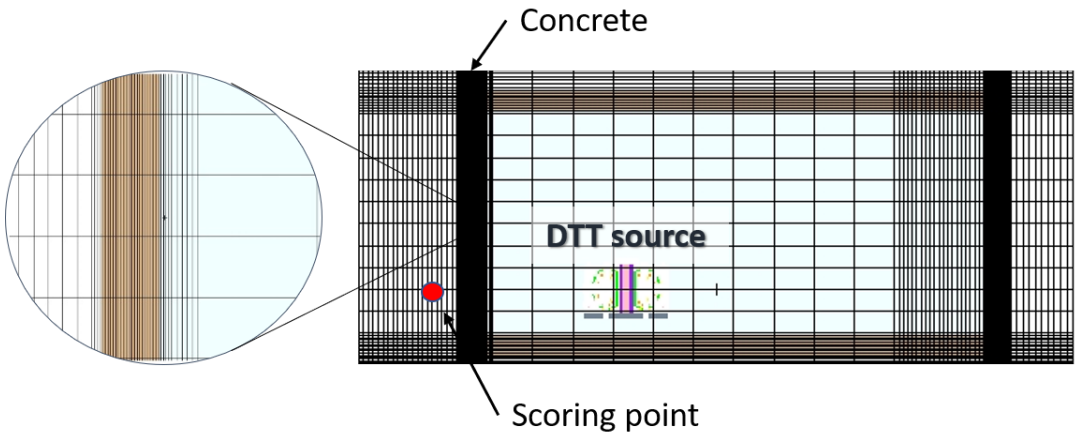

Figure 2-4 example of weight windows mesh in DTT studies for tokamak building

2.5 Activation Issue

Radioactivity induced by neutron interaction is a major issue of fusion power and directly affect the choose of materials and their composition, especially for the stell. Long-term radiation hazard also determines material radioactive waste strategies such as recycling and disposal. Short-term radiation hazard determines safety during normal and off-normal operation conditions. Several situations are related to the material activation and there are a number of codes which evaluate the effect of activations. The following formula describes the transmutation of the nuclei:

$$\frac{dN_j(t)}{dt} = \sum_i \sigma_{ij}\Phi N_i - \lambda_j N_j(t) = \sum_i R_{ij} - \lambda_j N_j(t) \qquad (2.6)$$

Where N_i and N_j are the number of nuclides i,j at the time t, λ_j is the decay constant of the nuclide in s^{-1}, σ_{ij} is the cross section of the reaction of *i* producing *j* in s^{-1} and Φ is the neutron flux density expressed in $cm^{-2}\ s^{-1}$.

The study of the activation issue is of fundamental importance in the fusion machines and the prediction of the induced activation and resulting dose rates is a main issue in fusion framework of maintenance operation and access of the operators in the reactor hall.

The inventory code FISPACT [26] is commonly used for the inventory assessment and to provide the contact dose rate. The used approximation is that of the Jaeger [27]. It assumes that the contact dose rate is calculated throughout a semi-infinite slab of material. The calculation with FISPACT is particularly useful for waste assessment and to investigate the dominant nuclide activated during the reactions and to find reaction pathways responsible of the activation dose.

The shutdown dose rate calculation is particularly important and is nowadays one of the major research field within the fusion neutronics. Although the shutdown dose rate analysis is not the main focus of this work some results regarding DTT

machine will be discussed in later chapter and a brief overview of the calculation methods is presented.

The Shut Down Dose Rate (SDDR) is the dose due to the decay gammas emitted from radioactive nuclides generated by neutron activation. The assessment foresees the coupling of the radiation transport and activation codes.

Two approaches have been developed in the frame of fusion technology to perform the SDDR assessment:

- Rigorous two-step (R2S) methods
- Direct one step (D1S) method.

2.6.1 Rigorous two step methods

In R2S approach a regular neutron transport calculation provides the spatial distribution of the neutron flux spectra (radiation transport, first step); the decay gamma source distribution is obtained through a nuclide inventory calculation using the neutron flux spectra calculated in the first step and the irradiation history; finally, a pure gamma transport calculation (radiation transport, second step) using the decay gamma source distribution from the inventory code provides the dose rate at the specified locations. The main advantage of R2S is the full calculation of the nuclide inventory, so that all potential reaction chains are implicitly included. In this respect the method is problem independent. On the other hand, the R2S results are dependent on the mesh resolution because the neutron fluxes and the decay gamma source are spatially averaged over the voxels and the multi-groups gamma energy resolution leads to inaccuracies. Furthermore, the uncertainty includes only the gamma transport statistical error (i.e., no error propagation).

2.6.2 Direct one step methods

The Direct One Step (D1S) method [28] is an approach in which the decay gammas are emitted as prompt and, thus, the neutrons and decay gammas are transported in the same single Monte Carlo radiation transport simulation. Special ad-hoc

libraries are used where the neutron cross sections are replaced with those from the activation library for selected reactions and the prompt gammas are replaced by decay gammas emitted by the generated radionuclide.

D1S methods are based on modified version of MCNP in which fictitious delay times in terms of "shakes" are linked to the emitted gamma according to the parent radionuclide in order to distinguish the dose contributions due the different radionuclides. The assumption in the coupled radiation transport calculation is that both irradiation and decay are instantaneous. Thus, temporal correction factors are needed to take into account the build-up and the decay of each radionuclide dependent on the neutron irradiation history. These factors can be calculated analytically or are derived using an inventory code.

The D1S main advantage is the direct coupling between the decay gammas and the neutrons, thus the results are independent on the mesh resolution, it has an intrinsic correlation between the neutron and gamma errors, and it is much faster than R2S. However, the transport libraries have to be adapted to the specific problem and limitations are foreseen in case of high burn-up and multi-chain reactions (not relevant for DTT, ITER and existing machines but important for DEMO and future power reactors) and when the machine configuration shows significant changes in on and off operations phases.

The analyses for this work of thesis have been performed with the Advanced D1S tool developed in ENEA Frascati research centre [29]. The tool is based on MCNP5 and it uses FISPACT inventory code to derive the temporal correction factor. It has been extensively used for ITER, JET and DEMO and validated through benchmark experiments at JET.

3 The Divertor Tokamak Test (DTT) Facility

"The saddest aspect right now is that science gathers knowledge faster than society gathers wisdom"
Isaac Asimov

Within the multiple issues through the realization of the fusion energy, one of the most important is related to the power exhaust. This problem is described in the fusion roadmap [30] as a potential "*showstopper*" for fusion[9]. For this reason, one of the most important steps to the road to DEMO is the *Divertor Tokamak Test facility* (DTT) which is a machine with the aim at studying the power exhaust issue in a DEMO relevant environment. In the next paragraphs a description will be given in order to have an overview of the machine and its components.

3.1 The power exhaust issue

In 2012 the EFDA consortium wrote the general roadmap through the realization to the fusion energy [30]. It is divided into eight points which represent the critical issues and the strategy to face up the problems. Among them, the point number #2 clearly describes the power exhaust as a milestone challenge for the fusion.

The confinement of the plasma with the required conditions and for sufficient time is the fundamental requirement to be satisfied to achieve the thermonuclear power. The confinement time is proportional to the temperature of the ions and electrons and inversely proportional to the total power input. The confinement is limited by

[9] Appendix C: "*Roadmap to Fusion Energy*"

the thermal conduction and convection processes. Nevertheless, the radiation is also a source of energy loss [31].

The plasma is confined by means of strong magnetic fields forming a set of closed, nested magnetic surfaces. However, the confinement is not perfect and, at the boundaries of the plasma, a few millimetres thick layer, where the magnetic field is open is observed (fig. 3.1). This layer is commonly known as the *scrape-off layer* (SOL). From the SOL the charged particle escape from the magnetic confinement and, eventually, are exhausted in a narrow region of the chamber called *divertor*.

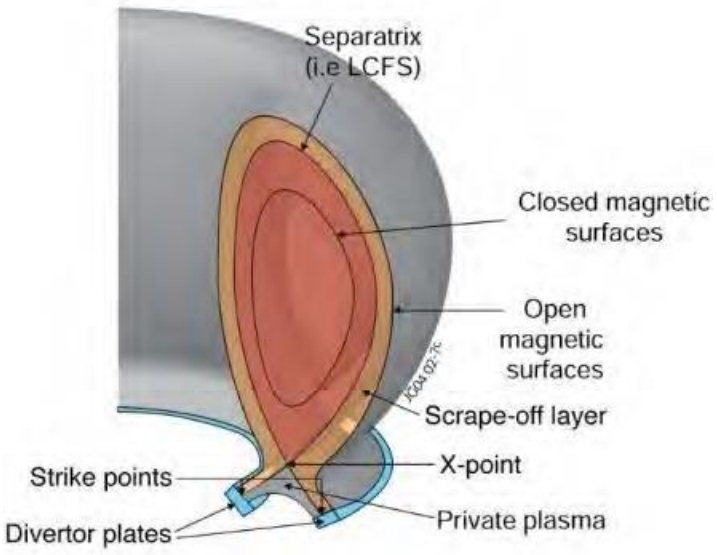

Figure 3-1 Plasma edge: geometry of the Crape-off layer (SOL) and of the divertor plates

This component (figure 3.2) is particularly stressed by the heat loads coming from the charged particle escaped from the plasma towards the *separatrix* (the last closed magnetic surface). It's worth noting that the heat flux parallel to the magnetic field, in the SOL region of ITER and DEMO, is expected to be comparable to that on the surface of the sun. The loads on the plasma facing components are expected to be greater than 10 MW/m^2 (in ITER is expected to reach the 50 MW/m^2 [32]) so a strategy to cope with this problem is necessary considering the following steps:

- Development of plasma facing components able to withstand large heat flux on the divertor.
- Selection of suitable divertor geometry and magnetic flux map to reduce the normal heat flux on the divertor.
- Reduce the heat power impinging on the divertor by increasing the edge plasma density and injecting impurities in the SOL region.
- Recycling of the particles released by the wall and increase of the density close to the plates, resulting in a "*detachment*" from the wall of the plasma.

Anyway, it should be considered that the present level of technology allows the experiment on the "*detached*" condition in a small-medium size machines with a very different SOL region with respect to that of ITER and DEMO. Furthermore, the level of the simulation of the SOL is not sufficiently reliable and various problems could be arise during the integration of this solution with the plasma core and the other reactor subsystems (i.e. impurity contamination of the core, compatibility with the plasma bulk, …). Moreover, neither the nuclear aspects nor the limits of temperature related to the materials could be neglected.

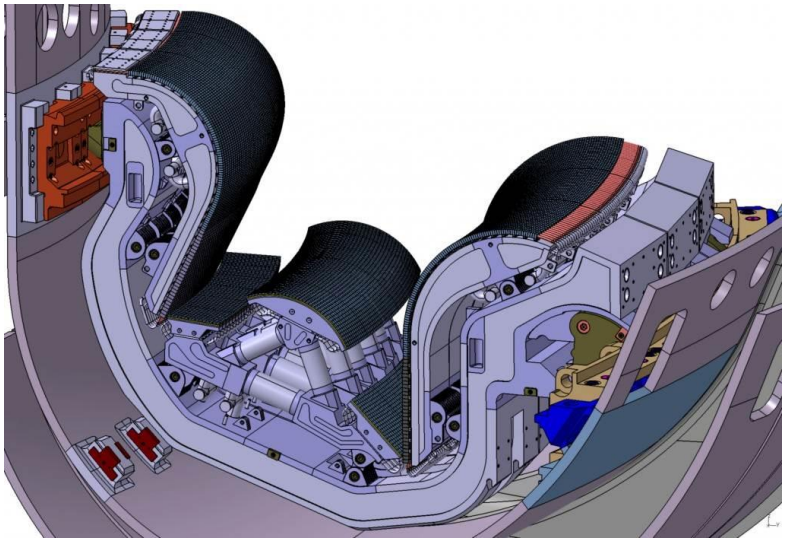

Figure 3-2 isomeric view of ITER tungsten divertor

3.2 DTT role and objective

The Divertor Tokamak Test facility (DTT) find its perfect role from the physics and technology point of view in the study of the SOL and power exhaust. As suggested by name, the main goal of the DTT machine is to test alternative divertor concept able to operate in a DEMO relevant conditions. In fact, after many years of experiments and theoretical simulations, the fusion community agreed to the fact that ITER could not provide alternative solutions to the heat exhaust problems. The risk is that the strategy adopted in ITER [33], coming from the operational experience in medium-large size tokamaks, could be not extrapolated in a reactor-scale device as DEMO will be. In the "European Research roadmap to the Realisation of Fusion Energy" a three-step program [34] has been wrote in order to develop alternative solution to the ITER strategy, mainly based upon the study on material able to work with large heat flux and upon the study of the plasma scenarios and exhaust process.

In this frame DTT plays a unique role as a facility able to investigate all the three lines of the EUROFusion program in regimes relevant for ITER and DEMO and where plasma core and edge properties are fully integrated. It will operate in an unexplored sector by other machines, including JT-60SA. For this reason DTT will have a relevant role also for the state-of-art integrate study of tokamak physics, as recommended by the EUROfusion ad-hoc group "*strategy for the Plasma Exhaust*" (PEX) [35]. To face up to all these challenges it will be flexible, available and accessible.

3.3 DTT engineering design

To satisfy the requirements mentioned above, and also meet the budget constraints, a compact, high magnetic field approach based on the weak similarity scaling has been chosen [36]. The result is a machine with the following main parameters:

- Major radius R=2.11 m
- Minor radius a= 0.64 m
- Maximum plasma current = 5.5 MA
- On axis toroidal magnetic field B= 6 T

An auxiliary power of 45 MW, provided by a set of additional heating systems like Electron Cyclotron Resonance Heating (ECRH), Ion Cyclotron Resonance Heating (ICRH) and Negative Neutral Beam Injector (NNBI), in order to reach the DEMO relevant condition is also foreseen. The superconductive magnets allow for a 100 s discharge duration.

To create the relevant environment condition, the key parameter is the P_{sep}/R has to be equal to 15 MW/m, very close to that foreseen in ITER and DEMO. The availability of 45 MW coupled to the plasma through different means in a high field, high density, compact and superconducting device allows both for unprecedented combination of power loads on divertor and first wall materials and discharge duration and for tailoring plasma core performance in a variety of regimes, including high radiation ones [36]. The flexibility of the machine is the main characteristics which allows to test different plasma configurations. It should be designed flexible enough to host the EUROfusion divertor in the next years. DTT will be full symmetric and the up-down symmetry ensure the possibility to put in the machine both the lower and upper divertor, thus a symmetric magnetic divertor configuration.

3.3.1 Vacuum Vessel

The first aim of the Vacuum Vessel (VV) [37] is to host the fusion reactions and acts as a first safety containment. In general, it could be doughnut-shaped or torus-shaped in a tokamak machine and the plasma particles moves continuously around in a spiral path without touching the walls. The vacuum vessel provides high vacuum environment for the machine. It is also the first barrier for the radiation

coming from the plasma and provides support for the in-vessel components like blanket and divertor. Inside the VV the water flows to remove the heat generated during the pulses. The size of the VV is an important parameter to confine the plasma: the larger is the VV volume, the easier is to confine the plasma.

In DTT the vacuum chamber is a stainless-steel torus vessel with a "D" shape cross section (fig. 3.3). 18 modules of 20° each will be welded together to compose the DTT-VV. Each module has several access to ports for several purposes. VV has these main functions:

- Provide high a reliable vacuum;
- Provide a consistent first barrier able to withstand postulated accidents without losing confinement;
- Support the nuclear loads within the allowable temperature and stress limits;
- Host and support the in-vessel components and their loads during and off-operations;
- Maintain a specific toroidal electrical resistance;
- Provide the access port or feedthroughs for in-vessel component, diagnostic, heating system, service and maintenance.

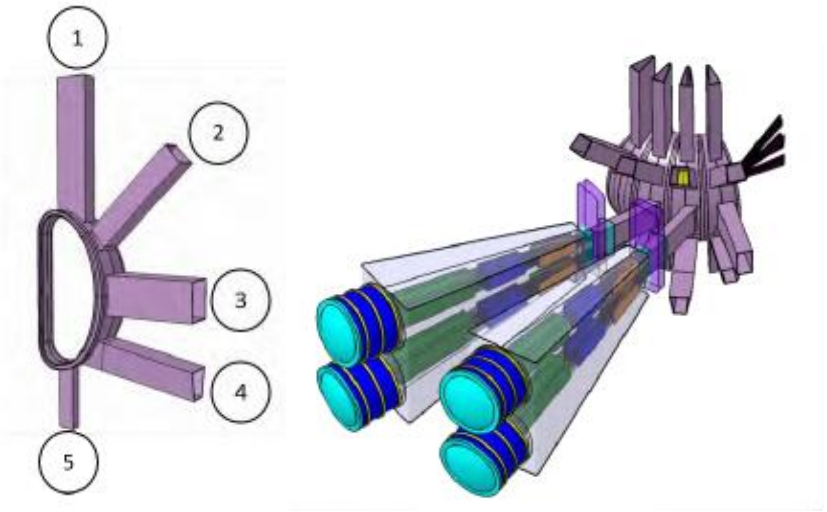

Figure 3-3 standard and NNBI modules

Moreover, four sectors must allow the commissioning and decommissioning of the outboard (OB) first wall (FW), the lower and upper divertor.

Among the sectors, two of them must allow the hosting of the negative neutral beam injectors (NNBI) (fig.3.4) and the port position is defined taking into account the interface with the Poloidal and Toroidal Field Coils. Fig. 3.4 shows the main sector in black and the magnet system.

In the current configuration the main vessel is a 15 mm thick AISI 316L(N) stainless stell double-wall structure. The maximum height is 3940 mm with a radius of 1265 mm in the inboard side and 3400 mm in the outboard. The AISI 316L(N), among the possible suitable materials, has the best mechanical and chemical properties.

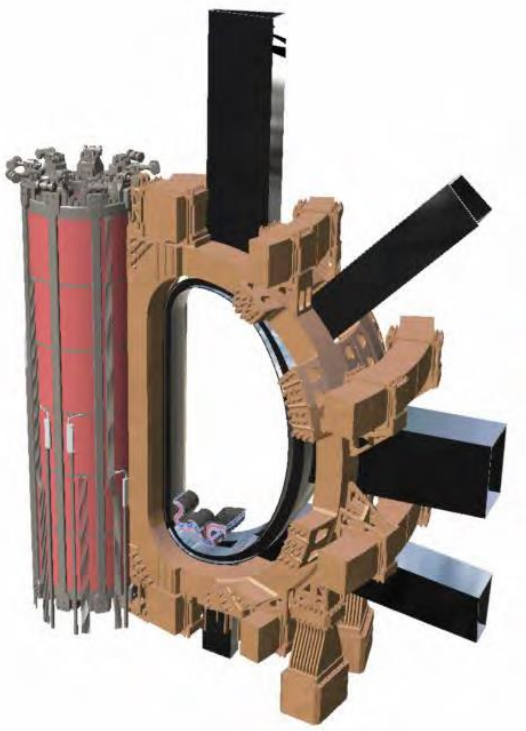

Figure 3-4 Isometric view of a Vacuum Vessel sector (in black) with schematic representation of magnets and divertor

Every VV sector has 5 openings in which the ports (25 mm thickness at present) are directly welded for the diagnostic, the vacuum system, the additional heating systems ect. Every port should have the space to host the cooling pipes of in-vessel components (i.e. the divertor). The VV is cooled by borated water flowing in the space in between the VV double shell. Borated water has been chosen in order to moderate and absorb neutrons to reduce the nuclear loads on the magnets. The borated water is at 60 °C with 5% of Boron content. During normal operation the water is at 50 °C with the maximum temperature foreseen below the 80 °C in order to prevent the corrosion effects of the boric acid.

3.3.2 Cryostat

The cryostat [37] is the vacuum container. It surrounds the whole machine and is a part of the secondary containment barrier. It provides high vacuum and ultra-high cool environment for the DTT vacuum vessel and for the magnets. It will provide the space allocation for the ports and penetrations, with proper bellows necessary

to compensate the differential movements, to the vacuum vessel. The pipes pass to through the cryostat to connect the elements outside with the correspondent inside. The structure of this components will allow the safe access of the personnel, will ensure the required vacuum and the limitation of the gas leakage which will be determined in the next design phase.

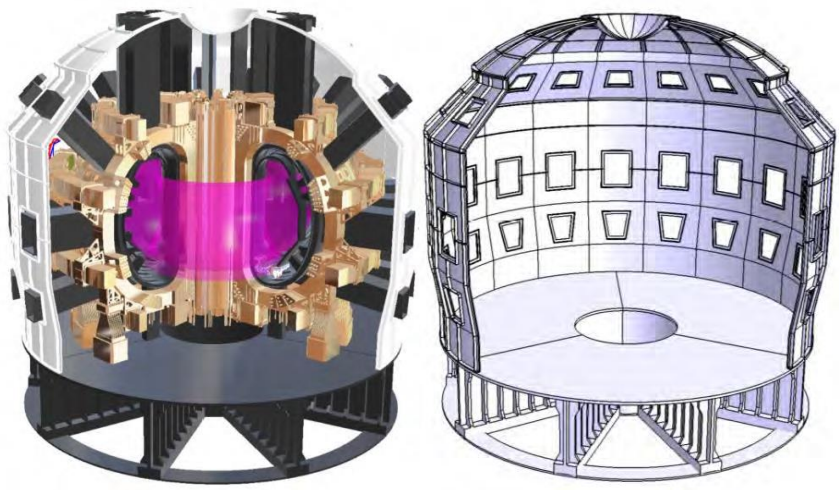

Figure 3-5 Pictorial view of DTT tokamak basic machine (left); 3D CAD model of DTT Cryostat (right).

The DTT cryostat, showed in fig. 3.5 is composed by a single-wall cylindrical vessel with stiffness ribs, a basement made of welded plates and a tori-spherical top lid, with 16 tons estimated weight. The main cylindrical body is composed by three sectors of about 120°. Its maximum diameter is 11.2 m, and its height is about 7.5 m. The whole dimensions have been studied in order to ensure the proper access to the personnel and facilitate the installation of the components. The weight of the cylindrical body is about 66 tons with 30 mm thickness. The cryostat is a fully welded AISI 304L(N) stainless steel with impurity content controlled (Co < 0.05% wt%, SA-240) in order to reduce the neutron activation. The cryostat is supported by a stainless stell basement (with impurity content controlled) with a 220 tons weight, showed in fig. 3.6.

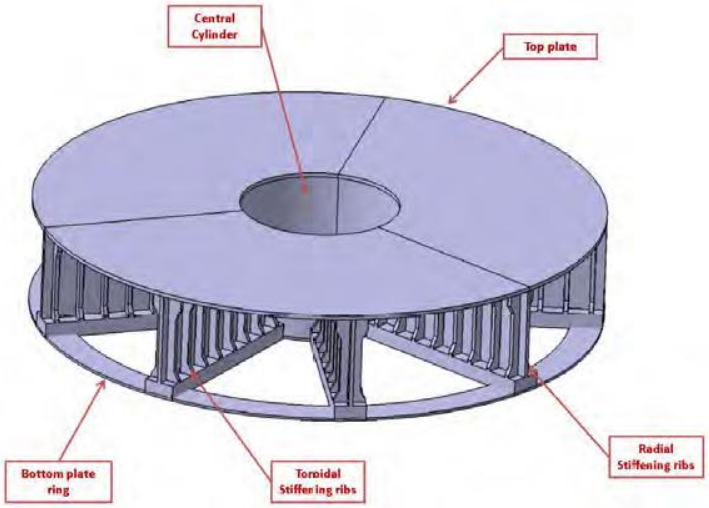

Figure 3-6 Cryostat steel basement

3.3.3 Thermal Shield

The temperature difference between the tokamak warm components and the superconductive magnets (4.5 K) point out the necessity of a structure which has to minimize the heat loads on the magnets: the so-called Thermal Shield (TS) [38]. In DTT it is subdivided in three regions which cover three different components of the machine: the Vacuum Vessel (VVTS), the ports (PTS) and the cryostat (CTS). It is composed by 18 electrical isolated sectors, made by AISI316L(N). The cooling to the TS is provided by the helium gas at 80 K and 1.8 MPa. The DTT TS is shown in fig. 3.7.

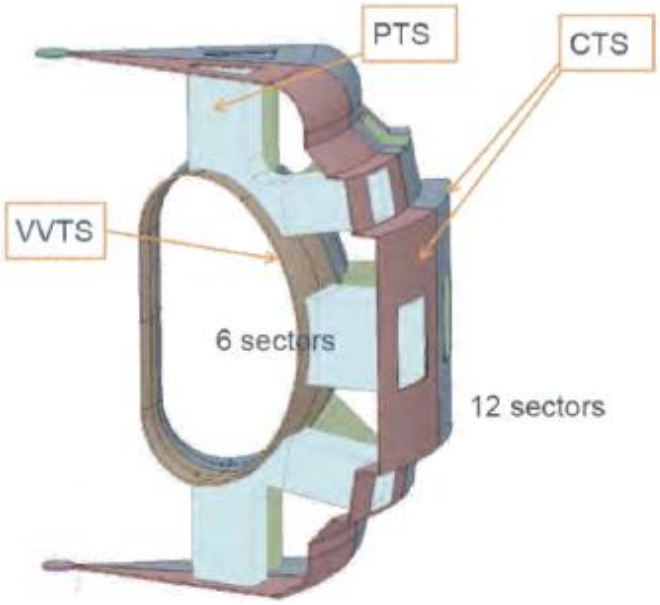

Figure 3-7 Schematic view of the DTT thermal shield

3.3.4 Neutron Shield

DTT is expected to produce in its high-performance phase up to 1.5×10^{17} n/s DD 2.45 MeV neutron plus about 10^{15} n/s 14.1 MeV DT neutron due to the triton burn up. With this level of neutron production, the critical components of the machine must be shielded and protected from the neutron effects, in particular from the nuclear heating which can increase the temperature of the components up to critical values. During the evolution of the machine design more than 50 shielding configurations of the VV have been examined using water, borated water, boron carbide (B4C), tungsten carbide (WC) and Borated Steel (SSB) to reduce the nuclear heating.

The most critical zone for the nuclear heating is the first layer of the inboard TF coil at the equatorial plane. Without a proper shield, the value of the nuclear heating is greater than the value of 1 mW/cm^3 (about 8 mW/cm^3 considering a safety factor of 1.5 in order to include the uncertainties in the model and nuclear data). Thus, a suitable shielding is needed to protect the TF coils because the double-wall VV filled with normal water is not sufficient. The adding of boron in water reduce the value

of nuclear heating, due to the shielding properties of the boron, but is not sufficient to reach the expected values (1.76 mW/cm^3 including safety factor).

The neutron shield [39] has been chosen among several feasible options and the best configurations consists in a combination of borated water and 2.5 cm of B4C compacted powder an W inside a SS container. The present configuration of the neutron shield is composed by 0.1 cm of steel, 1 cm of B_4C powder, 0.5 cm of tungsten, 0.9 cm of B_4C powder and 1.5 cm of rear steel shell. With this configuration the design limit is reached.

As the boron content in water induces corrosion at high temperatures, the strategy chosen for DTT is to use borated water only during high performance phase. Indeed, the calculations show that the machine might operate with pure water in several phase of DTT lifetime depending on the performances.

3.3.5 First Wall

The First Wall (FW) [38], as suggested by the name, represent the first "solid" component after the plasma and it is particularly important because it has to satisfy several requirements and face up with different components with their own needs.

The DTT FW must satisfy the compatibility requirements with:

- the liquid lithium divertor, which will be one the most relevant experiment in the DTT life. This experiment foresees the possibility to recover the amount of metal evaporated from the divertor region by making it condensate without solidifying on the FW. For this experiment the temperature of the plasma facing surface must be 200 °C (above the melting point of lithium with margin).
- Remote Handling (RH) system for the assembly.
- Electromagnetic loads.
- Diagnostic systems. The FW must host the diagnostic in a reserved space.

- DEMO. Those materials with moderate and high activation (i.e. copper) must be avoided as structural materials.

The DTT FW has been designed considering three different main components: the inboard FW (IFW), the outboard FW (OFW) and the top FW (TFW). The last one could be replaced by another divertor in the double null scenario.

The IFW has to be designed to withstand the loads due to the current ramp-up phase which means a load up to 1.5 MW/m^2 in 15 s. The OFW is designed to withstand up to 0.55 MW/m^2. The TFW is designed for disruption loads. The maximum radial build of the FW is 55 mm in order to satisfy the nominal tolerance of the distance between the FW and the separatrix.

3.3.6 Divertor

Presently, the divertor foreseen for ITER is a full tungsten divertor but it could be not extrapolated in a reactor scale machine like DEMO.

For this reason, the study of the power exhaust will be done by means a number of plasma configurations and alternative divertor types which will be tested in DTT [40]. The machine is designed to host the actual single null (SN) configuration which is consider the "*conventional*" configuration and, thus, divertor. Other configurations which will be tested are: X Divertor (XD), Super-X divertor (SXD), Snow Flake divertor (SFD) or Double Null (DN).

The possibility of study Liquid Metal Divertor is also foreseen considering the flexibility of the machine. The use of the liquid metal requires specific characteristic and requirements of the machine regarding the VV, the Ports and the Remote handling which will be suitable to remove such components.

During the first experimental phase of DTT, the magnetic configuration will be chosen together with EUROfusion consortium according to the most promising Plasma Exhaust solutions identified for DEMO.

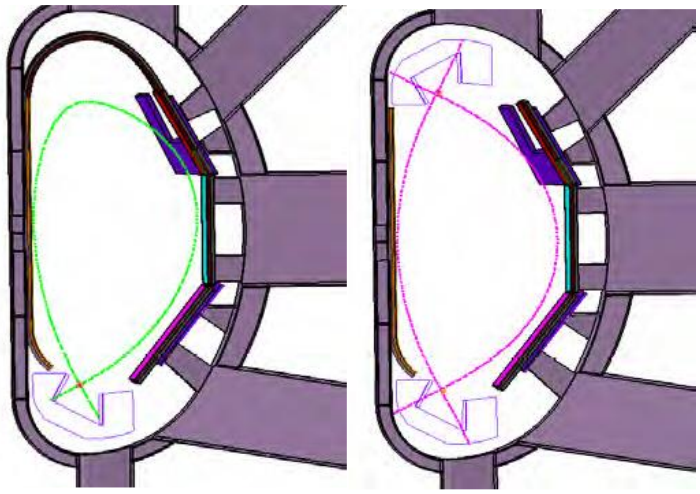

Figure 3-8 Single Null (a) and Double null (B) configuraitons

Presently, the magnetic configuration forseen for the first operational phase of DTT is the conventional divertor of Single Null confiuration showed in fig. 3.8.a. Moreover, the Double Null (fig. 3.8.b) configuration which comprehend the second upper divertor is also forseen in order to test this solution.

Since the divertor mission is to exhaust the major part of the plasma ions thermal power in a region far from plasma core in order to control plasma pollution, the mosto important requirement is related to the power exhaust and vacuum pumping needs.

Furthermore, the design of the DTT divertor cassettes should consider several constraints:

- Incidence angle of plasma legs on divertor targets.
- Thermal loads on the divertor targets.
- Alignment between adjacent targets to avoid edge effects.
- Interfacing system – FW, VV, Ports.
- Remote handling for divertor replacement
- Supports to transmit loads during normal operation, baking, major disruption, seismic events.
- Coolant supply.
- Diagnostic.

From those constraints the design of the DTT conventional divertor results in 54 toroidal sectors or cassettes. Each sector is composed by a cassette body supporting the plasma facing components (PFCs), an inner vertical target (IVT) and outer vertical target (OVT) coupled with a dome (fig. 3.9)

Figure 3-9 Design of a FAST-like divertor

The IVT and the OVT are made of Tungsten, design-based upon the old FAST divertor concepts [41], [42]. The cassette body is made of AISI 316L(N) and serves as a support of the plasma facing units and to route the coolant able to sustain large stresses even with the highest plasma current conditions.

Since the main goal of the DTT is to test different divertor concepts, a certain number of ports should be dedicated to the divertor remote handling.

3.3.7 Additional heating systems

The aim of DTT to test different divertor concepts in a DEMO-relevant environment requires to fulfil a particular requirement: the power to the separatrix, compared to the major radius of the machine should be greater than 15 MW/m: $P_{sep}/R \cong 15$ MW/m. This requirement can be satisfied by adding an additional amount of power of 45 MW to the plasma using a mix of heating systems[9]: Electron Cyclotron Resonance Heating (ECRH), Ion Cyclotron Resonance Heating (ICRH) and Negative Neutral Beam Injection (N-NBI). The distribution of the additional Heating and Current Drive (HCD) systems is, at present, under evolution and

discussion. The total power requested to simulate the reactor environment will be reached after many years of operations. At the so-called "*day-1*" (day-0 being the first commissioning of ohmic machine), the foreseen power is defined as that required to reach the H-mode in a 4 MA plasma. This could be obtained using 25 MW of additional power, progressively available after one year from the machine start-up. Later, the selection of the mix of the additional power will be based in terms of the plasma quality and divertor material/configuration performances. In other terms, the selection of the additional heating depends upon the functionality of a particular system to obtain a high plasma performances.

3.4 DTT site and current layout

At the beginning of the 2018 the "*Italian National Agency for New Technologies, Energy and Sustainable Economic Development*" (ENEA) published a public call for tenders for the choice of the DTT site. Many Italian regions participated to the call and in the end Frascati ENEA centre, place in the centre of Italy (fig. 3.10) has been chosen to host the DTT machine. The choice of the site is important for the distribution of the buildings and for the radiation protection constraints. In the Frascati ENEA research centre already exist a Tokamak machine known as Frascati Tokamak Upgrade (FTU). This tokamak is surrounded by several building which could be reused for the new site configuration for DTT.

The site in mainly composed by the torus hall building (THB) surrounded by auxiliary buildings (figure 3.11). DTT represents a significant upgrade with respect to FTU tokamak, so even though many buildings could be reused as they are some others must be built as new in order to host the required systems. This is particularly important for the good realization of the project and the coordination activity for the organization of the site is one of the most important among the activities within the DTT project. Moreover, since DTT is a machine which is expected to produce a great amount of neutrons during its life, the Italian regulations imposed a strict

licensing procedure that will be described in the next chapter. This means that the buildings must be developed in order to respect the radiation protection constraints adding significant difficulties to the project. So, the site, will be the results of the collaborations between civil and nuclear knowledge.

Figure 3-10 Frascati location in Italy

The main changes, in addition to the main THB, in the Frascati centre regard:

- Building for the additional heating system;
- Cryogenic plant;
- Sub-station for the HV 150 KV grid transformers;
- Area for the AC/DC converters;
- Area for the secondary water-cooling system;

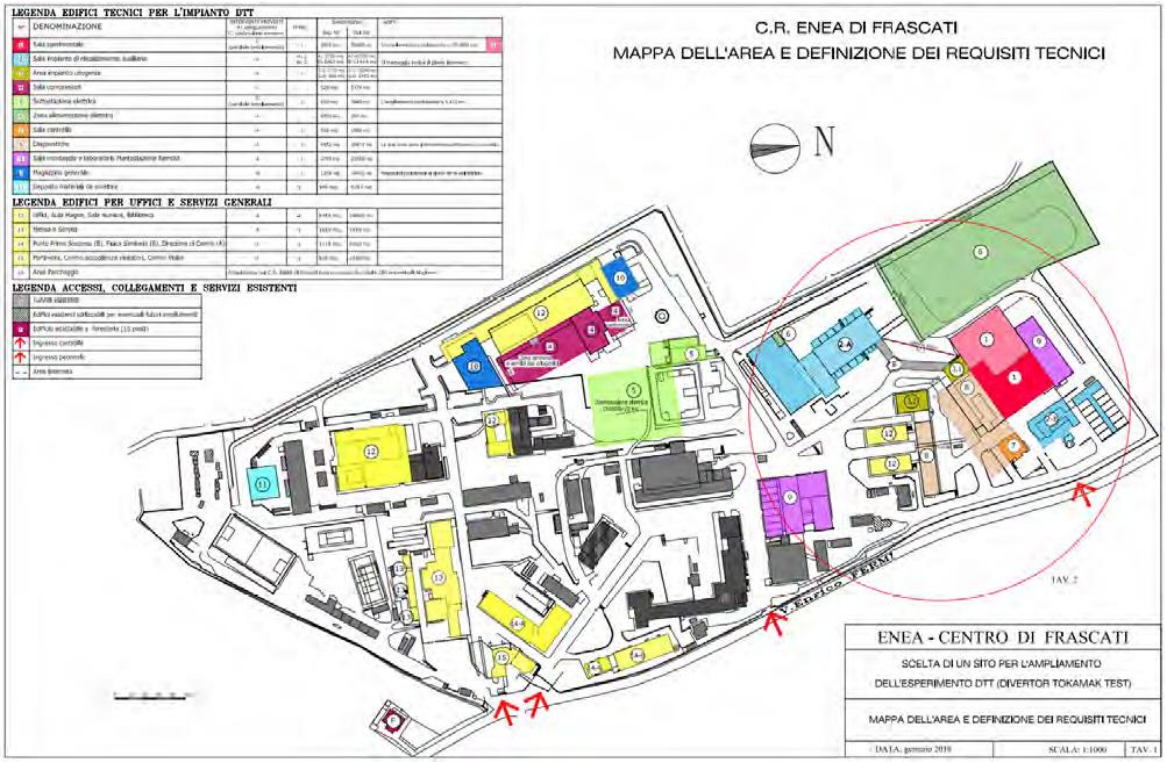

Figure 3-11 Distribution of the buildings in DTT site layout

This means that a big activity for the integration of these new buildings with the existing buildings is foreseen and will be included in the project as one of the most relevant activity within the DTT facility development.

4 Neutronics of the Divertor Tokamak Test (DTT) Facility

"Science never solves a problem without creating ten more"

G. B. Shaw

The Divertor Tokamak Test facility will produce up to 1.5×10^{17} n/s 2.45 MeV DD neutron plus 1.5×10^{15} 14.1 MeV DT neutrons [39]. This means that the neutronics studies play a fundamental role in the DTT machine development. There are many aspects of the problem which require the neutronics studies. The first is the project of the machine itself: the effect of the neutron on the structural materials requires deep studies for the machine development. The second aspect regards the radiation protection: the great amount of neutron production implies great neutron and gamma fluxes even outside the cryostat where the personnel operates. Even in this case the neutronics studies are necessary to evaluate the doses inside and outside the Torus Hall Building (THB) and in the rear buildings, which host the auxiliary systems, as well as the shutdown dose rate (SDDR), fundamental for the accesses inside the main hall and for the maintenance operations. Furthermore, at the boundaries of the ENEA Frascati research centre, the radiation protection limits for the population, imposed from the Italian regulation, must be respected.

Another aspect regards the integration of the components such as the HCD systems and diagnostic inside the machine. Those systems have their own requirements

regarding the neutron and gamma fluxes for the electronics, nuclear loads and shielding needs.

4.1 DTT neutron production

The fusion reaction rate and the neutron yield produced by those fusion reactions are related to the plasma parameters (elongation, triangularity, ion and electron density and velocity), behaviour and complex geometry. It's too difficult to generate a realistic tokamak neutron source model for transport calculations for Monte-Carlo calculations.

The emitted neutron rate from a plasma is a weighted average of the velocity distribution of the particles with cross section and relative velocity and the neutron spectrum is simply the energy-dependent probability of neutron emission per steradian [43]. DTT is a fusion device with magnetically confined plasmas experiments carried out with deuterium fuel for simulation of the plasma, so the following treatment refers to the DD plasma neutron source.

In the case of neutral-beam-heated plasmas, the distribution of the particles velocity $f_D(v)$ can be split into a thermal and non-thermal part, called "*beam*", part $f_b(v)$**.** The major issue is to distinguish between the thermal and non-thermal part. A conventional division, where all slowing-down particles above $1.5v_{th}$ are classified as "beam" and those below are classified thermal [44] is used in many codes. However, the most natural way of splitting the velocity distribution is by defining an isotropic Maxwellian $f_{th}(v)$ which coincides with the distribution $f_D(v)$ when $v \rightarrow 0$:

$$f_d(v) = f_{th}(v) + f_b(v) \qquad (4.1)$$

The corresponding densities are n_D, n_{th} and n_b.

Thus, the fusion reactivity may be written as the sum of the three different reactivities:

$$< \sigma v >_{DD} = < \sigma v >_{th} + < \sigma v >_{bt} + < \sigma v >_{bb} \qquad (4.2)$$

Where $< \sigma v >_{th}$ describes the thermal part of the plasma, the second term, $< \sigma v >_{bt}$, describes the reactivity between the fast particles and the thermal plasma, and the latter, $< \sigma v >_{bb}$, is the reactivity of the fast particles among themselves.

Following this strategy, the total neutron rate Q_n could be divided into three different neutron rates the thermal Q_{th}, the beam-termal Q_{bt} and the beam-beam Q_{bb}. Thus, the neutron rate emitted by the plasma is:

$$S_n = \int Q_n dV \qquad (4.3)$$

Where V is the plasma volume.

The neutron yield Y_n is the integral of the neutron source strength:

$$Y_n = \int S_n dt \qquad (4.4)$$

It's, also, worth noting that it's important, for the definition of the parameter, to define the *peaking factor*, that is the radial dependence of a given plasma parameter, defined as:

$$Z = \frac{Z(0)V}{\int Z(\rho)\, dV} = \frac{Z(0)}{< Z(\rho) >} \qquad (4.5)$$

Fig. 4.1 shows a typical geometry used to represent a plasma source with the main parameters to be considered.

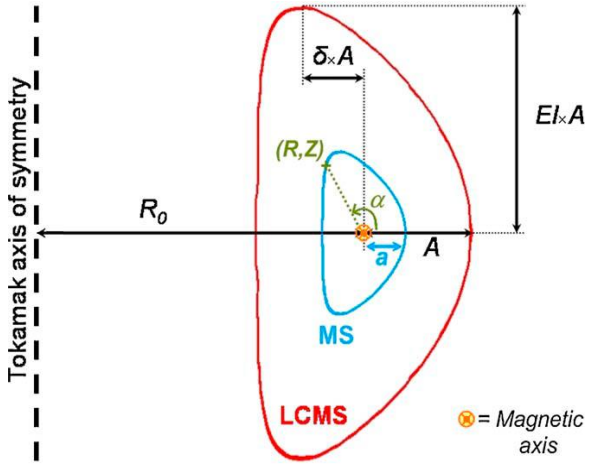

Figure 4-1 typical geometry used for plasma sources and main parameters

This approach has been used to calculate the DTT neutron yield rate. This has been assessed by considering conservative assumption on mono-dimensional analyses considering both thermal and non-thermal components due to plasma, beam-plasma and beam-beam interaction with the maximum NBI power injected. [39]

From the results of these evaluations, the maximum Deuterium-Deuterium 2.5 MeV neutron production in DTT H-mode high-performance operations is expected to reach the considerable value of 1.5×10^{17} n/s, with a flat-top up to 50 s. Moreover, high energy 14 MeV neutrons are produced from the Deuterium-Tritium reactions due to the Triton burn-up inside the plasma. This value is expected to reach the 1% of the total amount of DD neutron productions, i.e. 1.5×10^{15} n/s.

For the DTT operational life, an optimistic history of irradiation has been foreseen, considering 28 years of operational program, basically composed by 6 month of operation alternate with 6 month of shutdown per year. Table 4.1 report the irradiation history for DTT.

The maximum yield rate, mentioned above, of 1.5×10^{17} will be reached after many years of operations. According to the foreseen operational plan, reported with more details in [36], the high performance phase, where the maximum yield rate will be reached, is foreseen after eight years of operation, with an annual DD neutron yield rate of 1.53×10^{21} n/year (1.53×10^{19} DT neutrons).

At the end of its life, DTT is expected to produce a great amount of neutrons, equal to 3.73×10^{22} (3.73×10^{20} DT neutrons) which are equivalent to 2.49×10^{5} s of operations at full power. This great amount of neutrons, although conservative, leads to deep and complicate three-dimensional neutronics studies to assess the fluxes and doses inside and outside the tokamak building and the evaluation of the shutdown dose rate for the safety purposes, for the remote handling and for the radioactive waste assessment.

Table 4-1 DTT irradiation history from [36]

Year	**Maximum DD neutron yield rate(n/s)**	**Annual DD neutron yield (n/year)**
1	$3.60 \cdot 10^{14}$	$9.00 \cdot 10^{18}$
2	$2.70 \cdot 10^{1}$	$6.75 \cdot 10^{19}$
3	$1.80 \cdot 10^{16}$	$4.50 \cdot 10^{20}$
4	$4.30 \cdot 10^{16}$	$8.60 \cdot 10^{20}$
5	$6.00 \cdot 10^{16}$	$1.20 \cdot 10^{21}$
6	$9.30 \cdot 10^{16}$	$1.26 \cdot 10^{21}$
7	$1.00 \cdot 10^{17}$	$1.35 \cdot 10^{21}$
8	$1.10 \cdot 10^{17}$	$1.49 \cdot 10^{21}$
9 to 28	$1.50 \cdot 10^{17}$	$1.53 \cdot 10^{21}$

4.2 Strategy for DTT neutronics studies

As mentioned in the previous paragraph, the neutronics studies for DTT include a wide range of mandatory calculations related to the machine itself, to the calculation of the level of neutrons and gammas fluxes and doses inside the Torus Hall (TH) and surrounding buildings and to the auxiliary components, such as diagnostic and heating systems, which must be integrated in the machine and in the site layout. Moreover, the shutdown dose rate analyses, although are not the main focus of this thesis, have to be implemented for safety purposes and for the remote handling assessment.

For all these calculations is necessary to elaborate an *ad-hoc* strategy which is reliable and suitable for the nuclear assessment of the machine and site layout that lead to be as precise as possible in characterizing the nuclear loads and fields.

For this reason, two different approach have been used for the neutronics assessments by developing two different Monte-Carlo MCNP models, useful for different scopes:

- a single 20° MCNP DTT detailed model representing a remote handling (RH) sector of the machine (i.e. with almost empty ports).
- a full 360° MCNP DTT simplified model of the machine including the building and NBI.

For the neutronics calculations performed in this work of thesis the 3D neutron and photon transport calculations have been performed using MCNP5 v1.6 [19]. FENDL2.1 and 3.1 [45], [46] have been used for the nuclear data libraries. Standard cell based (i.e. track length estimators) f4 and customized mesh tallies (i.e. superimposed "FMESH" talles) with proper multiplier have been widely used to map the radiation fields. Flux-to-dose conversion factors from ICRP-74 [47] have been used for the calculations of the effective dose rates. ADVANTG [22] hybrid transport code and iWW_GVR [48] provided by Fusion For Energy (F4E) tool were

used to generate the variance reduction parameters and manipulate the results. ENEA AdD1S code [29] has been used for the SDDR assessment.

Simulations have been performed on High Performance Computing (HPC) resources: ENEA CRESCO [49] and EUROfusion MARCONI [50] Clusters.

MCAM [51], CAD-to-Monte Carlo conversion tool has been used as a support to create the MCNP neutronics model and Ansys Spaceclaim CAD software [52] has been used for the simplification of the CAD models.

4.2.1 The 20° DTT MCNP single sector

Figure 4.2 shows the isometric view of the 20° model single sector model. This model has been used for the nuclear loads, shielding studies, activation and shutdown dose rate analyses inside and close to the cryostat.

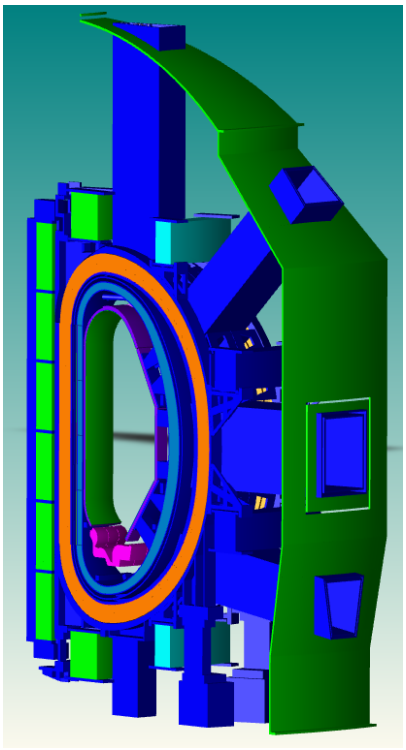

Figure 4-2 isomeric view of 20° MCNP DTT detailed model

This model, developed within the ENEA Frascati neutronic group, showed in detail in figure 4.3 and 4.4, includes the reflecting surfaces in order to simulate the whole

tokamak configuration. To have an idea of the complexity of the model, it is composed by 1119 cells and 1341 surfaces and represent the basic model used for the representation of the sector. The complexity of the tokamak geometry makes impossible the generation of the model by hand. Usually, to build these models an auxiliary 3D CAD model, generate din ANSYS SPACECLAIM [52] is used as a base to simplify the geometry and remove the spline surfaces which are not recognized in MCNP. One the CAD model is ready with all the simplifications, is converted with CAD-to-MCNP interface SuperMC [51] code. This procedure has been followed for the generation of the DTT single sector model.

It includes the Central Solenoid (CS), the Toroidal Field Coils (TFC) winding pack, case and ground insulator, the double wall Vacuum Vessel (VV), made of Stainless Steeel (SS) filled with borated water (0.8% weight of B, enriched with 95% of ^{10}B) with an additional shield in the inboard side, the First Wall (FW), a SS-316 water cooled duct with a tungsten armour.

In-vessel coils (IVC), Poloidal Field Coils (PFC) and Inter-Coil Structures (ICS) have been modelled as well on the bases of the latest CAD model. Regarding the divertor, a ITER-like simplified divertor in Single Null configuration has been added to the model. In particular, the Divertor cassette is made of a mixture of SS316L(N) with 60% and water 40% in volume. The Plasma Facing Components (PFC) is modelled as a 5 cm thick layer with a W (71% in volume), CuCrZr (8.1% in volume), Cu (6.4% in volume) and water (14.5% in volume) mixture. The five ports in the sector are empty, covered with a 1.5 cm thick SS plate only and they are extended up to the cryostat. Since the empty ports cause a large neutron streaming, a 2 cm thick collars made of B_4C compressed powder with B enriched in ^{10}B at 95% (2.3 g/cm^3) have been inserted around the equatorial port walls to reduce the nuclear load on the TF coils. In the upper and upper-oblique ports some additional shielding plates are included to mitigate the streaming. The thermal shield between the VV and the TF is a double-shell structure of SS. Shells are 3mm thick, separated by a vacuum gap

of 15mm and cooled by helium which flows into some internal cooling pipes (not modelled). The cryostat is made of SS304 steel. The inboard (IB) and outboard (OB) sides of the VV have different thickness and composition. In IB the total thickness of the VV is 12 cm (at the equatorial plane) and is composed of 1.5 cm thick front and rear shells of SS-316 and a layer of 9 cm of borated water and steel ribs inside. A 1.5 cm thick shield made of W and B4C (with B enriched at 95 % in 10B) is attached on the rear shell (more details are given in section 4). The OB side of the VV is 23 cm thick (at the equatorial plane) and is made of a 1.5 cm thick steel shell, 20 cm of borated water and steel ribs and a 1.5 cm thick steel rear shell. For some particular studies, since the ports are empty and do not include any NBI system o diagnostic, a dummy port plug, composed by 60%$_{vol}$ of SS316L(N) and 40%$_{vol}$ pure water, has been inserted. [39]

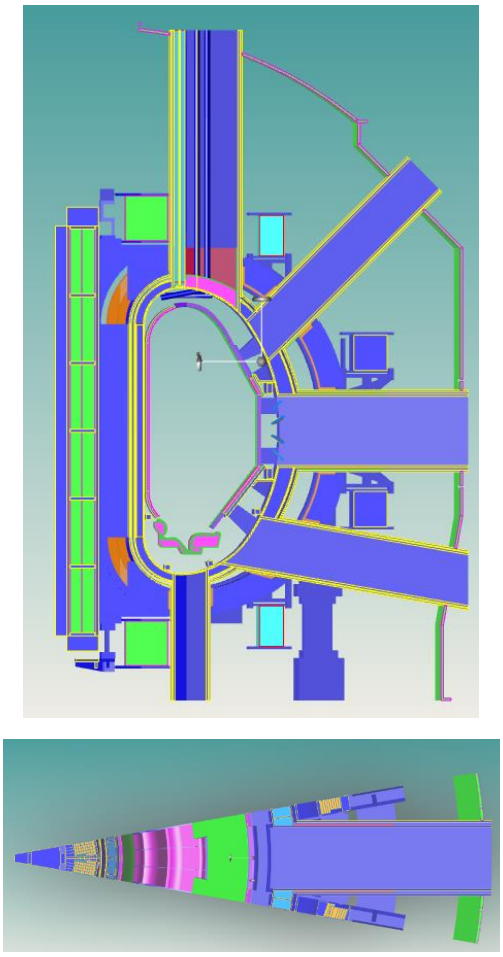

Figure 4-3 Y=0 section of the DTT 20° MCNP neutronic model (up), equatorial section (down)

4.2.2 The 360° DTT MCNP model

The 360° simplified model, showed in fig 4.4, is used for the calculation of the relevant quantities outside the cryostat. In its basic configuration it presents more than 600 cells and 1670 surfaces. The model includes a simplified version with respect to the 20° model of the DTT tokamak with the THB with 220 cm thick walls, choosen after several design calculations described in the next chapter, and two Negative Neutral Beam Injectors, modelled according to the last design of the NBI [53]. The dimension of the hall follows the actual design the THB: 35x35x24 m. Around the Torus Hall other buildings have been represented following the site layout, so different versions of this model has been applied depending on the needs for the rear buildings around the TH.

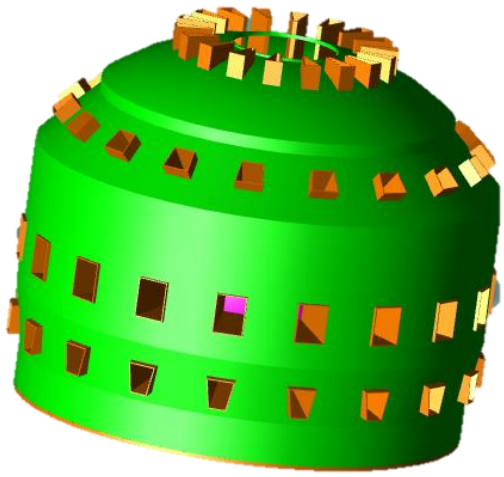

Figure 4-4 isomeric view of 360° DTT MCNP simplified model

Since the purpose of this model is to calculate the nuclear quantities inside and outside the main hall, the components inside the cryostat have been simplified in order to make the model as light as possible from the computational point of view. Anyway, the geometrical simplifications adopted have a negligible impact on the calculated quantities because they have been done in order to keep the attenuation of the particles unaltered. Some preliminary calculations were performed to verify

the consistency between the two models. Neutron and gamma fluxes, calculated in some positions outside the tokamak presents a good agreement, within 10%.

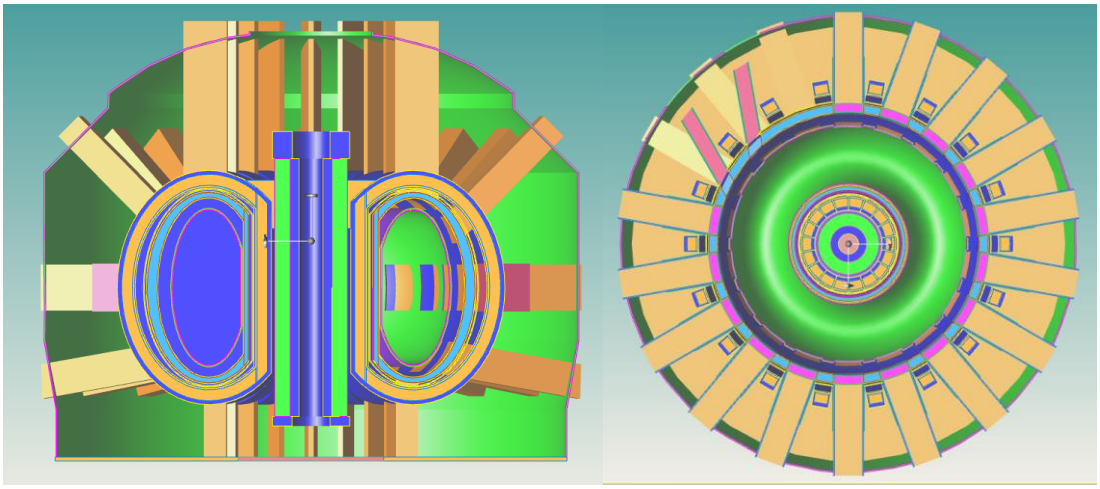

Figure 4-5 3D view of Y=0 section (left) and equatorial section (right) of the 360° MCNP model

The inboard side of the machine has been represented as a cylinder, whereas the outboard side of the machine has been layered using the tori feature of MCNP. The shape of the cryostat has been represented as is it is in the CAD model in SS304 and no divertor has been added to the model because it does not have significant impact outside the cryostat.

As in the 20° all the ports in the model are empty, covered with a 1.5 cm thick SS plate only and they extend up to the cryostat. The 2 cm thick collars made of B_4C compressed powder with B enriched in ^{10}B at 95% (2.3 g/cm^3) have been inserted around the equatorial port walls. In the upper and upper-oblique ports no additional shielding plates are included. According to the present layout of the machine, three of the eighteen sectors host the two NBI as shown in fig. 4.5&4.6.
The Central Solenoid (CS), the Toroidal Field Coils (TFC) winding pack, case and ground insulator, the double wall Vacuum Vessel (VV), made of Stainless Steeel (SS) filled with borated water (0.8% weight of B, enriched with 95% of ^{10}B) have been reported in a simplified layered version.

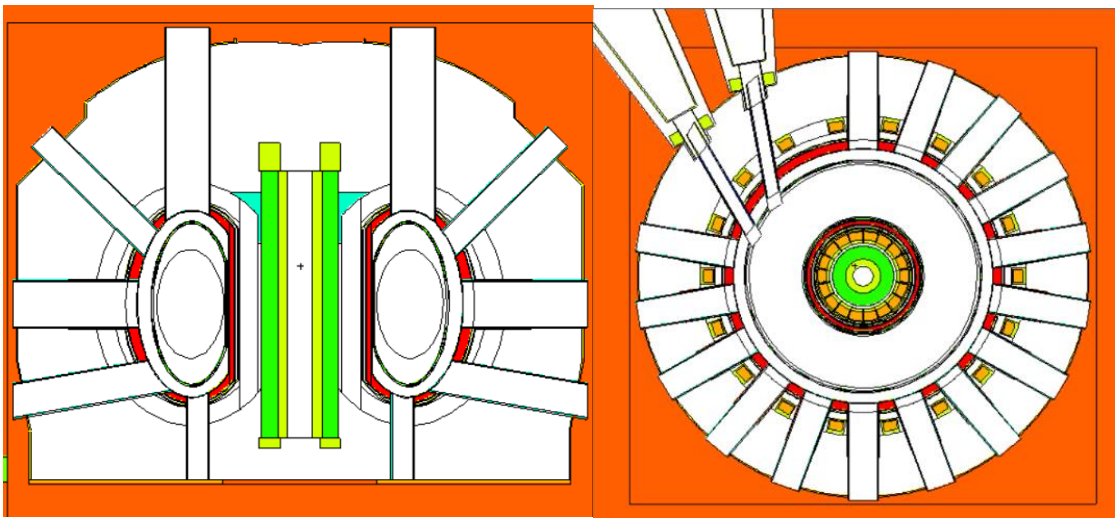

Figure 4-6 Y=0 section (left) and equatorial section (right) of the 360° MCNP model

As in the 20° model the calculations have been done also considering dummy port plug to compensate the effect of the empty ports.

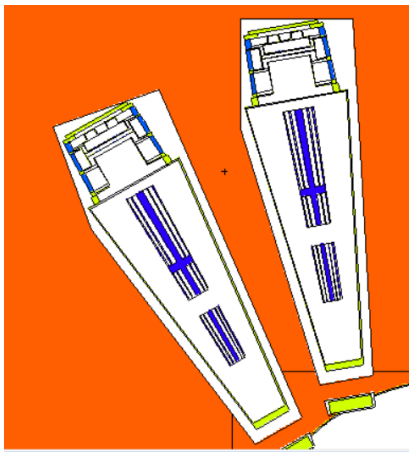

Figure 4-7 top view of the equtorial NBI section

The main hall is almost empty outside the cryostat, except for the NBI and a thin layer of Fe to represent the floor of the machine. Fig. 5.6 shows the 3D view of the 360° model and building. [54]

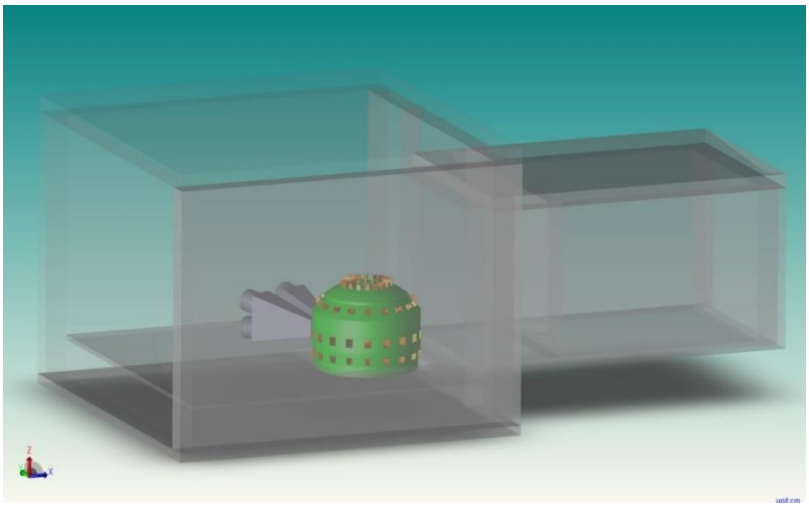

Figure 4-8 3D view of the 360° MCNP model with building

4.3 DTT within the Italian Regulation

The Italian regulation regarding the ionizing and non-ionizing radiation take inspiration from the intense nuclear activity, related to the fission reactors and nuclear research, done in the latest decades of the '900.

In the 1987, just after the Chernobyl nuclear disaster, the Italian people, through a public referendum, were claimed to choose if they wanted Italy to continue to produce electricity with fission power plant or not. Most of the Italian people chose for the closing of the Italian nuclear power plant, which were four in 1987 (Latina, Caorso, Garigliano and Trino Vercellese).

As a result of this situation, the focus of the Italian nuclear experts changed and the decommissioning of the power plant and, thus, the management of the radioactive waste became the main focus of the nuclear activities in Italy.

In parallel the nuclear science was applied in the nuclear medicine fields and the accelerator coupled with the nuclear research which continued with an intense activity.

Among all these fields of application the nuclear fusion science and, in particular, the activities related to the tokamak machines, although for research purposes, were neither considered nor mentioned in the Italian regulation. Anyway the great

amount of neutron and gamma production coupled with the detention of the sealed radioactive sources for calibration lead DTT, and FTU (Frascati Tokamak Upgrade) before, to undergo under a strict licensing procedure, even if they are not classified as nuclear power plant but only a radiogenic machine.

4.3.1 The Italian Regulation

Recently the Italian Government published a new revised version of the Regulation regarded the radiation protection: the 101/2020 Decree-law [55]. This new regulation follows the previous Decree-Law 230/1996. This update is due to the new guidelines, written in the Directives 2013/59 published by the EURATOM consortium: "*laying down basic safety standards for protection against the dangers arising from exposure to ionising radiation*" [56].

According to the Decree-Law 101/2020, and as already foreseen by the previous one, it is required to present a documentation for most of the applications in which the use of the radioactive sources, such as α, β γ particles, electrons, protons or neutrons with a certain energy or production rate, are expected. This document must be presented by the owner of the activity to the Italian Authority specified in the regulation, with the help of a Radiation Protection Expert which has the task of evaluating the risk related to the radiation exposure.

The types of the licensing document are divided, within the law, in two different permits according to the connected risk for the population and workers related to the specific activity: category "A" and category "B" permits.

DTT will be classified as a radiogenic machine of a category A. In fact, among the many constraints which must be followed to obtain the permits, the procedure to obtain the category "A" licence is required for those machines which is intended to produce neutron fluxes greater than 10^7 n/s over the whole solid angle averaged on time (in one year).

The procedure to obtain the licence is graphically showed in fig. 4.8. The permit is granted by the Italian Ministry of Economic Development in agreement with the Ministry of Labour, the Ministry of Health, the Ministry of the Environment and the Ministry of interior.

The documentation, prepared by the DTT operator, must be sent to the Ministry of Economic Development (MISE) with a formal application. Then, the MISE, ask the other Ministries, the ISIN (National Inspectorate for nuclear Safety and Radiation Protection) and the Region that will host the machine (i.e. Lazio Region) to review the documentation and to provide a formal review.

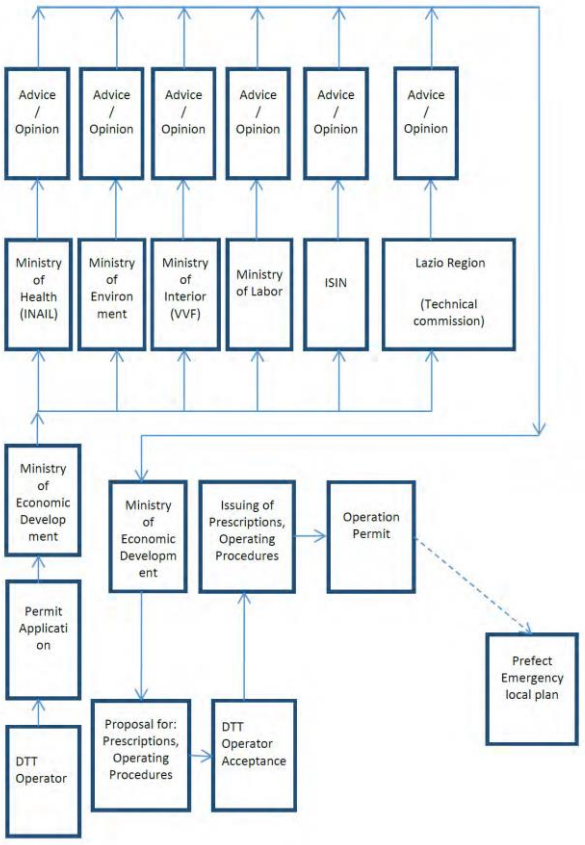

Figure 4-9 schematic view of the licensing procedure for DTT from [36]

The licensing document is generally compiled with the following information:

- General information of the applicant (i.e. tax code, company name ect.);
- Type of the practice;

- The location and description of the area where is intended to operate;
- For each radiogenic machine; the acceleration type and the maximum energy of charged particles, maximum current and power, utilization factor and the number of machine involved in the activity;
- General assessment of the radioactive material production and the total amount of radioactive radionuclides;
- Neutron production;
- Assessment of the radioactive waste
- Recycling or reuse of materials.

The Radiation Protection Expert must compile additional documentation related to the matter of his competence and it has to be filled with the main following information:

- Accurate and detailed description of the involved areas including drawings and the criteria of classification of those areas;
- Description of the operations to be carried out, radiation sources and equipment to be used by the radiation workers;
- A Set of radiation protection rules to followed by the personnel and normal people.
- Description of the criteria for the radiation workers classification based on the provisional exposure rate during the activities;
- An identification of the possible incident scenarios involving potential exposure of the workers and people;
- Methods for the decommissioning for DTT;

Once the Ministry of the Economic Development obtained the positive opinions from the other Ministries and related Organizations, the licensing procedure for the construction and operation of the machine has been completed.

The last step to begin the normal operations is the permits of the local Prefect after the including in the local emergency plan of the DTT machine.[36]

5 Building Design Studies

"Study hard what interests you the most in the most undisciplined, irreverent and original manned possible"

R. P. Feynman

The development of a tokamak machine like the Divertor Tokamak Test facility requires multiple knowledge and skills to deal with very different issues. Most of these skills are related to conventional engineering design, such as civil, mechanical and thermomechanical engineer, whereas the others refer to the unconventional matters like plasma physics applied to the fusion science, neutronics or superconductive engineering.

Within a tokamak project those wide range of competences must collaborate to produce a unique result as DTT will be.

One of the most representative examples of this collaboration is the project of the DTT Torus Hall, the main building that will host the machine, where the civil engineers have to deal with the neutronics and radiation protection requirements.

5.1 DTT Torus Hall Building: design of the wall thickness

The choose of the wall thickness of the THB is the first step along the road to the final design of the DTT main hall.

The thickness of the wall is strongly connected to the radiation protection constraints which impose the level of effective dose outside the building and to the economic evaluation for the choose of the structural material: in line of principle,

materials which have higher shielding properties, usually have a higher commercial cost so an accurate evaluation, balancing the shielding needs and the price of the material is fundamental for the realization of the building.

In 2018 an early version of the simplified 360° model of DTT machine, showed in fig. 5.1, was placed inside a primitive idea of the bunker with dimension 57 x 40 x 25.5 m showed in fig 5.2. The main scope of the work was to address the thickness of the wall for the Torus Hall Building and their material in order to respect the radiation protection constraints. The calculation of the neutron and gamma fluxes distribution was done considering empty ports and without the DTT subcomponents inside the ports (i.e. diagnostic, additional heating systems) and the NBI systems were not modelled as well.

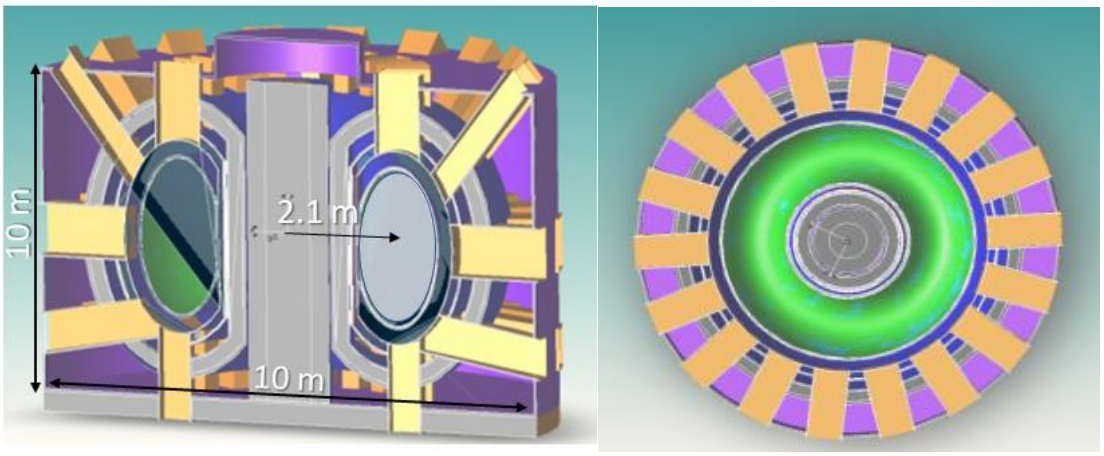

Figure 5-1 3D view of the DTT 360° model version used in 2018

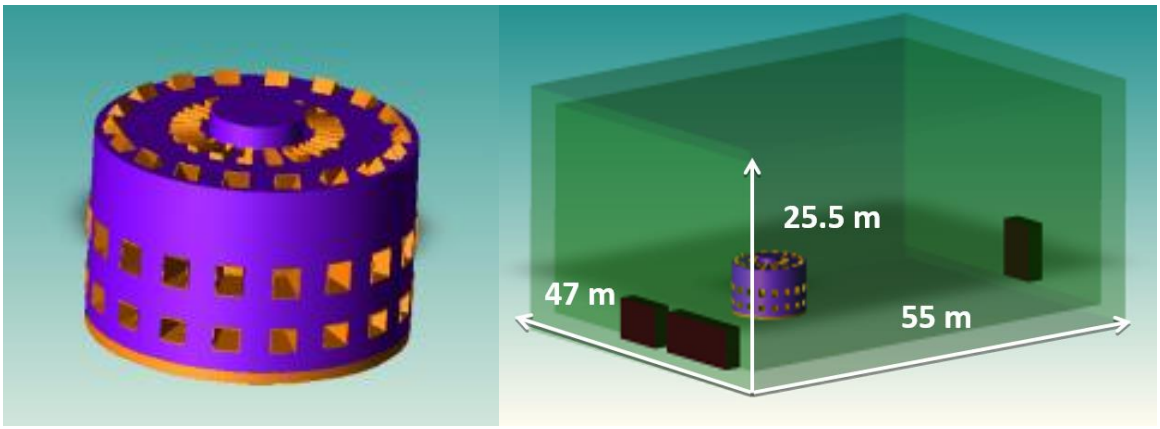

Figure 5-2 isomeric 3D view of the 2018 version of 360° model (left) and 2018 360° model inside the first version of building

This approach to the calculation is conservative for the radiation protection issues.

The bunker walls, made of ordinary concrete (ρ=2.2 g/cm^3) with composition reported in tab. 5.1, are 220 cm thick in the reference configuration. This value has been changed for the wall closest to the machine, 12 m far from the cryostat, in order to study the variation of the fluxes and dose rates outside the bunker as a function of the wall thickness.

Table 5-1 composition of ordinary concrete used for the DTT building studies

Baseline	Weight Fraction (%)	Atom density (at/b-cm)
H	0.56	1.0 x10^{-1}
O	49.75	5.8 x10^{-1}
Na	1.71	1.4 x10^{-2}
Mg	0.26	2.0 x10^{-3}
Al	4.69	3.3 x10^{-2}
Si	31.47	2.1 x10^{-1}
S	0.13	7.5 x10^{-4}
K	1.92	9.2 x10^{-3}
Ca	8.23	3.9 x10^{-2}
Fe	1.24	4.2 x10^{-3}

For these calculations the total DTT DD neutron yield rate of 1.5 x 10^{17} n/s and annual DD yield rate of 1.53 x 10^{21} n/y has been used. An evaluation of the 14.1 MeV neutrons, coming from the triton burn-up, was also done.

Nuclear quantities have been evaluated by track length estimator MCNP tallies and both, cell based and superimposed FMESH tallies have been used to map the building. In particular, three spherical cells with 50 cm of radius have been used for the scoring tallies. These spheres have been located on the equatorial plane, where the intensity of the flux is greater with respect to the other positions. The position #1 is located in front of the equatorial port, close to the cryostat, the position #2 is inside the bunker, close to the wall and the position #3 is located outside the bunker as shown in figure 5.3. [54]

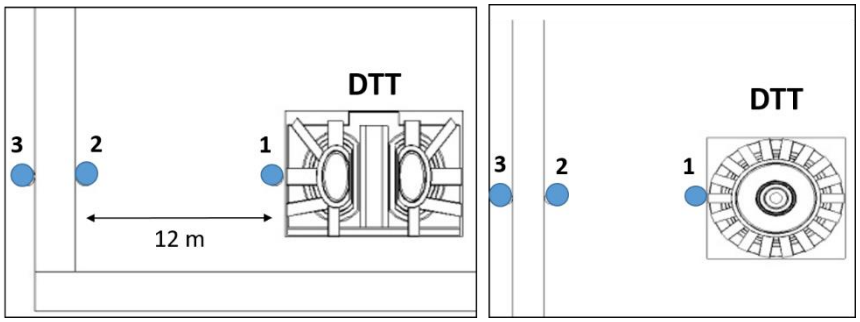

Figure 5-3 Three selected positions in poloidal (left) and equatorial plot (right). The origin of the axis is in the center of DTT machine.

A secondary neutron source has been used for the calculating the gamma flux in position #3 and the neutron spectrum in the inner surface of the bunker closest to the tokamak was calculated in the full 3D model and used to define a secondary neutron source in the inner wall to correctly compute the gamma generation from the neutrons inside the concrete wall due to the (n,γ) reactions. This secondary source has been also used to perform a sensitivity analysis necessary to optimize the wall thickness and assess the minimum thickness needed to protect workers and public, detailed explained in the next paragraph.

Figure 5.5 shows the neutron flux map inside the DT hall. The contour lines show that the neutron flux varies in the range 10^{10} n/cm^2/s, at the cryostat, to 10^{9} n/cm^2/s

at the wall. In fig 5.6 the neutron maps across the wall are shown. The attenuation factor with 220 cm of normal concrete result to be more than 6 order of magnitude. Outside the wall, closest to the tokamak at the equatorial plane, i.e. the most critical position, the maximum neutron flux is of the order of 10^3 n/cm²/s. The values of neutron and gamma fluxes and annual fluence at the three selected positions are reported in tab 5.2. Despite a larger value of the neutron flux inside the bunker, the radiation field outside is dominated by the gammas. This effect can be explained by the moderation effect of the concrete on neutrons, producing a larger thermalized flux which favours (n,γ) reactions inside the walls. Neutron spectra for positions #1, #2 and #3 mentioned above is shown in fig. 5.4

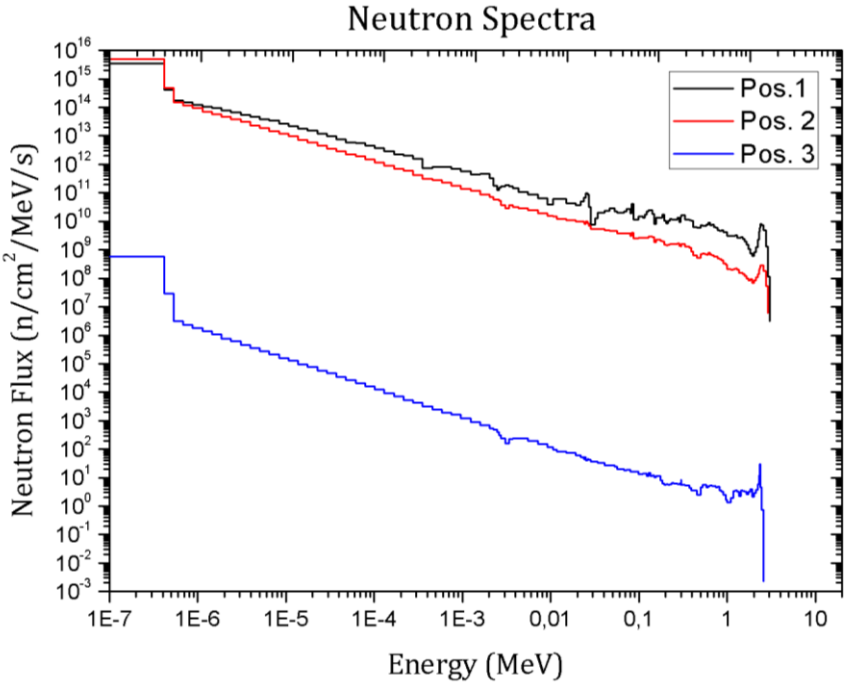

Figure 5-4 neutron spectra in the three selected positions

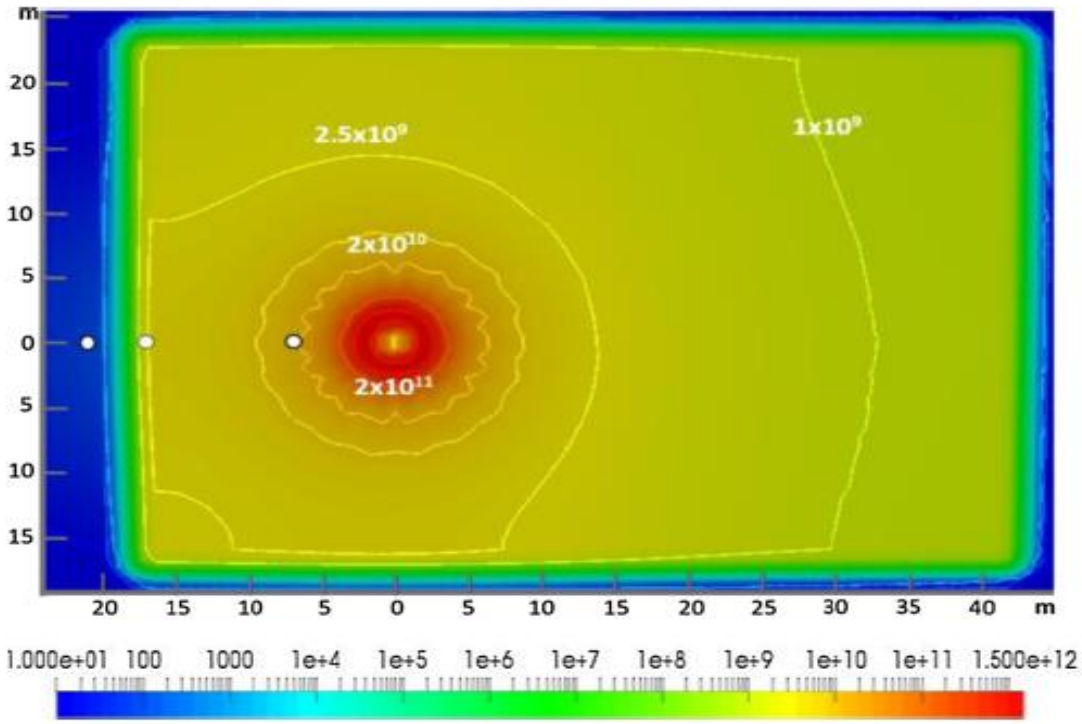

Figure 5-5 neutron flux map inside the bunker (n cm^{-2} s^{-1}). The origin of the axes is in the centre of the machine

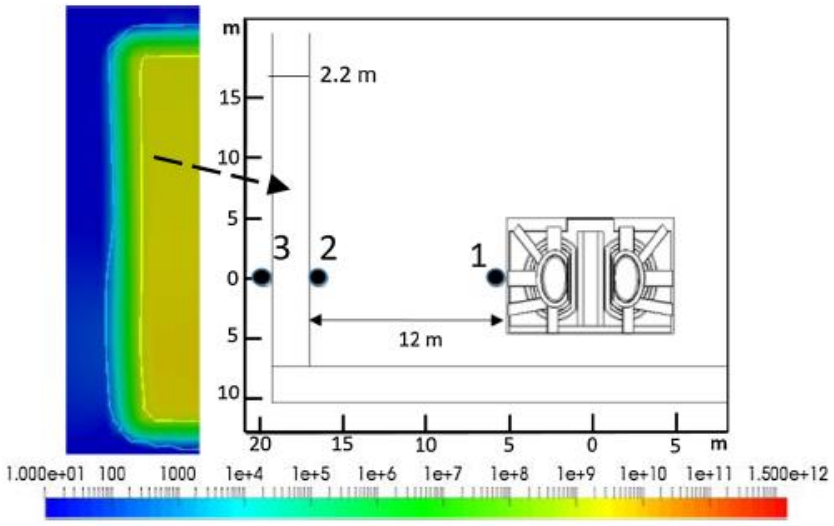

Figure 5-6 neutron flux map (n cm^{-2} s^{-1}) across the bunker wall. The origin of the axes is in the centre of the machine

Table 5-2 neutron and gamma fluxes in the three position considered

Total Neutron and Gamma Fluxes				
	n		γ	
Pos.	**n/cm²/s**	**n/cm²/y**	**γ/cm²/s***	**γ/cm²/y***
1	$1.80\cdot 10^{10}$	$1.83\cdot 10^{14}$	$3.35\cdot 10^{9}$	$3.41\cdot 10^{13}$
2	$3.23\cdot 10^{9}$	$3.29\cdot 10^{13}$	$7.24\cdot 10^{8}$	$7.4\cdot 10^{12}$
3	$9.53\cdot 10^{1}$	$9.72\cdot 10^{5}$	$2.6\cdot 10^{3}$	$2.65\cdot 10^{7}$

*values for gammas are calculated through a II source

The fast neutron component (> 0.1 MeV) contributes for 68% of the total flux at position 1, for 33% at position 2 and for 12% in position 3. The attenuation of the fast neutron component from position 1 to 2 is due to the radial distance (i.e. geometrical effect) and moderation in air. On the contrary, the thermal component increases due to the back scattering of from the wall.

The effective dose rate in the three position has been calculated using the "flux-to-dose" conversion factor from the ICRP 74 publication [47].

Fig. 5.7 shows the map of the neutron effective dose inside the bunker. It varies from 2×10^{11} to 2×10^{10} pSv/s.

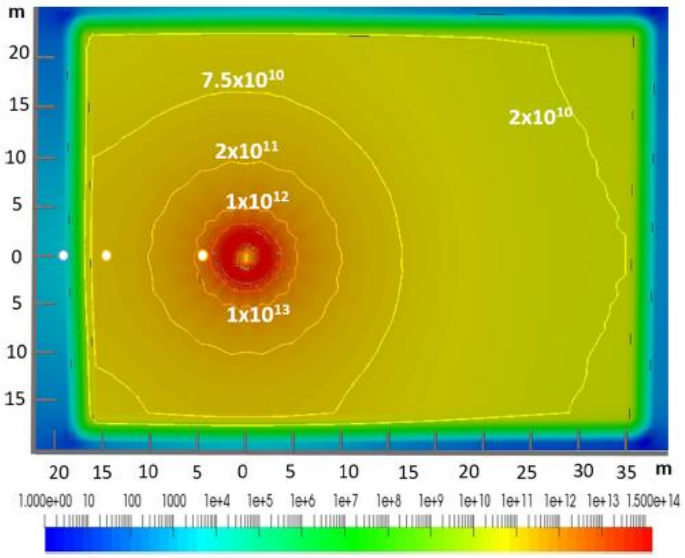

Figure 5-7 maps of neutron effective dose inside the bunker (pSv/s). The origin of the axes is in the centre of the machine

In table 5.3 the values of annual effective dose for neutron and gamma and the total is shown. Outside the bunker, the effective dose is dominated by the gamma.

Table 5-3 Annual effective doses for the three positions considered

Total Neutron and Gamma Effective Dose				
	n		**γ**	
Pos	**μSv/s**	**μSv/y**	**μSv/s***	**μSv/y***
1	$1.36 \cdot 10^{6}$	$1.39 \cdot 10^{10}$	$1.08 \cdot 10^{4}$	$1 \cdot 10^{8}$
2	$1.10 \cdot 10^{5}$	$1.12 \cdot 10^{9}$	$2.34 \cdot 10^{3}$	$2.38 \cdot 10^{7}$
3	$1.95 \cdot 10^{-3}$	$1.99 \cdot 10^{1}$	$1.3 \cdot 10^{-2}$	$1.3 \cdot 10^{2}$

*values for gammas are calculated through a II source

In order to observe the Italian limit for the annual effective dose to the public and non-radiation workers, imposed as 1 mSv/y considering all the activities which are not related to the natural radioactivity background, specific design constraints of regulation practice have been adopted. In particular, for non-radiation workers the assumed criteria are 300 μSv/y assumed as 1/3 of the limit. For the public, Italian authority requires to respect an effective dose constraint of 10 μSv/y. These values must be respected just outside the torus hall building (i.e. at 30 cm from the wall) for the workers and at the ENEA Frascati centre boundaries which is at 38 m from the machine in the closest positions.

5.1.1 Sensitivity studies for the wall thickness

In order to choose the minimum thickness of the wall which ensures the protection of the workers and public a sensitivity studies, using the concrete described in the previous paragraph as baseline material, has been done.

To perform this study, the neutron spectrum in a circular surface in the inner wall has been used to create a secondary neutron source as shown in fig. 5.8. The spectrum has been calculated by setting the importance of the wall to 0 in order to avoid the double counting of the particles reflected by the wall.

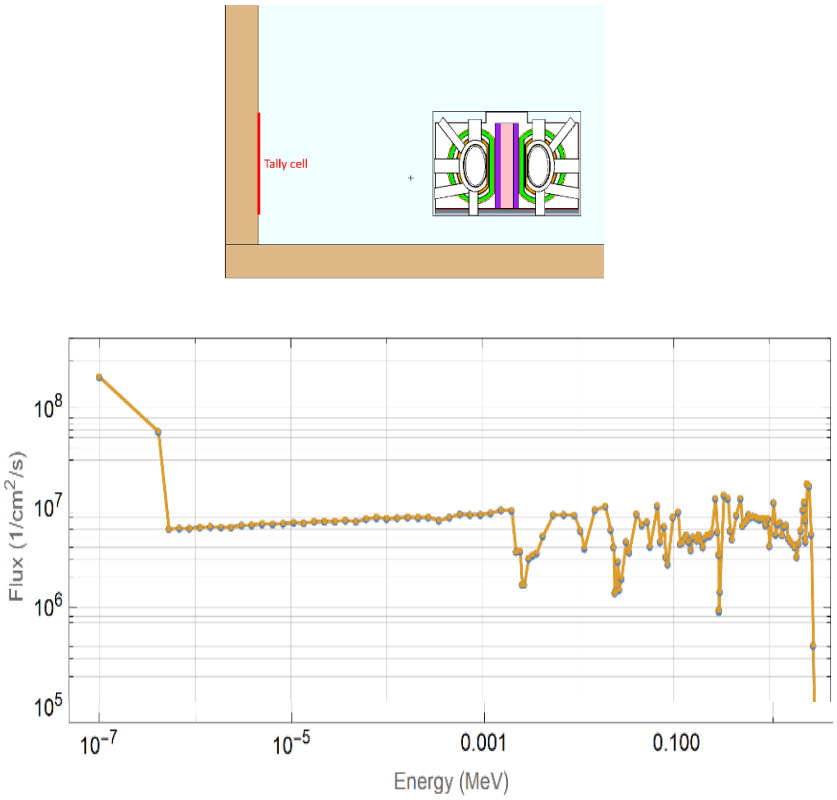

Figure 5-8 geometry of tally cell used to sample the neutron for II source (up), neutron spectrum in the position of sampling(down)

Once the secondary source has been created, through the Source Definition (SDEF) MCNP card, a simplified model, composed as an "infinite" wall was built. In this model with the secondary source the thickness of the wall has been varied and the relevant quantities, neutron and gamma fluxes and doses, have been calculated even far from the building (i.e. distance greater than 5 m). However, for the large distances, it was not possible to obtrain reliable results, as the statistical errors of the Monte Carlo simulation increase sharply with the distance to the wall. Therefore, the effective dose rates were calculated for distances up to 5 m from the building, and the results were extrapolated for distances up to 40 m. Exponential functions of the form Ae^{-kx+b} were fitted to the data, using Mathematica's *FindFit* function with the *NMinimize* method [57].

Five thicknesses of the wall have been chosen to perform this study, using the baseline concrete showed in table 5.1: 150 cm, 175 cm, 200 cm, 220 cm and 250 cm.

In figure 5.9 and 5.10 the values of the neutron and gamma fluxes as a function of the distance from the wall for the five distances chosen for the calculations are shown.

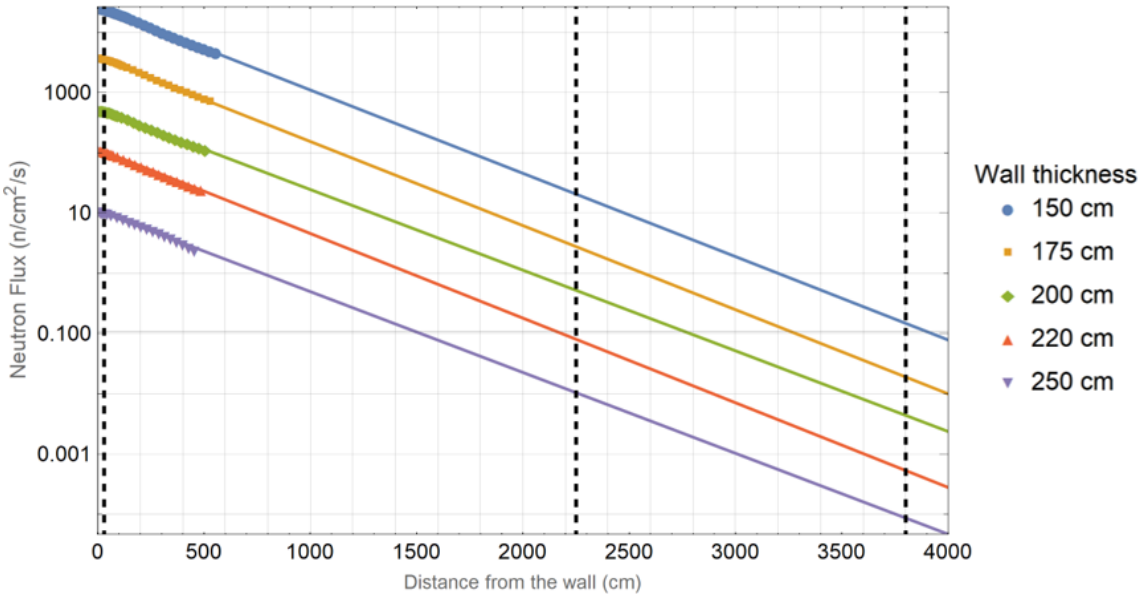

Figure 5-9 neutron flux behaviour Vs. distance from the wall for the five wall thicknesses considered

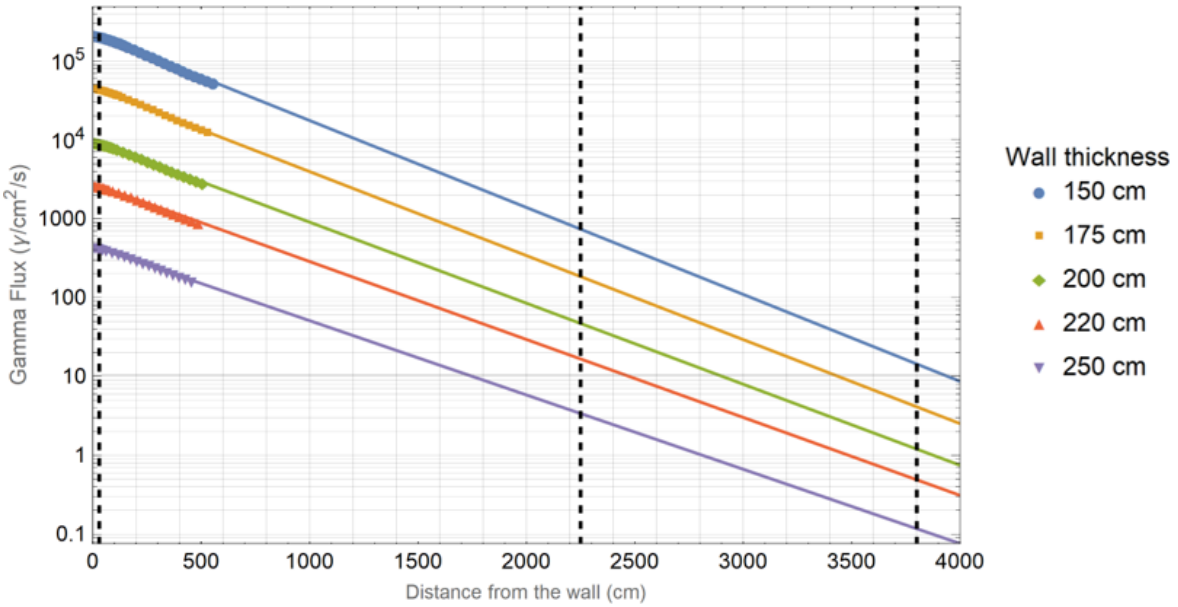

Figure 5-10 gamma flux behaviour Vs. distance from the wall for the five wall thicnkess considered

The results for the total effective dose, showed in fig. 5.11, clearly shows that the calculated annulas dose levels are below the constraint to the public for all the wall

thicknesses at the site boundaries (i.e. 38 m away from the wall), while the annual dose to exposed workers are below the limit for wall thicnkesses ≥ 220 cm. However, considering a 200 cm wall thicnkess, the dose is below 300 uSv/y at 4 m from the wall. For lower thicnkesses, the estimated dose rateds exceed the targets.

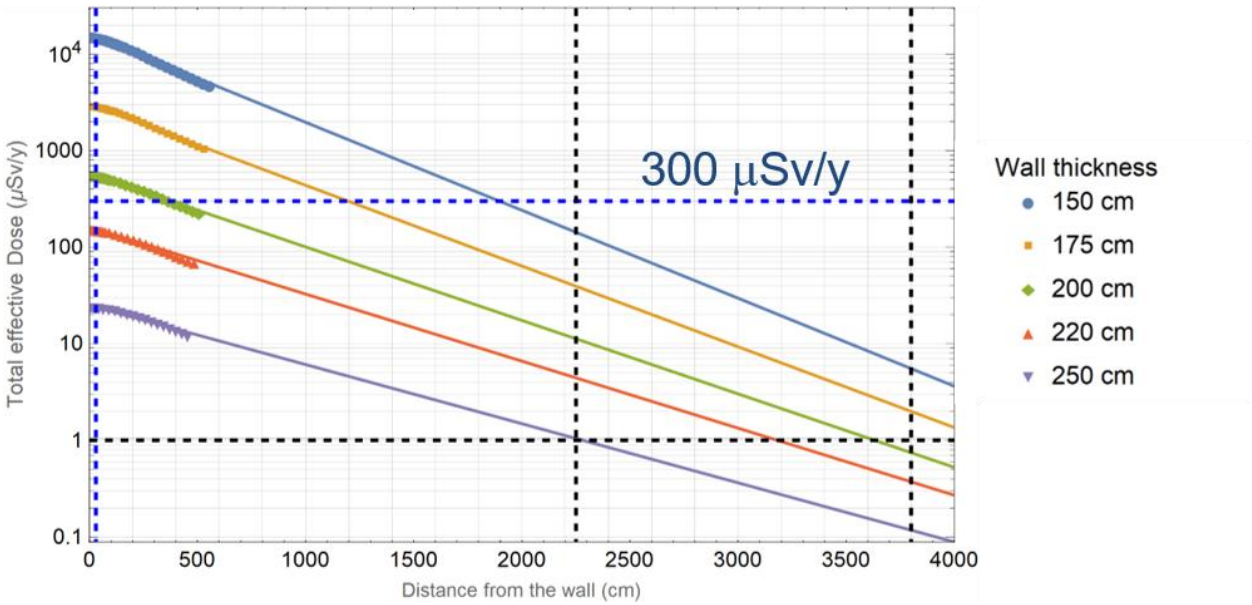

Figure 5-11 Annual effective dose rate (μSv/s) as a function of the distances from the wall for the five configuration studied

Values for neutron and gamma fluxes and total effective dose, also divided in neutron and gamma contribution, are summarized in tab 5.4 for 30 cm away from the wall for the five thicknesses considered.

Table 5-4 values of nuclear and gamma fluxes and doses 30 cm away from the wall for the five wall thicknesses studied

Wall thickness (cm)	Neutron Flux (n/cm²/s)	Gamma Flux (γ/cm²/s)	Effective Dose Rate by Neutrons (μSv/y)	Effective Dose Rate by Gammas (μSv/y)	Total Effective Dose Rate (μSv/y)
150	2.44 x10⁴	2.07x10⁵	5.1 x10³	9.9 x10³	1.5 x10⁴
175	3.5 x10³	4.3 x10⁴	7.3 x10²	2.09 x10³	2.8 x10³
200	4.9 x10²	8.98 x10³	1.01 x10²	4.5 x10²	5.5 x10²

220	1.06×10^2	2.6×10^3	23	1.3×10^2	1.5×10^2
250	10	4.2×10^2	2.3	22	24

5.1.2 Studies on different shielding materials

Usually, for the nuclear application, the most used materials for fission reactor shielding, are the so-called heavy concretes. Even for the medical applications, i.e. for the accelerator or for the radiogenic machine like the X-ray, the heavy concrete is one of the best among the shielding materials. The density of these types of concrete are usually much greater than the ordinary concrete, typically around 3 g/cm^3 but they could reach even greater densities, of the order of 4-5 g/cm^3.

These materials could be obtained by adding to the normal concrete natural aggregated such as barites or magnetite or manufactured aggregates such as iron or lead shot. Offshore, heavyweight concrete is used for ballasting for pipelines and similar structures. EN 206/2013 [58] defines heavyweight concrete as having an open dry density greater than 2600 kg/m^3.

The density achieved strongly depends on the type of the aggregate used. By adding the barites, the increase of the density should be around 45% greater than the ordinary concrete, reaching the value of 3.5 g/cm^3. Greater values could be reach by adding the magnetite, with which the density arise to the value of 3.9 g/cm^3, 60% greater than the ordinary concrete.

Values in the range 5.9 – 8.9 g/cm^3 could be reached by adding iron or lead aggregate, respectively. In that cases the concretes are called are very heavy concretes. [59].

The water/cement ratio is very similar to that of the normal concretes, but the aggregate/cement ratios will be significantly higher, because of the higher density of the aggregates. These types of concretes could be batched, transported, and

placed by means of conventional equipment. The way of making of these concretes are certainly different and the formwork pressures must be increased. Moreover, compaction will require more energy than the ordinary concrete.

Of course, the heavy weighted concretes have a considerably higher cost with respect to the ordinary. The advantage, that could be crucial in those situations where the space doesn't allow considerable concrete thicknesses, is that the attenuation factor against the neutron is considerably higher to that of the normal concrete, so the same attenuation could be reached with less thickness, thus less amount of material.

Basically, there is a sort of "*break-even*" point, where the function of the cost meets that to the radiation attenuation and is strongly related to the ALARA (*As Low As Resonably Achievable*) principle which considers even the social and economic issues.

For the DTT Torus Hall, a number of special concretes has been analysed to evaluate the possibility to reduce the thickness of 220 cm of ordinary concrete. The same calculations for fluxes and doses have been done and compared to the baseline configurations. The following special concretes have been considered for the analyses:

- Concrete Boron Frits-Baryte: $\rho = 3.1$ g/cm^3 (BFB)
- Concrete Colemanite-Baryte: $\rho = 3.2$ g/cm^3 (CCB)
- Concrete Luminite-Colemanite-Baryte: $\rho = 3.1$ g/cm^3 (CLCB)
- Concrete Magnetite and Steel: $\rho = 4.64$ g/cm^3 (CMS)

The compositions of those materials, reported in tables from 5.5 to 5.8, have been taken from the MCNP compendium [60].

Table 5-5 Boron Frits Beryte concrete composition

ConcreteBoron Frits-baryte 3.1 g/cm³	**Weight Fraction (%)**
H	0.56
B	1.04
O	33.96
F	0.23
Na	1.22
Mg	0.23
Al	0.64
Si	3.33
S	9.19
K	0.10
Ca	6.29
Mn	0.02
Fe	2.20
Zn	0.66
Ba	40.32

Table 5-6 Magnetite and steel concrete compositions

Concrete Magnetite and Steel 4.6 g/cm³	**Weight Fraction (%)**
H	0.24
O	13.77
Mg	0.37

Al	1.04
Si	1.58
Ca	5.57
Ti	1.60
V	0.06
Fe	75.79

Table 5-7 Colemanite Baryte concrete composition

Concrete Colemanite-baryte 3.2 g/cm³	**Weight Fraction (%)**
H	0.86
B	0.99
O	35.15
Na	0.11
Mg	0.22
Al	0.61
Si	1.77
S	9.70
Ca	8.52
Mn	0.01
Fe	1.04
Ba	41.01

Table 5-8 Luminite colemanite baryte concrete composition

M87 Concrete Luminite-colemanite-baryte 3.1 g/cm³	**Weight Fraction (%)**
H	1.10
B	0.88
O	37.14
Na	0.11
Mg	0.14
Al	1.77
Si	0.97
S	9.11
Ca	5.51
Ti	1.28
Mn	0.12
Fe	3.09
Ba	38.79

A first evaluation of the effectiveness of these materials has been done keeping the wall thickness at 220 cm and calculating the neutron fluxes as a function of the distance from the wall and comparing with the baseline configuration, reported in fig. 5.12

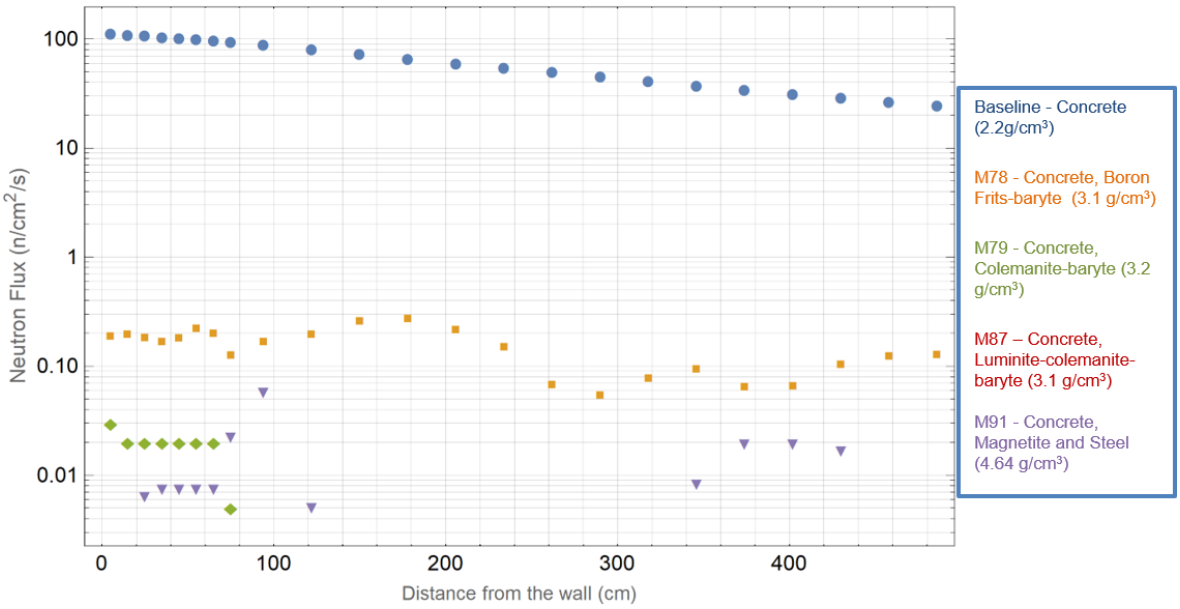

Figure 5-12 neutron flux as a function of the distance for the considered concrete with 220 cm wall thickness

Values are very low for all the special concretes compared to the baseline configuration. As a consequence, the gamma fluxes are very low as well. For some concretes the statistics far from the wall is very poor due to the low counting.

A second evaluation has been done by reducing the thickness of the wall to 150 cm and compared with a 150 cm thickness with the ordinary concrete. Figures from 5.12 to 5.15 show the neutrons and gamma fluxes and doses as a function of the distance for the heavy concretes together with the baseline concrete. Fig. 5.16 is particularly interesting because shows the comparison between neutron and gamma fluxes.

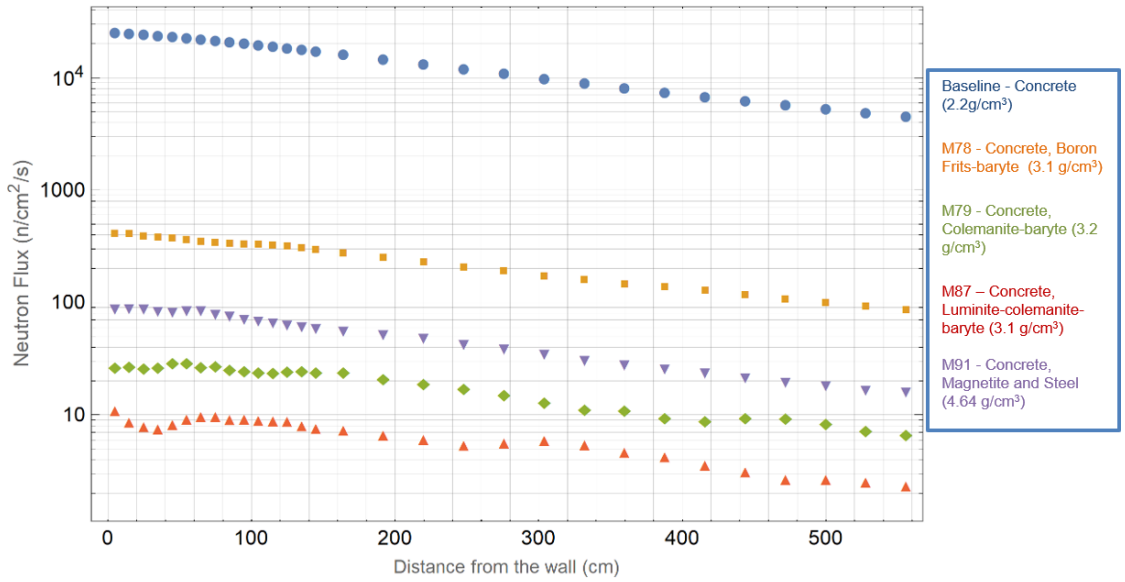

Figure 5-13 neutron flux as a function of the distance for the considered concrete with 150 cm wall thicknesses

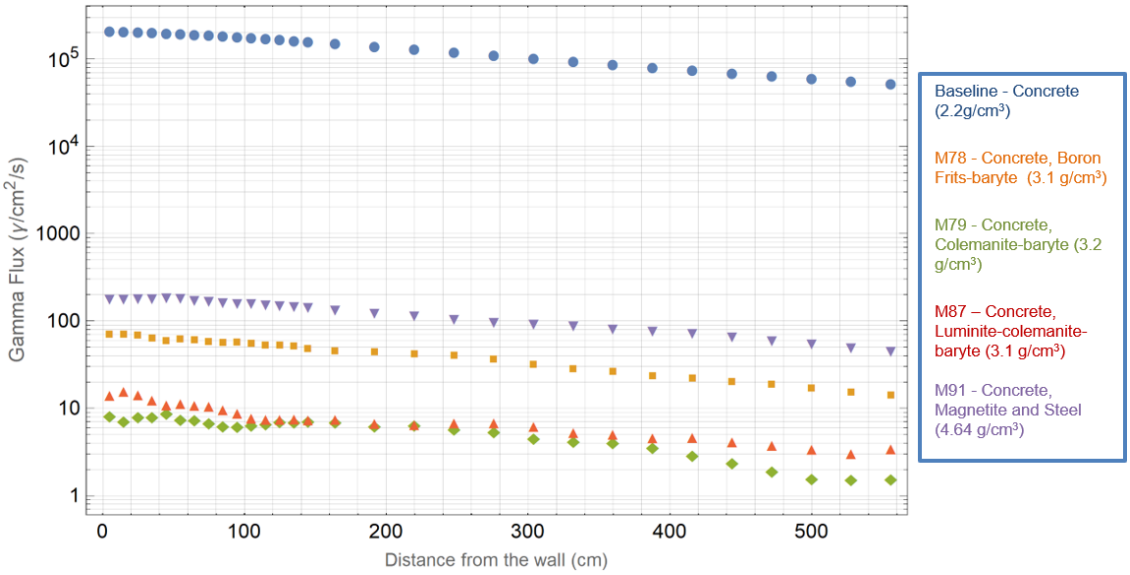

Figure 5-14 gamma flux as a function of the distance for the considered concrete with 150 cm wall thicknesses

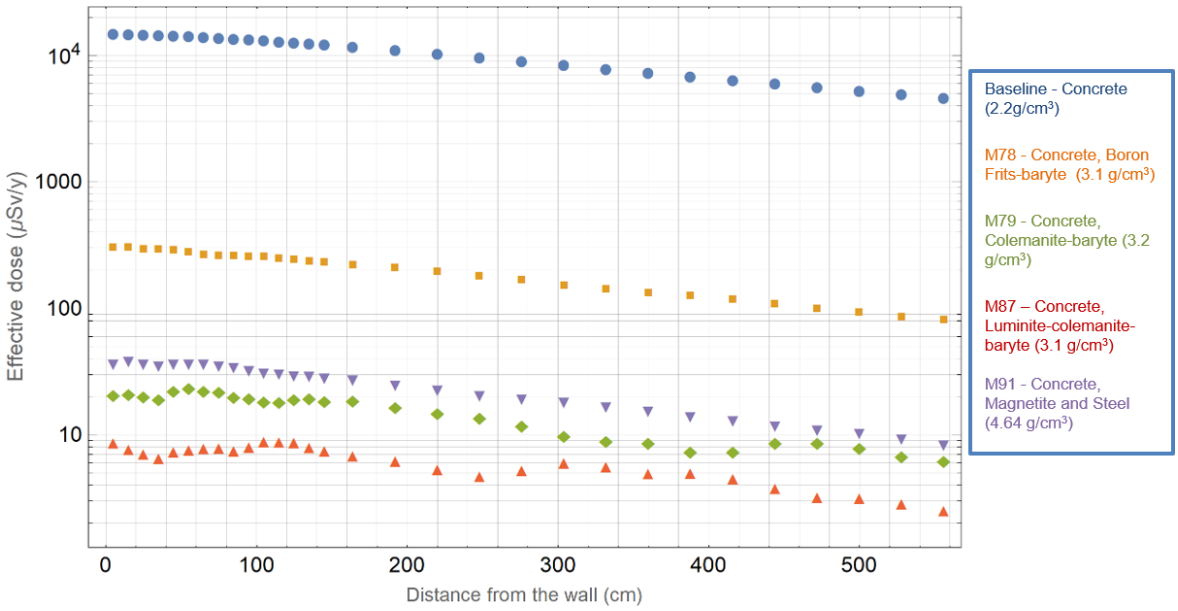

Figure 5-15 Total annual effective dose as a function of the distance for the considered concrete with 150 cm wall thicknesses

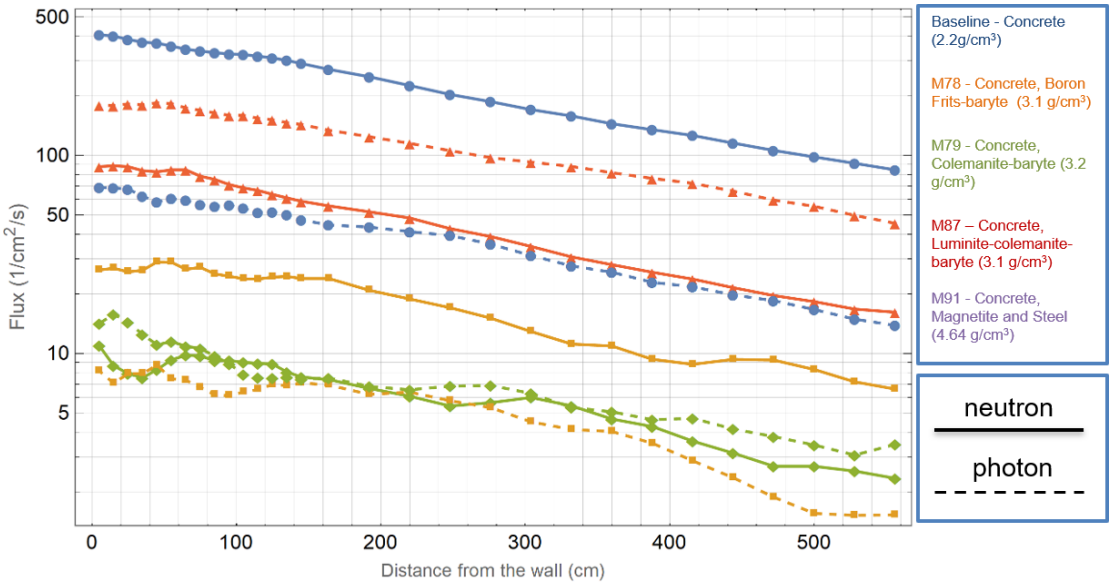

Figure 5-16 neutron and gamma fluxes as a function of the distance for the considered concrete with 150 cm wall thikness

The Boron-Frits-Baryte concrete is much more effective than the baseline one. It has 40% higher density with respect to the ordinary concrete, it contains 1.04% of boron and 40% of Barium which is a very effective gamma shield and this explains the reason why the neutron fluxes are much higher than the gamma ones when this material is used.

The Concrete Magnetite and Steel has the higher density among the concrete studied. It is 4-5 times more effective than the Boron-Frits-Baryte. Despite the higher hydrogen and boron content the concrete BFB is less effective for the neutron than the CMS. On the contrary it is more effective for the gammas because of the barium content. Despite the high iron content, the CMS is much less effective than the remaining materials because of the absence of the barium in its chemical composition.

The concrete MS is 45% density higher that the concrete CB and is 2/3 times less effective for the neutron shielding. The high Barium content acts as a diffuser.

The concrete CB is much more effective than the CBFB due to the 60% higher hydrogen content.

The concrete LCB has similar density with respect to the others, except for the CMS. It is 2/3 times more effective in neutron shielding with respect to the CCB due to the higher hydrogen content and, overall, is the most effective material among the concrete studied.

From these sensitivity studies is clear that increasing the hydrogen and boron contents, the material improves the neutron shielding performances. The Barium is an important nuclide for the gamma attenuation and neutron diffusion.

Presently, the concrete chosen for DTT is the ordinary concrete with the chemical composition reported in tab 5.1 of the previous paragraph. This choice takes into account the studies on the different concretes. The advantages of using those heavyweight concretes are clear but, in the case of DTT the disadvantages are more evident.

In fact, in most of cases, heavyweight concrete cannot be used as structural material. The DTT TH is a very big building with volume approaching 30000 m^3 so, the use of these materials, could be difficult during the installation phase. Although heavy concretes have a considerable attenuation factors for neutrons and gamma, as

shown in the figures 5.12 – 5.15, the homogeneous distribution of the solid aggregate, such as boron, baryte, luminite and others, could be very difficult for these large volumes, thus the attenuation of the particles could vary with the position in the walls without ensuring the respect of radiation protection constraints.

Furthermore, the cost of these types of concretes is much greater than the ordinary one and the space for the building in Frascati area is enough to allow the use of the ordinary concrete and to be sure that the radiation limits will be respected.

5.2 Present configuration of the DTT THB

The design of the Torus Hall has been changed and evolved with the passing of the time. Several studies have been done between 2017 and 2020 to verify the status of the site and evaluate the possible reuse of the existing building in the Frascati Centre. The building which presently host the Frascati Tokamak Upgrade (FTU) for example, will be reused for the cryogenic systems and for the radioactive waste repository.

Nowadays the DTT THB, shown in fig 5.17, has a squared-shape cross section of 35 x 35 m with a height of 25 m. Anyway, the height of the THB is still under discussion so, presently, is not fixed. This is due to environmental technical factors. In fact, a 29 meters height, foreseen at the beginning, implies some difficulties related to the Italian Regulation and permission from the environmental point of view. On the other side, a too small height leads to difficulties in movement of big components like the TFCs and CS. For these reasons, the height of the hall should be in the range 23-26 m.

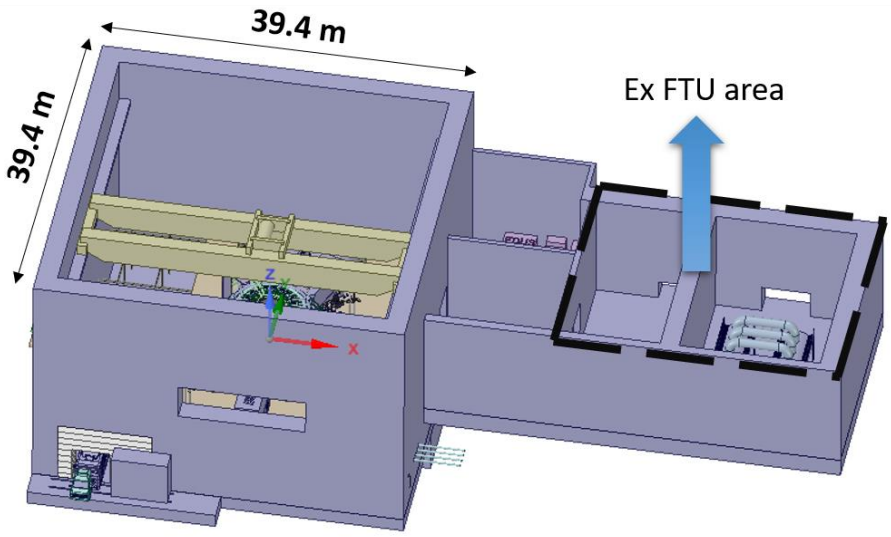

Figure 5-17 3D CAD view of the actual configuration of DTT THB with dimensions

Plan and perspective are shown in fig 5.18 and 5.19.

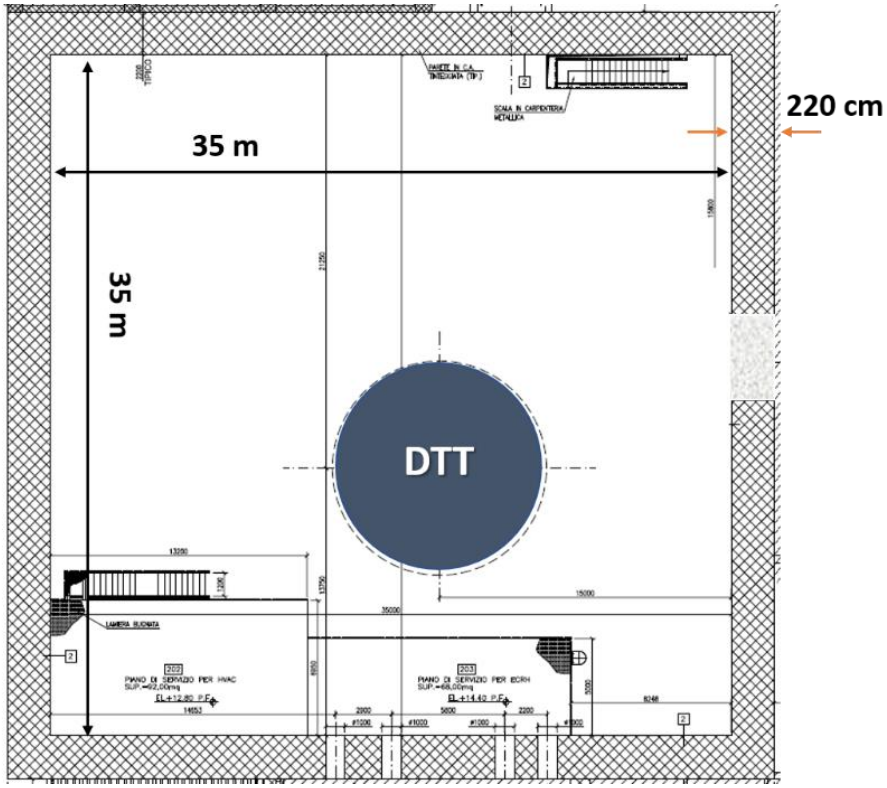

Figure 5-18 CAD view of the equatorial section of the DTT THB

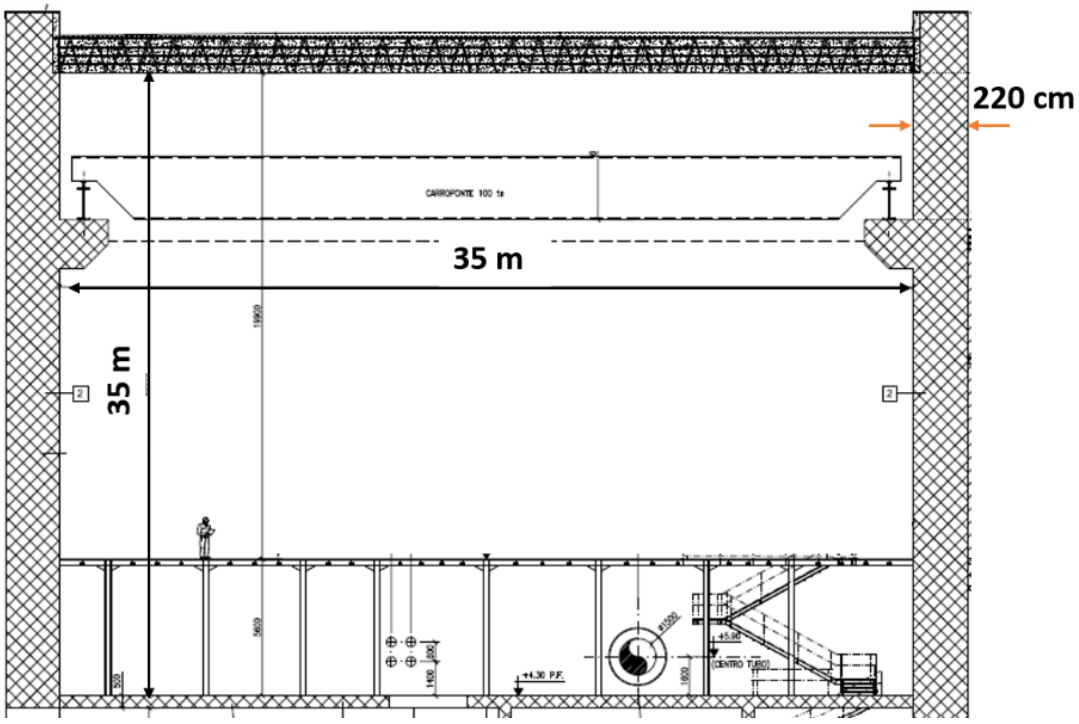

Figure 5-19 longitudinal cross section of the DTT THB

According to the present layout the MCNP DTT 360° model has been updated in and the maps of neutron and gamma fluxes inside the hall has been recalculated and they're shown in fig. 5.21 for neutron and 5.22 for gammas together with the cross section of the MCNP model showed in figure 5.20.

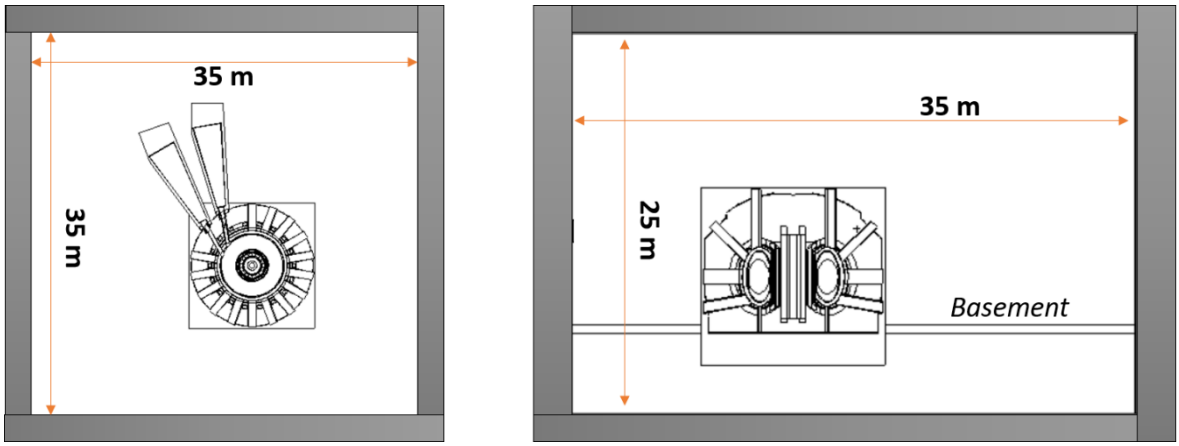

Figure 5-20 top view at the equatorial level (left) and lateral view at Y=0 (right) of the MCNP 360° simplified model inside the actual THB configuration

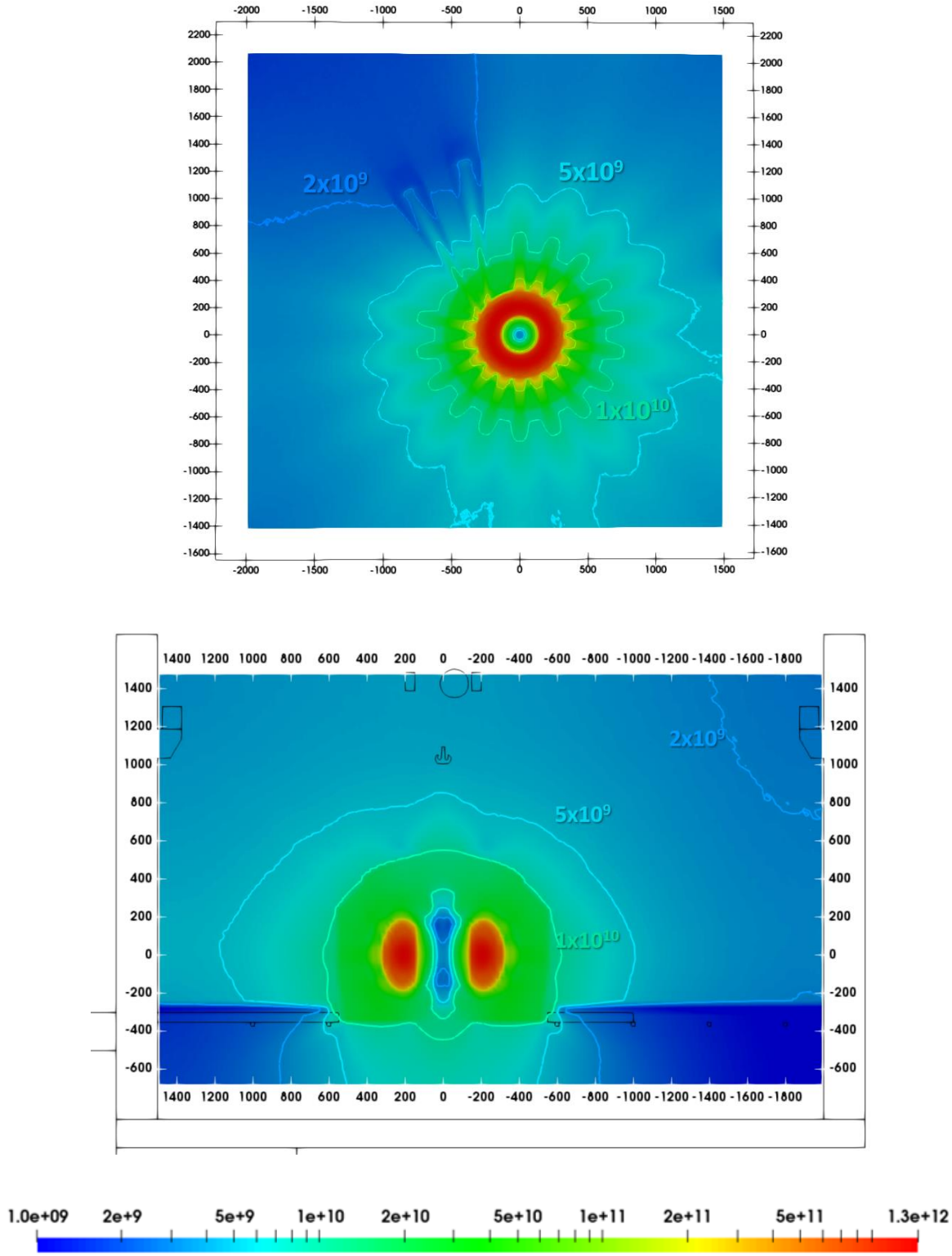

Figure 5-21 maps of neutron flux (n cm^{-2} s^{-1}) inside the DTT THB actual configuration, equatorial cross section (up) and lateral cross section Y=0 plane (bottom)

The neutron flux inside the hall, during the high-performance phase, is very high and varies from $1x10^{9}$ n/cm^2/s near the bunker wall to $1x10^{10}$ n/cm^2/s in the rear zone of the cryostat.

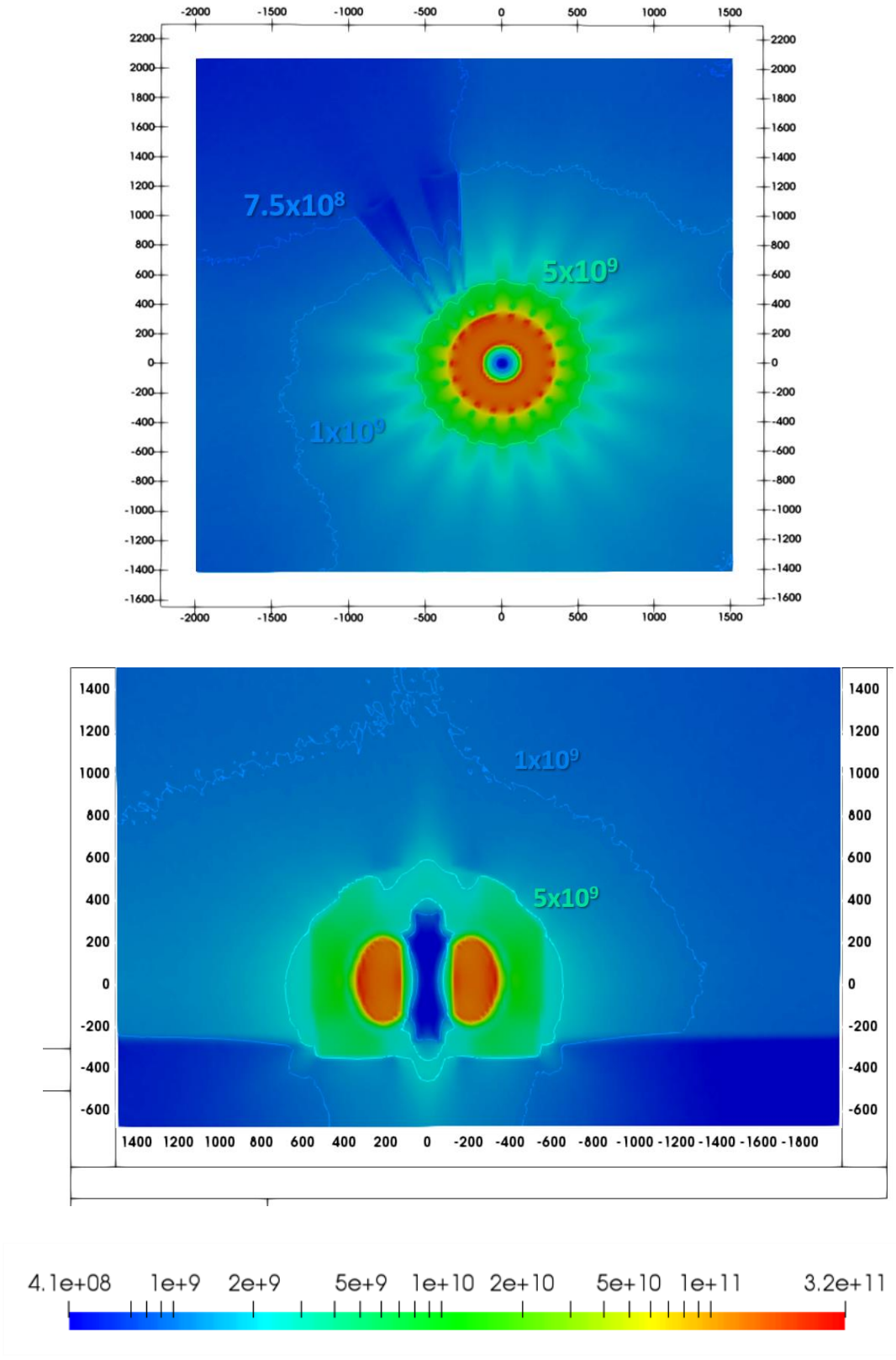

Figure 5-22 maps of gamma flux (γ cm-2 s-1) inside the DTT THB actual configuration, equatorial cross section (up) and lateral cross section Y=0 plane (bottom)

The gamma fluxes inside the hall varies from $5x10^9$ g/cm^2/s in the rear zone of the cryostat to $4x10^8$ γ/cm^2/s in the zone near the wall.

It's worth noting that the calculations regarding the thickness of the Torus Hall wall have been done considering the hall totally closed, without any door and without penetrations. In the DTT machine, several auxiliary systems, diagnostic and cooling systems will be necessary for the DTT operations, and these systems will be hosted in buildings around the tokamak hall. Thus, a number of penetrations, even large and complex, will be foreseen in DTT main building. These penetrations have a significant impact on the fluxes and doses outside the building and some of them will be studied and showed in the next chapters.

6 The Skyshine Effect in DTT

"The passion that left the ground to lose itself in the sky"

R. Browning

In the previous paragraph, calculations to determine the thickness of the wall and the material for the DTT Torus Hall Building have been showed and the results have been discussed.

In the frame of the studies regarding the radiation protection limits for the public another effect must be evaluated: the *Skyshine* phenomenon. This effect is particularly important for the choise of the material and the thickness for the THB roof. It is related to the interaction of the neutrons with the air nuclei and cause an increment of the fluxes and, thus, of the doses even at large distance from the radiation source (i.e. even hundreds of meters away). The rigorous and general physical treatment of this phenomenon is very complex. In this work, only the evaluation of the Skyshine with the aim at ensuring the respect of the limit of 10 μSv/y at the ENEA Frascati boundaries, i.e. at 38 m from the DTT machine, has been done. It is presented and discussed in the next paragraphs.

6.1 The Skyshine physical phenomenon

The Skyshine is a well-known phenomenon in the accelerator field, for nuclear fission power plant and for nuclear medicine applications. For the fusion devices it has been not yet studied in depth and only few papers have been published on this matter [61], [62]. Most of the bibliography on the evaluation of the Skyshine effect is related to the particle accelerators. [63] in which the Skyshine has been observed

for the first at Berkeley [64]. This accelerator was built without any upper shields and, sometimes, the radiation coming from the neutron skyshine was sufficiently intense to interfere with the accelerator activities.

The neutrons constitute a great component of the dose nearby the machine and, at great distances, are the major contributor to the dose. The rigorous treatment of this phenomenon is, anyway, too difficult because of the variability of the parameters involved in the problems. Moreover, the soil, can't be considered as a perfect absorber, even though it has an absorption coefficient much greater than the air. For the neutrons with energy laying between 1 MeV and 10 MeV it has a backscattering coefficient between 0.5 and 0.8 [65] so, the ground effect can't be neglected to know the radiation energy and intensity.

Even though the difficulties explained above, Lindembaum [63] has conceived a semi-empirical theory that results in very good agreement with the empirical results.

Lindembaum represented in a simulation a point isotropic source with the aim at describing a particle accelerator. The energy of the simulated neutrons was in the range of few MeV.

Then, he modified the neutron transport equation, described in chapter 2, in order to take into account, the presence of the earth surface and derived the formula considering the variation of the neutron flux density with the distances of the source. He also divided the neutron contribution in two different terms in order to "isolate" the contribution coming from the accelerator roof. The first contribution, the one that he called "*direct contribution*" expresses the neutron flux variation with distances considering only the absorption and the scatting out of the particles but not in-scattering. This contribution dominates the fluxes when the distances are very small (few meters). The second contribution, called *"indirect"* or scattered is dominant for the large distances (several meters away from the source) and Lindembaum called "*Skyshine*". In particular, he observed that this is the sole

contribution which is affected by the presence or absence of the roof shielding over the source.

Some experience in the early fifties [65], [66] clearly shows that the facilities which produce more than 10^9 n/s [67] requires an overhead shielding for the roof. Further studies and experiment [68], [69] show that the main component of the radiation measured outside the shielding of high energy accelerators is neutron components with energy ranging between the thermal energies and the energy of the primary beam. The gamma rays, which is important in a facility like DTT, usually contributes, at large distances, no more than 10 or, at least, 20% of the total dose. Other types of particles, i.e. protons or muons, have a great importance in the Skyshine evaluation but they are not considered in this work for obvious reasons.

6.2 Theoretical treatment

The theory elaborated by Lindenbaum [70], [71] regards the high-energy proton accelerators, considering the transport of low energy neutrons (few MeV) through the atmosphere. Presently this is the sole theory about the Skyshine effect related to the low energy neutron transport.

Basically the theory of Lindenbaum uses the expression of the neutron flux produced by a point isotropic source in an infinite isotropic scattering medium [72]. This expression was derived from the one by Case et al. [73] using the diffusion theory. The expression of the neutron flux density is as follows:

$$\phi(r) = \frac{Qe^{-\Sigma r}}{4\pi r^2}\varepsilon(c,r) + \frac{Qk(c)e^{-\Sigma_0 r}}{4\pi Dr}$$

Where Q is the neutron source strength in n/s, $\sum_t r$ is the macroscopic total cross section, $\sum_s r$ is the scattering cross section, D is the diffusion coefficient, $1/k_0$ is the diffusion length, $c = \Sigma_s/\Sigma_t$ is the ratio between the scattering cross section and the total cross section, ε(c,r) and k(c) are functions of c.

Case applied some assumptions to this formula:

- This solution is for the uncollided flux at the scoring point distance from the source;
- The source is a point isotropic source;
- Neutrons diffuse in an infinite uniform absorbing medium, as air in the Lindenbaum treatment;
- The scattering is isotropic in the centre of the mass of the system.

Applying these assumptions, the formula becomes:

$$\phi(r) = Q\,[\frac{7.9 \cdot 10^{-2}}{r^2}\exp\left(-\frac{r}{1.4 \cdot 10^4}\right) + \frac{1.4 \cdot 10^{-5}}{r}\exp\left(-\frac{r}{2.5 \cdot 10^4}\right)]$$

With the flux in n/cm^2/s, r in cm and Q in n/s.

Lindenbaum also suggested to change the value of *c* to consider the presence of the ground.

The first term of the equation is basically identical with the equation that described the propagation of the neutrons from a point source with absorption and no scattering. This first term becomes negligible when the distances are too large than about 3 mean free paths in air (i.e. 300 m).

Whereas the second term in the equation, represents the scattered components to the point of scoring from all directions: practically is the common term of Shkyshine.

Successive studies [15] found a good agreement with the Lindenbaum formula and the experimental values for the accelerators.

Ladu et al. [74] did a Monte Carlo calculation for an isotropic 5 MeV neutron point source at air-earth interface. They also studied the influence of the lateral shielding by performing the calculations for different values of the solid angle subtended upward by the source. In [74] Ladu et al. summarized their results with the following empirical expression:

$$\phi(r) = Ar^{-\alpha} \qquad 20\ m \leq r \leq 300\ m$$

$$\phi(r) = Be^{-r/\lambda} \qquad r > 300\ m$$

The values of α and λ are strongly related to the value of the angle chosen. α varies from 1.5 to 1.6 and λ from 200 to 230 m.

Fig. 7.1 shows the god agreement between the results obtained by Ladu et al. and Lindenbaum theory for the low-energy neutron.

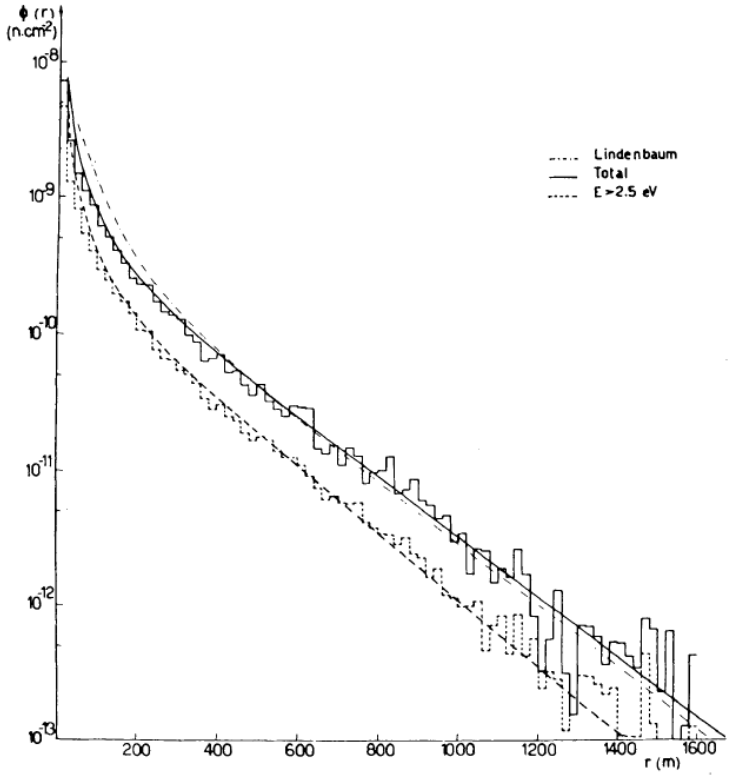

Figure 6-1 Calculated neutron fluence as a function' of the distance from an isotropic source (0 = 90°). The histograms represent the Monte Carlo calculations performed by the authors for the total fluence and the fluence of neutrons of energy > 2.5 eV. A smooth curve has been plotted over the histograms. Calculations using the Lindenbaum expression are also shown (from [74])

6.3 The DTT Skyshine evaluation

DTT is will be hosted in the Frascati ENEA research centre. The boundaries of the centre are not far from the DTT THB, as explained in the previous chapter, the closest boundary is at 38 m from the THB, as shown in fig. 6.2.

This means that the calculation of the Skyshine is particularly important for the respect of the radiation protection limits, i.e., 10 μSv/y for the public. Moreover, the distances of the order of 30-40 m are too small with respect to the distances indicated in the treatment showed in the previous paragraph.

Once the thickness and the material of the THB have been chosen, the thickness of the roof is of fundamental importance for the radiation protection and also for the civil engineer which have their own constraints in terms of weight of the roof, of the seismic rules[10] and all concerned the civil engineering aspects of such a building.

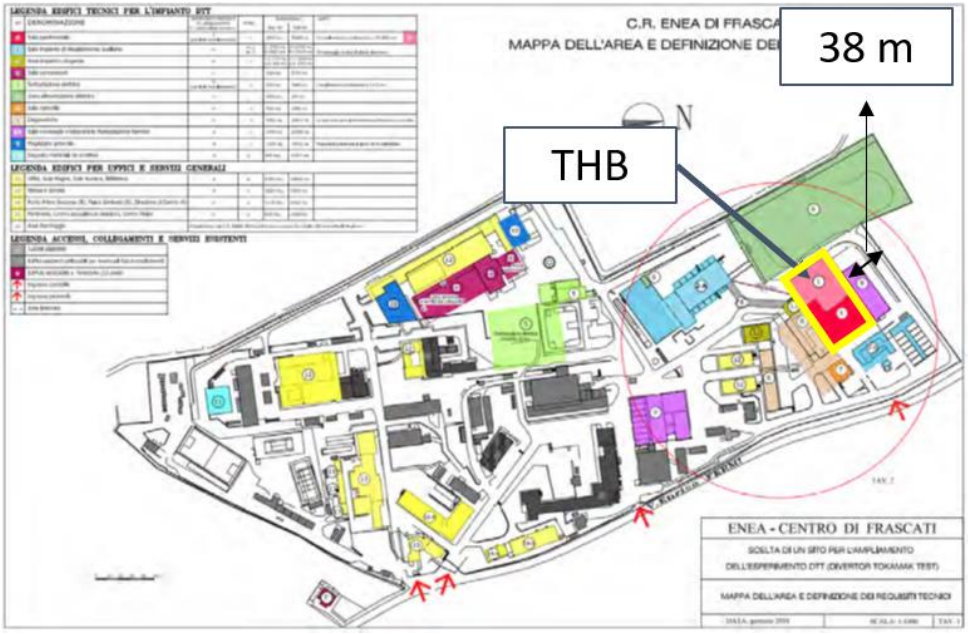

Figure 6-2 DTT site layout

6.3.1 Sensitivity analyses on the roof composition

The first step for the choise of the roof composition was done by performing a sensitivity study with the different materials and compositions to establish the attenuation factor of the different configurations.

The configurations for the roof assumed as a reference in this calculation is a layer of 180 cm of ordinary concrete. This configuration has been reported in the 360° MCNP simplified model, with an old configurations of THB 29 m tall, and the spectrum were calculated in the inner surface of the roof, showed in fig. 6.3.

[10] Frascati is considered a low seismic region

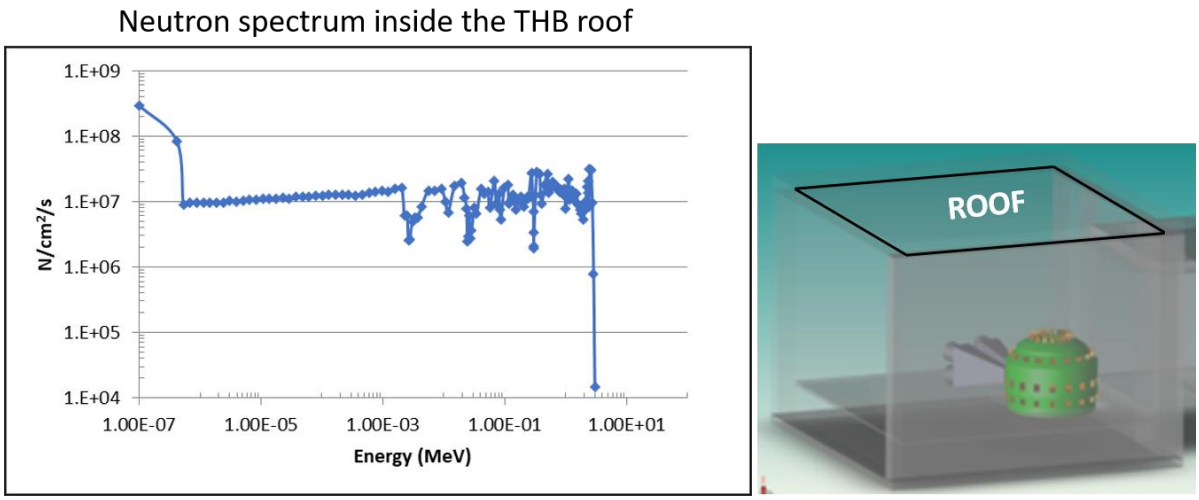

Figure 6-3 neutron spectra calculated in the roof inner surface

The maximum value of the neutron flux inside the roof is in the zone just above the machine and it's equal to $2x10^{9}$ n/cm²/s and $1x10^{9}$ γ/cm²/s regarding the gamma fluxes with a correspondent value of maximum effective dose rate of 70 mSv/s during high-performance phase.

The scoring region has been settled 20 cm outside the roof and the nuclear quantities, neutron and gamma fluxes and doses, have been calculated considering the DD DTT maximum neutron yield of $1.5x10^{17}$ n/s and $1.53x10^{21}$ n/y. The sensitivity studies have been done by modelling a secondary neutron and gamma semi-isotropic source on the inner surface of the ceiling by means of the SDEF MCNP card, normalized to the maximum value of neutron flux under the ceiling.

For the reference configuration the values 20 cm above the roof are 8.75 n/cm²/s and 9.77 γ/cm²/s for the fluxes and the total effective dose rate is $6x10^{-2}$ μSv/s. This configuration provides and attenuation of more than six orders of magnitude regarding the neutron flux and about six orders of magnitude regarding the total effective dose rate. For the gammas the problem of the Skyshine, as explained in the first paragraph of this chapter, is less important at great distances with respect to the neutrons. Anyway, is important to pay attention to the values of gamma fluxes in order to limit the doses.

Materials for the sensitivity studies have been chosen above all for their shielding properties against the neutrons. The normal concrete, same to that used for the building wall, has been left for the first 50 cm for structural reasons. Other materials considered are the LCB (Luminite-Colemanite-Baryte) concrete with density of 3.1 g/cm^3, polyethylene and borated polyethylene for the neutrons and the lead has been used for some configurations to limit the gamma production. Compositions of this materials are shown in tables from 6.1 to 6.3.

Table 6-1 Polyethylene composition

Poliethylene Pol 0.94 g/cm3	**Weight Fraction (%)**
H	14.37
C	85.63

Table 6-2 Borated Polyethylene compositions

Borated Poliethylene BPol 0.94 g/cm3	**Weight Fraction (%)**
H	11.6
C	61.2
B	5
O	22

Table 6-3 Luminite Colemanite Baryte Concrete composition

Concrete Luminite-colemanite-baryte ConLCB 3.1 g/cm^3	**Weight Fraction (%)**
H	1.10
B	0.88
O	37.14
Na	0.11

Mg	0.14
Al	1.77
Si	0.97
S	9.11
Ca	5.51
Ti	1.28
Mn	0.12
Fe	3.09
Ba	38.79

The use of polyethylene and borated polyethylene could reduce the neutron fluxes and the weight of the structure as well.

Twelves configurations have been studied in order to evaluate the attenuation factor and the weight of the roof and they are listed in the table 6.4. In the last column the weight ratio with respect to the reference configuration (180 cm of normal concrete) is listed.

Table 6-4 weight ratio of the configurations considered with respect to the reference configuration (180 cm of ordinary concrete)

Number of configuration	Configuration of the roof	Weight ratio compared to reference
Ref	180 cm Concrete	-
1	150 cm Con	0.83
2	50 cm Con + 40 cm ConLCB+ 50 cm Pol	0.71
3	100 cm Con + 50 cm Pol	0.67
4	100 cm Con + 50 cm Bpol	0.67
5	50 cm Con + 40 cm ConLCB	0.59

6	50 cm Con + 30 cm Pol + 30 cm ConLCB	0.58
7	50 cm Con + 20 cm ConLCB+ 50 cm Pol	0.55
8	50 cm Con + 50 cm Pol + 20 cm ConLCB	0.55
9	50 cm Con + 20 cm ConLCB+ 50 cm Bpol	0.55
10	50 cm Con + 20 cm ConLCB+ 30 cm Bpol	0.51
11	50 cm Con + 70 cm Pol	0.44
12	50 cm Con + 50 cm Pol	0.4

Some configurations have a weight ratio very small compared to the reference. The configuration number 10 has half of the weight of the reference configurations. The relative values of the calculated nuclear quantities are shown in tab 6.5 for all the configurations.

Table 6-5 Attenuation factor for neutron flux and total effective dose for the configuration studied

config	n_flux (n/cm²/s)	gamma_flux (p/cm²/s)	Total Eff dose rate n+γ (microSv/s)	Attenuation n flux: Ratio N flux below(inside TH) /above roof (outside TH)	Attenuation total Effective dose rate: Ratio Effective dose rate below(inside TH) /above roof (outside TH)
ref	8.75×10^{2}	9.77×10^{3}	0.06	2.28×10^{6}	1.10×10^{6}
1	8.85×10^{3}	6.40×10^{4}	0.47	2.26×10^{5}	1.47×10^{5}
2	2.05×10^{-1}	5.86×10^{4}	0.21	9.74×10^{9}	3.28×10^{5}
3	4.96×10^{-1}	3.43×10^{5}	1.28	4.03×10^{9}	5.41×10^{4}
4	1.84	3.21×10^{5}	1.22	1.08×10^{9}	5.68×10^{4}
5	3.8×10^{4}	1.93×10^{5}	4.16	5.30×10^{4}	1.67×10^{4}
6	4.7×10^{1}	2.59×10^{5}	1.33	4.27×10^{7}	5.23×10^{4}
7	2.42	2.46×10^{5}	0.9	8.27×10^{8}	$7.68E \times 10^{4}$
8	9.31×10^{-1}	3.88×10^{5}	2.04	2.15×10^{9}	3.40×10^{4}
9	8.66	4.65×10^{5}	1.69	2.31×10^{8}	4.11×10^{4}
10	6.74×10^{2}	8.98×10^{5}	3.22	2.97×10^{6}	2.16×10^{4}

11	1.63×10^{-1}	2.64×10^{6}	9.33	1.23×10^{10}	7.45×10^{3}
12	2.88×10^{1}	5.49×10^{6}	18.57	6.95×10^{7}	3.74×10^{3}

Among the configurations studied, all of them which have a high attenuation factor for the neutron present the higher values of total effective dose outside the roof. This is due to the presence of the polyethylene that is a very efficient neutron shield but produces a great amount of gammas due to the (n,γ) reactions inside the material. The configuration number 10, with 100 cm of thickness, and an attenuation factor for the neutrons of 3×10^{6} and for effective dose greater than 4 orders of magnitude, have a promising composition and shows how the heavyweight concrete are effective in radiation shielding.

In general, except for the options without polyethylene, all configurations provide a significant lower neutron flux outside the roof compared with the 180 cm configuration (ref). No evident benefits are observed in using Borated Polyethylene instead of normal Polyethylene.

All options produce more gammas and, therefore, higher total effective dose than reference configuration.

Regarding the neutrons, except for the configurations without the Polyethylene, all other options provide better attenuation than the reference. Fig 6.4 the radiation attenuation performances are shown.

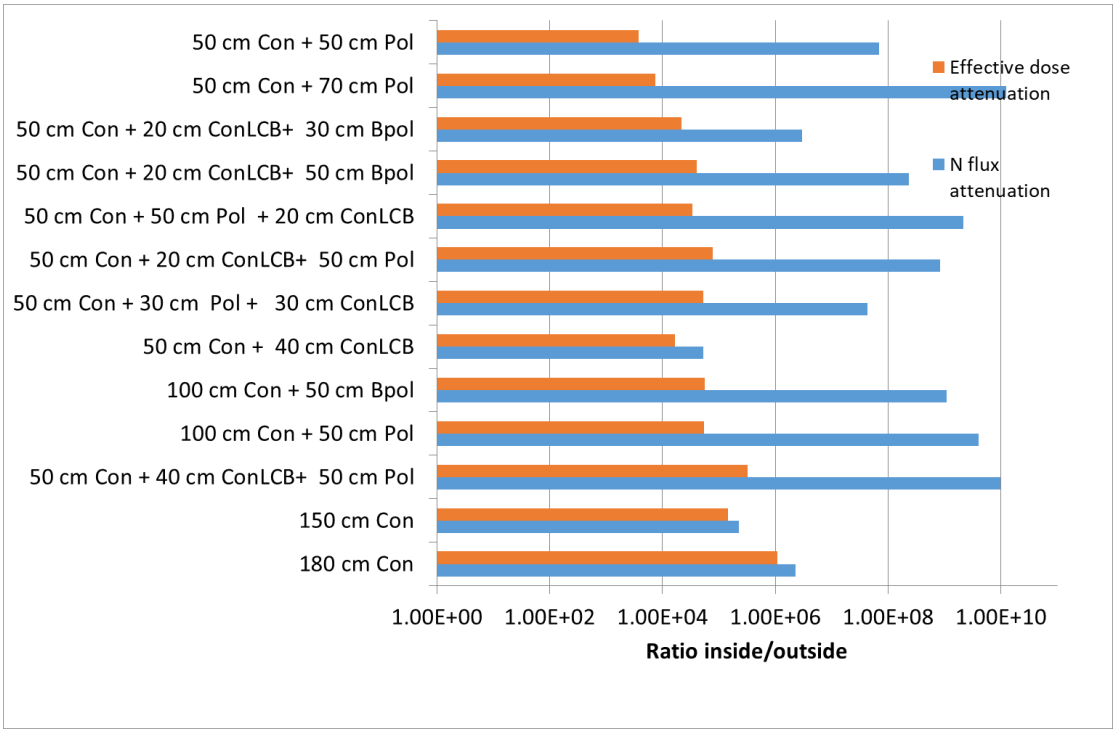

Figure 6-4 radiation attenuation performances for the roof configurations studied

6.4 Skyshine Calculations

The Skyshine calculation has been done using the 23 m THB height. Presently, as explained in the chapter 6, the height of the hall has been settled to 25 m. Although the discussion about the height of the hall is still ongoing, the calculations presented in this chapter are anyway conservative and a higher height of one or two meters doesn't affect the calculations in a significant way.

The results presented in the paragraph 6.3.2 for the nuclear quantities above the roof have been renormalized on the basis of the new height of the THB by means a full 3D calculations and maintaining 180 cm concrete as reference.

The neutron and gamma fluxes have been calculated 20 cm out of the roof in the configuration showed in fig 6.5, considering the surface with and without the contribution of the lateral wall (i.e. the green zone in the figure).

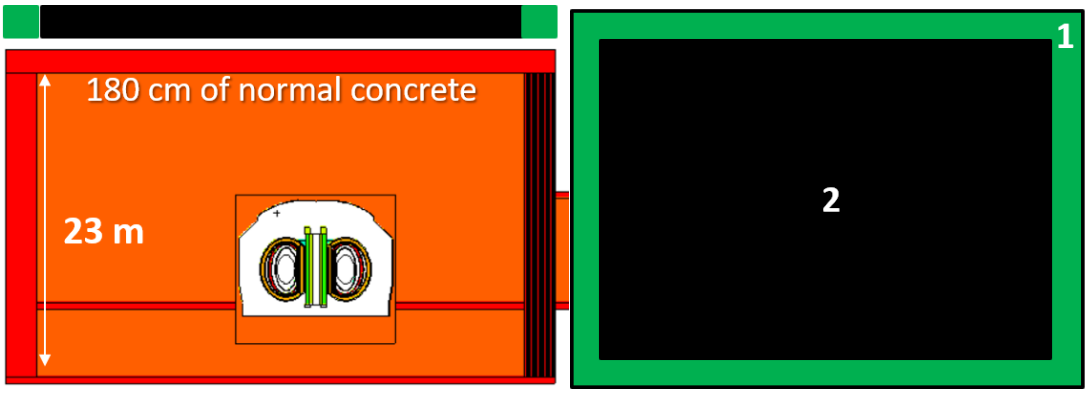

Figure 6-5 scoring region for the skyshine evaluation

The black zone (#2) is the internal area of the roof with 35 x 35 m dimensions whereas the green zone is the area (#1) above the roof.

The values of neutron and gamma fluxes and effective doses derived from these calculations and showed in table 6.6 have been used to renormalized the data showed in the previous paragraph (table 6.5) on the top of the roof.

Table 6-6 Values of neutron and gamma fluxes (cm^{-2} s^{-1}) and effective doses (uSv/y) in the scoring region with the plasma source

New results with plasma source (180 cm concrete roof)				
	n_flux (n/cm²/s)	**g_flux (g/cm²/s)**	**n_eff_dose (uSv/y)**	**g_eff_dose (uSv/y)**
1	4.72×10^{1}	2.07×10^{3}	6.1	92.64
2	5.00×10^{2}	1.72×10^{4}	71.01	834.61
<1+2>	**4.04×10^{2}**	**1.40×10^{4}**	**57.32**	**678.14**

The calculation has been repeated in order to calculate the dose rate at 38 m from the THB. This has been done in three steps:

1) Neutron and gamma fluxes inside the THB impinging on the roof has been calculated for generating neutron and gamma secondary sources;

2) The secondary sources have been used to transport particles across the roof, to calculate fluxes outside the THB and generate external secondary sources
3) Particles generated by the secondary sources above the roof have been transported up to 38 m from the THB.

In the first step the scoring cell is located just above the roof. In between the scoring cell and the roof it has been placed a void cell in which all entering particles are killed, in order to avoid double counting of particles being back scattered from the roof and then coming back on it. The resulting fluxes are 1.03×10^9 n/cm²/s and 2.33×10^8 γ/cm²/s and the spectra are shown in fig. 6.7.

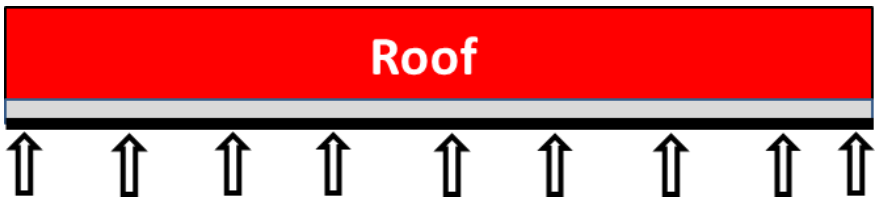

Figure 6-6 calculation surface in the inner part of the roof

Using the secondary sources created in this way paricles are then transported up to the top of the roof, where again fluxes and spectra are calculated for generating further neutron and gamma secondary sources with a semi-isotropic emission.

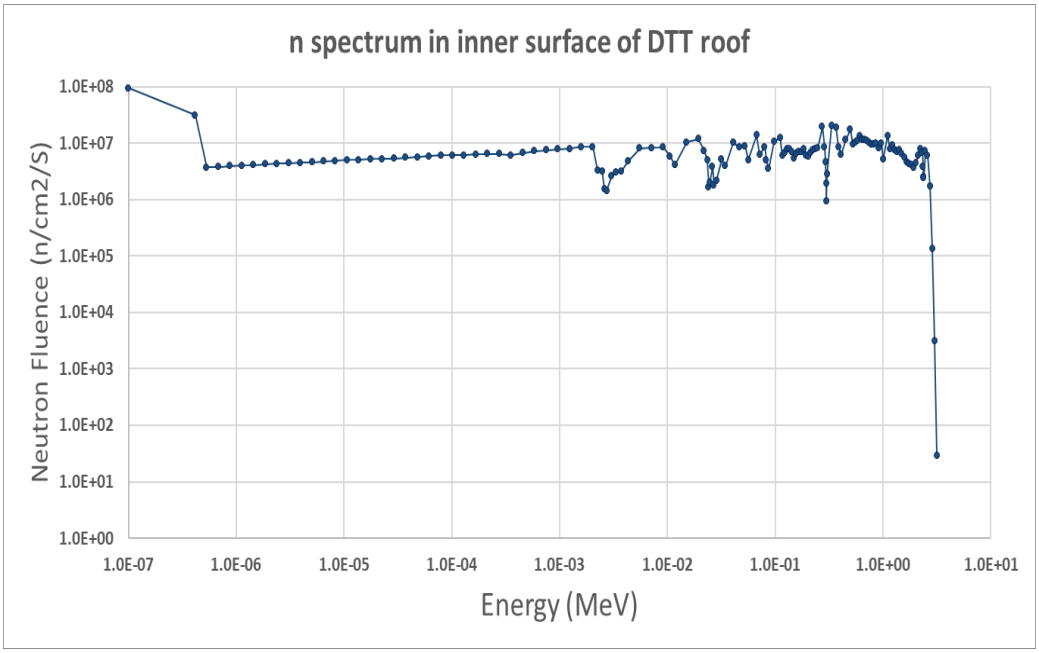

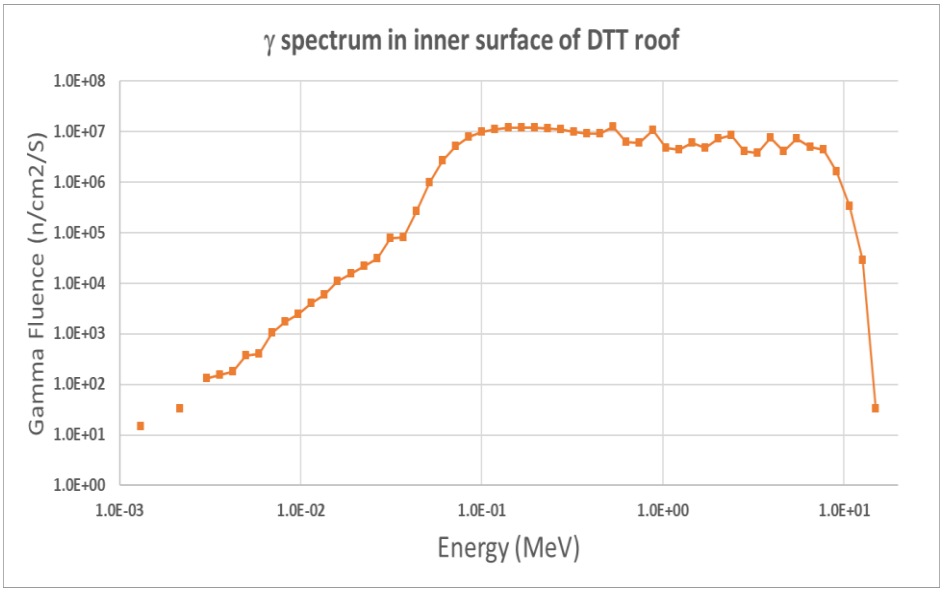

Figure 6-7 neutron (up) and gamma (down) spectra in the inner surface of the roof with 23 m THB height

Once the secondary sources have been created, the scoring point have been placed 38 m from the THB, as shown in figure 6.8.

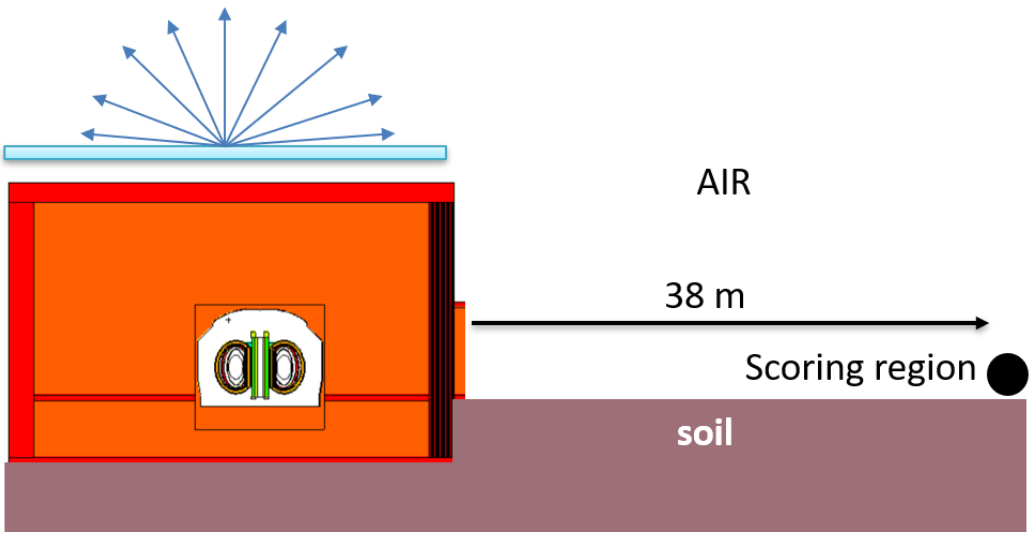

Figure 6-8 configuration for the skyshine evaluation

Values calculated with this configuration and 180 cm of roof thickness are reported in tab 6.7

Table 6-7 neutron flux and effective dose rate 20 cm above the roof and 38 m away from the THB with 180 cm thickness of the roof

Component	**Flux top (n/cm2/s)**	**Flux38 m (n/cm2/s)**	**Effective Dose top (μSv/y)**	**Effective Dose at 38 m (μSv/y)**
Neutrons	293	2.94	$7.74x10^{1}$	$4.49x10^{-1}$
γ from atm	8.16	0.547	$6.20x10^{-1}$	$3.31x10^{-2}$
γ from primary n	$7.66x10^{3}$	29.4	$5.15x10^{2}$	$3.03x10^{-1}$
γ from primary g	437	1.63	$3.18x10^{1}$	$1.73x10^{-2}$
Tot			$6.25x10^{2}$	$8.02x10^{-1}$

From the results is clear that the gamma contribution on the top of the roof is dominant in terms of fluxes and doses where contribute more than 80% to the total. On the contrary, at 38 m from the source the contribution of neutrons, according to the Skyshine theory for the few energy neutrons, is dominant, even though the contribution of gammas is not negligible. By calculating the ratio of the values on the top of the roof over those calculated at 38 m, the values in the table 6.7 have been renormalized in order to evaluate the Skyshine contribute to the effective annual dose rate for DTT and the results are shown in table 6.8.

Many configurations, among those studied, cause a very high contribution to the total dose rate at 38 m from the building even though they provide a significant attenuation factor for neutrons. The production of the gammas is determinant for the doses even at 38 meter and could not be neglected in these studies.

All the configurations enlighten in red in the table can't be used for the DTT purposes because overcome the limit of 10 μSv/y for the only Skyshine contributions.

Table 6-8 values of annual effective dose rate due to the skyshine effect at 38 m away from the THB for the configurations studied

Configuration of the roof	SKYSHINE Annual TOTAL_eff_dose rate (μSv/y)
180 cm Con	0.731
150 cm Con	5.92
50 cm Con + 40 cm ConLCB+ 50 cm Pol	1.87
50 cm Con + 40 cm Poly + 30 cm Con + 5 cm Pb	2.17
50 cm Con + 40 cm Poly 20 cm ConLCB + 5 cm Pb	2.07
100 cm Con + 50 cm Pol	11.4
100 cm Con + 50 cm Bpol	10.8
50 cm Con + 40 cm ConLCB	67
50 cm Con + 30 cm Pol + 30 cm ConLCB	11.8
50 cm Con + 20 cm ConLCB+ 50 cm Pol	8.00
50 cm Con + 50 cm Pol + 20 cm ConLCB	118
50 cm Con + 20 cm ConLCB+ 50 cm Bpol	14.9
50 cm Con + 20 cm ConLCB+ 30 cm Bpol	29
50 cm Con + 70 cm Pol	82.5
50 cm Con + 50 cm Pol	164

All the configurations pointed out in green are suitable for the DTT THB but some of them implies the use of the heavyweight special concrete.

The configuration with 150 cm of concrete seems suitable from different point of view. It is a conventional solution from the civil aspects and doesn't imply the use of special materials with consequent issues. The annual effective dose is relatively

high, around 6 μSv/y, but it is under the limit[11] with sufficient margin to respect it also considering the direct contribution from the machine.

[11] 10 μSv/y according to the Italian Regulation

7 Neutronics Studies of the DTT site

"Art is I; science is we"
C. Bernard

In the chapters 5 and 6 all the analyses regarding the Torus Hall Building and the shielding needs to respect the radiation protection constraints for the workers and the limit for the public has been presented and discussed.

Anyway, around the main building there are others important buildings and areas which have strict requirements in terms of fluxes, doses and nuclear loads on the components, especially for the electronics which are particularly sensitive to the neutron and gamma effects. These areas must be characterized from the nuclear point of view in order to maintain the relevant nuclear quantities as low as possible to avoid the failure of these systems.

Furthermore, the calculations for the thickness of the walls have been done considering the THB completely closed with no penetrations at all. DTT, as an innovative fusion machine which have to investigate multiple physical aspects like new divertor and plasma configurations, requires several systems hosted outside the THB and connected to it through penetrations, sometimes larger and close to each other. Plasma parameters, in all the configurations, must be monitored, so a number of diagnostics will be installed in DTT and its electronics and acquiring systems will be placed outside. The additional heating systems, described in chapter 3, have big transmission lines which will penetrate the THB wall to allow the wave to be transmitted from the gyrotrons to the plasma.

From the neutronic point of view these penetrations mean that a large neutron streaming will cause a significant increment of the neutron and gamma fluxes and doses and proper shielding strategy must be adopted to limit the streaming effects.

In this chapter, the shielding studies for the South and East wall of the THB, showed in fig. 7.1, is presented. The South area will host ECRH corridor in which the four EC transmission lines are located and some laboratories for the diagnostic systems. The layout of these laboratories and the diagnostic are currently under study and not yet defined so the analyses for the East area regards only the ECRH penetrations.

The East side of the THB will host the Fast Discharge Unit (FDU) area for the TF coils and a passage area where the Helium cryogenic line is located.

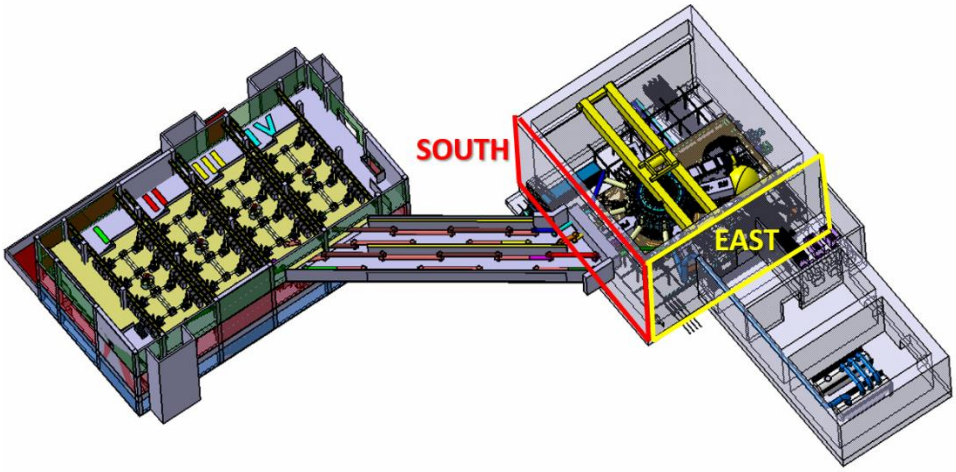

Figure 7-1 CAD view of the DTT area. In red the south area with ECRH penetrations and in yellow the east area with FDU room and He cryogenic line

7.1 Neutron streaming analyses for the ECRH penetrations

A DEMO relevant environment is of fundamental importance for the main scope of DTT [36]. The DEMO conditions could be reached only if the ratio between the power across the separatrix (P_{sep}) and the major radius (R) is P_{sep}/R= 15 MW/m. This condition can be obtained by coupling to the plasma an additional power of 45 MW. This means that a mix of additional heating systems is necessary. In DTT three

additional Heating and Current Drive (HCD) systems are foreseen: Electron Cyclotron Resonance Heating (ECRH), Ion Cyclotron Resonance Heating (ICRH) and Negative Neutral Beam Injection System (NNBI) [36]. Three big systems which will be connected to the machine through transmission lines penetrating the THB and causing large neutron and gamma streaming. Accurate evaluation of this streaming through the penetrations is necessary to evaluate the impact on the radiation level outside the THB. Thus, proper shielding strategy is needed to guarantee the protection of the workers and the building classifications.

7.1.1 The ECRH system

The main issue for the ECRH system is to provide the required power exhaust for the divertor to be tested in relevant condition and, in parallel, to perform the tasks necessary to sustain the plasma scenario in an integrated way [75]. The ECRH main assignments are:

- Main plasma heating for high confinement regimes;
- Magneto-hydrodynamic (MHD) models control;
- Localized Current Drive (CD) for profile tailoring;
- Plasma current start-up;
- Wall cleaning.

The injection of EC waves at different poloidal and toroidal directions is foreseen for the ECRH systems in order to fulfil all these requirements and ensure the flexibility and power deposition and control. The basic architecture of the ECRH consists of a *cluster* composed by 8 sources, called *gyrotrons*, fed by four main high voltage power supplies (MPS) for the cathode, 8 for the body power supplies (BPS) and the possible use of anode power supplies. The 8 microwave beams are transmitted by a multi-beam (MB) Quasi-Optical (QO) line and delivered to one DTT sectors where 6 independent launching mirrors systems are located in one equatorial port launcher and 2 are hosted in the corresponding upper port. In total

4 Multi-Beam Transmission Lines (MTBLs) and 4 equatorial ports with the corresponded upper ports are occupied by the ECRH [76].

Figure 7-2 sketch of the QO TL section.

The Gyrotrons are hosted in a separate building placed in the south part of the DTT site and it is connected to the THB through a corridor in which the MB Transmission Lined are located. The corridor is about 40 m long and 10.4 m above the ground level (fig. 7.3)

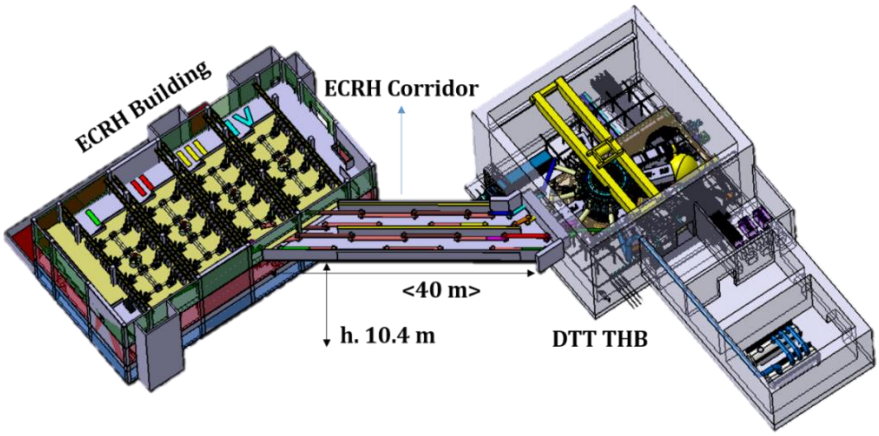

Figure 7-3 view of the ECRH area with ECRH building, Torus Hall and connection corridor

The requirements for the transmission lines are a target efficiency greater than 90% and a power handling of 1 MW or more. Considering the large number of single beams (about 24-32) the MBTLs concept is envisaged, for its compact arrangement and simplicity, the required volumes and number of MBTLs components. The design ex-ploits QO propagation and is based on large confocal mirrors layout with up to 8 single beams (corresponding to one EC cluster) on the same optical surface. The single TL module consists of a straight path and a dogleg with a couple of plane

and shaping mirrors for beams refocusing. Inside the MBTLs, mirrors transmit the beams towards the lines close to the tokamak where a splitting mirror separates the bundle in 8 Single Beam Transmission Lines (SBTL) [76].

The design of the MTBLs is rigorous in order to transmit the waves to the tokamak with sufficient energy. This means that the neutron and gamma shielding must be adjusted in order to avoid modifying the design of the MTBLs.

7.1.2 MCNP Neutronic model

For the streaming analyses of the ECRH corridor the 360° MCNP DTT model has been used. The MCNP neutronic model for the ECRH tunnel features the four MTBLs made of SS with 80 cm of diameter and 0.8 cm thick. The corridor is about 13 m large and 2 m high, with a 24 cm thick rectangular building shell made of standard concrete. In addition, in the first part of the corridor, for a length of 5.5 m from the THB, is surrounded by a 1 m concrete collar needed to mitigate the radiation streaming outside. [77]. The configuration of the corridor and the MCNP model are shown in fig. 7.4 and 7.45

The penetrations are located 2.6 m above the DTT equatorial plane and the MTBLs lines are represented in the MCNP neutronic model for all their length, from the DTT THB to the ECRH building in order to represent in the maximum realistic way the radiation field inside and outside the corridor.

During the development of the layout of the corridor two main aspects must be take into account:

- The level of the dose rate at the ground level;
- The level of the fluxes and doses inside the corridor inside the Gyrotron Building.

The neutronic calculations have been divided in two steps in order to finalize the neutronics requirements for the shielding.

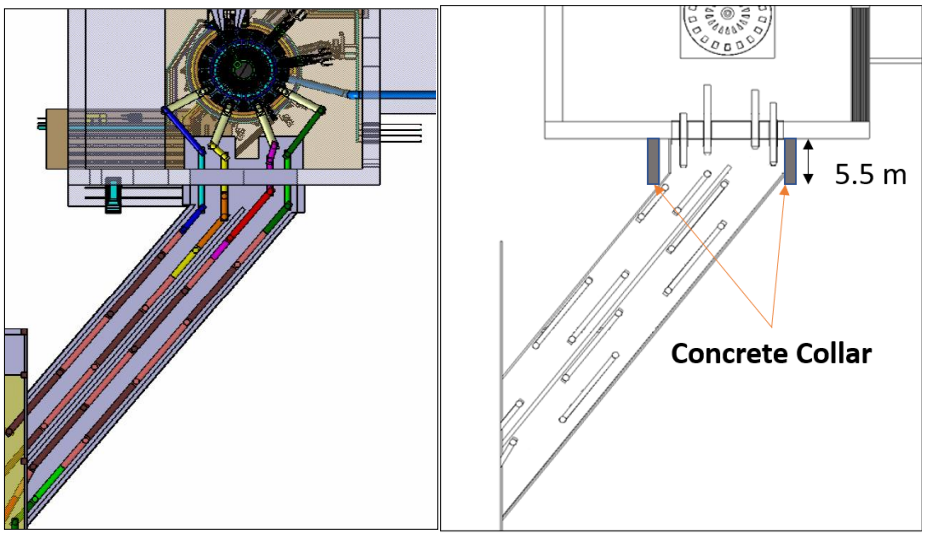

Figure 7-4 top view of the ECRH corridor, CAD model (dx), MCNP model (sx)

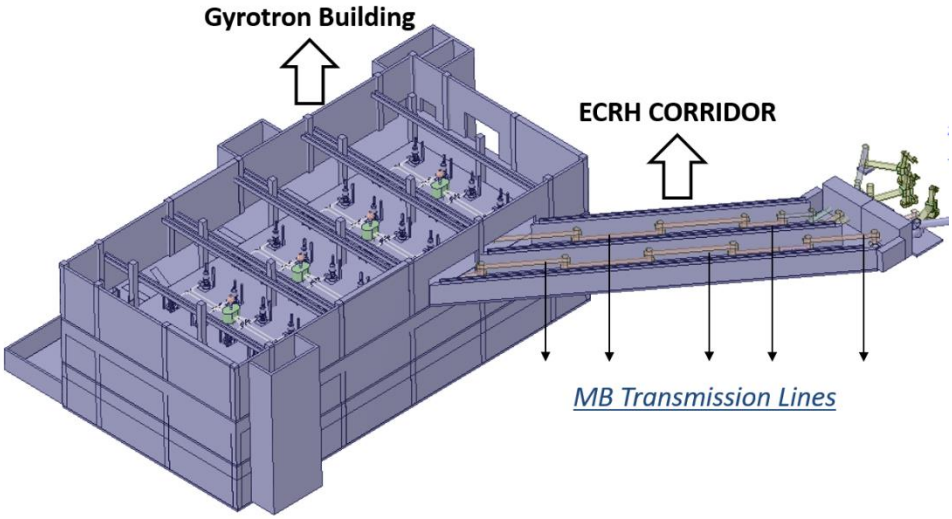

Figure 7-5 focus of CAD model of ECRH corridor, Gyrotron building and MBTLs

7.1.3 Shielding optimization for the ground level

The most relevant issue in the design of the corridor layout is the level of annual effective dose at the ground, where the workers must safely access even during the DTT operations, so the level of the doses must be maintained under the 300 μSv/y.

The penetration of the MBTLs have a significant impact on the neutron streaming and the level of neutron and gamma fluxes outside the penetrations is up to $2x10^8$ n/cm^2/s and $7x10^7$ γ/cm^2/s. Figure 7.6 shows the maps of neutron and gamma fluxes at the penetration quote without any shields.

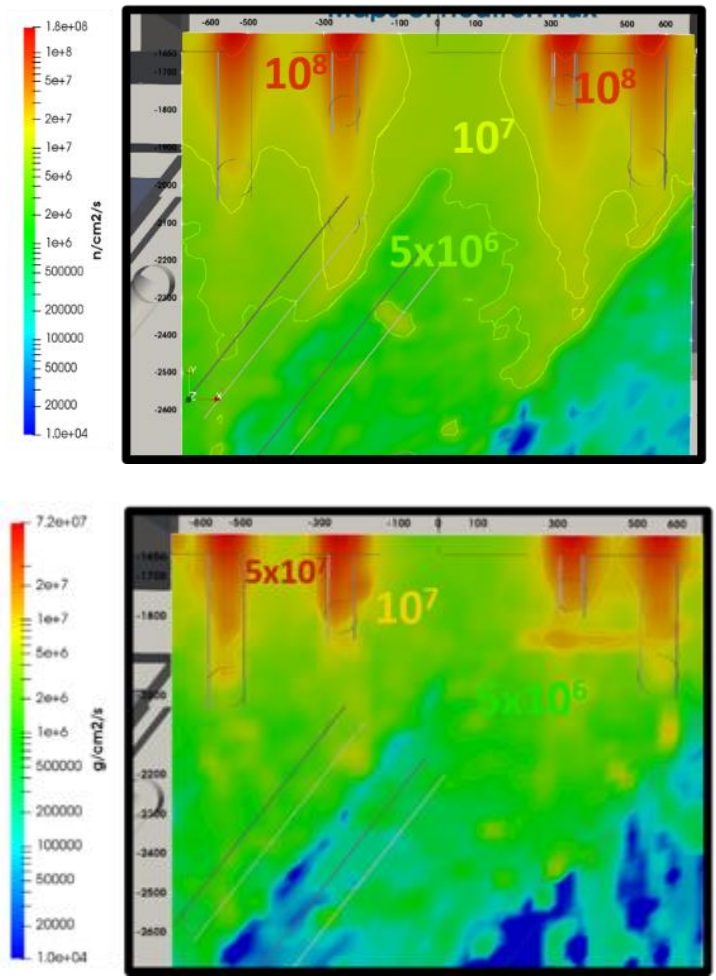

Figure 7-6 Maps of neutron (up) and gamma (down) flux close to the ECRH penetrations - top view

This intense streaming of neutron and gamma fluxes implies a huge level of fluxes and doses even at the ground level, up to 3.5 mSv/y.

For this reason, two configurations to mitigate the level of effective dose have been proposed using a combination of fixed and removable shielding to the corridor:

1. External shield + floor shield;
2. MTBLs removable shielding + oblique shield in addition to the option 1

The 1st option features a shield inside the corridor, called external shield, made by 90 cm of polyethylene (ρ= 0.94 g/cm^3) surrounded by 5 cm of Stainless Steel (ρ= 7.93

g/cm^3) has been located around the MTBLs and 30 cm of polyethylene covered by a thin layer of SS has been used to cover the corridor floor (fig. 7.7a)

In the 2nd configuration 4 removable shields pieces made of polyethylene and SS have been added in proximity of MBTLs dogleg to obstruct the straight-line path of propagation of neutrons and gammas. Since this was not sufficient to respect the constraint of 300 μSv/y an additional shield made of 30 cm of polyethylene has been added in the oblique wall of the bridge (fig. 7.7b)

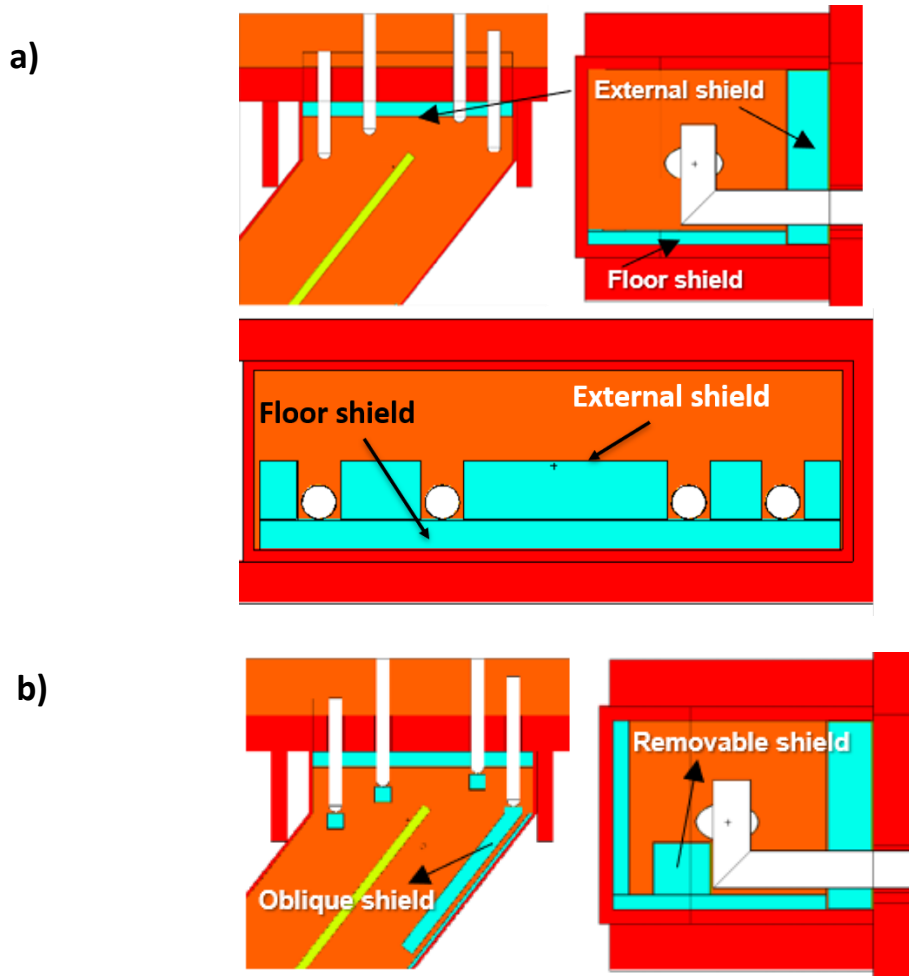

Figure 7-7 option 1 (a) and option 2 (b) for the shielding configuration studied

The area under the tunnel has been mapped by means the use of 15 spheres of 1 meter of radius placed in 15 positions at the ground level as shown in fig 7.8.

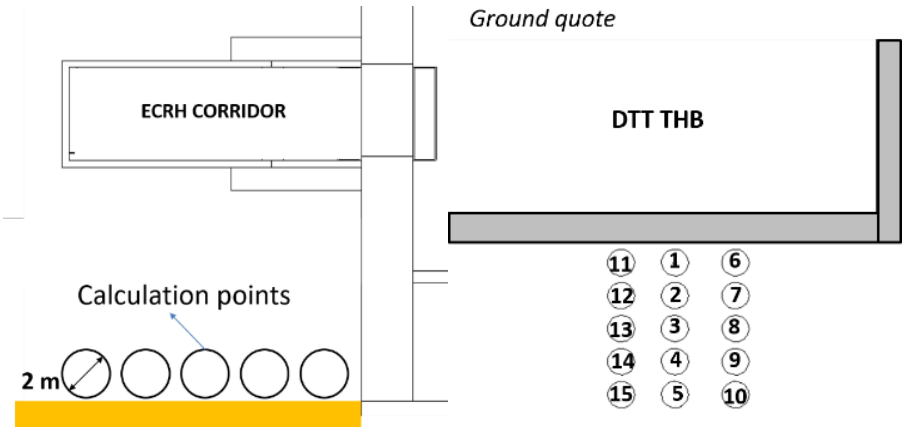

Figure 7-8 calculation position on the ground: lateral view (left), Top view (right)

A standard calculation was not sufficient to reach good statistic in the scoring region of interest. ADVANTG hybrid transport code [22] has been used to generate the weight windows file in order to split the particles towards the scoring region and reach sufficient statistics. In particular, the ADVANTG calculation has been optimized for the farthest sphere (i.e. #5 #10 #15). The ADVANTG output has been then manipulate with the F4E tool "iww_gvr generator" [48] in order to smooth and soften the wwinp resulting file. An example plot for the neutron weight window map generated with ADVANTG is shown in figure 7.9. This procedure has allowed to reduce the statistical error, which was greater than 40% without the use of variance reduction techniques, at level below the 10%.

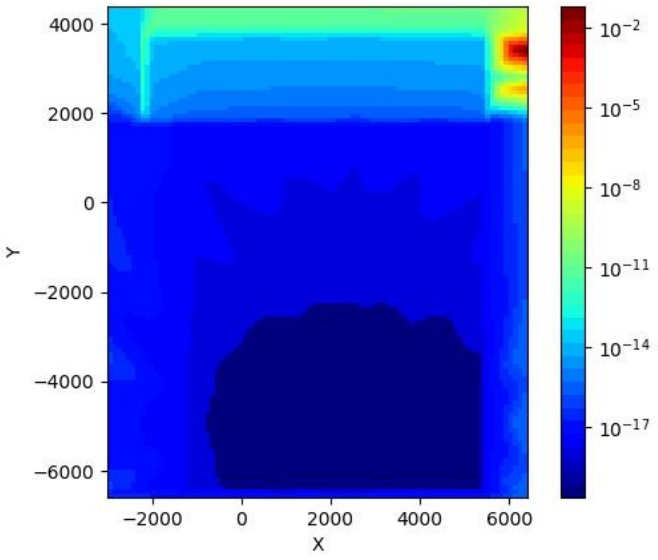

Figure 7-9 Example of the weight windows map generated by ADVANTG at the ground level

The results of calculations are shown in fig. 7.11. These results clearly show the effectiveness of these shielding configurations adopted. The external shield limits the crosstalk between the MBTLs and collimates the fluxes.

The removable shielding in front of the TLs dogleg avoid the straight path of the neutrons. Thus, the second option ensures the respect of the design constraints even for the non-radiation workers.

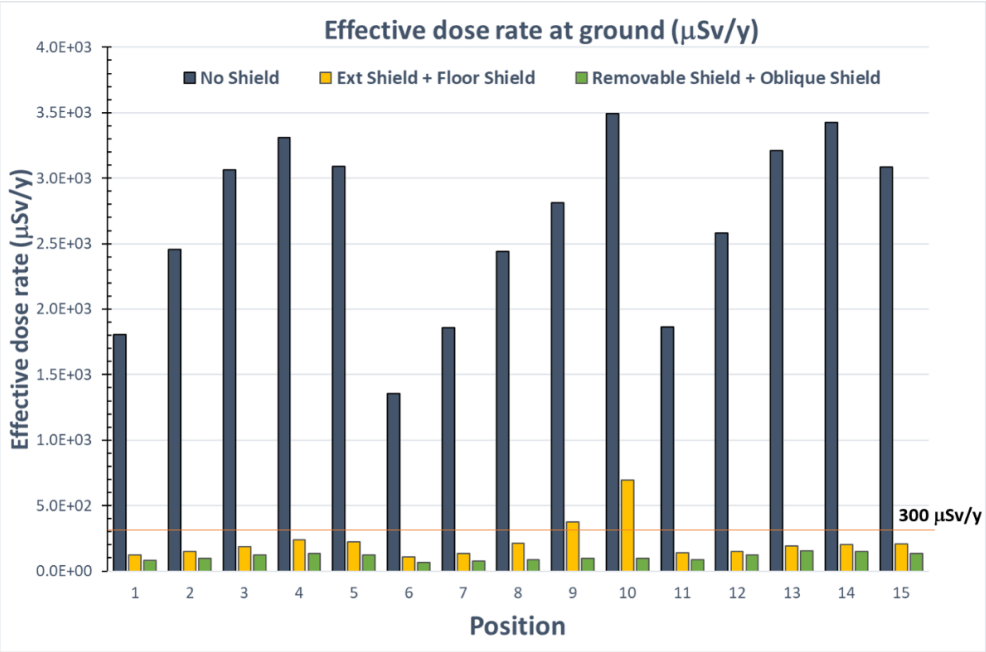

Figure 7-10 and graph of the annual effective dose rate in mSv/y at the ground level for the baseline and the 2 configurations studied

Positions #9 and #10 presents the greater values among the positions considered in all configurations. This is due to the shape of the corridor which is oblique and turn left just above the positions #9 and #10. This causes a reduction of the shielding effectiveness above those spheres causing a hotspot.

7.1.4 Mitigation of the radiation level inside the ECRH corridor

The characterization of the radiation field inside he ECRH corridor as well as the level of the Shutdown Dose Rate (SDDR) is important for the maintenance operations of the MBTLs and for the control of the effective dose level close to the gyrotron building, 40 m far from the penetrations.

7.1.4.1 Methodology

The major neutronic issue for the gyrotron building is the access during the DTT operation. To propagate the particles 40 m far from the penetration, two neutron and gamma secondary sources have been generated using the MCNP "SDEF" card. The only usage of the weight windows, although necessary, was not sufficient and, thus, a two steps strategy has been adopted for the calculations [78].

For the first step 5 different surfaces have been created in the MCNP model (fig. 7.11). Four of them were placed in front of the four penetrations and the latter covers the ECRH window.

In order to prevent the double scoring of the particles, two different calculations were done using the 3D plasma source coupled with the variance reduction techniques. In these two simulations neutrons and gammas have been sampled, considering energy and angle, with the aim at calculating, separately, the number of particles crossing the holes and the window.

It was found, as expected, that the number of the particles crossing the window surrounding the MBTLs was several orders of magnitude lower than those crossing the holes, so the window contribution was not considered for the secondary source.

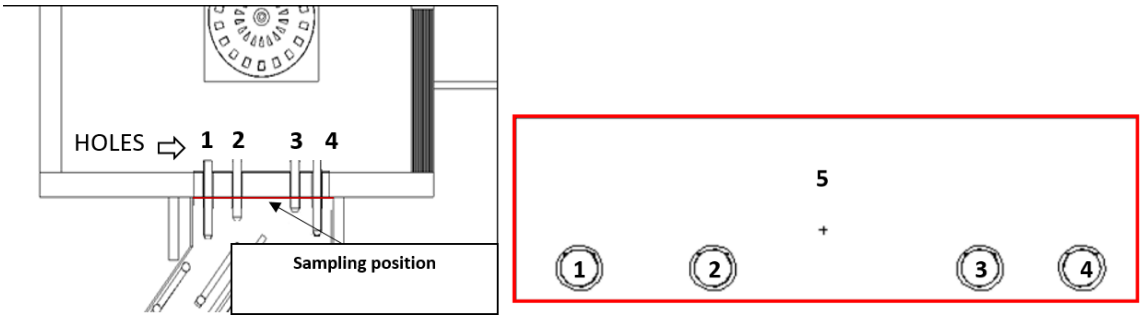

Figure 7-11 sampling position for the secondary sources: top view (left), frontal view (right)

In the second step a secondary neutron and gamma source has been created to propagate the neutrons up to the ECRH building. It has been compared to the calculation done with the plasma source to verify the effectiveness using the PTRAC reader from the MCNPTools package [79]. In fig. 7.12 a comparison between the

spectra calculated (7.12a) and angular distribution (7.12b) in the sapling positions with plasma source and with secondary neutron source is shown.

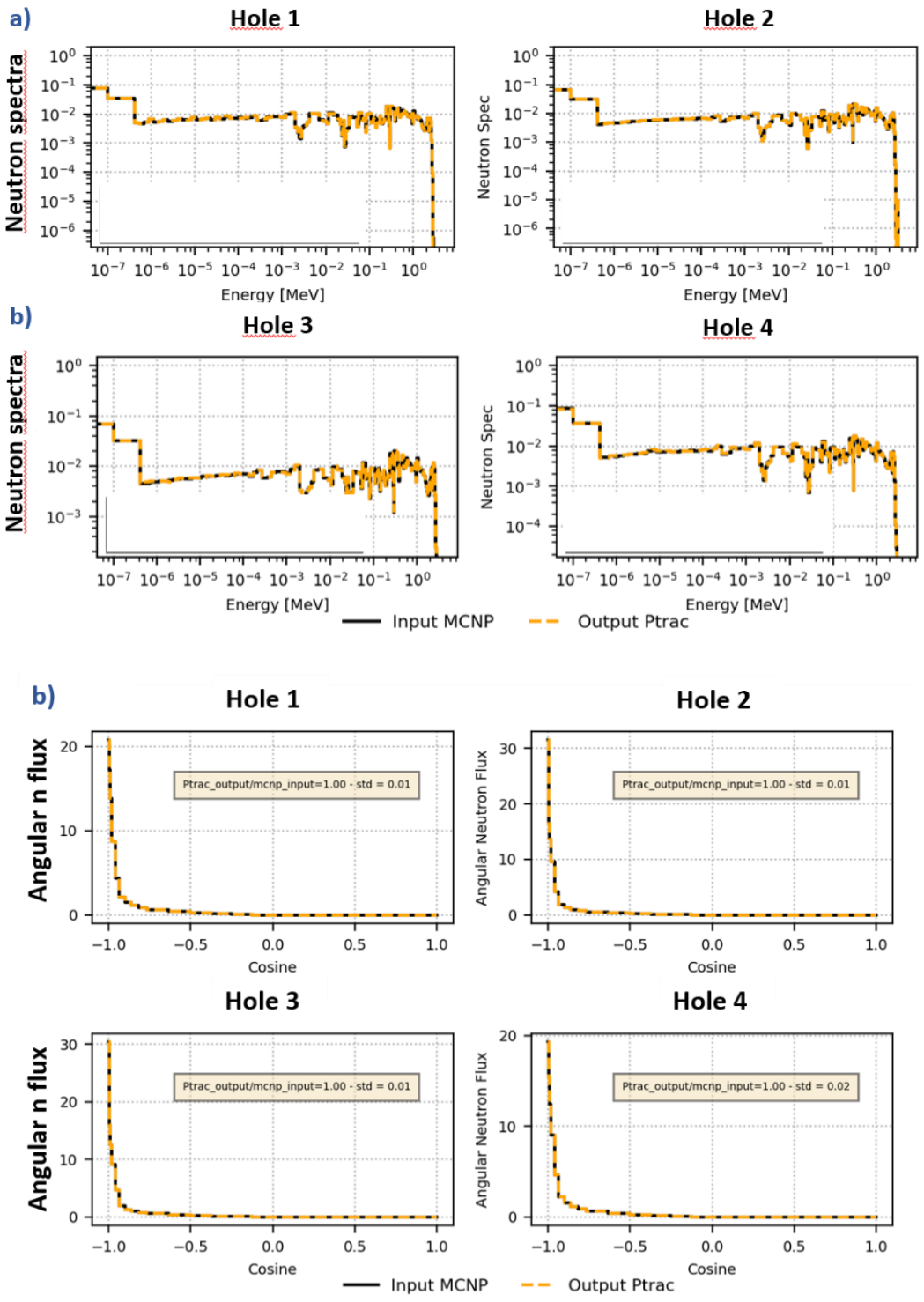

Figure 7-12 a) comparison between the spectra calculated with plasma source and II source; (b) angular comparison between calculation with plasma source and II source

Fig. 7.12 shows the very good agreement between the secondary source and the primary calculations done with the original 3D plasma source coupled with ADVANTG.

7.1.5 Results

Once the secondary neutrons and gamma source have been written, the calculations to assess the level of neutron and gamma fluxes and doses have been done with the configuration #2 described in previous paragraph.

The first evaluation with this configuration produced level of neutrons and gamma fluxes nearby the gyrotron buildings respectively up to 10^3 n cm^{-2} s^{-1} and up to 10^2 γ cm^{-2} s^{-1}. The effective dose is larger than 1 mSv/y, well above the limit.

In order to reduce the dose and to allow the personnel to enter and operate inside the ECRH building even during the operational phases, a 20 cm shielding gate made of 10 cm of polyethylene + 10 cm of concrete has been added inside the corridor. The configuration is shown in fig. 7.13.

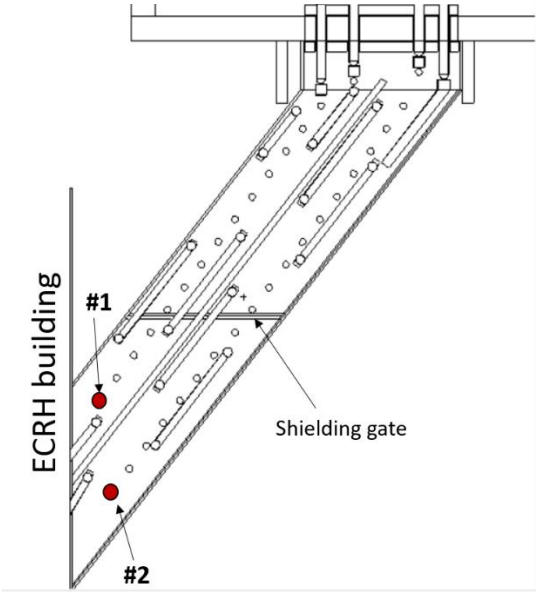

Figure 7-13 top view of the ECRH corridor with shielding gate and calculation position

Maps of neutron and gamma fluxes during operations with and without the shielding gate are shown in fig. 7.14 while the comparison of the level of effective dose in the two configurations is shown in fig. 7.15.

The shielding gate allows to reduce the nuclear quantities and the protection of the workers during operations. Table 7.1 shows the values of neutron and gamma fluxes and doses in the position pointed out in fig. 7.13 (#1 and #2), i.e. close to the gyrotron building.

The reduction of the fluxes in the rear zone of the ECRH building is larger than 2 orders of magnitude for the gamma flux.

Concerning the total annual effective dose rate, the reduction is larger than 2 orders of magnitude.

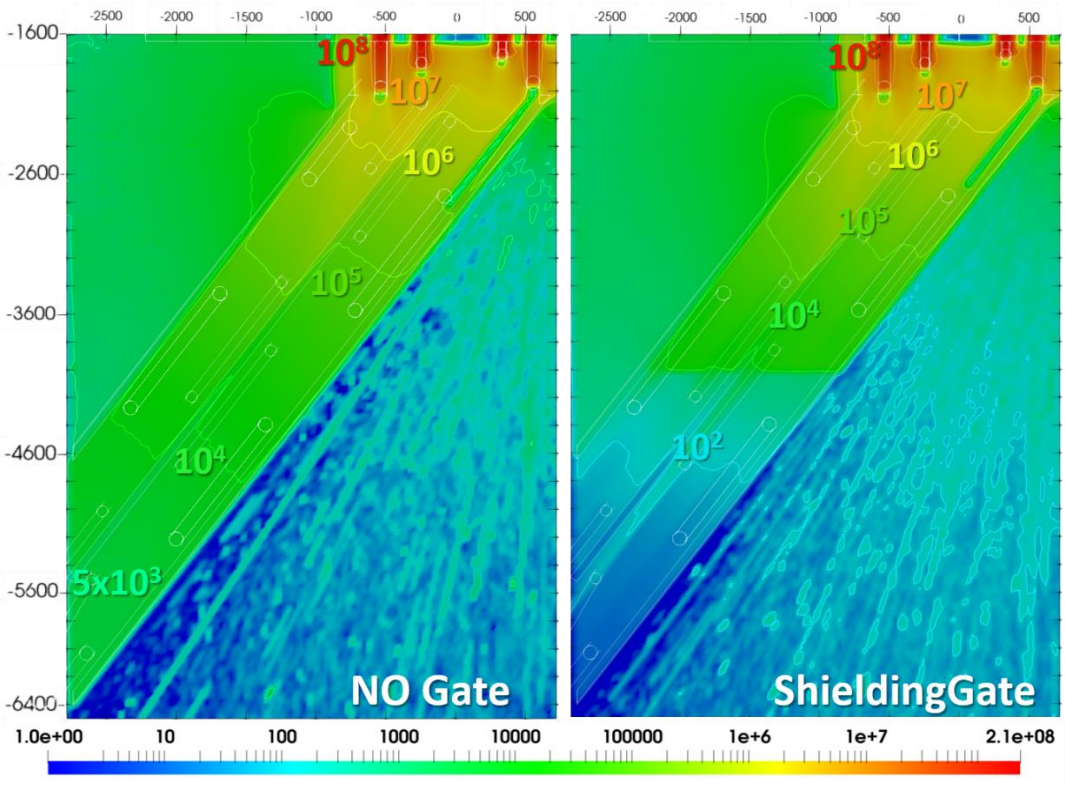

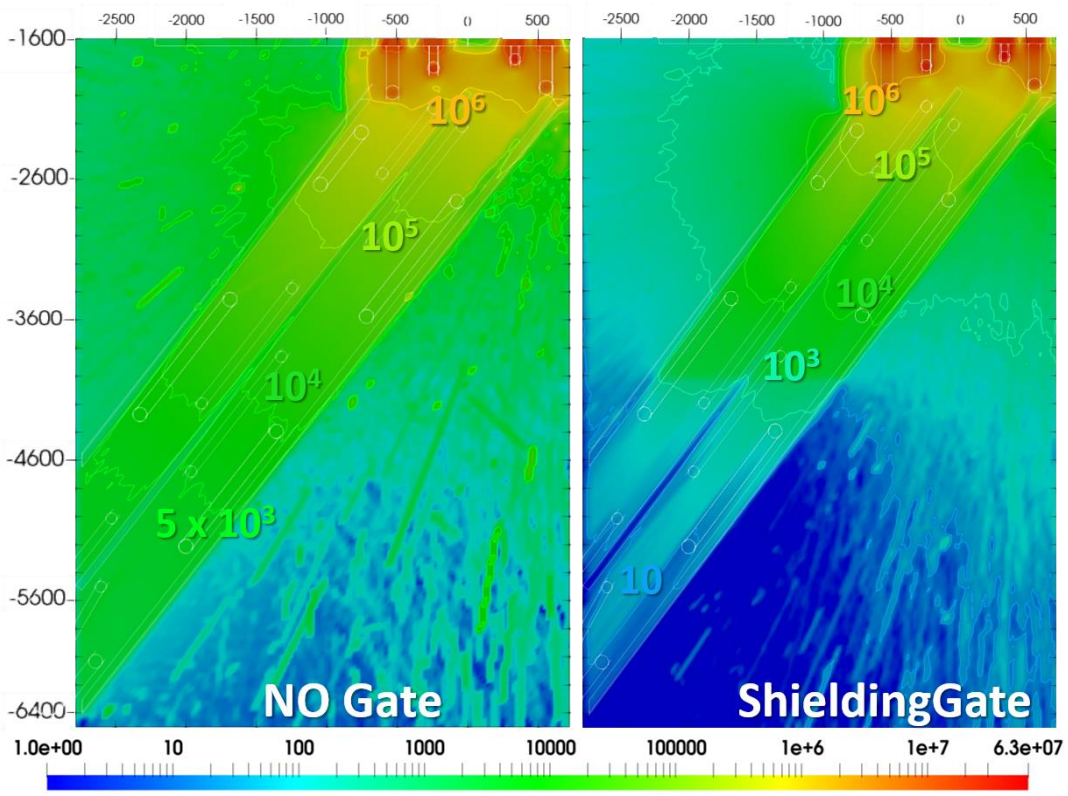

Figure 7-14 maps of neutron (up) and gamma (down) fluxes (1/cm^2/s) with and without the shielding gate inside the corridor

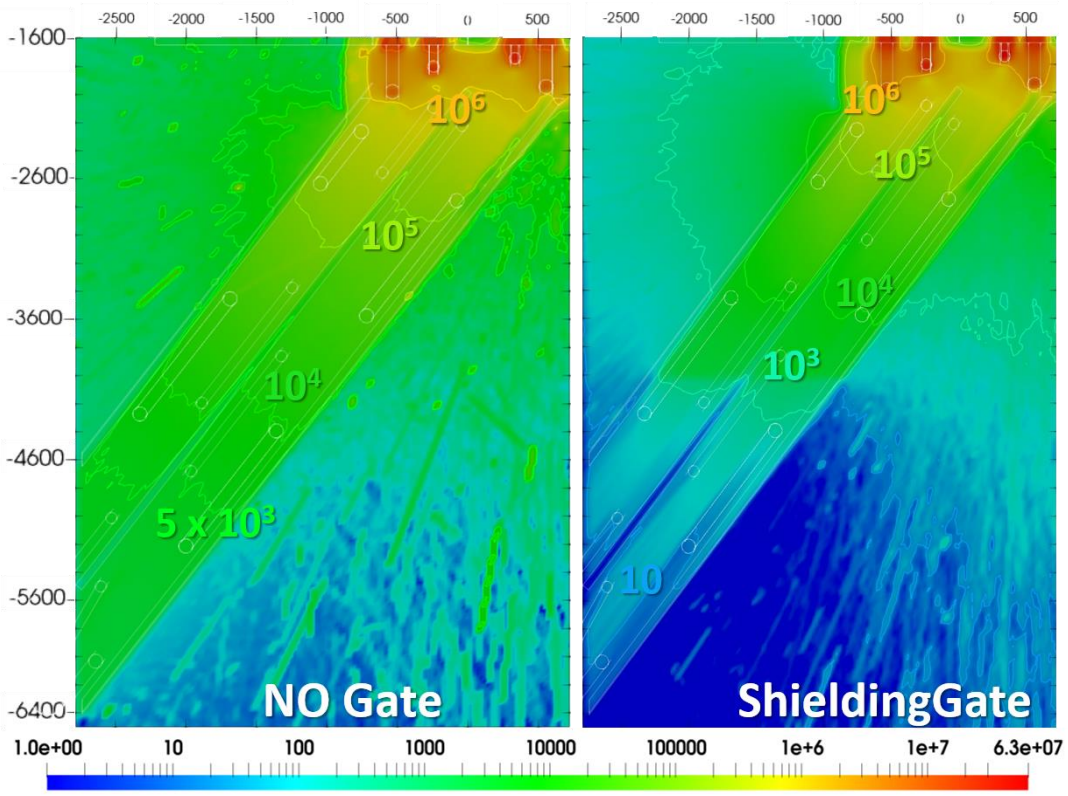

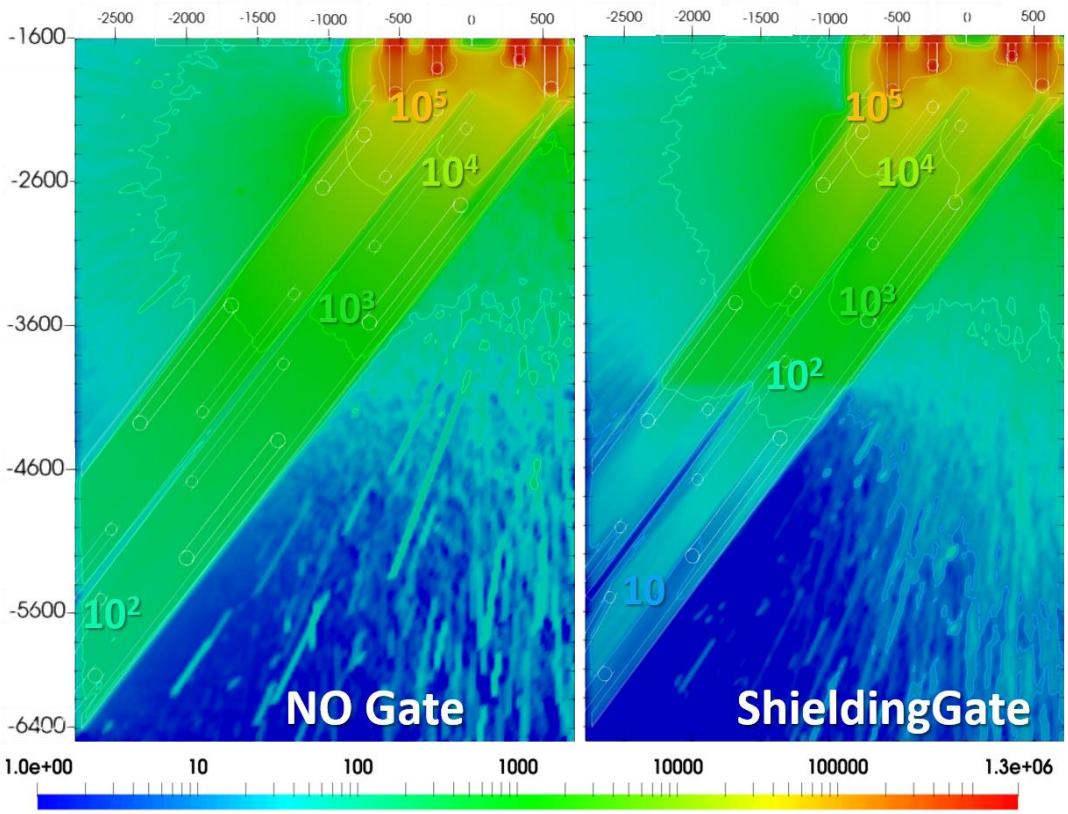

Figure 7-15 maps of neutron (up) and gamma (down) effective dose (μSv/y) with and without the shielding gate inside the ECRH corridor

Table 7-1 Values of neutron and gamma fluxes and effective annual dose rate in the position #1 and #2

	n flux (n/cm^2/s)		**γ flux (γ/cm^2/s)**		**Total eff. dose (μSv/y)**	
	No Gate	**Gate**	**No Gate**	**Gate**	**No Gate**	**Gate**
1	7.5 x 10^3	71	5.4 x 10^3	4 x 10^2	1.9 x 10^3	43
2	4 x 10^3	17	3.8 x 10^3	3 x 10^2	1.7 x 10^3	30

7.1.6 Evaluation of the SDDR inside the ECRH tunnel

Another important aspect for the nuclear design of the corridor concerns the level of shut down dose rate inside the tunnel. This evaluation is particularly important for the maintenance of the EC MBTLs.

The calculations has been don using the Advanced D1S ENEA code [29] using the II neutron source. The calculation has been settled in order to evaluate the SDDR 1 second after the DTT shutdown, i.e. considering the total expected DTT DD neutron yield at the end of its life: 3.73×10^{22} n.

The map of dose rate at 1 second after the shutdown is shown in fig. 7.16. The level of the SDDR can be considered sufficiently low to ensure the access in the corridor during off-operational periods. In fact it is well below the 10 μSv/h considered the design constraints for the maintenance operations (red contour line in the figure).

The contribution to the SDDR of the decay gamma streaming, coming from the activation of the components inside the THB, has been evaluated but it is marginal with respect to the direct activation (several orders of magnitude lower).

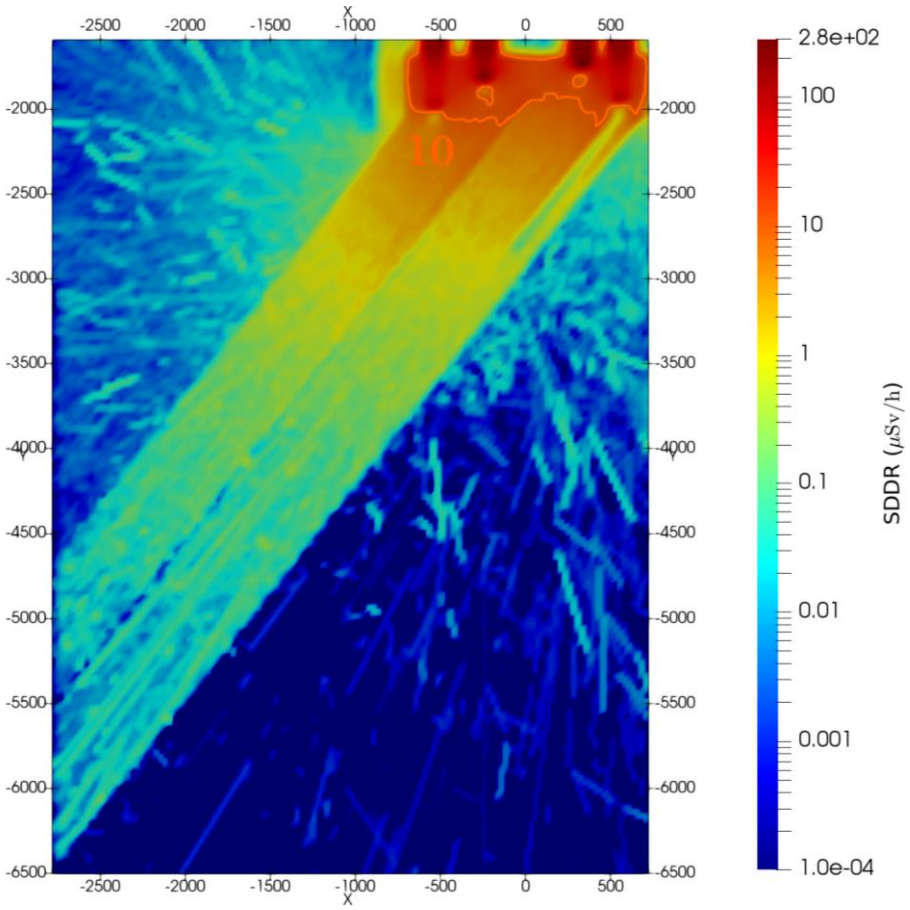

Figure 7-16 maps of shutdown dose rate 1 second after the shutdown at the end of DTT life

7.2 Neutronics analyses for the DTT east corridor

During the environmental survey for the DTT site layout, especially in the frame of the development of the new DTT THB, the necessity of a linking corridor between the existing FTU building and the new Torus Hall has been found. In the first evaluation, the new DTT THB, should have been connected directly to the existing FTU building by demolishing one FTU building wall.

For structural reasons, including seismic ones, it has been found that this coupling was not possible, so it has been decided to move the THB by 15 meters in the west direction and build a new corridor to connect the buildings.

This corridor is a crucial space for the site for the reason listed below:

- It is one of the entering points inside the THB at the ground level (i.e. 9.9 m from the basement of the Building);
- It is the passage area between the THB and the hot cell which contains the radioactive materials;
- It will host in an upper floor a diagnostic laboratory;
- It will host in a dedicated room the Fast Discharge Units (FDU) of the Toroidal Field coils. It has very strict requirements for the nuclear loads due to the neutrons and gammas effect on electronics which could induce the quenching of the magnets.
- It will host the Helium Transmission line coming from the cryogenic area placed in the far east side of the main building. It will cause large penetration through the east wall of THB that must be shielded.

An overview of this linking corridor is shown in fig. 7.17.

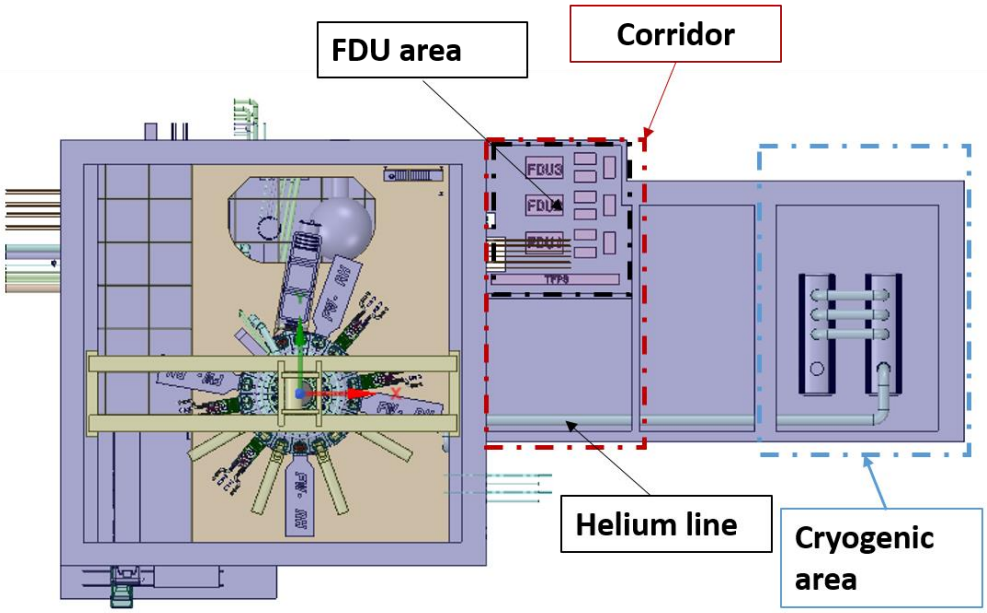

Figure 7-17 CAD top view of the DTT THB, connection corridor and cryogenic area

7.2.1 Radiation effects on electronic

The problem of radiation effects on electronic devices is of paramount importance in the nuclear facilities, accelerators and for the unmanned or manned spatial missions. [80], [81]

In a facility like DTT these effects can appear progressively due to the accumulated ionization or accumulated atomic displacements, or instantaneously, due to a single highly ionising particle.

Radiation effects on electronics could be divided into three main groups [82]:

- *The total ionizing dose (TID)*: this effect causes the threshold voltage MOS (Metal Oxidize Semiconductor) transistor to change because of trapped charges in the silicon dioxide gate insulator. For sub-micron devices these trapped charges could "escape" by tunnelling effects.
- *Displacement Damage*: the hadrons, thus neutrons, could induce displacements in atoms in the silicon lattice of active devices and thereby affect their functions. The total effects of different types of hadrons at

different energies are normalized to 1 MeV Neutrons using the NIEL (Non Ionizing Energy Loss) equivalent.

- *Single Event Effects (SEE)*: these kind of effects which are not cumulative as the previous explained effects. This effect regards the single event that could damage the electronics equipment and disturb the function of electronic circuits.

A *low-dose* environment doesn't mean that the electronics devices won't be damaged by the particles. Some experiences could be found in the conventional nuclear power plant. Near a fission reactor vessel, the ionizing dose produced by neutrons during a given time slot may be too low to induce significant damages in most of the semiconductors, whereas the atomic displacements produced by these particles can result in severe damages in most of the electronic and optoelectronic device using minority carriers.

In the same manner, *low-fluence* of ionizing particles or which can produce atomic displacements also doesn't mean no damage in electronics. In airplanes the natural environment radiation of cosmic origin generally doesn't induce significant damage in electronics. Anyway, the small amount of high energy particles contained in this environment have a significant probability of corrupting the electronic circuits. Concerning the neutrons issues, the industrial standards for these electronics have been produced be integrated circuits manufacturers [83] and flight equipment manufacturers of the aircraft industries [84] to establish good practices of design and test of semiconductor and circuits.

The maximum fluxes considered to produce these requirements are several orders of magnitude larger with respect to those in a nuclear fusion machines like DTT (i.e. up to 10^{10} n/cm^2/s in rear zone of the cryostat).

Concerning the DTT tokamak complex, inside or outside the THB, the electronics play an important role and it can be divided in *critical* and *non-critical* electronics. The first one is the electronics which are involved in nuclear safety functions, occupational safety functions, investment protection functions, and those systems whose failure will cause loss of plasma operations. Other critical electronics are those diagnostics which are mandatory for the tokamak functioning. Other electronics is classified as *non-critical*.

Exposing electronics devices to severe radiation environment implies significant risk of failure for the Commercial Off the Shelve (COTS) unless the radiation-hard electronics is used. Anyway, the rad-hard electronics is difficult to use for the high cost and for the qualification difficulties.

7.2.2.1 ITER threshold for critical – noncritical electronics

The International Thermonuclear Experimental Reactor (ITER), after many years of research and experiments, considering the different critical areas of its layout set the thresholds explained in [85] and summarized below:

- For the critical electronics:
  - Accumulated dose (whole machine life): 1 Gy
  - Neutron Flux : 10^{-2} n/cm^2/s (natural background)
  - Accumulated neutron fluence: 10^8 n/cm^2 (1 MeV Si eq. n/cm^2)
- For non-critical electronics:
  - Accumulated dose (whole machine life): 10 Gy
  - Neutron Flux : 10^2 n/cm^2/s (natural background)
  - Accumulated neutron fluence: 10^{10} n/cm^2 (1 MeV Si eq. n/cm^2)

For DTT these levels have been used as a reference in the electronics shielding analyses.

7.2.2 Shielding analyses for the FDU area

The position chosen for the FDU area, showed in fig. 7.17, is on the east side of the tokamak building and a passage area through the east wall dimensions 3.5 x 4 m has been opened (actual configurations in fig. 7.18a). The streaming through this opening, considering the high-performance phase, is relevant for several reasons related to the licensing procedure and site layout.

Concerning the licensing, have such an opening in the THB means that the level of the doses inside the corridor could be significantly high and supporting neutronics calculations are fundamental for the zone classifications.

The shape of the corridor underwent several updates during the design process considering the shielding needs (materials, thicknesses required) for the FDU area.

Moreover, the Helium penetration (fig. 7.18b) has a big impact on the level of neutron and gamma fluxes and doses, thus must be shielded to mitigate the streaming.

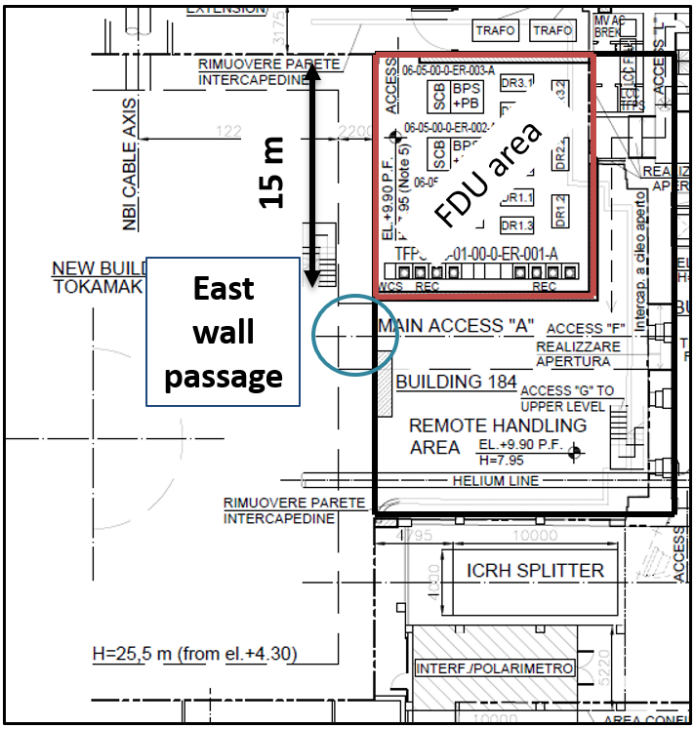

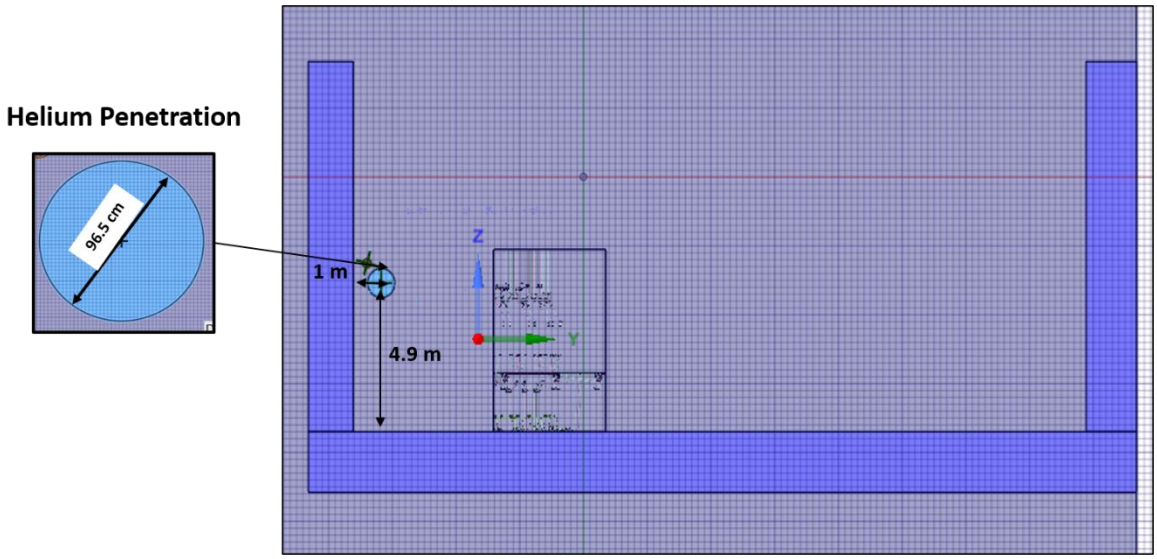

Figure 7-18 **a**) position of the openings between the THB and connection corridor. **b)** frontal layout of the east wall of DTT THB

7.2.3 Streaming evaluation through the door

The first evaluation of the level of fluxes and doses has been done with primitive layout of the corridor were the FDU area was smaller, but very similar, than the present one, but very similar to the present one. Maps of neutron and gamma fluxes without any shielding are shown in figure 7.19 for the openings quote and Helium penetration quote and in figure 7.20 maps of neutron and gamma annual effective dose is shown.

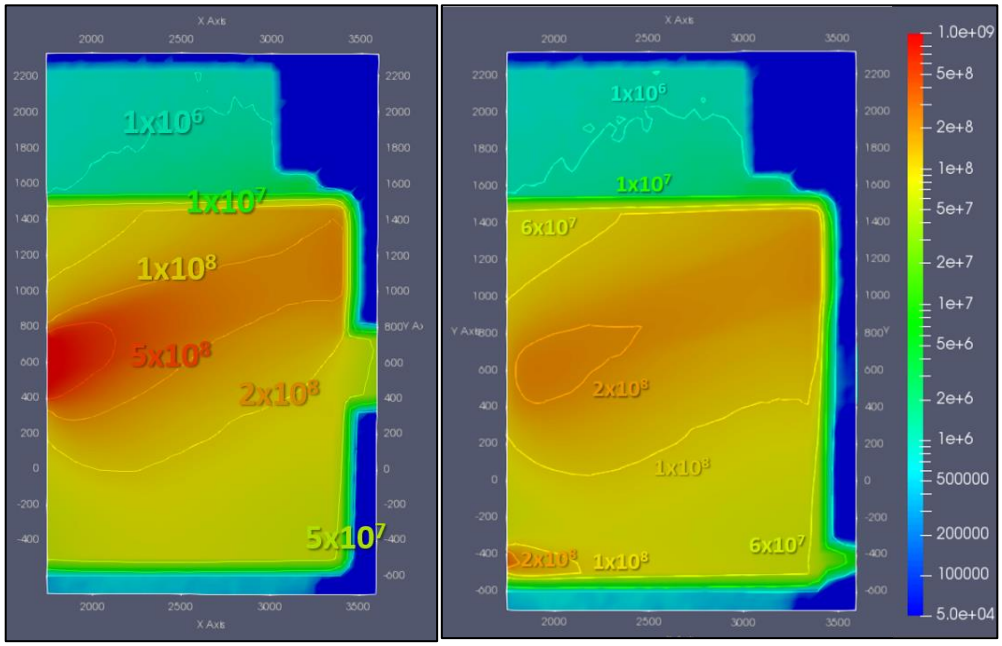

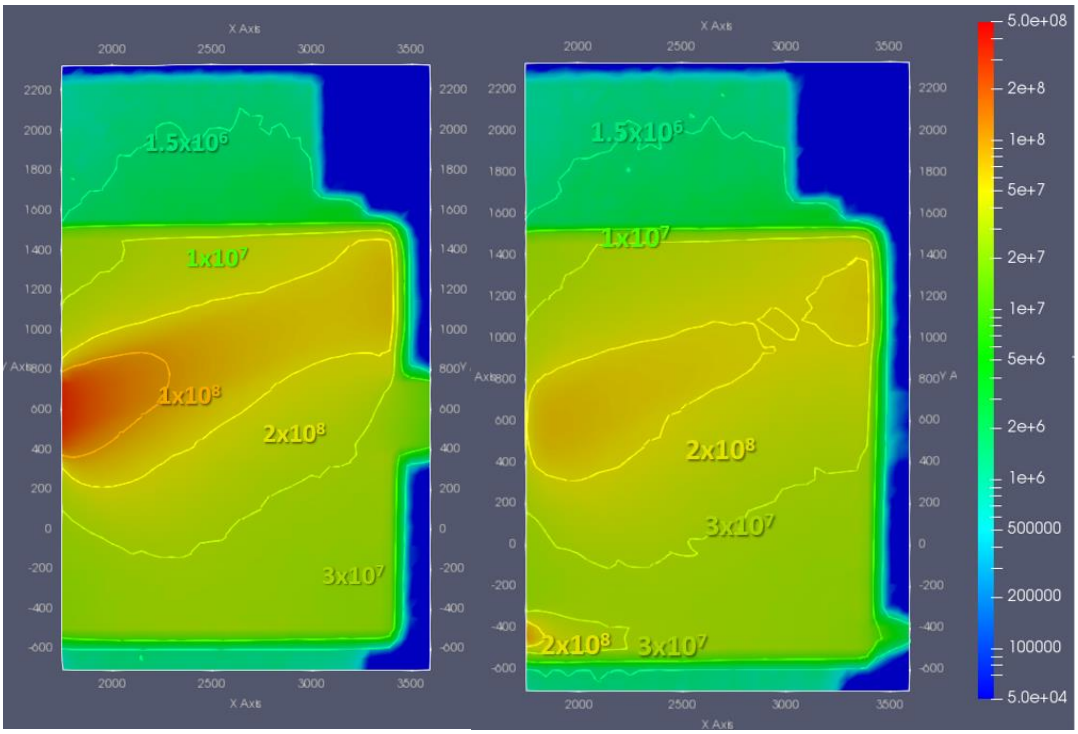

Figure 7-19 **up)** maps of neutron flux (n cm^{-2} s^{-1}), **bottom)** maps of gamma flux (g cm^{-2} s^{-1}) in at penetration quote and at Helium quote

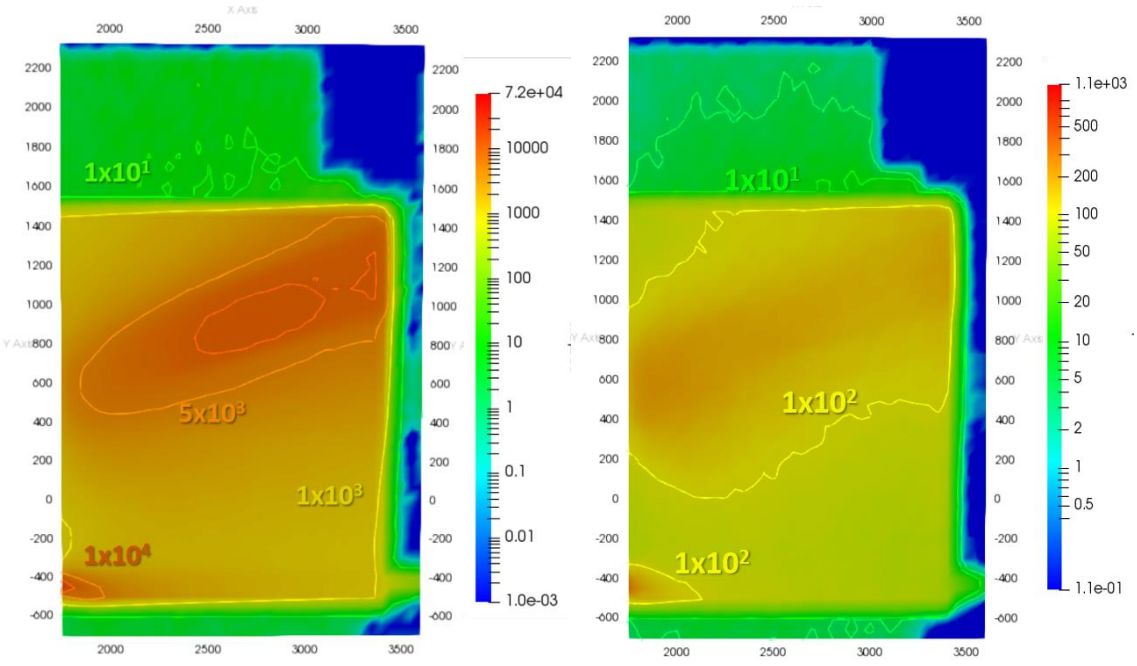

Figure 7-20 maps of neutron (left) and gamma (right) annual effective dose rate (uSv/y) at Helium penetration quote without any shielding

As it can be seen from the maps, the streaming in the corridor zone is extremely high during operations. The neutron flux reaches values up to $9x10^8$ n/cm^2/s close to the opening and $8x10^7$ n/cm^2/s in rest of the corridor. The FDU area, in the north

part of the corridor reaches values of about 10^6 n/cm^2/s, too high for the critical electronics. Gamma fluxes ranging between $2x10^8$ γ/cm^2/s, close to the openings and $1.3x10^6$ γ/cm^2/s. The total effective dose, in terms of μSv/y, considering both neutrons and gammas reaches values of about $6x10^8$ μSv/y and is mainly due to the neutrons. Seven representative positions showed in fig. 7.21, have been chosen and the relative values in tab. 7.1 with no shields and no doors.

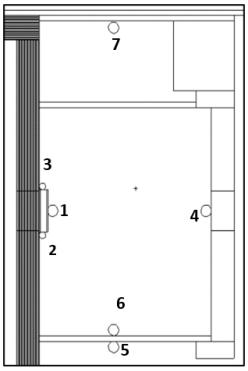

Figure 7-21 calculation positions

Table 7-2 neutron and gamma fluxes and annual effective dose in position selected

Position	n_flux (n/cm2/s)	n_eff_dose (uSv/y)	g_flux (g/cm2/s)	g_eff_dose (uSv/y)
1	$9.27x10^8$	$5.72 x10^8$	$2.37 x10^8$	$7.65 x10^6$
2	$2.53 x10^8$	$5.47 x10^7$	$8.27 x10^7$	$2.76 x10^6$
3	$3.11 x10^8$	$1.02 x10^8$	$1.02 x10^8$	$3.41 x10^6$
4	$8.92 x10^7$	$3.02 x10^7$	$2.93 x10^7$	$8.96 x10^5$
5	$4.87 x10^5$	$3.58 x10^4$	$1.20 x10^6$	$5.14 x10^4$
6	$7.46 x10^7$	$1.15 x10^7$	$2.63 x10^7$	$8.28 x10^5$
7	$8.90 x10^5$	$4.34 x10^4$	$1.34 x10^6$	$4.54 x10^4$

These very high values in the table showed that a proper shielding door is mandatory for the radiation protection constraints and for the electronics protection.

7.2.4 Shielding door evaluations

To choose the best shielding performances for the door three different configurations have been considered by evaluating not only the impact of the thickness and composition but also the width and eight of the doors.

The configurations studied are shown in fig. 7.22 with relative properties:

Composite Door

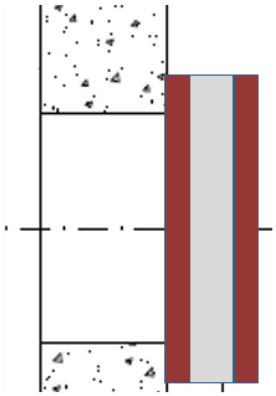

- **5 cm of SS** (7.93 g/cm3)
- **70 cm of Poly** (0.94 g/cm3)
- **5 cm of SS** (7.93 g/cm3)

Dimensions

- 410 x 80 x 450 cm
- V= 1.476x 10^7 cm^3
- 29383 kg

Concrete Door

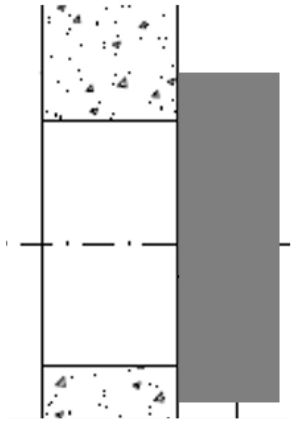

- **100 cm of normal concrete** (2.2 g/cm3)

Dimensions

- 410 x 100 x 450 cm
- V= 1.845x 10^7 cm^3
- 44550 kg

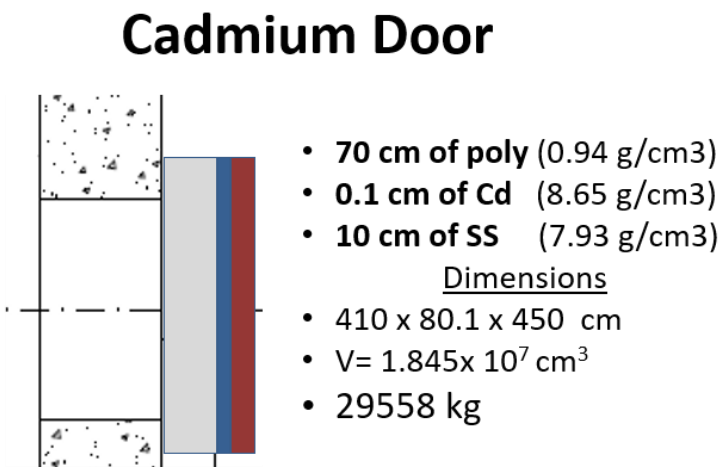

Figure 7-22 composition of the door considered

With those three configurations the calculations showed in the previous paragraph have been repeated in order to evaluate the shielding performances. Results of these calculations are shown in tables 7.2, 7.3 and 7.4 for the positions in fig 7.21.

Table 7-3 neutron and gamma fluxes and annual effective dose rate for composite door

Pos.	n_flux (n/cm2/s)	n_eff_dose (μSv/y)	γ_eff_dose (μSv/s)	γ_eff_dose (μSv/y)
1	1.36×10^{6}	2.24×10^{5}	1.38×10	1.41×10^{5}
2	2.69×10^{6}	3.45×10^{5}	2.22×10	2.26×10^{5}
3	2.55×10^{6}	3.79×10^{5}	4.76×10	4.86×10^{5}
4	1.10×10^{6}	2.10×10^{5}	1.44	1.47×10^{4}
5	1.40×10^{4}	8.57×10^{2}	1.48×10^{-1}	1.51×10^{3}
6	4.37×10^{6}	1.19×10^{6}	4.45	4.54×10^{4}
7	8.47×10^{3}	5.20×10^{2}	9.25×10^{-2}	9.43×10^{2}

Table 7-4 neutron and gamma fluxes and annual effective dose rate for concrete door

	100 cm concrete door			
Position	n_flux (n/cm2/s)	n_eff_dose (μSv/y)	γ_eff_dose (μSv/s)	γ_eff_dose (μSv/y)
1	2.87×10^{6}	4.54×10^{5}	4.75×10^{6}	2.05×10^{5}
2	5.12×10^{6}	4.96×10^{5}	9.72×10^{6}	3.92×10^{5}
3	1.03×10^{7}	1.37×10^{6}	1.86×10^{7}	8.05×10^{5}
4	1.05×10^{6}	2.09×10^{5}	7.22×10^{5}	2.53×10^{4}
5	1.17×10^{4}	6.81×10^{2}	5.83×10^{4}	3.95×10^{3}
6	4.10×10^{6}	1.17×10^{6}	2.84×10^{6}	5.69×10^{4}
7	9.88×10^{3}	6.58×10^{2}	1.75×10^{4}	1.37×10^{3}

Table 7-5 neutron and gamma fluxes and effctive dose for the Cd door

	Cd door			
Pos	n_flux (n/cm2/s)	n_eff_dose (uSv/y)	γ_eff_dose (μSv/s)	γ_eff_dose (μSv/y)
1	1.21×10^{6}	2.17×10^{5}	2.48×10^{6}	1.15×10^{5}
2	2.25×10^{6}	2.93×10^{5}	1.48×10^{7}	4.30×10^{5}
3	1.84×10^{6}	2.09×10^{5}	2.58×10^{7}	7.65×10^{5}
4	1.01×10^{4}	1.95×10^{5}	4.58×10^{5}	1.53×10^{4}
5	1.15×10^{4}	6.59×10^{2}	3.52×10^{4}	1.33×10^{3}
6	4.09×10^{6}	1.24×10^{6}	1.31×10^{6}	4.15×10^{4}

7	7.25×10^{3}	4.43×10^{2}	1.14×10^{4}	3.64×10^{2}

The configuration named *Cadmium door* has the best shielding performances compared to the other door configurations. It reduces the level of neutron flux and gamma fluxes of more than two orders of magnitude and the annual effective dose rate of about one order of magnitude.

Regarding the absorbed dose rate in Silicon, used to evaluate the total ionizing dose (TID) in electronics, it has been calculated through an F4 tally with proper multiplier. The maximum value of cumulated dose in Silicon over the whole DTT life, calculated using the expected DTT DD neutron production of 3.73×10^{22} n, is up to 30 Gy inside the bottom part of the corridor and, in the FDU area is 1.3×10^{-2} Gy, well below the ITER reference limit for the critical electronics. The level of neutron flux, around 7×10^{3} n/cm^2/s, is anyway not acceptable for the electronics devices.

7.2.5 Shielding optimization with actual configurations

According to the evolution of the layout of the site and to the analyses of the space needed for the FDU the internal space of the corridor has been changed (figure 7.23). The upper part is completely dedicated to the Fast Discharge Units. Beside this area, on the right, there is a little space needed for the passage through the ex FTU building inside the hot cell. The configuration of the Helium line has been not changed. The bottom part of the corridor should be left available for the Remote Handling (RH) operations and, during the DTT pulse, the entrance in this area is not allowed for the high level of effective dose. Considering this new internal layout, new calculations have been done in order to optimize the shielding in the FDU area with the aim at reducing the neutron fluxes in the upper part of the corridor.

Presently the FDU area is protected from the streaming during operation by ordinary concrete and polyethylene. In particular, in the south part 40 cm of

polyethylene plus 70 cm of concrete is foreseen and from the THB side has been decided to cover the internal wall with a 30 cm layer of poly in addition to the 220 cm of ordinary concrete of the THB wall. For the first the roof of the corridor is a 30 cm layer of ordinary concrete.

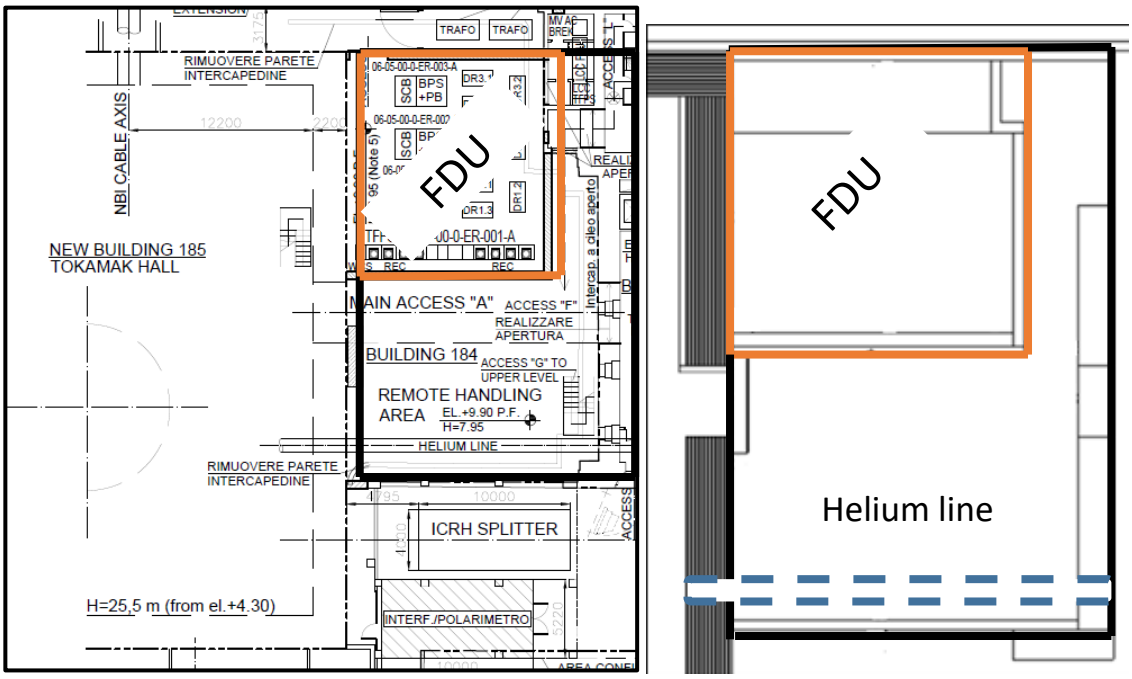

Figure 7-23 CAD layout of the corridor (left) and MCNP model (right)

This shielding configuration is not sufficient to reach an acceptable level of neutron fluxes in FDU zone which reaches values around the 10^4 n/cm^2/s, as shown in figure 7.24

From the maps of neutron fluxes is clear that some contributions have significant effects on the nuclear loads inside the FDU area. The first contribution comes from the Helium penetrations where the neutron flux is up to 10^8 n/cm^2/s nearby the hole; it affects the lateral side of the FDU area where the streaming is up to 10^5 n/cm^2/s. The second one arises from the ceiling of the corridor, up to 10^2 n/cm^2/s.

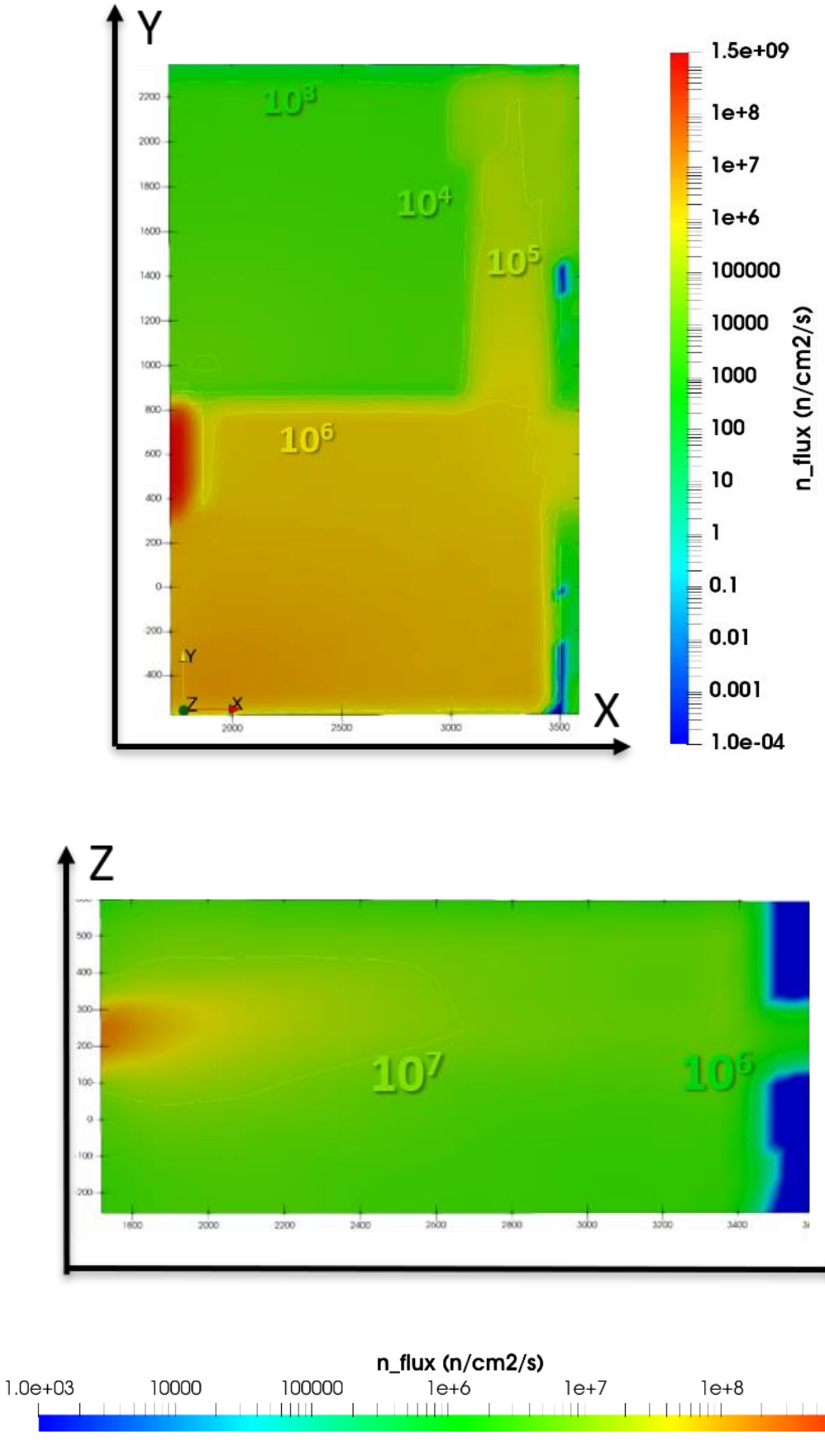
Y
X
Z
10^3
10^4
10^5
10^6
10^7
10^5
1.5e+09
1e+8
1e+7
1e+6
100000
10000
1000
100
10
1
0.1
0.01
0.001
1.0e-04
n_flux (n/cm2/s)
n_flux (n/cm2/s)
1.0e+03
10000
100000
1e+6
1e+7
1e+8
1.5e+09

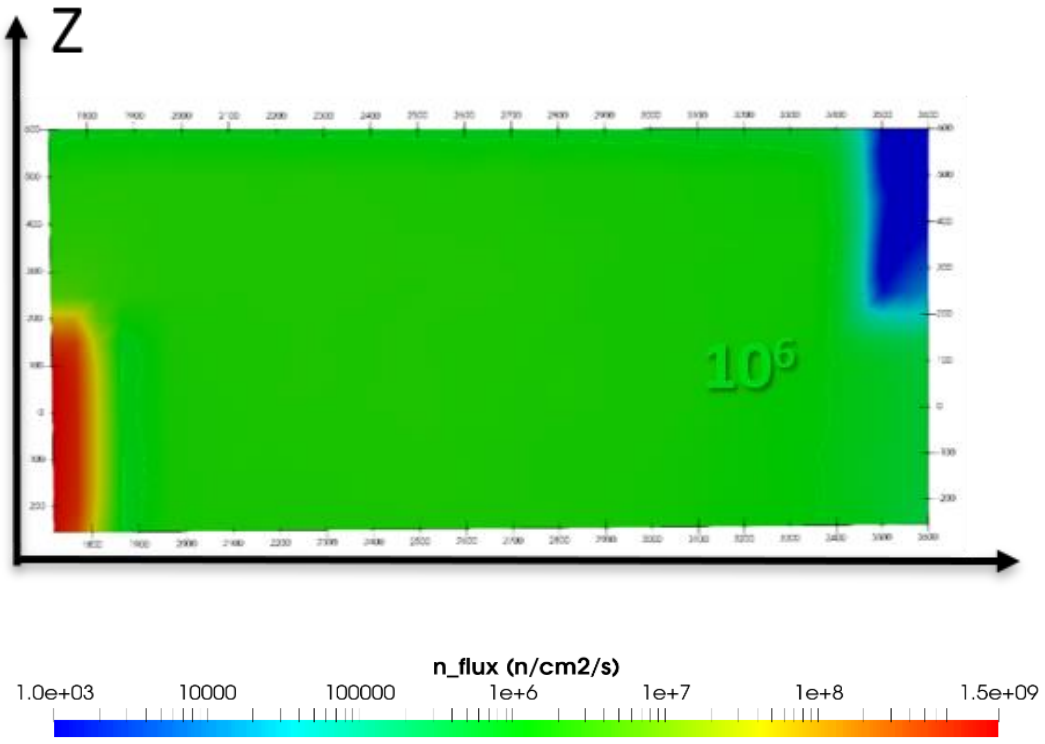

Figure 7-24 neutron flux map inside the corridor: top view (Top), Helium line lateral view (middle) and door lateral view (bottom)

The third contribution comes from the door streaming and the last contribution, even though it is a minor contribution, comes from the openings in the THB building wall.

Every contributes have been studied and evaluated by killing the particles (0 importance settled in MCNP model) in the zone around the FDU area in order to quantify the streaming effect. These studies are not reported in this dissertation.

Taking into account all these effects a new and optimized shielding configuration has been presented and it's shown in fig 7.25. It features the Cadmium door presented in the previous paragraph, 30 cm layer of polyethylene inside the THB opening before the door, an increase thickness of the roof (50 cm) and 50 cm of shielding gate in the right part of the FDU area composed by 25 cm of polyethylene + 25 cm of ordinary concrete. Furthermore, the dimension of the door has been

enlarged with respect to those showed in par. 7.2.4, in order to reduce the contribution from the door.

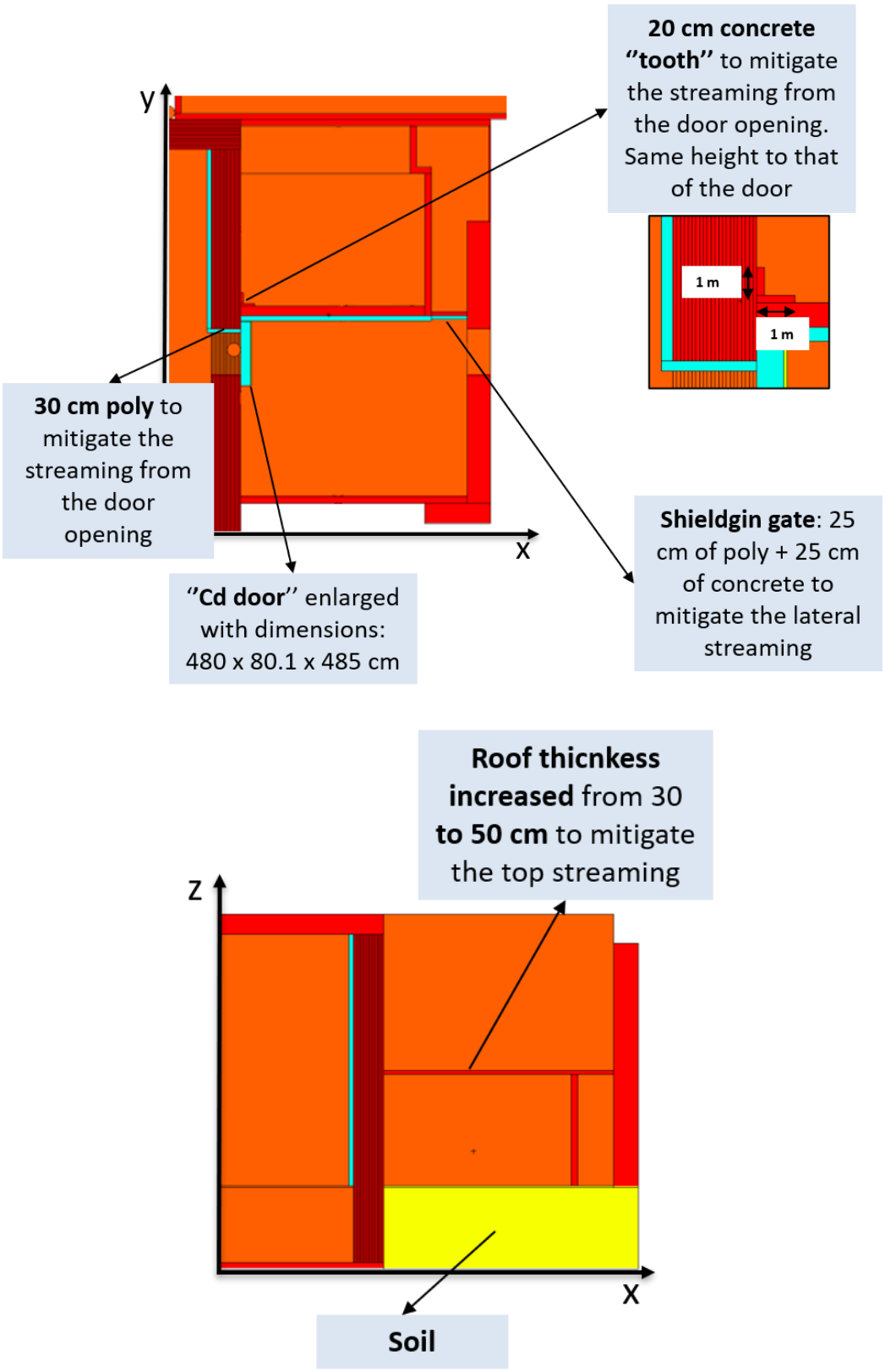

Figure 7-25top view (top) and lateral view (bottom) of the new shielding configuration layout

The shape of the helium line has been modified in with a short dog-leg and by adding a composite shield around made by 10 cm of polyethylene in the internal part and 10 cm of concrete: it is shown in figure 7.26.

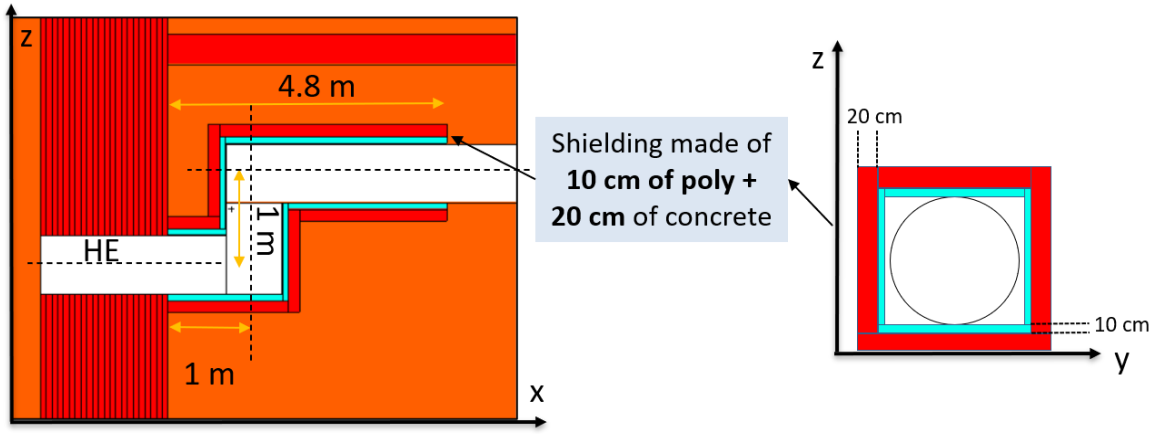

Figure 7-26 Dogleg configuration of the Helium line: lateral view (left) and frontal view (right)

The neutron flux in the FDU area is shown in the maps in figure 7.27-28-29 compared to the configuration with no additional shielding.

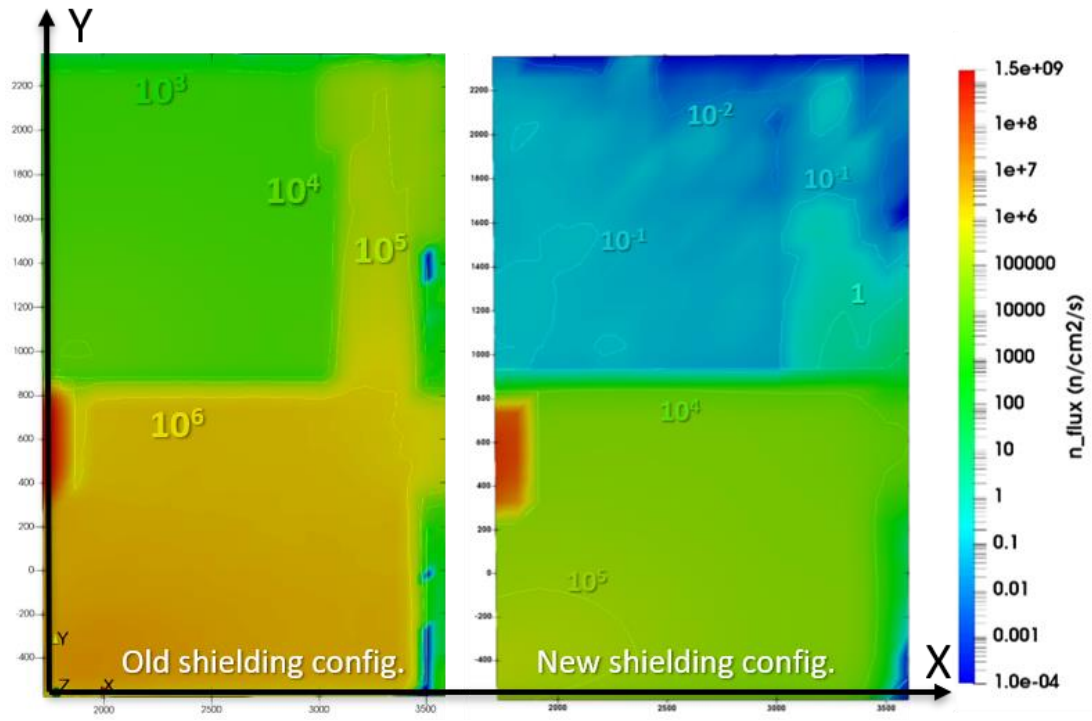

Figure 7-27 comparison of the neutron flux distribution map in the corridor zone with old and new configuration

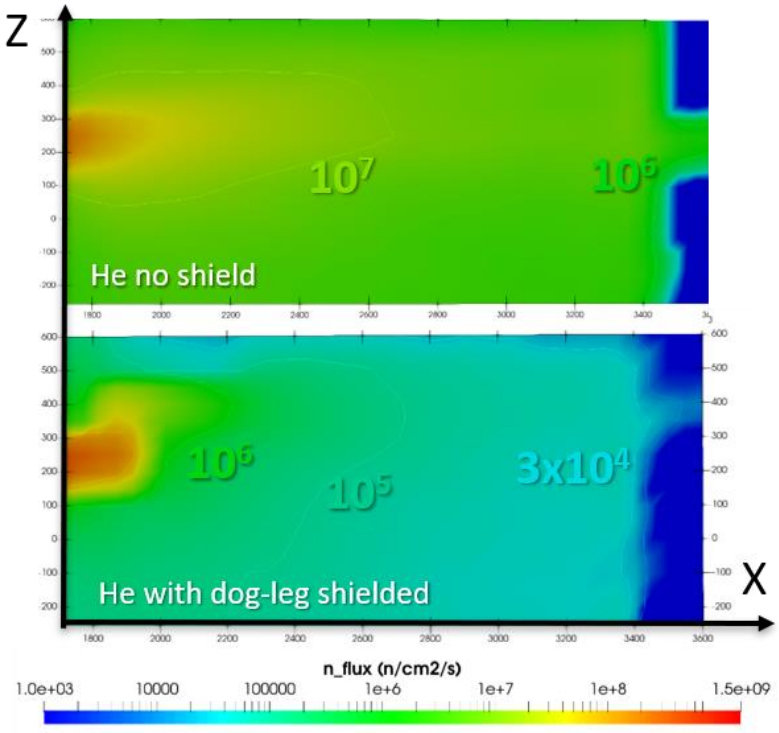

Figure 7-28 comparison of the neutron flux distribution map in the corridor zone - He section with old and new configuration

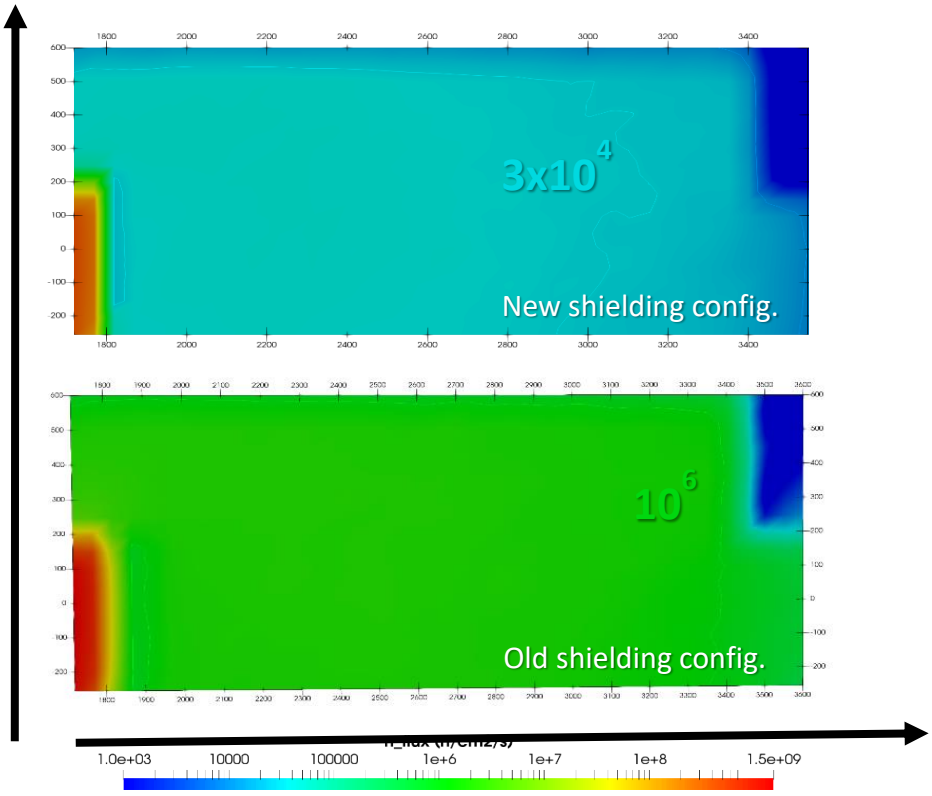

Figure 7-29 comparison of the neutron flux distribution map in the corridor – XZ section at door with old and new configuration

In the table n. 7.5 values of neutron and gamma fluxes are shown for the position showed in fig. 7.30. This configuration allows a sensible reduction of the fluxes inside the FDU room. It reduces the values of fluxes by more than five orders of magnitude, and the maximum value is recorded in pos. #4 where it is 9.5×10^{-2} n/cm^2/s, value very close to the ITER limits.

Regarding the cumulated dose in Silicon, a very low level, well below the 1 Gy cumulated over the whole DTT life, can be assumed considering the calculations shows in paragraph 7.2.4 where the gamma fluxes were two orders of magnitude higher than those calculated with this last configuration layout. In that case the level of cumulated dose rate was well below the 1 Gy thus in this case dose rate in Silicon could be considered negligible.

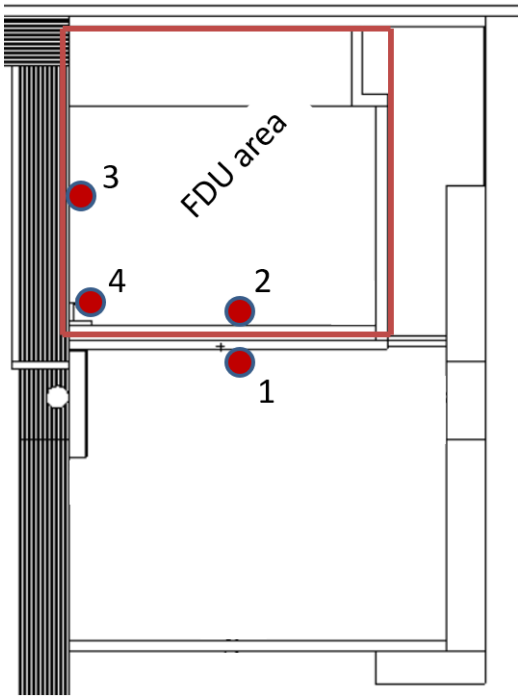

Figure 7-30 Calculation position for the new configuration

	Neutron flux (n/cm2/s)	**Gamma flux (g/cm2/s)**
1	3.5×10^{4}	3.5×10^{5}
2	8.8×10^{-2}	1.37×10^{2}

3	7.9×10^{-2}	2.47×10^{2}
4	9.5×10^{-2}	9.1×10^{2}

This shielding configuration allows, with some little risks, to respect the values pointed out by ITER for the critical electronics in the FDU area. Anyway, further studies is still foreseen to optimize the dimension of the shield proposed according to the evolution of the machine and the site layout.

8 Nuclear analysis for ECRH Equatorial launchers

"Everything is theoretically impossible, until it is done"

R.A. Heinlein

The activity of neutronics analyses for DTT also foresees the technical integration of the components inside the DTT ports. These components may regard the diagnostics, the HCD launchers (ICRH and ECRH), the pumps and some remote handling components.

These devices have to face up a harsh nuclear environment, especially in high performance phase, where the neutron and gamma fluxes are significantly high and induce some effects, described in chapter 1, which could be worsen the systems functioning and the materials of which they are composed of.

In particular, the nuclear heating (NH) is the main effect which could be critical for the DTT integrated systems and must be quantified.

The activation and the shutdown dose rate are, at the same time, of paramount importance for the maintenance of these components and for the management of their transport outside the THB. This involves the calculation of the contact doses rate generated by the activation of the materials under irradiation, mandatory to accomplish the remote handling needs.

In this chapter the integration of the ECRH launchers will be described and discussed in particular for the equatorial launcher. The layout of this components

is, indeed, at an advanced stage and is suitable for the nuclear integration inside the machine.

For this analysis the 20° DTT MCNP detailed model, described in chapter 3 has been used. This model is more suitable than the 360° simplified model for these types of analyses because it has detailed reproduction of the ports with all the components inside and gives a better representation of the nuclear fields in the integration zone.

8.1 Nuclear loads inside the cryostat

Evaluations of the nuclear loads inside the cryostat has been done by means of the 20° DTT neutron models. These analyses were done to support the project of the machine itself by calculating the loads on the magnets, the shielding needs and for many other issues regardengd the development of the DTT in-cryostat structures.

All these analyses are reported in [39] and the following figures report the maps of neutron and gamma fluxes inside the ports (figure 8.1 & 8.2)

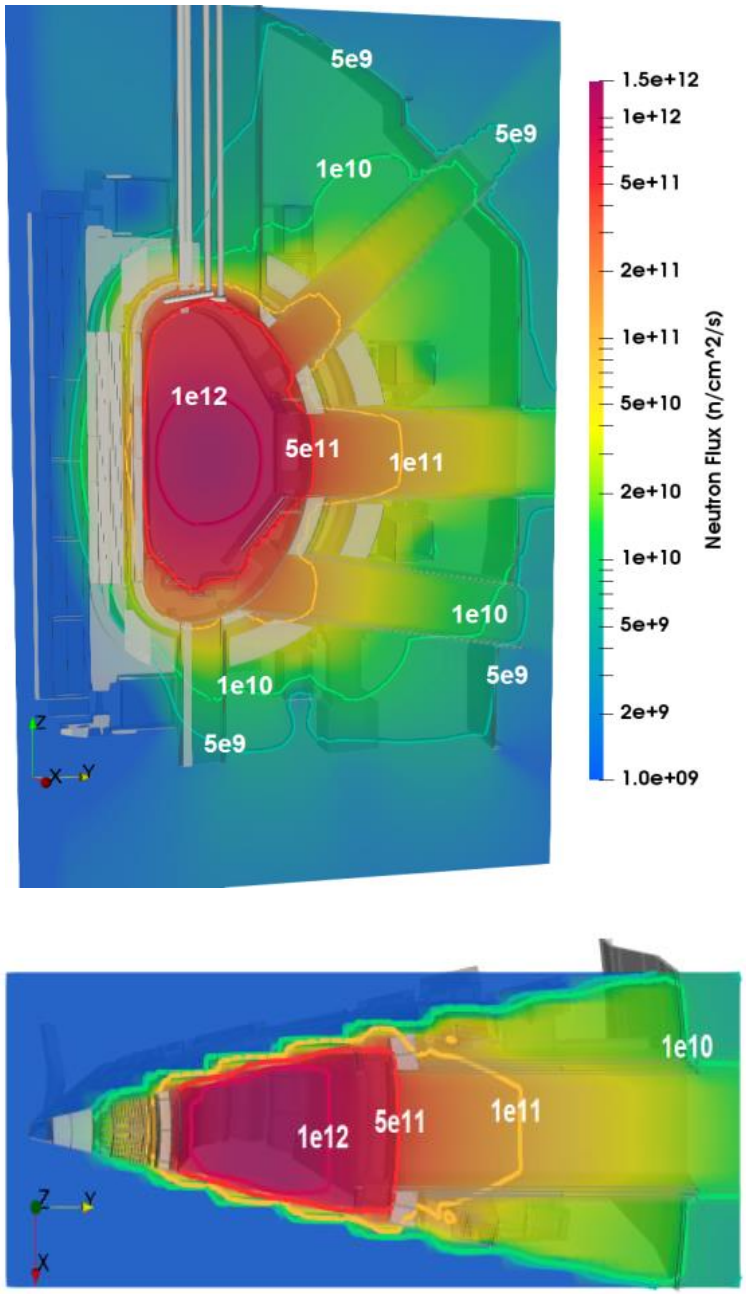

Figure 8-1 Maps of neutron fluxes inside the cryostat for Y=0 section (up) and equatorial section (down)

Neutron DD fluxes presents its maximum in the equatorial plane ranging between $5x10^{11}$ n/cm^2/s in the FW to $1x10^{10}$ n/cm^2/s in the cryostat zone also considering the 1% of DT production.

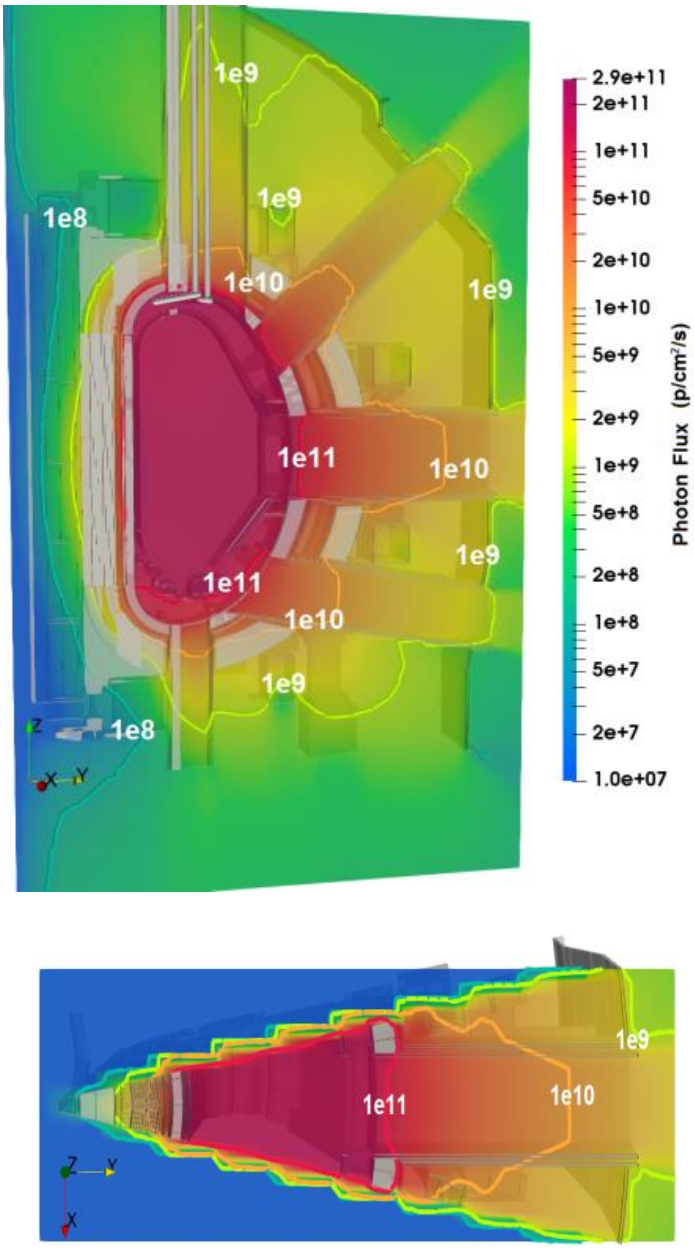

Figure 8-2 Maps of gamma fluxes inside the cryostat for Y=0 section (up) and equatorial section (down)

Gamma fluxes also have the maximum values in the equatorial plane and vary from $1x10^{11}$ γ/cm²/s to $1x10^{9}$ γ/cm²/s in the rear zone of the cryostat.

Figure 8.3 shows the radial profile at the mid-plane in high performance phase for the central and lateral section for neutron and gamma fluxes.

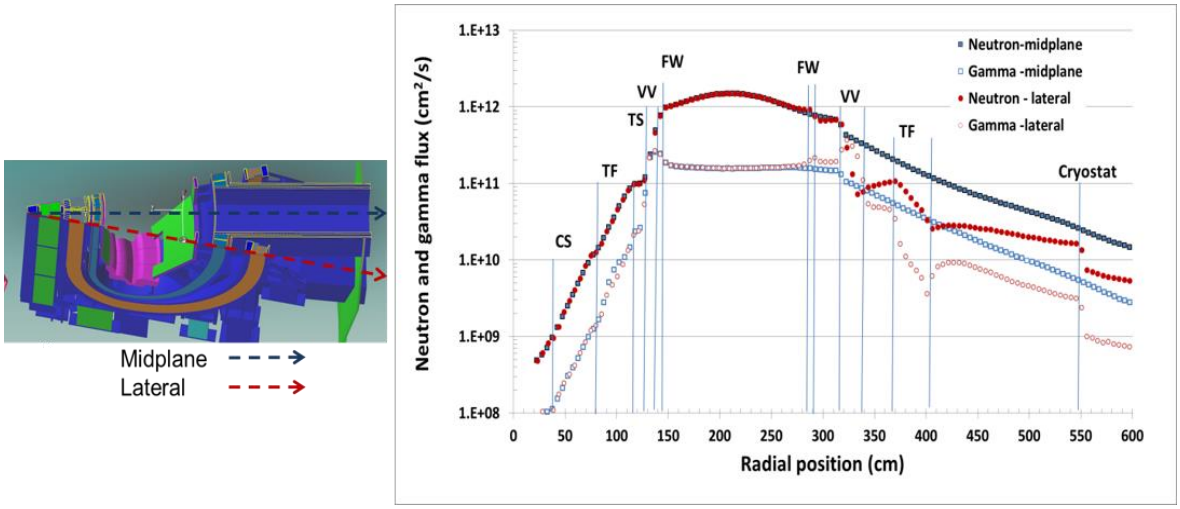

Figure 8-3 neutron and gamma radial profile at the mid-plane for central and lateral direction

Figure 8.4 shows the neutron spectra in the equatorial outboard of the DTT machine where the ECRH launchers will be integrated with the relative total values showed in table 8.1.

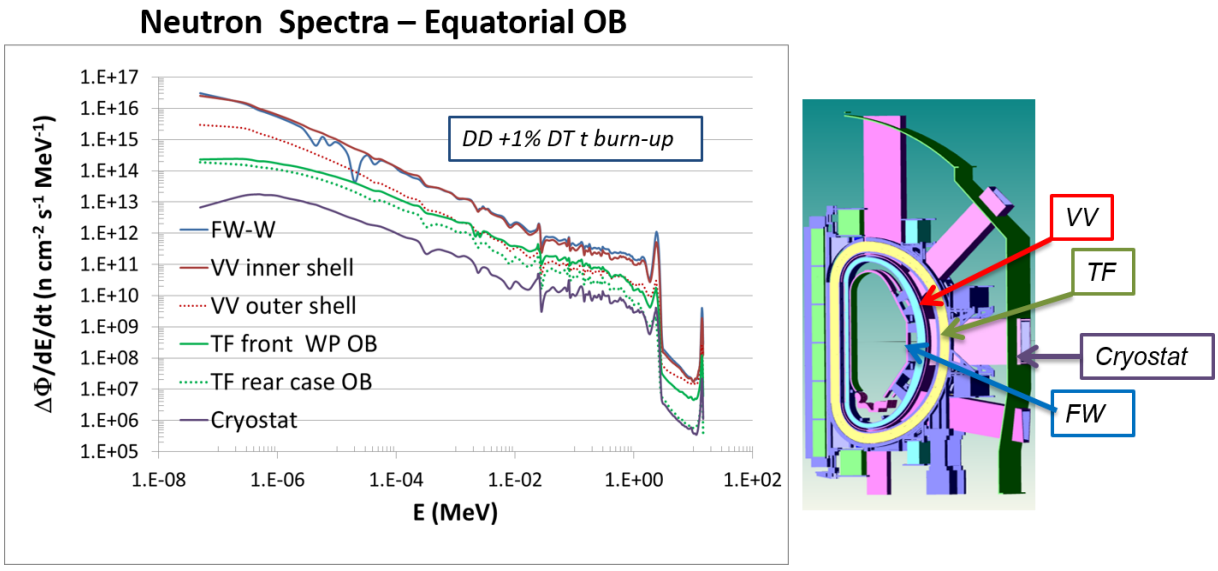

Figure 8-4 neutron spectra in equatorial Outboards for the different DTT components

The fast neutron fluxes (E > 0.1 MeV) contribution is about 80% of the total in the components faced to the plasma and drops to about 10% in the cryostat. The contribution of the neutrons with energy greater than 10 MeV is lower than 1%. [36]

Table 8-1 Values of nuclear quantities in the components inside the DTT cryostat

OB Components	**Total N flux DD+DT (n/cm²/s)**	**Total N fluence DD+DT (n/cm²) EOL**	**% E>0.1 MeV**	**% E>1 MeV**
FW Armour	9.04×10^{11}	2.25×10^{17}	80	55
VV inner shell	6.12×10^{11}	1.52×10^{17}	70	44
VV outer shell	1.01×10^{11}	2.50×10^{16}	68	29
TF -front case	9.15×10^{10}	2.28×10^{16}	67	19
TF- rear case	3.28×10^{10}	8.17×10^{15}	61	12
Cryostat	1.23×10^{10}	3.06×10^{15}	80	28

8.2 The ECRH launchers layout

In the first part of the chapter 7 the MBTLs transmission lines of the ECRH have been described and the calculation of the effects of their penetrations in the THB wall have been assessed and widely discussed.

Inside the TH the MBTLs are dived in two branches (figure 8.5) and connected to eight independent launching mirrors, six located in an equatorial port and two in an upper port in the same tokamak sector.

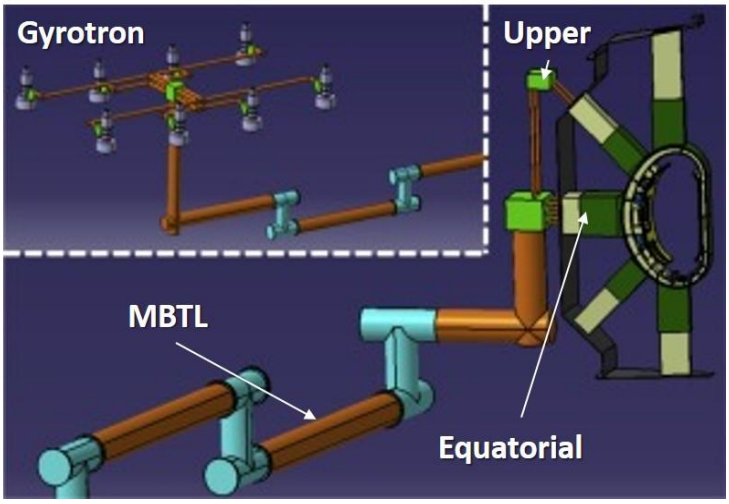

Figure 8-5 Preliminary schematic CAD design of a cluster unit.

Both launchers are based on the front steering concept with two mirrors for each line, the first shaping and other one, faced to the plasma, plane and movable. The dimensions of the mirrors are 150x210 mm for the firsts and 264x138 mm for the latter, compatible with a beam radius of 46 mm on the shaping mirror. [76]. An example of an equatorial launcher design is shown in figure 8.6.

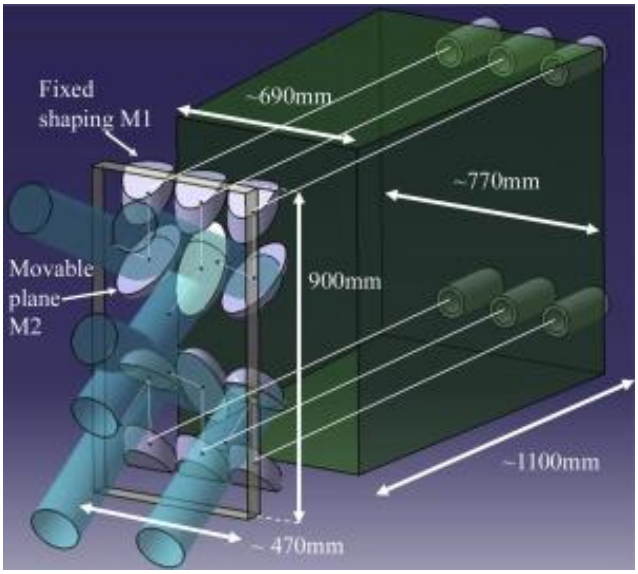

Figure 8-6 CAD preliminary design of the equatorial launcher

8.3 ECRH equatorial launcher integration

A preliminary design of the ECRH equatorial launcher has been integrated in the equatorial port of the 20° DTT MCNP model.

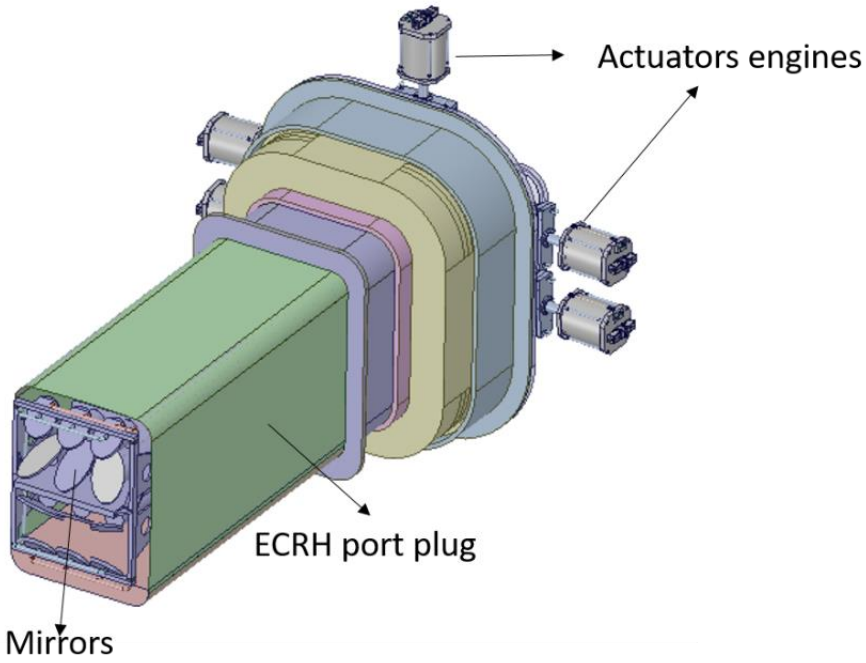

Figure 8-7 CAD model of the DTT ECRH equatorial launcher

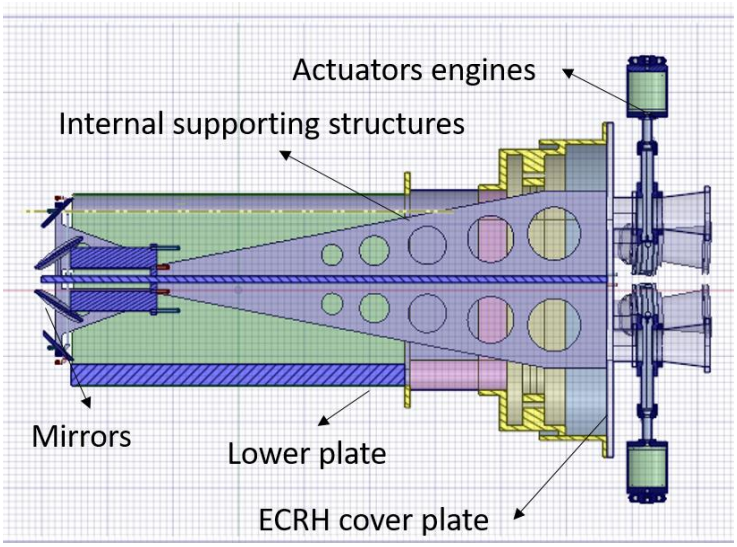

Figure 8-8 cross section of the DTT equatorial launcer

Figure 8.7 and 8.8 show the CAD model of the DTT ECRH equatorial launcher with the main components and the figure 8.9 shows the CAD of the EQ launcher integrated in the DTT 20° MCNP neutronic model.

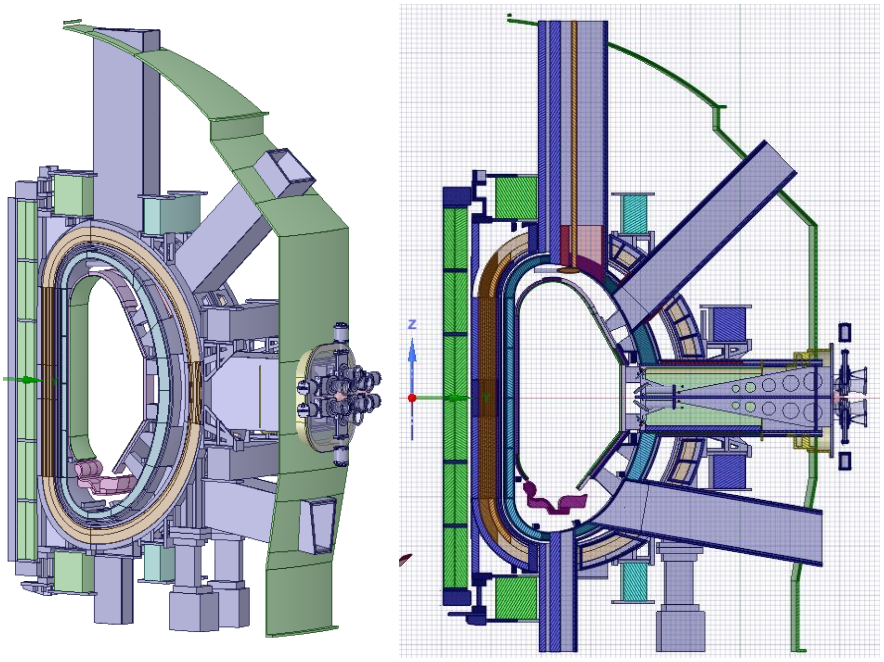

Figure 8-9 20° MCNP DTT neutronic model with CAD model of ECRH EL integrated

The MCNP model of the equatorial launcher features the ECRH port plug, the internal supporting structures and the ECRH cover plate made of SS316L (N), the lower plate, space for the water cooling tubes allocation, represented in MCNP model with a mixture of SS and water and the mirrors made of CuCrZr (ρ = 8.9 g/cm^3). The MCNP model of the equatorial launcher integrated in the 20° neutronic model is shown in figure 8.10.

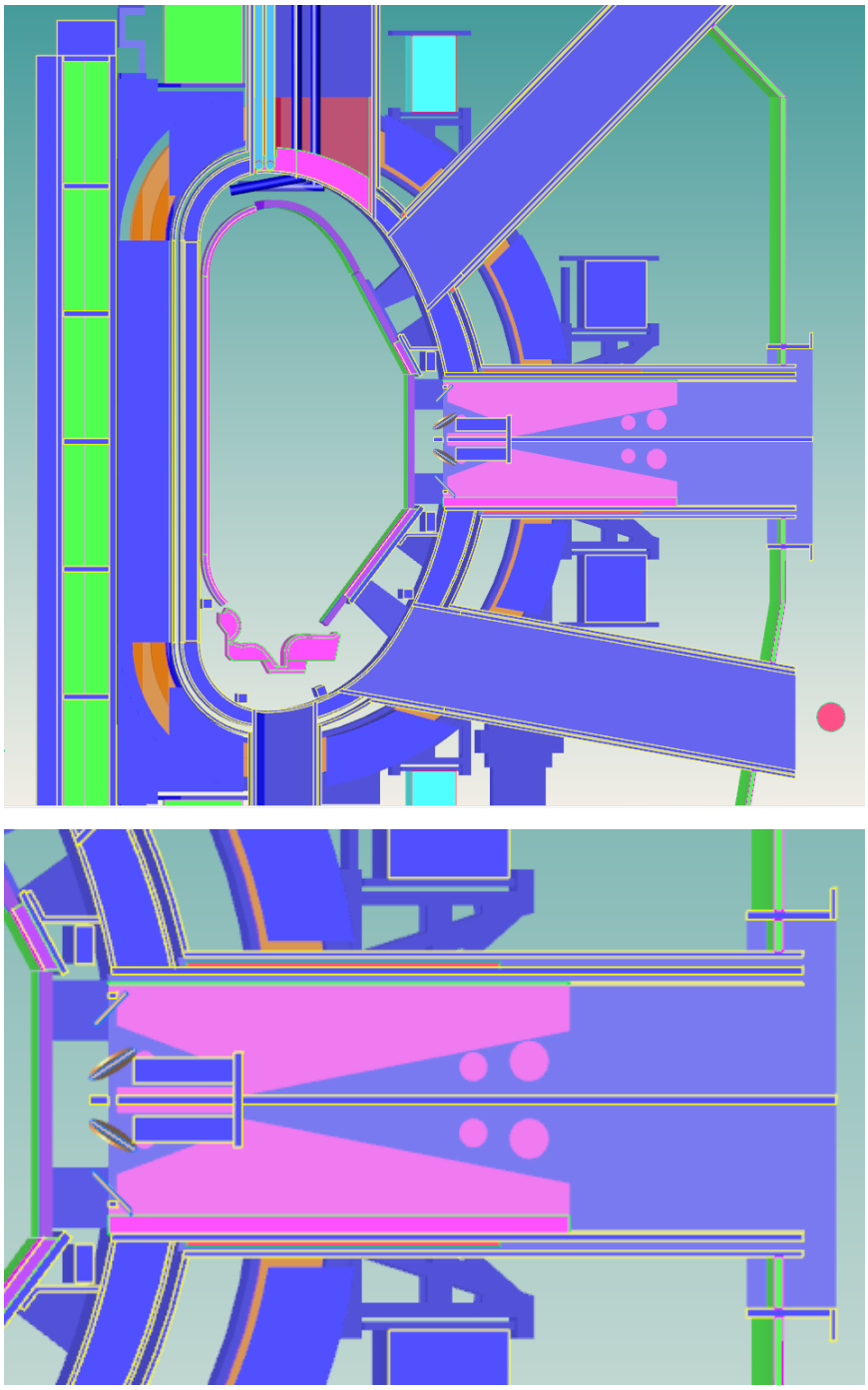

Figure 8-10 MCNP model of the DTT and ECRH MCNP model integrated

In figure 8.10 a view of the mirror positions is shown. Mirrors are placed just after the FW of the machine, in a position where the neutrons and gammas fluxes are very high and could induce significant effects on the CuCrZr like heating and activation.

8.4 Neutronic analyses

Neutronic analyses have been done considering the high-performance phase of the machine, i.e. $1.5x10^{17}$ n/s plus the 1% of 14.1 MeV neutron production.

Neutron and gamma flux spatial distribution and the nuclear heating in SS316L (N) have been assed as well as the contact dose rate on the mirrors and the shutdown dose rate with the integrated ECRH Equatorial Launcher using FISPACT II [26] for the activation and the AdD1S ENEA [29] code for the SDDR.

In figures 8.11 and 8.12 the spatial distribution of the neutron and gamma fluxes is shown. Neutron flux ranging between $5x10^{11}$ n/cm^2/s near the FW and $1x10^{10}$ n/cm^2/s in the rear zone of the ECRH port plug.

Gamma flux is of the order of $1x10^{11}$ γ/cm^2/s near the FW and $5x10^{9}$ γ/cm^2/s at the ECRH port plug.

Maps of nuclear heating in stainless steel, calculated with MCNP superimposed FMESH tally with proper multiplier, are shown in figure 8.13 in w/cm^3. The nuclear heating ranging between $9x10^{-5}$ W/cm^3 in the ECRH closure plate zone and $7x10^{-3}$ W/cm^3 in the mirror's zone.

Regarding the nuclear heating in the CuCrZr mirrors, showed in figure 8.13 presents its maximum in position #8 where the value is 7.26 mW/cm^3 and the minimum in the position #12 in the bottom part of the area where the NH is 6.73 mW/cm^3.

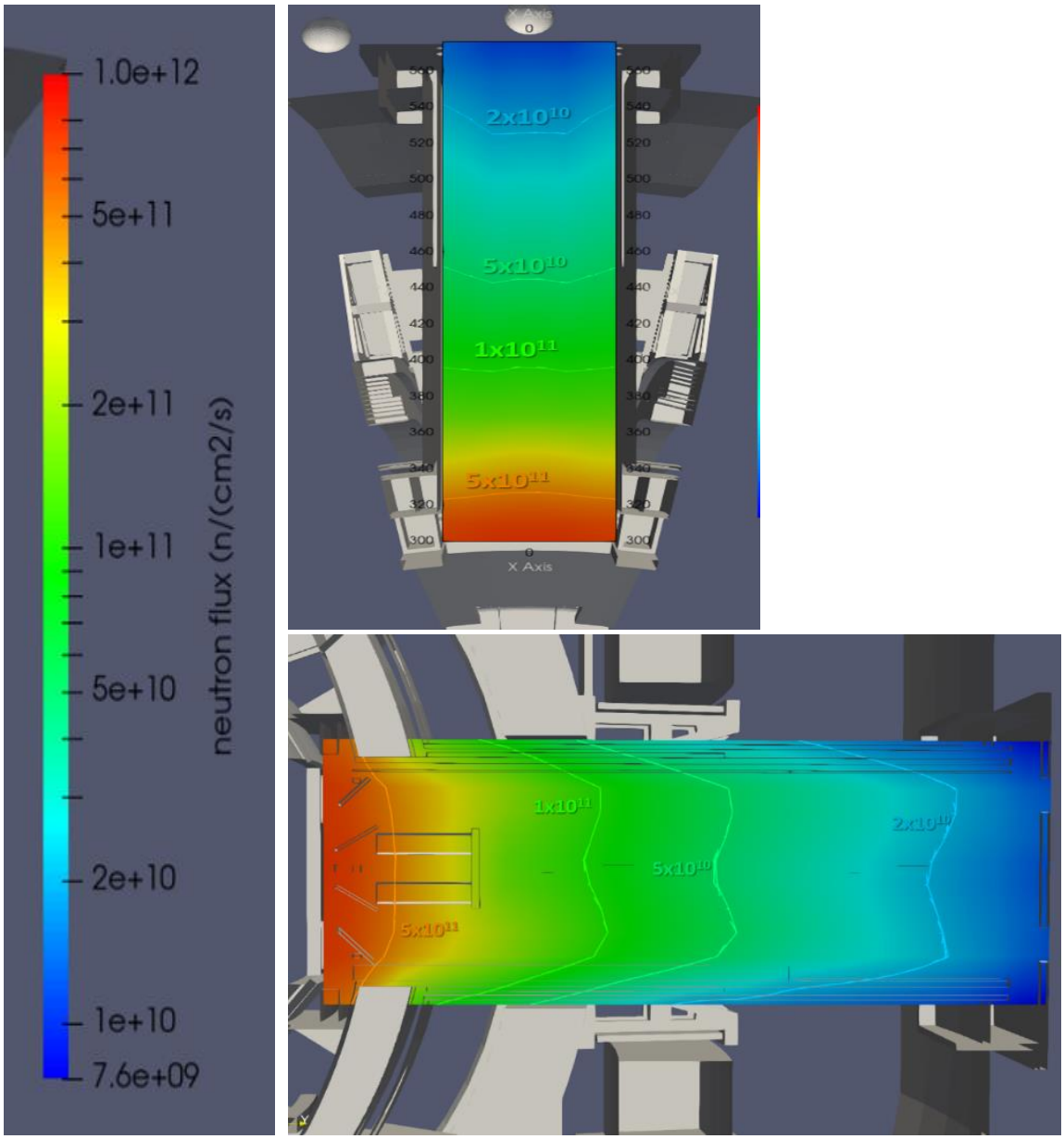

Figure 8-11 Maps of neutron flux inside the equatorial port eith ECRH EL integrated

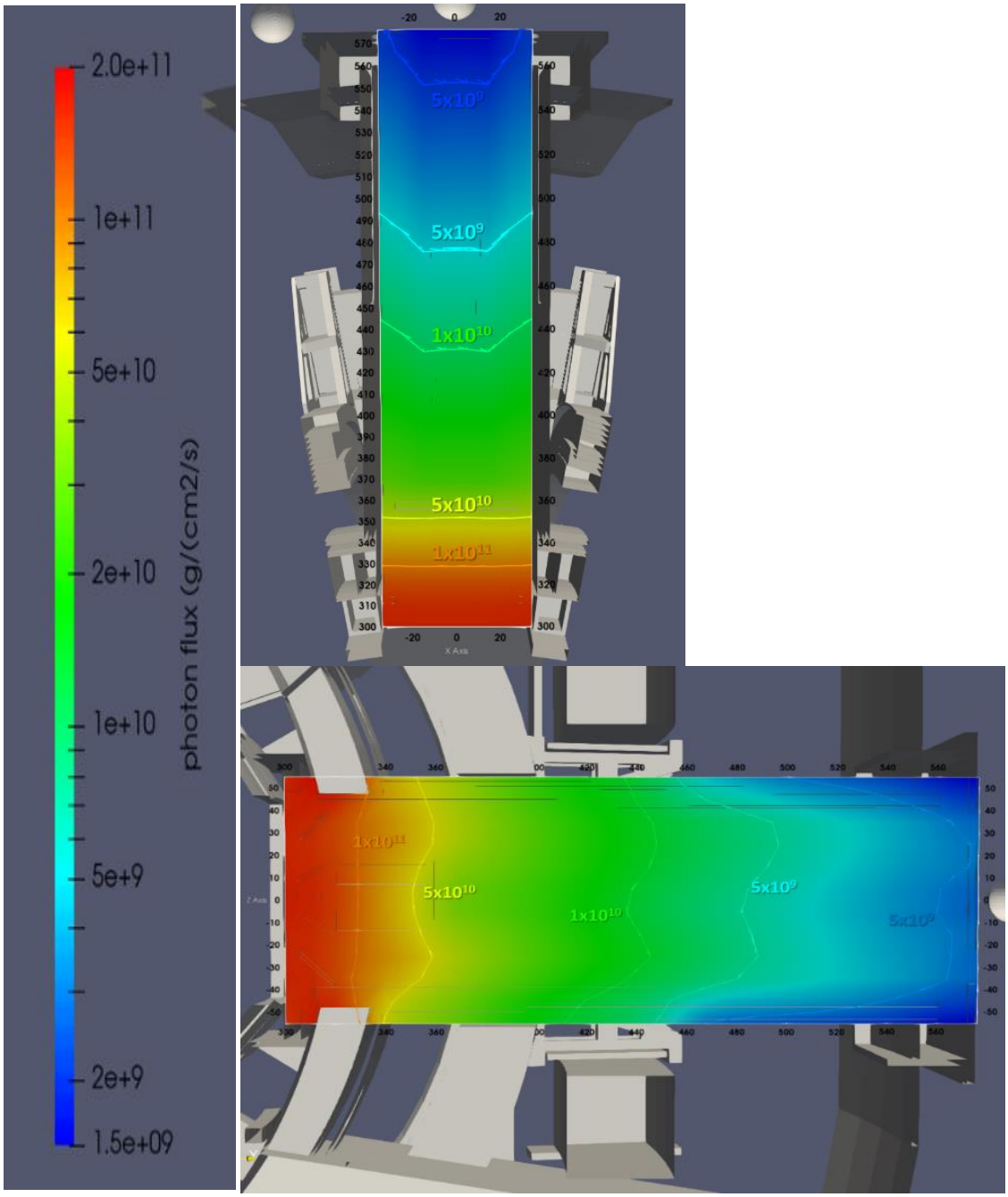

Figure 8-12 Maps of gamma flux inside the equatorial port with ECRH EL integrated

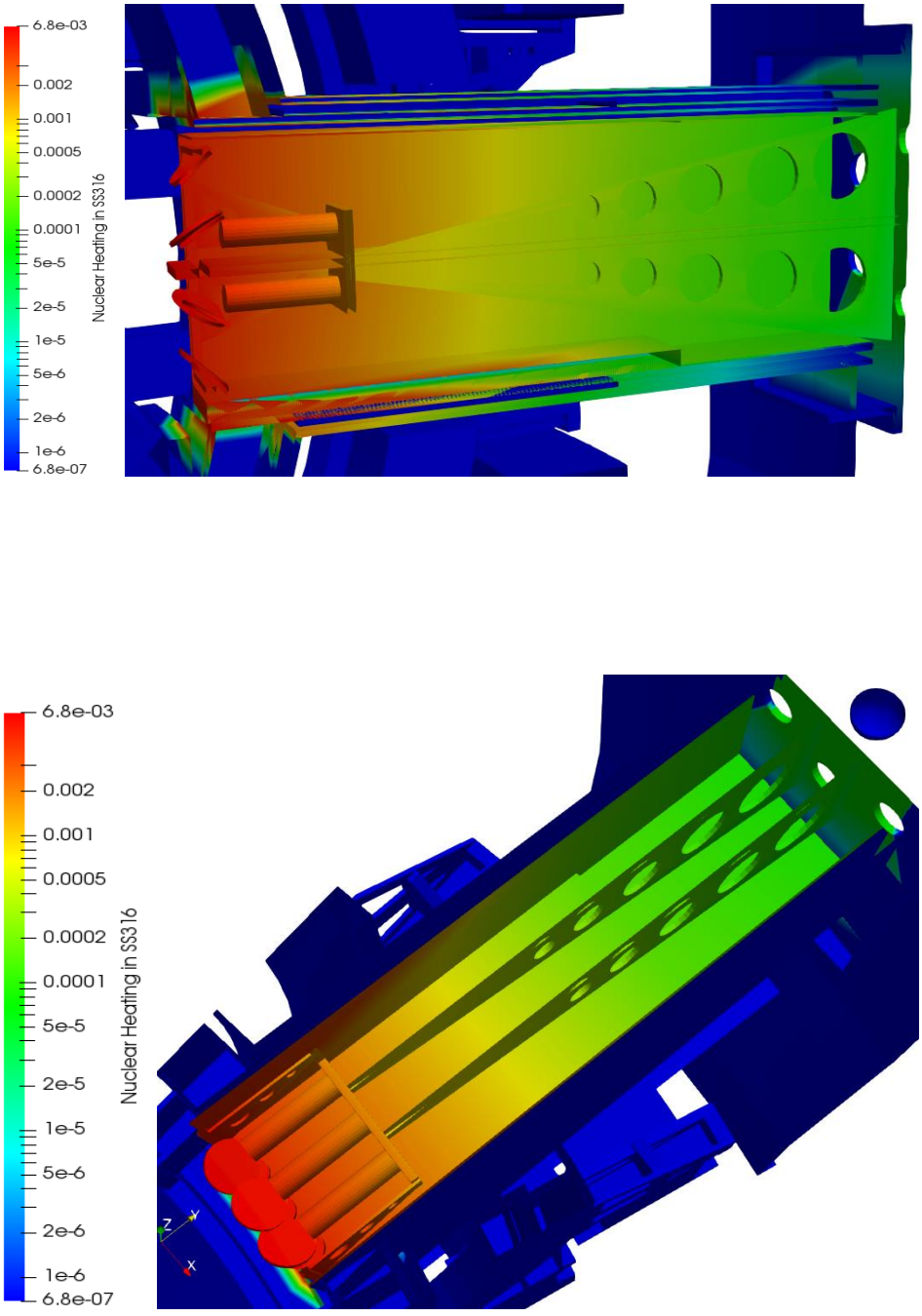

Figure 8-13 Map of Nuclear Heating in Stainless Steel

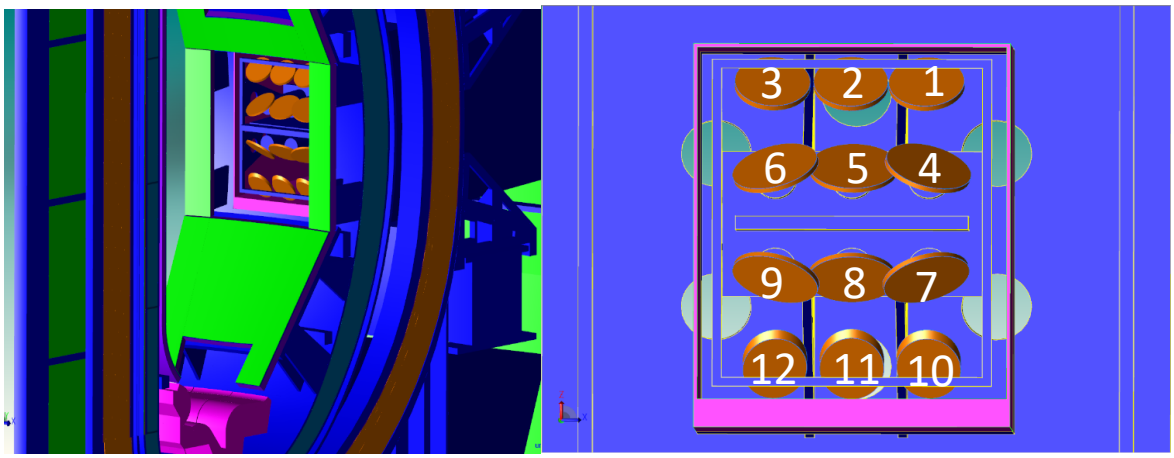

Figure 8-14 focus on the ECRH mirrors (left), frontal view of the ECRH mirrors with correspondent position numbers

8.5 Activation issues and SDDR assessment

Primitive analyses for the DTT activation and SDDR pointed out the problem of activation of the materials. To control the level of induced activation, especially in the Stainless Steel, the use of steels with controlled impurities, i.e. C0 < 500 wppm and Ta < 100 wppm, have been strongly recommended [39] for the structural materials of the tokamak. In the MCNP model of the ECRH equatorial port these materials have been used and the results of the contact dose rate as a function of the time after the shutdown in CuCrZr mirrors are shown in the graphs in figure 8.14. The analyses have been performed after 18, 42 months and at the end of DTT life. All the calculations have been done considering a safety factor 2.

After 18 months of operations, one week after the shutdown the level of contact dose rate is about 30 μSv/h; after 42 months of operations, one week after the shutdown the level of contact dose rate is about 400 μSv/h. At the end of DTT life the contact dose rate is about 2 mSv/h one week after the shutdown, whereas 10 years after the shutdown the level of the contact dose rate drops to 420 μSv/h and 50 years after the shutdown is below the 10 μSv/h.

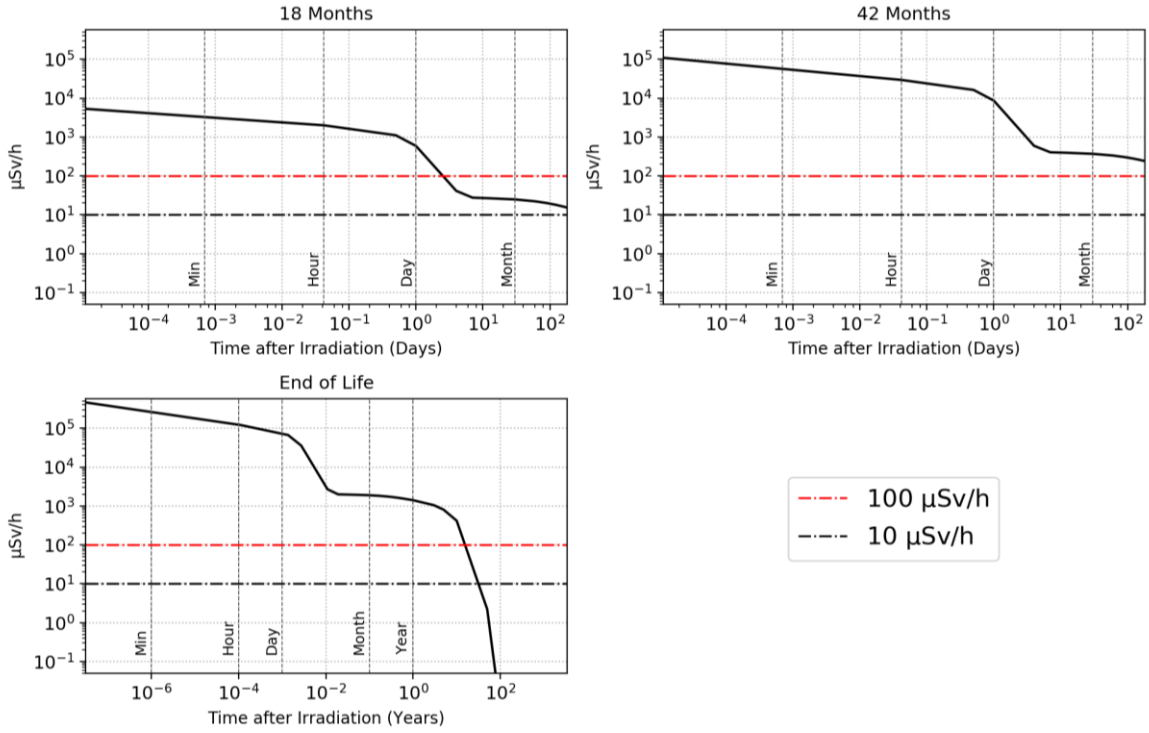

Figure 8-15 Temporal behaviour of the contact dose rate after 18 and 42 months and at the end of life for the ECRH mirrors

The red line in the graphs represents, as a reference value, the ITER limit in the port interspace 12 days after the shutdown at the end of ITER life. The black line, 10 µSv/h, is the radiation protection constraint adopted for the maintenance operations in DTT.

Levels of contact dose rate for the mirrors is very high. This means that the remote handling for the management of these components should be foreseen at the DTT end of life.

Concerning the temporary evolution of the SDDR at the end of DTT life, 4 positions showed in fig. 8.15 have been chosen. In particular, the position M3 is representative for the workers that could enter in the THB and operate on the ECRH launchers. In this position the level of SDDR is shown in table 9.2 for 1 day, 1 week, 3 months and 1 year after the shutdown at the end of DTT life.

Table 8-2 Values of SDDR in position M3 for different cooling time

Shutdown dose rate in position M3 (μSv/h)	
Cooling time	SDDR level
1 day	120
1 week	50
3 months	30
1 year	15

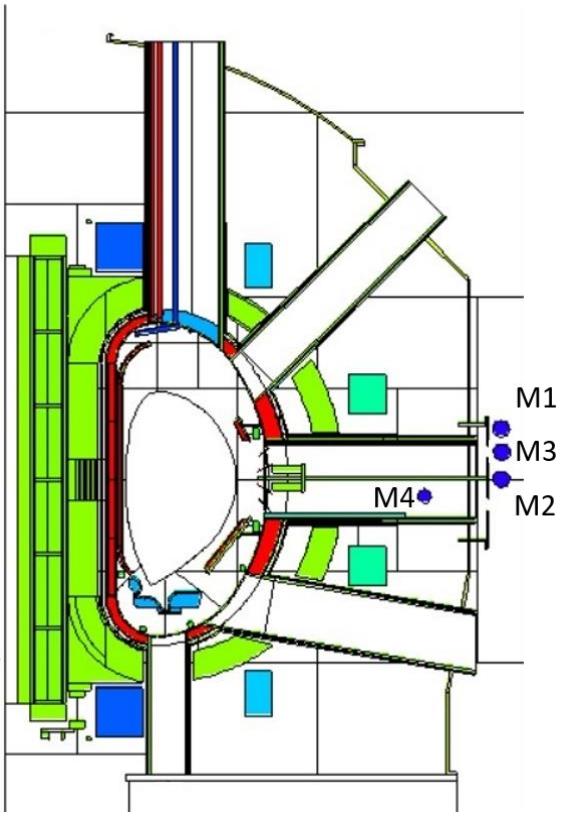

Figure 8-16 Position M1, M2, M3 and M4 for the calculation of the SDDR

Temporary evolution of the SDDR in positions M1, M2, M3 and M4 is shown in figure 8.16. Figure 8.17 shows the maps of SDDR at 1 day and 3 months after the shutdown at the end of DTT life.

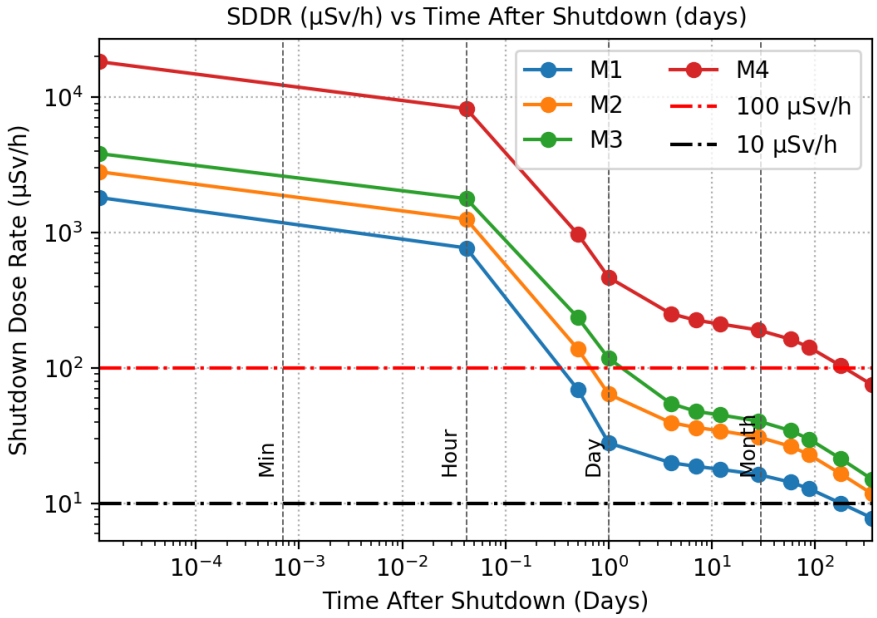

Figure 8-17 Temporal evolution of the SDDR at the end of life in position M1, M2, M3 and M4

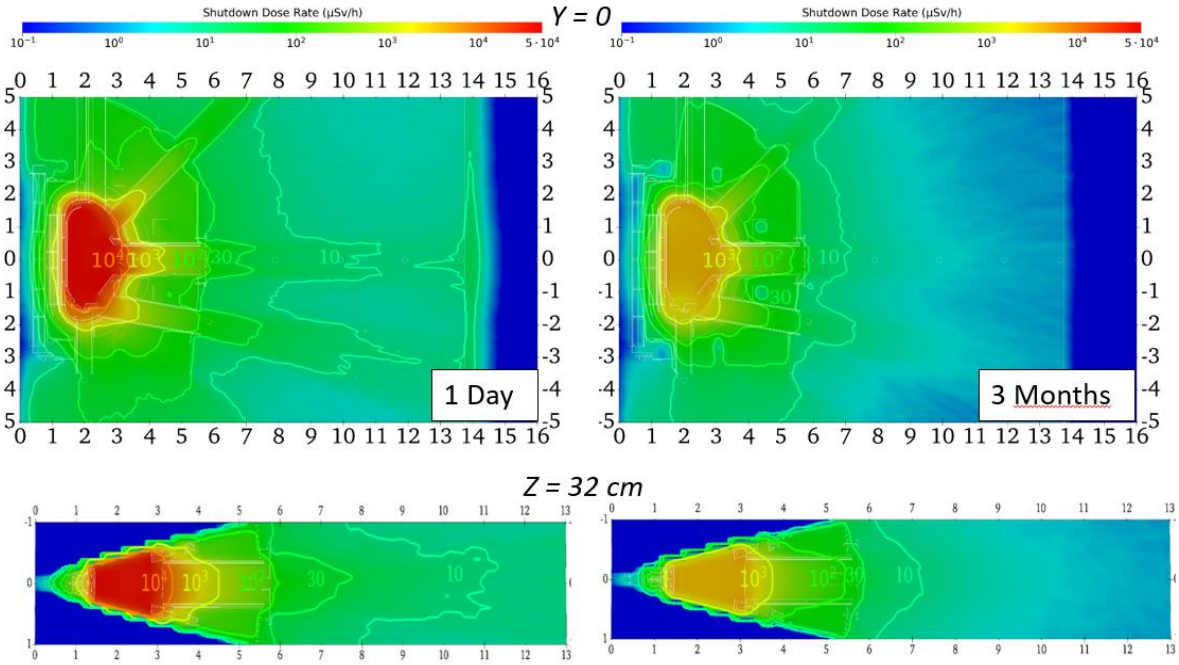

Figure 8-18 MAps of the SDDR 1 day (top lleft and bottom left) and 3 months (top right and bottom right) after the DTT shutdown at the end of life

Figure 8.18 shows the maps of SDDR at one day and three months after the shutdown at the end of DTT life.

9 Conclusions and future work

"Imagination is more important than knowledge. For knowledge is limited, whereas imagination embraces the entire world, stimulating progress, giving birth to evolution"

A.Einstein

The Divertor Tokamak Test (DTT) facility will be one of the most important fusion facilities in Europe and in the World. It will test, with the passing of the time, several types of divertors, starting from the "conventional" tungsten ITER-like divertor to the most advanced configuration and materials such as the liquid metal divertors. Many plasma scenarios are foreseen for DTT: the Single Null (SN), the Double Null (DN), the Snowflake (SN) and also the Negative Triangularity as the ultimate boundaries of the plasma confinement.

To accomplish to all these goals, DTT should be a flexible and fully symmetric machine in order to test also the configuration with upper and lower divertor.

Moreover, DTT will operate in a DEMO relevant conditions and to fulfil all these requirements a great amount additional heating power (45 MW) is needed to reach the maximum performances for the DTT H-Mode operational phase. Indeed, three additional heating systems will be installed in DTT: the Electron Cyclotron Resonance Heating (ECRH), the Ion Cyclotron Resonance Heating (ICRH) and the Negative Neutral Beam Injection (NNBI) systems.

Once all these systems will operate at full power, DTT will reach the DEMO-relevant condition for the Scrape Off Layer (SOL) region and many divertor types will be tested in this facility.

This great amount of power means, from nuclear point of view, a very intense neutron and gamma production. DTT, in fact, is expected to produce, in its high-performance phase, 1.5×10^{17} 2.45 MeV n/s from DD fusion reactions. Moreover, due to the triton burn-up, an additional amount of high energy neutrons of 14.1 MeV from DT reaction, estimated in 1% of DD neutron production, is also foreseen. According to the provisional operational scenario, which foresees six months of operation and six months of maintenance, DTT will produce in one year 1.53×10^{21} n/y plus the 1% of DT neutrons. At the end of its life 3.73×10^{22} n will be produced.

The analyses performed in this work of thesis are devoted to the shielding analyses for the DTT design. This great amount of neutrons and, thus, gamma production implies that a number of consequences should be taken into account due to the effect of the neutrons and gammas interactions with the materials and with humans.

Moreover, DTT will undergo to a strong licensing procedure as imposed from the Italian Regulation as it is a machine that will produce more than 10^7 n/s over the whole solid angle. For this reason, radiation protection constraints of 300 μSv/y for non-radiation workers have been imposed inside the ENEA centre by the radiation protection expert and 10 μSv/y (from the Italian Regulation) at the ENEA centre boundaries.

Neutronics studies are of paramount importance for the machine development and for the support to the licensing procedure. The calculation of the nuclear loads on the components inside the cryostat is fundamental for their protection, especially for the Toroidal Field Coils (TFC), and for the Vacuum Vessel cooling system where the use of borated water is foreseen after some years of DTT operation (and thus neutron production).

The evaluation of the nuclear fields in the Tokamak Torus Hall Building (THB) is the starting point for the main hall development. Inside the TH the neutron and gamma fluxes are very high during operation, and in the closest wall they result of the order of 10^9 n/cm^2/s and 10^8 γ/cm2/s.

To assess the thickness of the THB walls, several materials have been considered. Starting from the ordinary concrete, many other heavyweight concretes with a number of solid aggregates in the composition for the neutron and gamma attenuation (Barium, Luminite, Boron) have been tested.

Due to difficulties to use these types of concretes for such a big structure (35x35x25 m^3) and, moreover, due to their cost a 220 cm thick of ordinary concrete has been chosen for the walls of the tokamak hall. This thickness, in fact, guarantees an attenuation factors of more than 6 orders of magnitude and drops the n&γ flux to a value ~10^2 n/cm^2/s, ~$3x10^3$ γ/cm^2/s and effective dose well below the design constraint, i.e. $1.5x10^2$ μSv/y. Thus, it ensures the respect of the radiation protection constraints for non-radiation workers and the limit for the population outside the ENEA centre. To complete the basic nuclear design of the THB an evaluation of the Skyshine effect has been done by considering different materials and thickness in order to reduce as much as possible the dose due to the Skyshine at the ENEA site boundaries. After several calculations it has been found that 150 cm of ordinary concrete shield is enough to respect the 10 μSv/y limiting the Skyshine effective dose to ~6 μSv/y, below the limit even considering the direct contribution from the Torus Hall.

A second step has been done by considering the penetrations in the THB caused by the several additional systems (Heating and Current Drive, Diagnostics, cooling systems) necessary for the DTT operations and hosted in remote control buildings. These penetrations have a big impact on the level of neutron and gamma fluxes outside the Torus Hall and must be shielded in order to respect the limits.

In particular, two different zone of the site around the THB have been studied: the south wall, which will host the ECRH corridor for the ECRH MBTLs and the east wall where the FDU area, the Helium transmission line and the passage area for the remote handling is foreseen within a connection corridor between the THB and the ex FTU building.

For the four ECRH penetrations, laying about 10 m above the ground, a shielding configuration has been studied to limit the neutron and gamma streaming outside and inside the corridor. Fixed and removable shields made of Stainless Steel, common polyethylene and ordinary concrete, have been used in the configurations that leads to the respect of the design constraints at the ground level addressing the annual effective dose to ~150 μSv/y. Inside the corridor, the effective dose close the Gyrotron building (40 m far from the THB) has been limited by adding a 20 cm thick of shielding gate made of ordinary concrete and polyethylene. In this way the annual effective dose close to the Gyrotron building is of the level of 30-40 μSv/y ensuring the protection of the workers even during the DTT pulses. Moreover, to accomplish the requirements for the transmission lines maintenance, the level of SDDR has been assessed and a negligible level of dose, below 10 μSv/h, has been found even at the end of DTT life.

Regarding the east wall, the problem of the effects of the neutrons and gammas on the electronics has been assessed. To protect the FDU area a massive configuration of shielding has been proposed by covering the room with polyethylene and concrete. Furthermore, the Helium line penetration has been studied and a dogleg shield has been optimized to limit the streaming of neutrons and gammas. With this configuration the level of neutron fluxes has been settled at level of 10^{-1} n/cm^2/s and the absorbed dose in Silicon, mainly due to the gammas, is well below the reference value (i.e. adopted in ITER) of 1 Gy cumulated over the whole DTT life.

Last, but not least, the activity of the integration of the components inside the port has been started by integrating in the 20° MCNP DTT neutronics model the ECRH equatorial launcher.

Nuclear loads on the structural Stainless Steel and on the EC mirrors made of Copper Chromium Zirconium (CuCrZr) have been evaluated as well as the level of contact dose rate and shut down dose rate for a number of cooling time. Very high level of contact dose rate has been found even at the end of the first phase of DTT operations (greater than 30 μSv/h one week after the end of the first 18 months operations). This implies the need for the definition of proper strategies for remote handling maintenance, transport and disposals of radioactive components.

The activity presented in this work of thesis referred to only a small part of the whole activities done and foreseen for the development of DTT machine. Neutronics activities will continue in the future supporting the construction of the machine, the bunker around it and the integration of the components. In particular, some solutions presented in this work will be optimized and will change depending on the needs of DTT tokamak and of the layout. Many other penetrations in the building are not yet studied but need a deep evaluation of the neutron and gamma streaming in order to optimize the layout.

The nuclear integration of the components is at the very early stage of the project and several activities will be done before the call for tenders and before the definitive layout of the components.

Furthermore, once DTT will start its operations with a great amount of neutron production, neutronics will be involved in many experiments related to the diagnostic and for the analyses of many aspects, such as activation analyses, shutdown dose rate evaluation experiment, for nuclear data and Monte Carlo modelling.

A. Nuclear Reactions

Nuclear reactions, as for chemical reactions, are commonly and widely used in several applications, for the energy production, for medical applications, testing materials and many other fields of studies. Nuclear reactions are based on the differences in the nuclear binding energy, defined as the energy required to split a nucleus of an atom into the number of free unbound neutrons and protons it is composed of. The binding energy can be expressed through the Einstein's energy-mass relation:

$$E = \Delta m \cdot c^2 \qquad (A.1)$$

Where Δm is the mass defect and c is the speed of light.

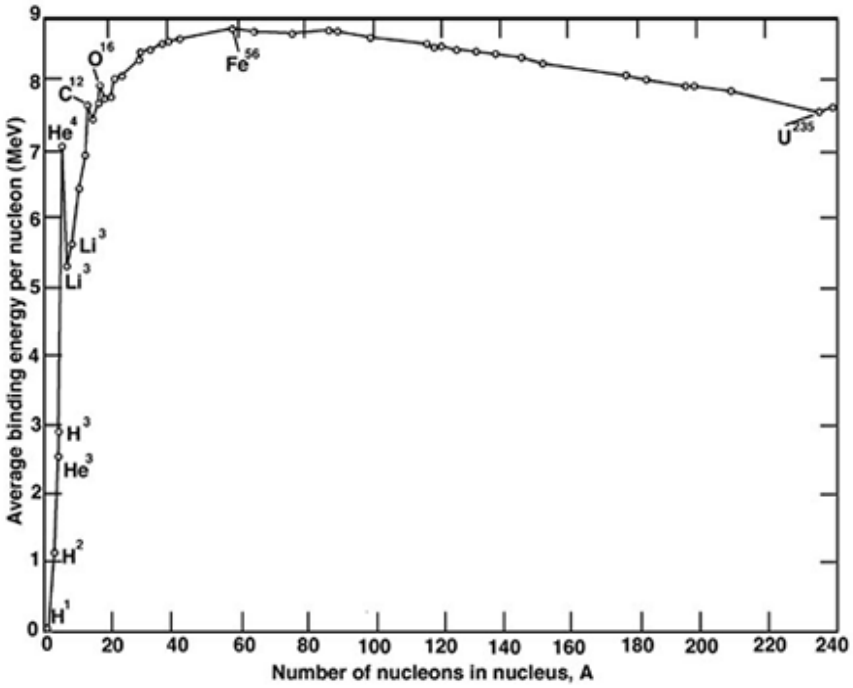

Figure A-19 Nuclear binding energy per nucleon as a function of the nucleon number A

In fig. A.1 the nuclear binding energy per nucleon in funtion of the atomic mass number A is shown. From this well known graph it's clear that the behaviour of the

curve is strongly affected by the strong nuclear forces which are the responsible for the binding of protons and neutrons into the atomic nucleous and repulsive Coulomb force between protons. [31]

The behaviour of the curve shows that the binding energy increases its value from Hydrogen and other light nuclei since Iron-56 peak (8.8 MeV per nucleon) and after it restart to decrease smoothly. The lower binding energy for the light nuclei is due to their large surface to volume ratio: the nucleons at the surface have missing partners so their contribution to the total binding energy is followed by a sequence from magnesium through xenon, characterized by a relative stability.

Elements wchich are hevier thant Iron-56 have a decreace of binding energy per nucleon. This is due to the electromagnetic repulsive force that becomes more important for heavier nuclei. The structures observed in fig.1.1 for ^{4}He, ^{12}C and ^{16}O are due to the quantum mechanical effects related to the nucleus shell model based on Pauli's exclusion principle.

Furthermore, there are some so-called "magic" atomic number, which have the nuclear shells filled: the nucleus formed has a higher average binding energy per nucleon than one would expect based on predictions such as the semi-empirical mass formula and are, hence, more stable against nuclear decay.

The first "magic" atomic number is 2, and corresponds to the local ^{4}He maximum in fig. A.1.

From the fig. 1.2 it's already clear that there are almost two ways to gain energy from nuclear reactions:

- *by splitting heavy nuclei into two smaller nuclei*: this is the well-known process called fission in which the released energy per nucleon is about 1 MeV;
- *by fuse light nuclei into heavier ones*: this is the process called fusion and the energy released per nucleon is in the order of some MeV. In particular, the

fusion of hydrogen into stable helium offers the highest energy released per unit mass.

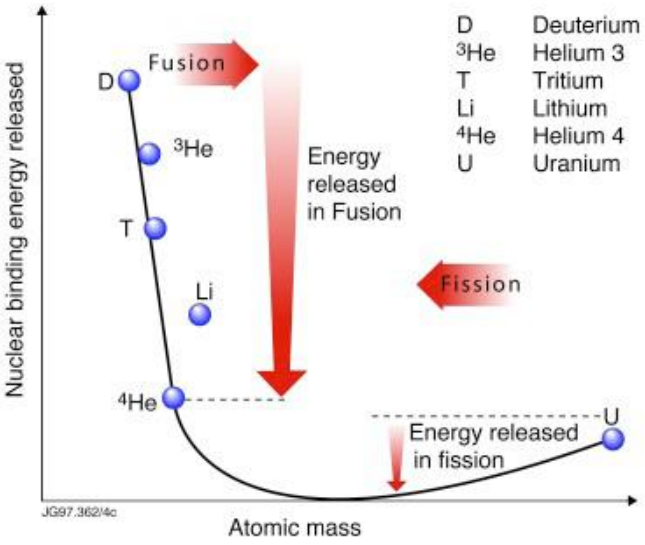

Figure A-20 - Nuclear binding energy released as a function of the atomic mass

In all the nuclear reactions, the strong nuclear force governs the process. It acts over very small distances, in the order of nuclei radius, even if at distances greater than few Fermi (10^{-15} m) the Coulomb repulsive force between the positive charged nuclei becomes dominant (fig. A.3). The depth and the height of the wall for small radii and few Fermi is determined by binding energy and Coulomb potential respectively, according to the following expression:

$$U = \frac{Z_1 Z_2 e^2}{4\pi \in_0 r_m} \qquad (A.2)$$

Where U is the potential energy, Z_1 and Z_2 are the atomic numbers of the two interacting nuclei, e is the electron charge, Ɛ is the vacuum dielectric permittivity and r_m is the mutual distance between the nuclei.

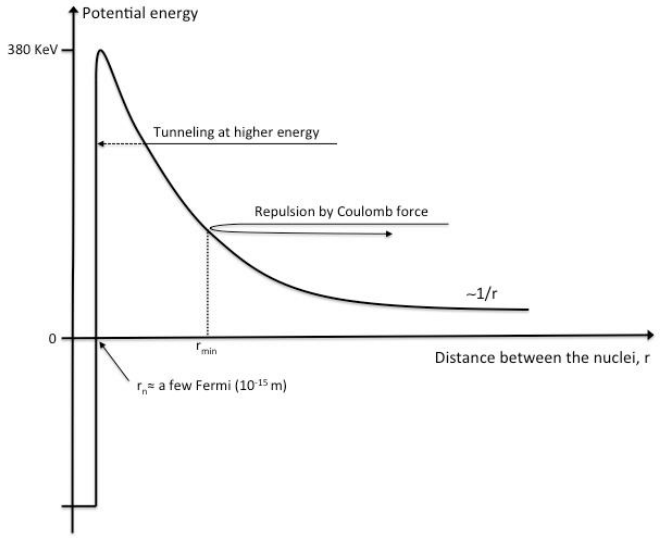

Figure A-21 - Potential energy U of two nuclei as a function of their distance. The energies showed refer to a D-T interaction

Following this diagram, the fusion of light nuclei requires the particles energy of the order of several KeV. Anyway, the quantum mechanical effect called tunnelling [86] allows the fusion reaction between light nuclei, even at energy far below the energy request to overcome the Coulomb barrier. The probability that this effect occurs is strongly related to the relative velocity v of the particle involved in the reaction, according to the following expression:

$$P_{tunneling} \sim \exp - \frac{2\pi Z_1 Z_2 e^2}{\hbar v} \qquad (A.3)$$

The equation shows that the reactant nuclei with small charge and mass are favoured and the reaction probability is strongly dependent from the temperature and thus from the velocity.

B. Thermonuclear Fusion

The fusion of light nuclei is the base for the energy production through thermonuclear fusion. As explained, to fuse two light nuclei like Deuterium (^2H) and Tritium (^3H) it's necessary to overcome the mutual repulsion due to their positive charge. From the equation (1.3) is clear that the higher is the temperature of the reactant the greater the tunnel probability will be. The value of the temperature necessary to overcome the Coulomb barrier is around 10 KeV, corresponding to 100 million °C. At this temperature the velocity of the reactants is high enough to produce the required reaction. At this temperature, the atoms are fully ionized, and the electrostatic charge of the ions is neutralized by the presence of an equal number of electrons resulting in an electrically neutral gas called plasma.

The reactions on the basis of the thermonuclear energy production, which are considered to be promising to gain energy from this process, are mainly related to the hydrogen isotopes, Deuterium and Tritium:

$$D + D \rightarrow {}^3He + n + 3.27\ MeV\ (50\%) \qquad (B.4)$$

$$D + D \rightarrow \quad T + n + 4.03\ MeV\ (50\%) \qquad (B.5)$$

$$D + T \rightarrow {}^4He + n + 17.6\ MeV \qquad (B.6)$$

$$T + T \rightarrow {}^4He + 2n + 11.3\ MeV \qquad (B.7)$$

And then, there the so-called a-neutronic reactions, which don't have neutrons as products of the reactions. They are, anyway, very difficult to use to produce energy:

$$D + {}^3He \rightarrow {}^4He + p + 18.35\ MeV \qquad (B.7)$$

$$p + {}^{11}Be \rightarrow 3\ {}^4He + 8.7\ MeV \qquad (B.8)$$

To characterize the probability that a certain nuclear reaction will occur, is customary to define, an "effective size" of nucleus called "cross section". It is the most important parameter to evaluate the feasibility of a fusion reaction. The graph in figure B.1 shows the measured cross-sections for different fusion reactions as a function of the centre-of-mass kinetic energy are plotted.

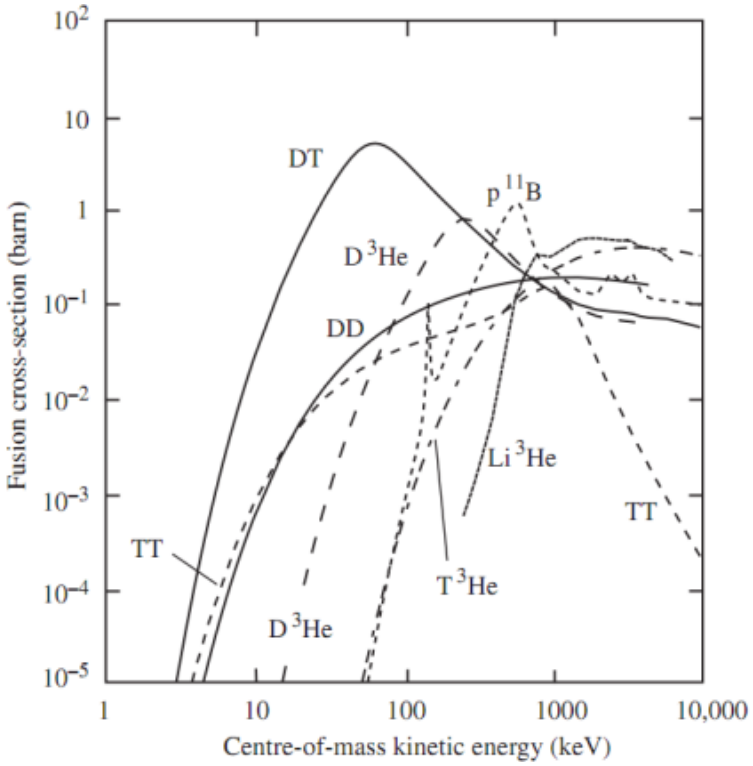

Figure B-1 Fusion reactions cross-sections (1 barn=10^{-28} m^2) as a function of the centre-of-mass kinetic energy

Regarding the calculation of the reaction rate into a plasma, an integration over the distribution function (f1, f2) of both species involved in the reaction is needed [31]. The following expression defines the amount of the fusion reactions per unit volume between particles with velocities v1 and v2:

$$R = \langle \sigma v \rangle f_1(v_1) f_2(v_2) \qquad (B.9)$$

where $v = |v_1 - v_2|$ and $f_1(v_1)$ and $f_2(v_2)$ are the distribution functions of the reactants.

Considering a Maxwellian velocity distribution function:

$$f(v) = n\left(\frac{m}{2\pi kT}\right)^{3/2} exp\left(-\frac{mv^2}{2kT}\right) \qquad (B.10)$$

where f is the number oh particles in the velocity interval between v and v+dv, n is the density of particles, m their mass and kT is their temperature[12]. Considering these parameters in Maxwellian distribution, the total reaction rate per unit volume is:

$$R = \iint \sigma\,(v) v f_1(v_1) f_2(v_2) d^3v_1 \mathrm{d}^3v_2 \quad (B.11)$$

Thaa can be written as

$$R = n_1 n_2 \frac{(m_1 m_2)^{3/2}}{(2\pi kT)^3} \times \iint \exp\left(-\frac{m_1+m_2}{2kT}\left(V\frac{1}{2}\frac{m_1-m_2}{m_1+m_2}v\right)^2\right) \sigma(v)\, v\, exp\left(-\frac{m_r}{2kT}\right)^2 d^3v\, d^3V$$

where $\boldsymbol{V} = \frac{\boldsymbol{v_1+v_2}}{\boldsymbol{2}}$ and $\boldsymbol{m_r}$ is the reduced mass. The integral over V is $\left(\frac{\boldsymbol{2\pi kT}}{\boldsymbol{m_1+m_2}}\right)^{\boldsymbol{3/2}}$ thus

$$R = 4\pi n_1 n_2 \left(\frac{m_r}{2\pi kT}\right)^{3/2} \int \sigma(v) v^3 \exp\left(\frac{m_r v^2}{2kT}\right) dv \qquad (B.12)$$

Expressing the cross-section in terms of the relative kinetic energy of the reactants (ε_r) an expression for the reactivity can be obtained:

$$\langle \sigma v \rangle = \frac{4}{(2\pi m_r)^{1/2}(kT)^{3/2}} \int \sigma(\epsilon_r)\, \epsilon_r \exp\left(-\frac{\epsilon_r}{kT}\right) d\epsilon_r \quad (B.13)$$

Figure B.2 shows <σv> for some important fusion reactions: here again, the D-T reaction shows the higher reaction rate at lower temperature.

[1] [2][12] K is the Boltzmann constant 1.38054x10^{-23}

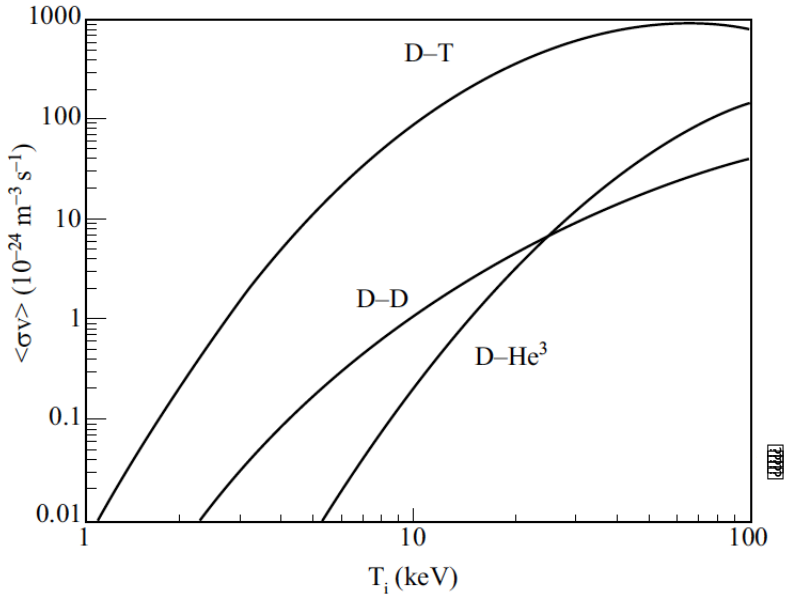

Figure B-2 Fusion reaction rate <σv> for D-T, D-D (total) and D-He3 as a function of plasma temperature

Ignition

The range of the temperature in fusion stands around hundred million K degree. At this temperature all the elements of the periodic table are ionized, and the fuel is in the plasma state. Into the fuel the α particles provide a substantial fraction of the total heating transferring part of their energy through elastic scattering.

If the energy balance between the transport losses and α particles heating is in a sort of draw, the plasma temperature is self-sustained and the *ignition* state has been reached [87].

All contributes to the energy loss (i.e. diffusion, convection, charge exchange) reduces the temperature of plasma. These contributes can be empirically described assuming a typical energy confinement time ◎◎◎leading to a power loss term:

$$E_{loss} = 3\frac{nkT}{\tau_\varepsilon} \qquad (B.14)$$

Where 3nkT is the inner thermal energy and n the electron density. A significant energy loss mechanism is the bremsstrahlung, which becomes dominant at high

energies and impurity concentrations. Next formula shows the bremsstrahlung losses:

$$P_{br} = c \cdot n^2 \cdot Z_{eff} \cdot (kT)^{1/2} \qquad (B.15)$$

where c is the bremsstrahlung constant ($c = 5.4 \cdot 10^{-37} W m^3 keV^{-1/2}$) and Z_{eff} the effective plasma charge, taking into account all the impurities species ($Z_{eff} = \sum_z n_z Z^2/n$).

The energy balance can be now expressed considering the effect of all the power loss processes:

$$\left(\frac{n}{2}\right)^2 \langle \sigma v \rangle \cdot \varepsilon_\alpha = 3\frac{nkT}{\tau_\varepsilon} + c \cdot n^2 \cdot Z_{eff} \cdot (kT)^{1/2} \qquad (B.16)$$

and can be rewritten highlighting the ignition condition:

$$n\tau_\varepsilon = \frac{12kT}{\langle \sigma v \rangle \cdot \varepsilon_\alpha - 4cZ_{eff} \cdot (kT)^{1/2}} \qquad (B.17)$$

where ε_α is the α-particles energy (3.5 MeV for a D-T plasma) . This equation shows that the product of the energy confinement time and particle density is a function of the plasma temperature with a minimum at about T=13 keV, corresponding approximately to 100 million °C.

The condition to reach the ignition in a fusion machine is strictly linked to the confinement of the plasma. In 1995 J. D. Lawson [88], [89]defined the first criteria to satisfy to reach the ignition: the heating of the plasma by the products of the fusion reactions is sufficient to maintain the temperature of the plasma against all losses without external power input. Lawson, in his first criteria formulation, gives the condition for the product of n (plasma electron density) and $\tau\varepsilon$ (time of confinement)

$$n\tau_\epsilon \geq 1.5 \times 10^{20} m^{-3} s \qquad (B.18)$$

Where n is the density of the electron inside the plasma and ◎∞is the confinement time. In the range of the 10 keV the reactivity <sv> I proportional to T^2, so the ignition condition can be expressed in terms of the so-called triple product:

$$n\tau_\varepsilon T = \frac{12kT^2}{\langle\sigma v\rangle \cdot \varepsilon_\alpha - 4cZ_{eff} \cdot (kT)^{1/2}} \qquad (B.19)$$

whose minimum is about $n\tau_\varepsilon T = 35 \times 10^{20} m^{-3} s\ keV$ around 10 keV for a D-T plasma (fig. B.3).

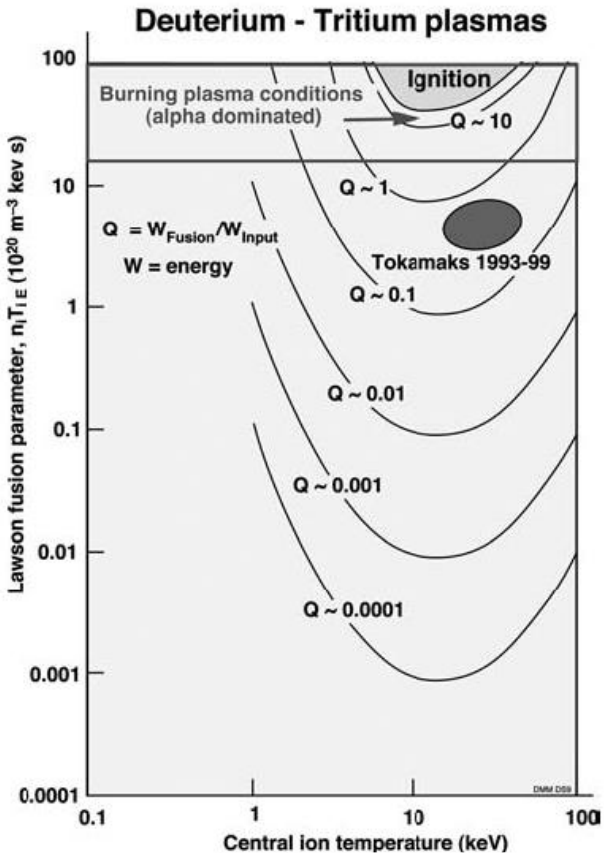

Figure B-3 triple product as a function of temperature for different Q value

The triple product clearly indicates the road to reach the ignition and develop fusion energy from a commercial device. According to the Lawson criteria the temperature of the fuel has to reach the 10 keV value and, contemporary, a sufficient density and energy confinement time have to be achieved.

The most important parameter, conventionally used to quantify the distance from the ignition, is the Q value, defined as the ratio between the reached fusion power

and the external heating power provided. Q > 1 will constitute the 'breakeven' on the plasma energy balance: the plasma will produce a larger amount of thermal power from fusion reactions than the amount of external power that must be provided in addition to the fusion power to maintain the plasma at thermonuclear temperature.

20% of the D-T fusion energy retained in the plasma in the form of an energetic alpha particle is sufficient to maintain the plasma at thermonuclear temperature without any external power (ignition condition, $Q=\infty$). However, no matter how good the confinement, future fusion reactors will operate with some external power for control purposes, so the practical definition of scientific feasibility is Q large enough that net electrical power can be economically produced, which is probably $Q > 10$. Two distinct approaches can be considered:

- Magnetic Confinement Fusion: trapping hot plasmas within the line of a strong magnetic field leading to a high density (order of magnitude $\sim 10^{20} m^{-3}$) and to an energy confinement time in the range of 2 to 4 seconds. Currently this method is the most promising in fusion research[90].
- Inertial Fusion: maximizing the density of a small D-T pellet heated symmetrically with lasers or particle beams, causing implosion due to momentum conservation[90], [91]. It's clear that in this concept the energy confinement time is extremely short. It's a possible alternative route to fusion power: examples of inertial fusion facilities are NIF[92], in phase of experimentation, and LMJ [93]and HiPER [94], in the design phase.

Considering the scope of this thesis, only magnetic confinement will be discussed.

Magnetic confinement

To maintain the plasma at thermonuclear temperatures is fundamental that it doesn't come in contact with the walls of the confinement chamber. Indeed, the vacuum chamber's materials could quickly cool the plasma temperature. As

explained before, the most promising method to confine the plasma avoiding the contact with the material of the chamber is the use of strong magnetic field.

A charged particle moving in a magnetic field will experience a Lorentz force which is perpendicular to both the direction of particle motion in the magnetic field direction. This force causes acceleration of the particle in the plane perpendicular to the magnetic field direction, producing a circular particle motion in that plane[95]. In fig. B.4 the motion of the charged particle in the magnetic field is shown.

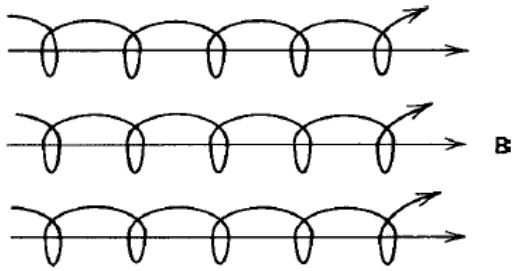

Figure B-4 Charged particles moving in a magnetic field

The motion results in a spiral about the field line. The radius of this spiral, or "*gyroradius*", is inversely proportional to the strength of the magnetic field.

A linear configuration is, however, practically impossible because of the large losses and confinement time. Thus, the solution is to confine the plasma into a closed configuration. The most reliable and simple configuration is the torus as shown in fig. B.5

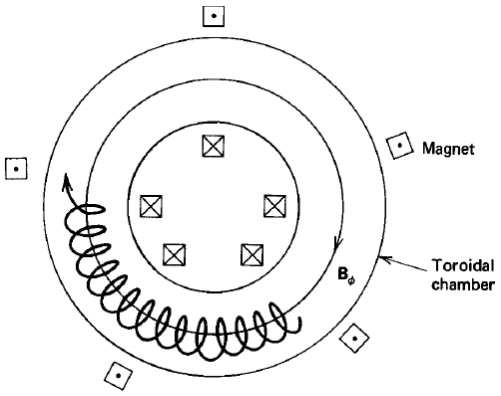

Figure B-5 Toroidal configuration for the particles confinement

A set of coils can be placed to produce the toroidal field **B**◎◎◎particles following the toroidal field lines would remain within the toroidal confinement chamber. Furthermore, the nonuniformity of the toroidal field coupled to its curvature produce a "*drift*" motion that are radially outward which would cause the particles to hit the wall.

Applying the Ampere's law to a circular surface (toroidal section) with radius R, it results:

$$\oint_L Bdl = 2\pi RB = \mu I \longrightarrow B \sim \frac{1}{R} \qquad (B.20)$$

Where B is the magnetic field, I the net current enclosed by the surface an ◎ the magnetic permeability. Consequently, the intensity of B decrease as 1/R. The particles drift is then characterized by the following velocity, due to the gradient of B:

$$v = \pm\frac{1}{2} v_\perp r \frac{B \times \nabla B}{B^2} \qquad (B.21)$$

Since the previous equation depends on the particle charge, ions will drift to the top of the toroidal section, while electrons to the opposite side. This charge separation induces an additional electric field that, coupled with the primary toroidal magnetic field, will induce a further drift of particles whose velocity can be written as:

$$v = \frac{E \times B}{B^2} \qquad (B.22)$$

This drift does not depend on particle charge and it is directed outwards from the centre of the toroid. Plasma is thus driven towards outer wall (also called low field side or LFS) of the torus losing confinement.
A poloidal magnetic field must be superimposed upon the toroidal one in order to

compensate the drift effect of the particles and maintain the plasma confinement. The result is a helical magnetic field contained within a toroidal chamber.

In early '50s a device capable to confine the plasma under the conditions explained above has been conceived in Russia and it has been officially presented for the first time during the International Conferences on the peaceful use of atomic energy in Geneva. The name of this device is Tokamak and It would become in the following years the most promising machine in the field of thermonuclear fusion.

The Tokamak

Tokamak is the Russian acronym of '*toroidal'naya kamera s magnitnymi katushkami*' (toroidal chamber with magnetic coils). It was proposed for the first by the two Russian scientists Igor Tamn and Andrei Sakharov, inspired by the original idea of Oleg Lavrentyev and realized by Lev Andreevich Artsimovich [96].

A simplified structure of the Tokamak with its main features is represented in fig. B.6

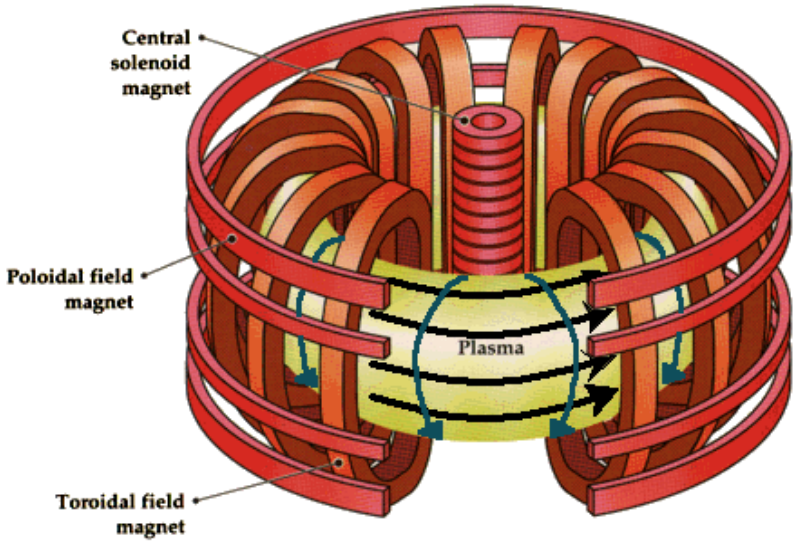

Figure B-6 Tokamak simple structure with main elements

The toroidal magnetic field is produced by a set of coils (Toroidal Field Coils) which encircled the plasma. Typical values of this filed are around 5-10 T. As explained

before, the sole toroidal field can't ensure a correct and stable confinement. Thus, a poloidal magnetic field that can keep the equilibrium between the plasma pressure and the magnetic forces is needed. This poloidal field is generated by the plasma current (15-25- MA) generated by the induction by the inner central solenoid acting as a transformer. The combination of the toroidal and poloidal filed results in a magnetic field with lines characterized by a helical trajectory around the torus that counteracts the typical drifting effect and also ohmically heats the plasma to electron temperatures T_e ~ 2-3 keV. The outer additional poloidal field coils are placed around the tokamak with the aim at controlling the shape of plasma. The shape of the plasma is important to control its confinement and a vertically elongated plasma shows advantaged in the confinement and in the achievable plasma pressure, thus increase its reactivity[96].

In a tokamak the heat losses are huge and they have to be compesated through a continous heating external sources in order to maintain the temperature needed for fusion reactions. The ohmic heating due to the plasma current is limited by the plasma resistivity that, being proportional to $T^{3/2}$, reduces its heating power with the increasing of temperatures. It becomes almost ineffective above 1 keV, significantly below the nedeed temperature to trigger the fusion reactions.

The main external heat sources used in large tokamak devices to supply the heating needs are:

- Neutral beam injection (NBI) system
- Absorption of radio-frequency (RF) waves

Into the NBI system a beam of ionized Deuterium is produced and accelerated in an electric field in a typical range from 60 to 150 keV which is successively guided through a neutralizer chamber inside the plasma. A population of fast ions, produced after charge exchange of fast particles, heat the plasma through elastic scattering.

In the RF the heating happens through resonant absorption of electromagnetic waves in plasma: waves with frequency typical of the ions and electrons cyclotron motion are absorbed resulting into an increased kinetic energy perpendicular to the magnetic field of the resonant particles. Collisions lead to the thermalization of the energy distribution at an increased temperature. Due to different ion and electron mass, different frequencies must be used: for ion cyclotron heating (ICRH) frequencies in the range of several tens of MHz are used, while the electron cyclotron resonance heating (ECRH) requires frequencies of the order of 100 GHz.

In the last few decades, the evolution of Tokamak machine undergoes to a fast development thanks to an enhanced capacity to control the plasmas, to have it in a more purity state and through the introduction of more stable magnetic configurations. This evolution can be evaluated in terms of fusion triple product plotted as function of the ionic temperature shows in fig. B.7

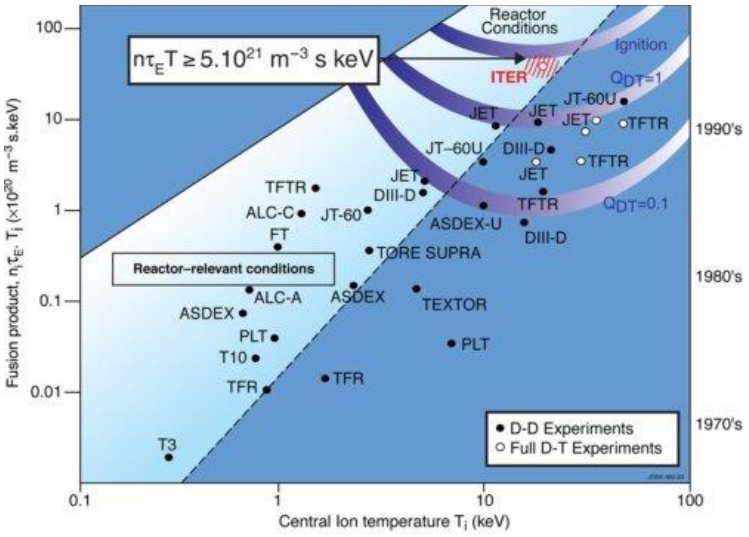

Figure B-7 Fusion 'triple products' and ion temperatures achieved in experiments over the past 25 years. The region in the top left corner is inaccessible because of the energy loss due to bremsstrahlung

The ignition condition can be reach with an improvement of the energy confinement time to values of several seconds. A machine with larger size of plasma in a reactor-scale experiment can be achieved this result. This is the main goal of the International Thermonuclear Experimental Reactor (ITER)[32], showed in figure B.8, a joint project involving many countries all over the World. This experiment,

which will start its operation in 2025, foresees the development of a Tokamak machine with major radius of 6.2 m, twice as the biggest Tokamak in operation JET (Joint European Torus) [97] which has 3 m of major radius. ITER will be able to produce 500 MW of fusion power for about 400 s with Q greater than 10.

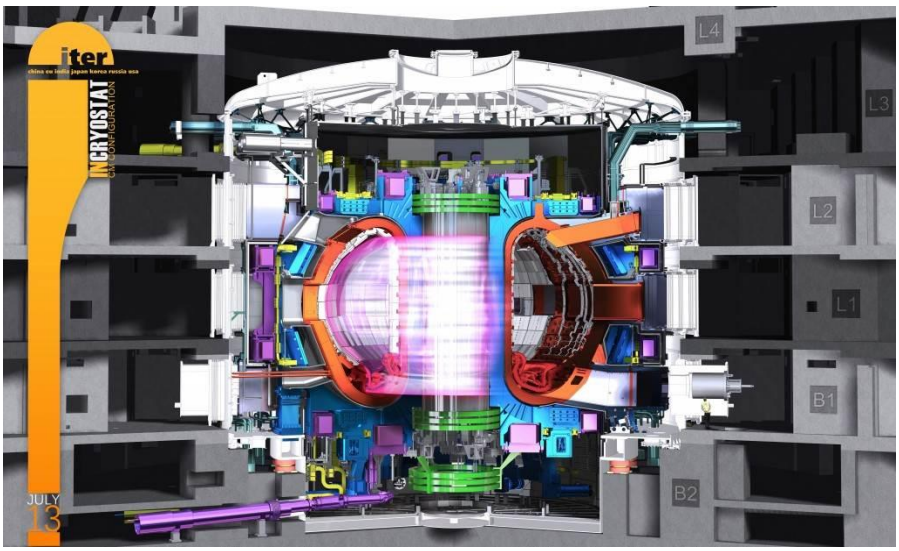

Figure B-8 ITER artistic view

The step to ITER, thanks to its large fusion power and neutron production, will allow to study dominant plasma heating by fast α-particles, confinement, plasma-wall interactions and test first-wall and low activation structural materials needed for an integrated power plant concept [98]. In tab.B.1 the ITER main parameters are shown.

Table B-1 ITER main parameters

Parameters	
Total Fusion Power	500 MW
Q = fusion power/additional heating power	≥ 10
Average neutron wall loading	0.57 MW/m^2
Plasma inductive burn time	≥ 300 s
Plasma major radius	6.2 m
Plasma minor radius	2.0 m

Plasma current (I_P)	15 MA
Vertical elongation @95% flux surface/separatrix	1.70/1.85
Triangularity @95% flux surface/separatrix	0.33/0.49
Toroidal field @ 6.2 m radius	5.3 T
Plasma volume	837 m^3
Plasma surface	678 m^2
Installed auxiliary heating/current drive power	73 MW (*NBI ~ 33 MW, ICRH ~ 40 MW*)

ITER is, without any doubts, the most important milestone toward the realization of fusion. Furthermore, on the way to the fusion energy many other devices have been programmed and many other aspect of plasma physics and fusion technology have to be investigated before the realization of the first fusion power plant in 2050: DEMO.

C. Roadmap to Fusion Energy

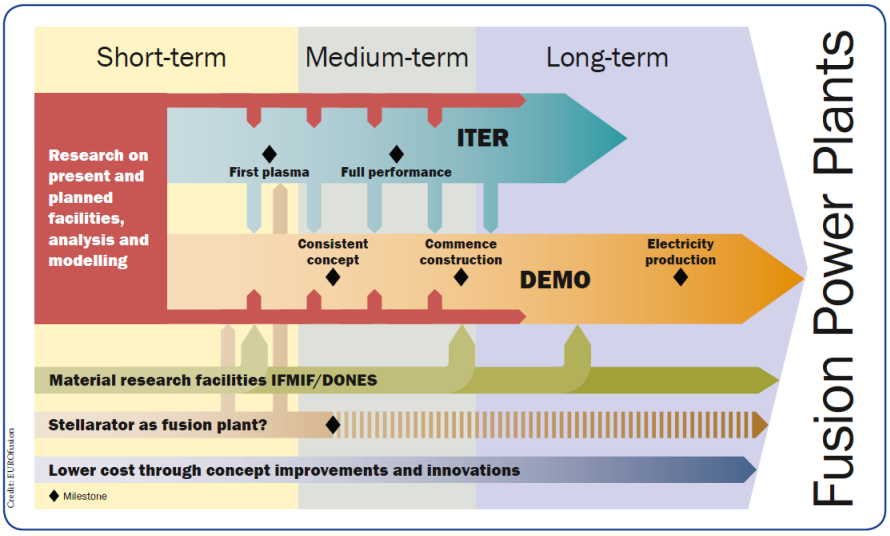

Figure C-1 Nutshell of the roadmap to the energy production from fusion energy

Fig. C.1 shows in a nutshell the roadmap to the production of electricity from fusion reactions. DEMO is the last step on a long and troubled path. Furthermore, there are many other challenges to be faced between ITER and DEMO. Inside the living document "*Fusion Electricity: a roadmap to the realisation of fusion energy*" [30]all these challenges are explained in details.

They can be summarized in 7 points which represents the key milestones:

- The first is the Plasma regimes of operations that deals with the confinement that must be reached at temperatures higher than the core of the sun.
- The second refers to the **power exhaust** and the particular machine component called **divertor** which has to withstand a large amount of heat loads. Inside the roadmap a facility called **"Divertor tokamak Test facility"** is foreseen. This point is particularly important for the aim of this thesis and it will be investigating in details in the next chapters.

- The third point is related to the Tritium self-sufficiency which requires efficient breeding and extraction systems to minimise tritium inventory.
- Another point is related to the safety of the power plant. Despite the intrinsic safety features of fusion, their implementation in a coherent architecture needs to be deeply investigated for DEMO.
- The sixth challenge refers to the reliability and availability of the components passing from ITER to DEMO, which will also require a complete Balance of Plant (BoP).
- Last but not least, fusion will have to demonstrate the potential for competitive cost of electricity, which will allow to penetrate rapidly the energy market.

The goal for all this seven points is to demonstrate that they can also work in a reactor scale. DEMO will be the first fusion reactor that will produce energy from fusion reactions. In the next chapter its state of art and main characteristics will be described.

D. DEMO fusion power plant – scope and main parameters

The DEMOnstration power plant, DEMO, will be the ITER's successor. Current fusion experiments were primarily designed to investigate plasma physics. However, DEMO must demonstrate the necessary technologies not only for controlling a more powerful plasma for safely generating electricity consistently, and for regular, rapid, and reliable maintenance for the plant. The plant has to take into account not only the physics requirements but also the engineering and technological limitations [99].

DEMO, a bridge between ITER and a fusion power plant (figure D.1), should demonstrate the feasibility of fusion by 2050. Its construction has to begin in the early 30s and start its operations in the next decade [30]. To meet such a dreaming schedule is of fundamental importance that ITER achieve its goals and a pragmatic approach is necessary. To meet its general objectives, DEMO will have to rely on simple and robust technical solutions and well established and reliable regimes of operation, as far as possible extrapolated from ITER, and on the use of materials adequate for the expected level of neutron fluence. Moreover, DEMO must be capable of addressing the third objective also through the test of the advanced components and technical solutions that will be developed in parallel for application in a fully-edged FPP, thus playing the role of a component test facility as part of its mission.

Currently a conceptual and definitive design of DEMO doesn't exist. At present the DEMO reactor design has been not formally selected and detailed operational requirements are not yet available. Is important, anyway, to establish performance

requirements and project development schedules linked to start objectives. Only in this way it will be possible to define a guideline in terms of constructions and selection of the technical features of the device.

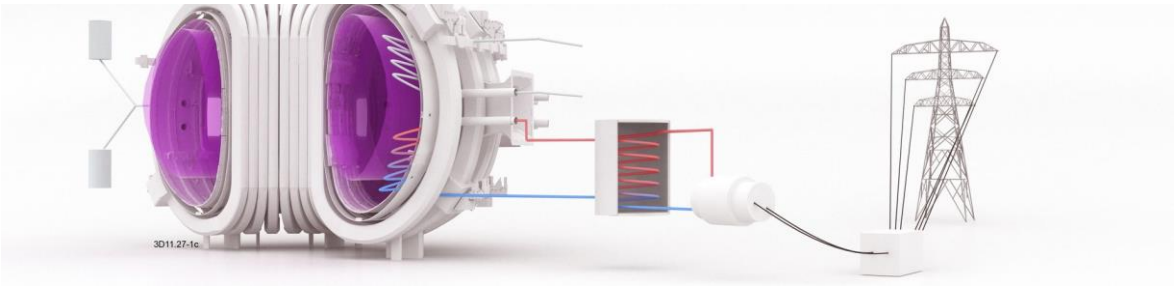

Figure D-1 DEMO power plant

To proceed in this manner is necessary to have a system engineering approach to understand the problems and evaluate the technical risks, to identify the design trade-offs and constraints addressing the most urgent issues (physics, technology and design), and to prioritize the R&D needs.

The design and R&D are expected to gain experience from the design and operation of ITER, furthermore there are several issue beyond ITER which requires a vigorous integrated design and technology R&D program. The principal open issues that It's necessary to highlight are [99]:

- the selection of the breeding blanket concept and, in particular, the selection of blanket coolant and the balance of plant (BoP) [100];
- the analysis of the divertor concept and its configuration. To achieve this goal, the Italian DTT machine will play a fundamental role;
- the selection of the first wall design and its mechanical and hydraulic integration to the blanket, taking into account that the first wall might see higher heat loads than assumed in previous studies;
- the selection of the heating and current drive (H&CD) mix;
- the selection of the remote maintenance scheme and a compatible plasma scenario.

One of the crucial point is the size of the machine and the amount of power that can be reliably produced and controlled in it. According to the last issue two different DEMO design options are currently investigated, in an attempt to identify a realistic range of possibilities:

- A near-term DEMO (DEMO1) is a rather \conservative baseline design", i.e. a DEMO concept deliverable in the short to medium term (e.g., construction possibly starting approximately 20 years from now), based on the expected performance of ITER (Q = 10) with reasonable improvements in science and technology; i.e., a large, modest power density, long-pulse inductively supported plasma in a conventional plasma scenario. The design of Balance of Plant (BoP) for a near-term DEMO must also make use of mature and reliable technology [99]. Figure D.2 shows the DEMO1 main parameters.
- A more advanced, DEMO design concept (DEMO2) based around more optimistic (but \less mature") physics assumptions, which are at the upper limit of what may be achieved in ITER phase-2, i.e., an advanced higher power density high current drive steady-state plasma scenario. It is clear that this can only be delivered on a longer term (e.g., construction to be started on a much longer time scale assuming that the required significant advances in the physics basis be demonstrated using ITER and the limited number of satellite fusion devices available in the next 10/20 years)[99].

It is not to be inferred that two DEMOs should be built but rather that there is a need to incorporate some flexibility to mitigate the uncertainty in the design requirements for DEMO[99].

EU DEMO1 2015	
No of TFCoils	18
Major radius R (m)	9.072
Minor radius a (m)	2.927
Aspect ratio (R/a)	3.1
Plasma elongation	1.59
Plasma triangularity	0.33
Fusion power (MW)	2037
Average neutron wall loading (PROCESS code)	1.05
Net electric power (MW)	500

Figure D-2 Main parameters of DEMO1

Bibliography

[1] K. S. Krane and W. G. Lynch, *Introductory Nuclear Physics*. 1989.

[2] G. R. Satchler and G. R. Satchler, "Some Background Information," in *Introduction to Nuclear Reactions*, 1990.

[3] G. Nelson and D. Reilly, "Gamma-ray interactions with matter," *Passiv. Nondestruct. Anal. Nucl. Mater.*, 1991.

[4] R. 0. Simmons, "Radiation Damage in Solids. Douglas S. Billington and James H. Crawford , Jr. Princeton University Press, Princeton, N.J., 1961. xi + 450 pp. Illus. $12.50," *Science (80-.).*, 1961, doi: 10.1126/science.133.3469.2007.

[5] M. Nastasi and J. W. Mayer, *Ion implantation and synthesis of materials*. 2006.

[6] T. D. Burchell, "Radiation effects in graphite," in *Comprehensive Nuclear Materials*, 2012.

[7] G. F. Knoll, *Radiation Detection and Measurement, Third Edition*. 2000.

[8] ICRP, "ICRP Publication 60: 1990 Recommendations of the International Commission on Radiological Protection," *Ann. ICRP*, 1990.

[9] Anon., "American National Standard: neutron and gamma-ray flux-to-dose rate factors." 1977, Accessed: Dec. 23, 2020. [Online]. Available: https://inis.iaea.org/search/search.aspx?orig_q=RN:15021593.

[10] A. N. Society, "Neutron and Gamma-Ray Fluence-to-Dose factors," 1996.

[11] B. T. Price, *Radiation shielding*. 1959.

[12] T. Rockwell, III, "Reactor Shielding Design Manual," U.S. Atomic Energy Commission, Mar. 1956. doi: 10.2172/4360248.

[13] T. J. Seed, W. F. Miller, and G. E. Bosler, "TRIDENT: A NEW TRIANGULAR MESH DISCRETE-ORDINATES CODE.," 1978.

[14] M. Z. Youssef and R. Feder, "Summary of the up-to-date 3-D nuclear analyses of iter diagnostics generic equatorial port plug (GEPP) performed with the attila design code," *Fusion Sci. Technol.*, 2013, doi: 10.13182/FST64-571.

[15] R. Eckhardt, "Stan ulam, john von neumann, and the monte carlo method," *Los Alamos Sci.*, 1987.

[16] N. Metropolis, A. W. Rosenbluth, M. N. Rosenbluth, A. H. Teller, and E. Teller, "Equation of state calculations by fast computing machines," *J. Chem. Phys.*, 1953, doi: 10.1063/1.1699114.

[17] N. Metropolis and S. Ulam, "The Monte Carlo Method," *J. Am. Stat. Assoc.*, 1949, doi: 10.1080/01621459.1949.10483310.

[18] N. Metropolis, "The beginning of the Monte Carlo method," *Los Alamos Sci. (1987 Spec. Issue Dedic. to Stanis?aw Ulam)*, 1987.

[19] X-5 Monte Carlo Team, *MCNP - A General Monte Carlo N-Particle Transport Code, Version 5 Volume II: User's Guide*. 2008.

[20] X-5 Monte Carlo Team, "MCNP - Version 5, Vol. 1: Overview and Theory," *La-*

Ur-03-1987, 2003.

[21] J. F. Briesmeister, “MCNPTM – A General Monte Carlo N-Particle Transport Code,” *Los Alamos Natl. Lab.*, 2000.

[22] S. W. Mosher *et al.*, *ADVANTG: An Automated Variance Reduction Parameter Generator*. 2015.

[23] T. M. Evans, A. S. Stafford, R. N. Slaybaugh, and K. T. Clarno, “Denovo: A new three-dimensional parallel discrete ordinates code in SCALE,” *Nucl. Technol.*, 2010, doi: 10.13182/NT171-171.

[24] J. C. Wagner and A. Haghighat, “Automated variance reduction of Monte Carlo shielding calculations using the discrete ordinates adjoint function,” *Nucl. Sci. Eng.*, 1998, doi: 10.13182/NSE98-2.

[25] J. C. Wagner, D. E. Peplow, and S. W. Mosher, “Fw-cadis method for global and regional variance reduction of monte carlo radiation transport calculations,” *Nucl. Sci. Eng.*, 2014, doi: 10.13182/NSE12-33.

[26] J.-C. Sublet, “The FISPACT-II User Manual,” 2015. doi: 10.13140/RG.2.1.4777.1281.

[27] *Engineering Compendium on Radiation Shielding*. 1968.

[28] D. Valenza, H. Iida, R. Plenteda, and R. T. Santoro, “Proposal of shutdown dose estimation method by Monte Carlo code,” *Fusion Eng. Des.*, 2001, doi: 10.1016/S0920-3796(01)00188-0.

[29] R. Villari *et al.*, “Shutdown dose rate assessment with the Advanced D1S method: Development, applications and validation,” *Fusion Eng. Des.*, 2014, doi: 10.1016/j.fusengdes.2014.01.071.

[30] F. Romanelli, “Fusion Electricity: A roadmap to the realisation of fusion energy,” *EFDA*, 2012.

[31] J. A. Wesson, *Tokamaks 3rd Edition*. 2005.

[32] ITER, “THE ITER TOKAMAK,” *https://www.iter.org/mach*, 2020. .

[33] R. A. Pitts *et al.*, “Physics basis for the first ITER tungsten divertor,” *Nuclear Materials and Energy*. 2019, doi: 10.1016/j.nme.2019.100696.

[34] A. J. H. Donné, “The European roadmap towards fusion electricity,” 2019, doi: 10.1098/rsta.2017.0432.

[35] H. Zohm, “Hold Points on the PEX programme (towards the realisation of the PEX phase 3 report),” 2018.

[36] R. Martone, R. Albanese, F. Crisanti, P. Martin, and A. Pizzuto, Eds., *DTT - Divertor Tokamak Test facility - Interim Design Report*. Frascati, 2019.

[37] G. Di Gironimo, D. Marzullo, R. Mozzillo, A. Tarallo, and S. Grazioso, “The DTT device: Advances in conceptual design of vacuum vessel and cryostat structures,” *Fusion Eng. Des.*, 2019, doi: 10.1016/j.fusengdes.2019.04.024.

[38] F. Maviglia, R. De Luca, S. Roccella, G. Maddaluno, G. Ramogida, and E. Visca, “Thermal-hydraulic analysis for first wall and thermal shield of Divertor Tokamak test facility,” *Fusion Eng. Des.*, 2019, doi: 10.1016/j.fusengdes.2019.03.157.

[39] R. Villari *et al.*, “Nuclear design of Divertor Tokamak Test (DTT) facility,” *Fusion Eng. Des.*, 2020, doi: 10.1016/j.fusengdes.2020.111551.

[40] G. Maddaluno, D. Marzullo, G. Mazzitelli, S. Roccella, G. Di Gironimo, and R. Zanino, "The DTT device: Divertor solutions for alternative configurations including liquid metals," *Fusion Eng. Des.*, 2017, doi: 10.1016/j.fusengdes.2017.03.172.

[41] G. Di Gironimo *et al.*, "Improving concept design of divertor support system for FAST tokamak using TRIZ theory and AHP approach," *Fusion Eng. Des.*, 2013, doi: 10.1016/j.fusengdes.2013.07.005.

[42] V. Pericoli Ridolfini, R. Ambrosino, S. Mastrostefano, P. Chmielewski, M. Poradziński, and R. Zagórski, "A comparative study of the effects of liquid lithium and tin as DEMO divertor targets on the heat loads and SOL properties," *Phys. Plasmas*, 2019, doi: 10.1063/1.5055017.

[43] B. Wolle, "Tokamak plasma diagnostics based on measured neutron signals," *Phys. Rep.*, 1999, doi: 10.1016/S0370-1573(98)00084-2.

[44] R. J. Goldston, D. C. McCune, H. H. Towner, S. L. Davis, R. J. Hawryluk, and G. L. Schmidt, "New techniques for calculating heat and particle source rates due to neutral beam injection in axisymmetric tokamaks," *J. Comput. Phys.*, 1981, doi: 10.1016/0021-9991(81)90111-X.

[45] "FENDL-2.1: Fusion Evaluated Nuclear Data Library ver.2.1," 2004. https://www-nds.iaea.org/fendl21/.

[46] "FENDL-3.1d: Fusion Evaluated Nuclear Data Library ver.3.1d," 2018. https://wwwnds.iaea.org/fendl/.

[47] ICRP, *ICRP Publication 74. Conversion Coefficients for use in Radiological Protection against External Radiation.* 1996.

[48] M. Fabbri and A. Cubì, "A tool to manupulate MCNP weight window (WW) and to generate Global Variance Reduction (GVR) parameters." 2019.

[49] "CRESCO ENEA High Performance Computing." .

[50] F. Iannone *et al.*, "MARCONI-FUSION: The new high performance computing facility for European nuclear fusion modelling," *Fusion Eng. Des.*, 2018, doi: 10.1016/j.fusengdes.2017.11.004.

[51] Y. Wu, "CAD-based interface programs for fusion neutron transport simulation," *Fusion Eng. Des.*, 2009, doi: 10.1016/j.fusengdes.2008.12.041.

[52] "Ansys SpaceClaim." https://www.ansys.com/it-it/products/3d-design/ansys-spaceclaim.

[53] P. Agostinetti *et al.*, "Conceptual design of a neutral beam heating & current drive system for DTT," *Fusion Eng. Des.*, 2019, doi: 10.1016/j.fusengdes.2018.12.087.

[54] A. Colangeli *et al.*, "Neutronics study for DTT tokamak building," *Fusion Eng. Des.*, 2019, doi: 10.1016/j.fusengdes.2019.04.047.

[55] "Italian 101/2020 Decree Law." [Online]. Available: https://www.gazzettaufficiale.it/eli/id/2020/08/12/20G00121/sg.

[56] European Parliament, "Council Directive 2013/59/Euratom of 5 December 2013," *Off J Eur Commun L13*, 2014.

[57] Wolfram Research Inc., "Mathematica 12.0," *Wolfram Research*. 2019.

[58] Bs En 206:2013:, "BSI Standards Publication Concrete — Specification , performance , production and conformity," *Br. Stand.*, 2013.

[59] “Concrete.” http://www.concrete.org.uk/.

[60] R. J. McConn, C. J. Gesh, R. T. Pagh, R. A. Rucker, and R. Williams III, “Compendium of Material Composition Data for Radiation Transport Modeling,” Richland, WA (United States), Mar. 2011. doi: 10.2172/1023125.

[61] S. Yoshida *et al.*, “Measurement of radiation skyshine with D-T neutron source,” *Fusion Eng. Des.*, 2003, doi: 10.1016/S0920-3796(03)00196-0.

[62] M. Wakisaka *et al.*, “Analysis of neutron propagation from the skyshine port of a fusion neutron source facility,” *Nucl. Instruments Methods Phys. Res. Sect. A Accel. Spectrometers, Detect. Assoc. Equip.*, 2005, doi: 10.1016/j.nima.2005.06.082.

[63] S. J. Lindenbaum, “Proc. Conference on Shielding of High-Energy Accelerators,” p. 28, 1957.

[64] B. J. (University of C. R. L. P. S. Moyer, “No Title.”

[65] M. S. Livingston and J. P. Blewett, *Particle Accelerators*. McGraw-Hill, 1962.

[66] M. S. Livingston, “Standard Cyclotron,” vol. 160, 1952.

[67] M. S. Livingston, “Synchrocyclotron,” *Annu. Nucl. Sci.*, vol. 167, 1952.

[68] H. W. Patterson, *Accelerator Health Physics*. 1973.

[69] T. M. Jenkins, “Accelerator boundary doses and skyshine,” *Health Phys.*, 1974, doi: 10.1097/00004032-197409000-00002.

[70] S. J. Lindenbaum, “Skyshine.”

[71] S. J. Lindenbaum, “Shielding of High Energy Accelerators,” *Annu. Rev. Nucl. Sci.*, 1961.

[72] A. Rindi, “Skyshine – A Paper Tiger,” *Part. Accel.*, vol. 7, pp. 22–39, 1975.

[73] K. M. Case and F. de Hoffman, *Introduction to Neutron Diffusion Theory*. 1953.

[74] M. Ladu, M. Pelliccioni, P. Picchi, and G. Verri, “A contribution to the skyshine study,” *Nucl. Instruments Methods*, 1968, doi: 10.1016/0029-554X(68)90614-9.

[75] G. Granucci *et al.*, “The DTT device: System for heating,” *Fusion Eng. Des.*, 2017, doi: 10.1016/j.fusengdes.2017.04.124.

[76] S. Garavaglia *et al.*, “Preliminary conceptual design of the DTT EC heating system,” *Fusion Eng. Des.*, 2019, doi: 10.1016/j.fusengdes.2018.12.018.

[77] S. Garavaglia and E. Al, “Progress of DTT ECH system Design,” 2020.

[78] A. Turner *et al.*, “Nuclear analysis and shielding optimisation in support of the ITER In-Vessel Viewing System design,” *Fusion Eng. Des.*, 2014, doi: 10.1016/j.fusengdes.2014.01.066.

[79] C. J. Solomon, C. R. Bates, and J. Kulesza, “The MCNPTools Package: Installation and Use.” 2017.

[80] E. G. Stassinopoulos and J. P. Raymond, “The Space Radiation Environment for Electronics,” *Proc. IEEE*, 1988, doi: 10.1109/5.90113.

[81] G. Lindström, “Radiation damage in silicon detectors,” 2003, doi: 10.1016/S0168-9002(03)01874-6.

[82] CERN, “Radiation Hardness.” .

[83] JEDEC, “Measurement and Reporting of Alpha Particle and Terrestrial Cosmic Ray Induced Soft Error in Semiconductor Devices,” *JEDEC Stand. JESD89A*, 2006.

[84] ISO 10303-21, “Industrial automation systems and integration — Product data representation and exchange — Part 21 : Implementation methods : Clear text encoding of the exchange structure,” *Int. Organ.*, 2016.

[85] M. Dental, “Proposed Strategy for Electronics Exposed to Nuclear Radiations in ITER,” 2015.

[86] G. Gamow, “Zur Quantentheorie des Atomkernes,” *Zeitschrift für Phys.*, 1928, doi: 10.1007/BF01343196.

[87] N. A. Krall, A. W. Trivelpiece, and K. R. Symon, “Principles of Plasma Physics,” *IEEE Transactions on Plasma Science*. 1974, doi: 10.1109/TPS.1974.4316834.

[88] J. D. Lawson, “Some criteria for a power producing thermonuclear reactor,” *Proc. Phys. Soc. Sect. B*, 1957, doi: 10.1088/0370-1301/70/1/303.

[89] T. J. M. Boyd and J. J. Sanderson, *The Physics of Plasmas*. 2003.

[90] D. Maisonnier, I. Cook, and P. Sardain, “A conceptual study of commercial fusion power plants,” *... Power Plant Concept. ...*, 2005.

[91] J. D. Lindl, R. L. Mccrory, and E. M. Campbell, “Progress toward Ignition and Burn Propagation in Inertial Confinement Fusion,” *Phys. Today*, 1992, doi: 10.1063/1.881318.

[92] W. J. Hogan, R. Bangerter, and G. L. Kulcinski, “Energy from Inertial Fusion,” *Phys. Today*, 1992, doi: 10.1063/1.881319.

[93] M. Tobin *et al.*, “Target area design basis and system performance for the national ignition facility,” *Fusion Technol.*, 1994, doi: 10.13182/fst94-a40248.

[94] N. Fleurot, C. Cavailler, and J. L. Bourgade, “The Laser Mégajoule (LMJ) Project dedicated to inertial confinement fusion: Development and construction status,” 2005, doi: 10.1016/j.fusengdes.2005.06.251.

[95] W. M. Stacey, *Fusion: An Introduction to the Physics and Technology of Magnetic Confinement Fusion*. 2010.

[96] L. A. Artsimovich, “Tokamak devices Review Paper TOKAMAK DEVICES,” *Nucl. Fusion*, 1972.

[97] D. L. Smart, “JOINT EUROPEAN TORUS (JET).,” 1983, doi: 10.13182/fst83-a22886.

[98] T. K. Fowler and W. Happer, “ The Fusion Quest ,” *Phys. Today*, 1998, doi: 10.1063/1.882155.

[99] G. Federici *et al.*, “Overview of the design approach and prioritization of R&D activities towards an EU DEMO,” *Fusion Eng. Des.*, 2016, doi: 10.1016/j.fusengdes.2015.11.050.

[100] G. Federici, L. Boccaccini, F. Cismondi, M. Gasparotto, Y. Poitevin, and I. Ricapito, “An overview of the EU breeding blanket design strategy as an integral part of the DEMO design effort,” *Fusion Eng. Des.*, 2019, doi: 10.1016/j.fusengdes.2019.01.141.

Ringraziamenti

"Tutto ciò che dobbiamo decidere è cosa fare con il tempo che ci viene concesso"

Gandalf, stregone della Terra di Mezzo

E così siamo arrivati alla fine, e come in tutte le storie è un onore ringraziare tutte quelle persone che questa particolare storia l'hanno vissuta accanto a me e mi hanno aiutato ad arrivare alla conclusione.

Il primo grazie va al prof. Romolo Remetti e alla dott.ssa Rosaria Villari, senza il loro aiuto e supporto tutto questo non sarebbe stato possibile. Ho avuto molti professori nella mia vita, tuttavia davvero pochi maestri.

Insieme a loro il mio grazie va al dott. Davide Flammini e al dott. Fabio Moro perché tutto questo è frutto non solo del loro aiuto tecnico ma anche e soprattutto di tutte quelle parole dette davanti alla macchinetta del caffè.

Grazie al dott. Nicola Fonnesu per la disponibilità e la cordialità, per tutto l'aiuto passato e per quello futuro. Grazie ai miei compagni di viaggio, il dott. Giovanni Mariano con il quale ho condiviso con estremo piacere tutto il percorso di dottorato fra risate, scherzi, sfide, ansie e qualche arrabbiatura, e al dott. Simone Noce, è sempre bello trovare un nuovo amico.

Grazie al dott. Raul Luis, dell'università di Lisbona per l'aiuto, la disponibilità, la gentilezza e la competenza dimostrata durante il lavoro fatto insieme, specie nelle fasi iniziali.

A tutto il gruppo di neutronica dell'ENEA, al dott. Mario Pillon, al dott. Maurizio Angelone, al dott. Antonino Pietropaolo al dott. Salvatore Fiore e al dott. Stefano Laureti va il mio grazie per avermi accolto e aiutato con gentilezza e professionalità.

Grazie a Roberta, per avermi letteralmente sopportato per tutti questi anni nel lavoro e nella vita di tutti i giorni, comprese le mie isterie.
Alla mia bellissima famiglia, a chi di loro non c'è più ma c'è sempre stato, ai miei genitori, ai miei zii, a mio fratello e mio cugino e alle loro famiglie il solo grazie non sarà mai sufficiente.
Grazie ai miei amici di una vita, a Matteo, a David e Alessandro: se gli amici sono la famiglia che ti sei scelto, non avrei potuto scegliere meglio.
In ultimo, ma non per importanza, un pensiero e un ringraziamento particolare a tutti gli amici di Sogna&Realizza, un gruppo speciale, un "*dream team*", all'interno del quale ho imparato tante cose e condiviso tante idee.

A tutti voi il mio *grazie* di cuore.

Andrea